Finite Element Modelling of the Expansion of Small Tubular Parts by Internal Pressure

By

David Chua Sing Ngie, B.Eng. (Hons.)

This thesis is submitted to Dublin City University as the fulfilment of the requirement for the award of the degree of

Doctor of Philosophy

Supervisors:

Professor M.S.J. Hashmi, Ph.D. D.Sc.

B.J. Mac Donald Ph.D.

School of Mechanical and Manufacturing Engineering

Dublin City University

June 2002

Declaration

I hereby certify that this material, which I now submit for assessment on the programme of study leading to the award of Doctor of Philosophy, is entirely my own work and has not been taken from the work of others save and to the extent that such work has been cited and acknowledged within the text of my work.

Signed: _____ ID No: 98970909

David Chua Sing Ngie

Date: 29-07-2002

Acknowledgements

I would like to express my sincere gratitude to Prof. M. S. J. Hashmi and Dr. B. J. Mac Donald for their guidance and help over the last three years, for the opportunity to work in a stimulating research environment and for the chance to present my work at international conferences.

I would also like to thank my technicians Mr. Liam Domican and Mr. Keith Hickey for their assistances during the experimental set up.

I would also like to thank my friend Mr. Clint Carolan for his assistance and support throughout the past years.

Finally, I thank my parents for their encouragement and support throughout my studies.

Finite Element Modelling of the Expansion of Small Tubular Parts by Internal Pressure

David Chua Sing Ngie B.Eng. (Hons.)

ABSTRACT

A stent is a device that is used to support arterial walls to alleviate the blockage of arteries by plaque. The slotted tube stent is one of the most common stent designs being widely used in many patients today. The amount of stent implantations is growing each year and for this it is becoming increasingly important in interventional cardiology. One of the reasons is that the use of stents has proved more effective in the therapy of coronary stenosis. However, it is evidenced that the success of the stent implantation is limited by re-stenosis, which is discussed almost entirely in terms of medical and biological reasons.

This work is concerned with investigating the deformation mechanism with variable conditions during slotted tube expansion processes using numerical simulation. The simulations were run and analysed using commercial finite element software. A non-linear explicit solution method was used in each case. The processes chosen for simulation were: slotted tube expansion without balloon catheter, slotted tube expansion with balloon catheter, scaling the stent size, stent production defect and slotted tube expansion with the presence of artery and plaque. A number of process parameters were varied for balloon catheter (i.e. balloon length, thickness and friction factor) and the subsequent effects on the process were identified. Some trial experimental tests were carried out to verify the finite element results from the computer simulations.

From the results obtained it was concluded that higher rate of pressure increase results in higher stresses in stent for similar levels of expansion. Deployment of higher magnitude pressure might increase the expansion in radial direction but it does not necessarily increase the uniformity of the slotted tube. Appropriate balloon length has to be chosen to obtain a uniform expansion. Friction could reduce the foreshortening of the stent. When scaling down the stent, displacement deceases proportionally for similar deployment pressure and stent geometry. It was found from the simulations that the tubular stent is not very sensitive to imperfections. Altering sent strut configuration and number has practical effects on the clinical use of vascular stents, as the magnitude of expansion will change. The deformation characteristic of the slotted tube during deployment is affected by the presence of artery and plaque.

Table of Contents

ABSTRACT I

NOMENCLATURE VII

LIST OF FIGURES IX

LIST OF TABLES XV

Chapter 1 1

INTRODUCTION 1

1.1 Introduction 1

1.2 Coronary Artery Disease 1

1.3 Arterial Bypass Surgery 3

1.4 Percutaneous Transluminal Coronary Angioplasty (PTCA) 4

1.5 Stent Implantation 5

1.6 Atherectomy 6

1.7 Laser Angioplasty 7

Chapter 2 11

LITERATURE SURVEY 11

2.1 History of Stent 11

2.2 Basic Initial Designs of Stent 12

2.2.1 Self-expanding mesh 12

2.2.2 Coil stent 12

2.2.3 Slotted tube stent 13

2.3 Stent Techniques 15

2.3.1 Shape memory alloy 15

2.3.2 Balloon expandable 15

2.3.3 Self-expanding 16

2.4 Overview of the first clinical stent applications 16

2.5 Mechanical Considerations 17

2.6 Stent Features 18

2.6.1 Flexibility 18

2.6.2 Radial (Hoop) Strength 19

2.6.3 Foreshortening 19
2.6.4 Expansion Rate 20
2.6.5 Vessel Coverage 20
2.6.6 Metal Fraction 20
2.6.7 Radiopacity 21
2.6.8 Fatigue Tolerance 21
2.7 Material Composition and Surface Characteristic 21
2.8 An Experimental Approach 23
2.8.1 Stent Geometry 23
2.8.2 Pressure Deployment 23
2.9 A Finite Element Analysis Approach 24
2.10 Summary of Literature Survey 26
Chapter 3 **27**
BRIEF INTRODUCTION ON FEA **27**
3.1 Introduction 27
3.2 The Finite Element Method 27
3.2.1 General Theory 29
3.2.2 Non-linearities 34
3.2.3 Solution Methodology 35
3.3 LS-DYNA3D Theoretical Methods 38
3.3.1 Solution Methodology 38
3.3.2 Element Formulation 39
3.3.3 Material Model 41
3.3.4 Contact Algorithm 43
Chapter 4 **46**
SIMULATION AND ANALYSIS OF STENT **46**
4.1 Stent Expansion without Balloon 46
4.1.1 Modelling 47
4.1.2 Boundary Conditions, Loading and Solution 50
4.1.3 Results and Discussion 52
4.1.3.1 Load Case I 53
4.1.3.2 Load case II 58
4.1.3.3 Load Case III 64
4.1.3.4 Load Case IV 69

4.1.3.5 Load Case V 74
4.1.4 Comparison of Results 80
4.1.5 Study Limitations 85
Chapter 5 **87**
SIMULATION AND ANALYSIS OF STENT AND BALLOON **87**
5.1 Stent Expansion with Balloon 87
5.1.1 Modelling 87
5.1.2 Boundary Conditions, Loading and Solution 91
5.1.3 Results and Discussion 92
5.2 Analysis of Deployment Pressure on Slotted Tube Stent Expansion 99
5.2.1 Modelling 99
5.2.2 Boundary Condition, Loading and Solution 103
5.2.3 Result and Discussion 105
5.2.3.1 Deployment pressure of 2 MPa 105
a) Deployment pressure vs. displacement 111
b) Elastic recoil 113
c) Slotted tube foreshortening 114
5.2.3.2 Deployment Pressure of 2.5 MPa 115
a) Deployment pressure vs. displacement 121
b) Elastic Recoil 122
c) Slotted tube foreshortening 123
5.2.3.3 Deployment pressure of 2.8 MPa 125
a) Deployment pressure vs. displacement 130
b) Elastic recoil 131
c) Slotted tube foreshortening 132
5.3 Analysis of Balloon Length on Slotted Tube Expansion 133
5.3.1 Modelling 134
5.3.2 Boundary Condition, Loading and Solution 136
5.3.3 Result and Discussion 138
5.3.3.1 Stress analysis 138
5.3.3.2 Deployment pressure vs. displacement 141
5.3.3.3 Elastic recoil 142
5.3.3.4 Foreshortening 144
5.3.3.5 Uniformity of the slotted tube 145

5.4 Analysis of Friction on Slotted Tube Expansion 147
5.4.1 Modelling and Loading 148
5.4.2 Result and Discussion 148
5.4.2.1 Stress analysis 148
5.4.2.2 Deployment pressure vs. displacement 152
5.4.2.3 Elastic recoil 152
5.4.2.4 Foreshortening 153
5.5 Analysis of Scaling the Slotted Tube Size 154
5.5.1 Modelling and Loading 155
5.5.2 Result and Discussion 156
5.5.2.1 Stress analysis 156
5.5.2.2 Deployment pressure vs. displacement 158
5.5.2.3 Elastic recoil 160
5.5.2.4 Foreshortening 161
5.6 Analysis of Stent Production Defects 162
5.6.1 Modelling and Loading 163
5.6.2 Result and Discussion 164
5.6.2.1 Stress analysis 164
5.6.2.2 Deployment pressure vs. displacement 170
5.6.2.3 Elastic recoil 171
5.6.2.4 Foreshortening 171
5.7 Analysis of Balloon Thickness on Slotted Tube Expansion 172
5.7.1 Modelling and Loading 172
5.7.2 Result and Discussion 176
5.7.2.1 Stress analysis and uniformity 176
5.7.2.2 Deployment pressure vs. displacement 182
5.7.2.3 Elastic recoil 183
5.7.2.4 Foreshortening 184
5.8 Analysis of Slotted Tube Stent Geometry 185
5.8.1 Modelling and Loading 185
5.8.2 Result and Discussion 192
5.8.2.1 Stress analysis 192
5.8.2.2 Deployment pressure vs. displacement 197
5.8.2.3 Elastic recoil 198

5.8.2.4 Foreshortening 200
5.9 Simulation of Balloon, Stent, Plaque and Artery 201
5.9.1 Modelling and Loading 202
5.9.2 Result and Discussion 205
5.9.2.1 Stress analysis within stent, plaque and arterial wall 205
5.9.2.2 Expansion characteristic 211
Chapter 6 215
EXPERIMENTAL WORK 215
6.1 Introduction 215
6.2 Experimental Equipment 215
6.3 Material Used 218
6.4 Experimental Procedures 221
6.5 Result and Discussion 222
Chapter 7 230
CONCLUSIONS 230
7.1 Expansion of Slotted Tube Stent without Balloon 230
7.2 Expansion of Slotted Tube Stent with Balloon 231
7.3 Analysis of Deployment Pressure on Slotted Tube Stent Expansion 231
7.4 Analysis of Balloon Length on Slotted Tube Stent Expansion 232
7.5 Analysis of Friction on Slotted Tube Stent Expansion 232
7.6 Analysis of Scaling the Slotted Tube Stent Size 232
7.7 Analysis of Slotted Tube Stent Production Defect 233
7.8 Analysis of Balloon Thickness on Slotted Tube Stent Expansion 233
7.9 Analysis of Slotted Tube Stent Geometry 234
7.10 Simulation of Balloon, Stent, Plaque and Artery 234
7.11 Experimental Work 235
7.12 Thesis Contribution 235
7.13 Recommendations for Further Work 236
REFERENCES 238
Appendix 1: 247
LIST OF PUBLICATIONS 247

NOMENCLATURE

Symbol	Definition	Dimension
c	Sonic wave propagation velocity	m/s
f	Force	N
l	Element characteristic length	m
t	Time	seconds
v	Element volume	m^3
x	Velocity of specific node	m/s^3
B	Strain-displacement matrix	-
C	Global damping matrix	-
E	Stress-strain matrix	-
E	Young's modulus	MPa
F	Concentrated force	N
G	Shear modulus	MPa
H	Displacement interpolation shape matrix	-
I	Identify matrix	-
K	Global stiffness matrix	-
M	Global mass matrix	-
R	Load vector	-
T	Period	-
U	Nodal displacement	m
$\overline{U}$	Virtual displacement in global X direction	m
$\dot{U}$	Nodal point velocities	m/s
$\ddot{U}$	Nodal point accelerations	m/s^3
$\overline{V}$	Virtual displacement in global Y direction	m
W	Strain energy density function	-
$\overline{W}$	Virtual displacement in global Z direction	m

Greek

α	Number of hourglass mode	-
δ	Stress	N/m^3
ε	Strain	-
κ	Damping property parameter	-
ρ	Density	Kg/m^3
Γ	Hourglass shape vector	-

Subscripts

p	Plastic	-
Tan	Tangent	-
CR	Critical	-
S	Surface	-
V	Volume	-

Superscripts

eff	Effective	-
i	Points in space	-
t	Time	seconds
B	Body	-
S	Surface	-
T	Transpose of a matrix	-

LIST OF FIGURES

Figure 1.1: Heart attack 2
Figure 1.2: Coronary artery bypass [3] 3
Figure 1.3: Balloon angioplasty [5] 5
Figure 1.4: Stent in place 6
Figure 1.5: Transluminal extraction catheter, rotational, and directional atherectomy [9] 7
Figure 1.6: Procedural stent rates in selected countries for 1997 8
Figure 3.1: Hourglass deformation mode 40
Figure 3.2: Contact algorithm with penalty method 44
Figure 4.1: Finite element model of half of the stent 48
Figure 4.2: Selected discretised geometry 49
Figure 4.3: Material model used for tube material 50
Figure 4.4: Five different load cases 51
Figure 4.5: Distribution of stress in the stent at 25% of final load by load case I 53
Figure 4.6: Distribution of stress in the stent at 50% of final load by load case I 54
Figure 4.7: Distribution of stress in the stent at 75% of final load by load case I 54
Figure 4.8: Distribution of stress in the stent at final load by load case I 55
Figure 4.9: Distinct local plastic deformation by load case I 55
Figure 4.10: Closer view of the central stent strut by load case I at final load 56
Figure 4.11: Stress level along the stent in z-direction at max expansion by load case I 57
Figure 4.12: Development of radial displacement and foreshortening by load case I 58
Figure 4.13: Distribution of stress at 25% of final load by load case II 59
Figure 4.14: Distribution of stress at 50% of final load by load case II 59
Figure 4.15: Distribution of stress at 75% of final load by load case II 60
Figure 4.16: Distribution of stress at final load by load case II 60
Figure 4.17: Distinct local plastic deformation by load case II 61
Figure 4.18: Close view of the central stent strut by load case II at final load 62
Figure 4.19: Stress level along the stent in z-direction at max expansion by load case II 63
Figure 4.20: Development of radial displacement and foreshortening by load case II 64
Figure 4.21: Distribution of stress at 25% of final load by load case III 64
Figure 4.22: Distribution of stress at 50% of final load by load case III 65
Figure 4.23: Distribution of stress at 75% of final load by load case III 65
Figure 4.24: Distribution of stress at final load by load case III 66
Figure 4.25: Distinct local plastic deformation by load case III 67
Figure 4.26: Close view of the central stent strut by load case III at final load 67
Figure 4.27: Stress level along the stent in z-direction at max expansion by load case III 68
Figure 4.28: Development of radial displacement and foreshortening by load case III 69
Figure 4.29: Distribution of stress at 25% of final load by load case IV 70

Figure 4.30: Distribution of stress at 50% of final load by load case IV 70
Figure 4.31: Distribution of stress at 75% of final load by load case IV 71
Figure 4.32: Distribution of stress at final load by load case IV 71
Figure 4.33: Close view of the central stent strut at final load by load case IV 72
Figure 4.34: Stress level along the stent in z-direction at max expansion by load case IV 73
Figure 4.35: Development of radial displacement and foreshortening by load case IV 74
Figure 4.36: Distribution of stress at 25% of final load by load case V 75
Figure 4.37: Distribution of stress at 50% of final load by load case V 75
Figure 4.38: Distribution of stress at 75% of final load by load case V 76
Figure 4.39: Distribution of stress at final load by load case V 76
Figure 4.40: Distinct local plastic deformation by load case V 77
Figure 4.41: Close view of the central stent strut at final load by load case V 78
Figure 4.42: Stress level along the stent in z-direction at max expansion by load case V 79
Figure 4.43: Development of radial displacement and foreshortening by load case V 80
Figure 4.44: Displacement vs. percentage increment of pressure at equal intervals 80
Figure 4.45: Foreshortening vs. percentage increment of pressure at equal intervals 81
Figure 4.46: Development of stress in stent under five different load cases 82
Figure 4.47: Comparison between the length of foreshortening and radial displacement 83
Figure 4.48: Plot of max radial displacement achieved with respect to pressure speed 84
Figure 4.49: Plot of maximum foreshortening achieved with respect to pressure speed 84
Figure 4.50: Development of von Mises stress at corner node for each load case 86
Figure 5.1: Finite element model of one quarter of the stent 89
Figure 5.2: Selected discretised geometry 89
Figure 5.3: Graph calculated values versus experimental data 91
Figure 5.4: Loading curve 92
Figure 5.5: Stent diameter versus pressure 93
Figure 5.6: Distinct local plastic deformation 94
Figure 5.7: Distribution of stress at maximum expansion 95
Figure 5.8: Distribution of stress in the stent at maximum expansion 96
Figure 5.9: Closer view of the end strut as highlighted in Figure 5.8 97
Figure 5.10: Closer view of the deformation at the end of the stent 97
Figure 5.11: Foreshortening of the stent with time 98
Figure 5.12: Finite element model of one eight of the slotted tube 102
Figure 5.13: ANSYS calculated values versus experimental data 103
Figure 5.14: Three different deployment pressures 104
Figure 5.15: Residual stress in the deformed slotted tube by loading curve 1 106
Figure 5.16: Development of stresses in node 487 107
Figure 5.17: Equivalent plastic strain at node 487 108
Figure 5.18: Deformation of the slotted tube by initial ramp loading at time 10 msec 109
Figure 5.19: Deformation of the slotted tube in steady state response at 15 msec 110

Figure 5.20: Deformation of the slotted tube at simulation time 18.4 msec 110
Figure 5.21: Deformation of the slotted tube at simulation time 20 msec 111
Figure 5.22: Expansion of slotted tube diameter with deployment pressure 112
Figure 5.23: Elastic recoil of the slotted tube 113
Figure 5.24: Foreshortening of the slotted tube with simulation time 114
Figure 5.25: The geometry of the slotted tube before and after the expansion 115
Figure 5.26: Residual stress in the deformed slotted tube by loading curve 2 116
Figure 5.27: Development of stresses in node 515 117
Figure 5.28: Initial ramp loading by deployment pressure 2.5 MPa at time 10 msec 119
Figure 5.29: Steady state response of the slotted tube at time 15 msec 119
Figure 5.30: Separation of the balloon from slotted tube at time 18.01 msec 120
Figure 5.31: Deformation of the slotted tube at simulation time 20 msec 121
Figure 5.32: Expansion of slotted tube with deployment pressure 122
Figure 5.33: Elastic recoil of the slotted tube 123
Figure 5.34: Foreshortening of the slotted tube with simulation time 123
Figure 5.35: The geometry of the slotted tube before and after the expansion 124
Figure 5.36: Residual stress in the deformed slotted tube by loading curve 3 125
Figure 5.37: Development of stresses in node 675 126
Figure 5.38: Initial ramp loading by deployment pressure of 2.8 MPa at time 10 msec 127
Figure 5.39: Steady state response of the slotted tube at time 15 msec 128
Figure 5.40: Separation of the balloon from the slotted tube at time 17.8 msec 129
Figure 5.41: Deformation of the slotted tube at simulation time 20 msec 129
Figure 5.42: Expansion of slotted tube diameter with deployment pressure 130
Figure 5.43: Elastic recoil of the slotted tube 131
Figure 5.44: Foreshortening of the slotted tube with simulation time 132
Figure 5.45: The geometry of the slotted tube before and after the expansion 133
Figure 5.46: One eight of the finite element model with balloon length equal to 52 mm 134
Figure 5.47: One eight of the finite element model with balloon length equal to 57 mm 135
Figure 5.48: One eight of the finite element model with balloon length equal to 62 mm 136
Figure 5.49: Loading curves 137
Figure 5.50: Development of stress at maximum stressed node 139
Figure 5.51: Deformation of the slotted tube after deflation by 52 mm balloon 140
Figure 5.52: Deformation of the slotted tube after deflation by 57 mm balloon 140
Figure 5.53: Deformation of the slotted tube after deflation by 62 mm balloon 141
Figure 5.54: Expansion of slotted tube diameter with deployment pressure 142
Figure 5.55: Elastic recoil of the slotted tube 143
Figure 5.56: Foreshortening of the slotted tube with simulation time 144
Figure 5.57: Slotted tube geometry before and after the expansion for 52 mm balloon 145
Figure 5.58: Slotted tube geometry before and after the expansion for 57 mm balloon 146
Figure 5.59: Slotted tube geometry before and after the expansion for 62 mm balloon 147

Figure 5.60: Development of stress at maximum stressed node 149
Figure 5.61: Residual stress in the slotted tube for friction factor of 0 150
Figure 5.62: Residual stress in the slotted tube for friction factor of 0.15 151
Figure 5.63: Residual stress in the slotted tube for friction factor of 0.3 151
Figure 5.64: Expansion of slotted tube diameter with deployment pressure 152
Figure 5.65: Elastic recoil of the slotted tube 153
Figure 5.66: Foreshortening of the slotted tube with simulation time 154
Figure 5.67: Deformation of the slotted tube after expansion by scaling factor of 1 157
Figure 5.68: Deformation of the slotted tube after expansion by scaling factor of 0.5 157
Figure 5.69: Deformation of the slotted tube after expansion by scaling factor of 0.1 158
Figure 5.70: Expansion of slotted tube diameter with deployment pressure 159
Figure 5.71: Elastic recoil of the slotted tube 161
Figure 5.72: Foreshortening of the slotted tube with simulation time 162
Figure 5.73: Finite element model of the slotted tube imperfection 163
Figure 5.74: Loading curve 164
Figure 5.75: Residual stress in the slotted tube after deflation 165
Figure 5.76: Close up view of the defected area 166
Figure 5.77: Development of stress at node 959 and 936 167
Figure 5.78: Development of von Mises, principal and directional stress at node 959 168
Figure 5.79: Development of von Mises, principal and directional stress at node 936 169
Figure 5.80: Expansion of slotted tube diameter with deployment pressure 170
Figure 5.81: Elastic recoil of the flaw and flawless slotted tubes 171
Figure 5.82: Foreshortening of the original and imperfection slotted tubes 172
Figure 5.83: One eight of the finite element model with balloon thickness = 0.6 mm 173
Figure 5.84: One eight of the finite element model with balloon thickness = 1.2 mm 174
Figure 5.85: One eight of the finite element model with balloon thickness = 1.8 mm 174
Figure 5.86: Loading curves 175
Figure 5.87: Residual stress in the deformed tube by 0.6 mm balloon thickness 176
Figure 5.88: Deformation of 0.6 mm balloon at maximum deployment pressure 177
Figure 5.89: Residual stress in the deformed tube by 1.2 mm balloon thickness 178
Figure 5.90: Deformation of the balloon and slotted tube at time 12.75 msec 179
Figure 5.91: Deformation of 1.2 mm balloon at maximum deployment pressure 179
Figure 5.92: Residual stress in the deformed tube by 1.8 mm balloon thickness 180
Figure 5.93: Deformation of the balloon and slotted tube at time 11.5 msec 181
Figure 5.94: Deformation of 1.8 mm balloon at maximum deployment pressure 182
Figure 5.95: Expansion of slotted tube diameter with deployment pressure 183
Figure 5.96: Elastic recoil of the slotted tube 184
Figure 5.97: Foreshortening of the slotted tube with pressure 185
Figure 5.98: Geometry of the slotted tube for design 1 186
Figure 5.99: Geometry of the slotted tube for design 2 186

Figure 5.100: Geometry of the slotted tube for design 3 187
Figure 5.101: Geometry of the slotted tube for design 4 187
Figure 5.102: Geometry of the slotted tube for design 5 187
Figure 5.103: Finite element model of the design 189
Figure 5.104: Finite element model of the design 2 189
Figure 5.105: Finite element model of the design 3 190
Figure 5.106: Finite element model of the design 4 190
Figure 5.107: Finite element model of the design 5 191
Figure 5.108: Loading curves 192
Figure 5.109: Residual stress in the deformed tube for design 1 193
Figure 5.110: Residual stress in the deformed tube for design 2 194
Figure 5.111: Residual stress in the deformed tube for design 3 195
Figure 5.112: Residual stress in the deformed tube for design 4 196
Figure 5.113: Residual stress in the deformed tube for design 5 197
Figure 5.114: Expansion of slotted tube diameter with deployment pressure 198
Figure 5.115: Elastic recoil of the slotted tube stents 199
Figure 5.116: Foreshortening of the slotted tubes with deployment pressure 200
Figure 5.117: Finite element model of the entire assembly 203
Figure 5.118: Loading curve 205
Figure 5.119: Residual stress in the slotted tube after deflation 206
Figure 5.120: Development of stresses in node 9102 207
Figure 5.121: Slotted tube stent in place at maximum load 208
Figure 5.122: Slotted tube stent in place when the balloon is deflated 209
Figure 5.123: The stress distribution of the plaque and artery 210
Figure 5.124: The von Mises stress across the thickness of the plaque and artery 211
Figure 5.125: Expansion of slotted tube diameters with deployment pressure 212
Figure 5.126: Elastic recoil of the slotted tubes 213
Figure 5.127: Foreshortening of the slotted tube with simulation time 214
Figure 6.1: Upper shelf section with specimens in place 216
Figure 6.2: Entire assembly of the apparatus 217
Figure 6.3: Design 1 (width of slot = width of strut) 218
Figure 6.4: Design 2 (20 % increase in width of the slot) 219
Figure 6.5: Design 3 (20 % decrease in width of the slot) 219
Figure 6.6: Design 4 (10 % increase in length of the slot) 220
Figure 6.7: Design 5 (50 % increase in the number of slot) 220
Figure 6.8: Slotted tube in place 221
Figure 6.9: The expansion of the slotted tube by polyethylene rubber 222
Figure 6.10: The expanding balloon near the point of rupture 223
Figure 6.11: Slotted tubes after the expansion process by polyethylene balloon 225
Figure 6.12: The expansion of the slotted tube by PVC 226

Figure 6.13: Closer view of the slotted tube during the expansion process 227
Figure 6.14: The expansion of slotted tube at 2.5 MPa 228
Figure 6.15: The expansion of the slotted tube after the rupture of the balloon 228
Figure 6.16: Slotted tubes after the expansion process by PVC balloon material 229

LIST OF TABLES

Table 2.1:	Advantages and disadvantages of each class of stents [44]	14
Table 2.2:	Overview of the first clinical stent applications	17
Table 2.3:	Metallic composition of intravascular stent	22
Table 4.1:	Dimensions of the stent	47
Table 4.2:	Material data used for material model	50
Table 4.3:	Five different load cases with different load speeds	52
Table 5.1:	Dimensions of the stent	88
Table 5.2:	Dimensions of the slotted tube	100
Table 5.3:	Dimensions of the scaled slotted tube size	156
Table 5.4:	Diameter achieved for three different scaling factors	159
Table 5.5:	Elastic recoil of the slotted tubes	160
Table 5.6:	Summary of dimensions for the five different designs	188
Table 5.7:	Number of elements used	188
Table 5.8:	Percentage shrinkage of the slotted tubes	199
Table 5.9:	Percentage foreshortening from the original length of the slotted tubes	201
Table 5.10:	Material properties used	204

Chapter 1

INTRODUCTION

1.1 Introduction

In western industrial countries coronary heart disease is the most common reason for death. In European countries like Germany, about 200 000 people have a heart attack every year and more than 800 000 patients world-wide undergo a nonsurgical coronary artery interventional procedure yearly. According to the American Heart Association, nearly 14 million Americans have coronary artery disease, which is responsible for half of all heart-related deaths [1].

1.2 Coronary Artery Disease

Coronary artery disease is specific to the arteries of the heart. Arteries that supply blood and oxygen to the heart muscles are called coronary arteries. Coronary artery disease also known as atherosclerosis occurs when excess cholesterol attaches itself to the walls of blood vessels. Embedded cholesterol also attracts cellular waste products, calcium and fibrin (a clotting material). This leads to a thickening of the vessel wall by complex interaction with constitutes of the artery. The resulting pasty build-up, known as plaque, can narrow or even block an artery. Due to the fact that these deposits narrow (stenosis) and harden the vessel (atherosclerosis), an increased

rate of thrombosis (clot) is possible and decrease of blood flow is inevitable. When the coronary arteries become narrowed or clogged and cannot supply enough blood to the heart, the result is coronary heart disease. The lacking of oxygen-carrying blood supply to the heart causes the heart to respond with pain called angina. The pain is usually felt in the chest or sometimes in the left arm and shoulder. If the blood supply is cut off completely, the part of the heart that does not receive oxygen begins to die and some of the heart muscle may be permanently damaged. This is called a heart attack (Figure 1.1).

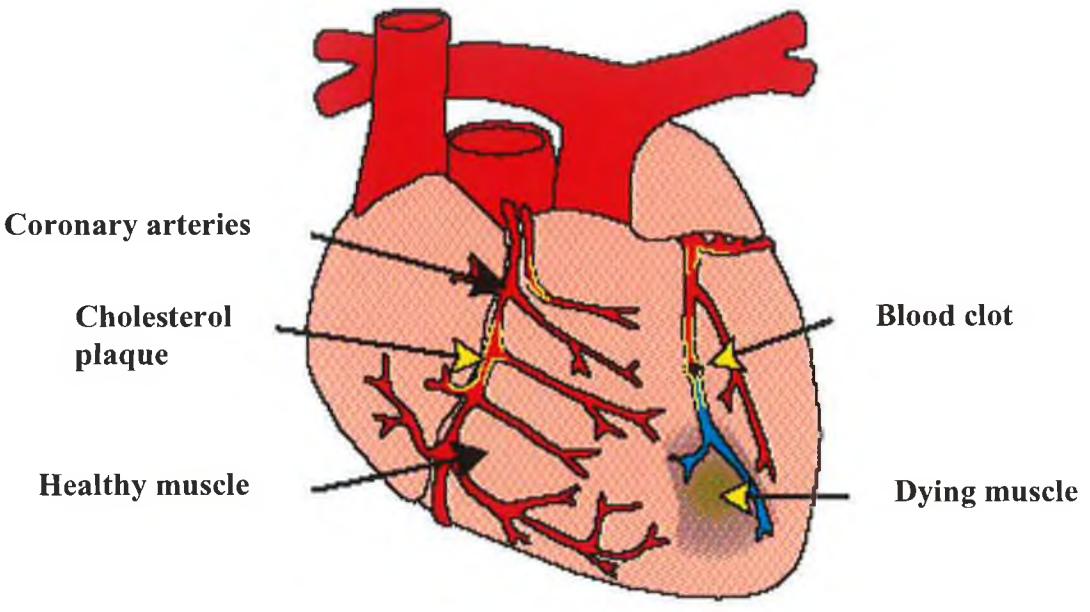

Figure 1.1: Heart attack

It has become a common practice that after taking careful medical history and doing a physical examination, some tests are carried out to see how advanced the coronary heart disease is. Coronary angiography (or arteriography) is a test used to explore the coronary arteries. A fine tube (catheter) is put into an artery of an arm or leg and passed through the tube into the arteries of the heart. The heart and blood vessels are then filmed while the heart pumps. The picture that is seen called an angiogram or arteriogram. An angiogram will show problems such as a blockage caused by atherosclerosis. Although coronary angiography has long been the standard for coronary stenosis assessment, it remains a limited means of assessing the acute stent

result. Intravascular Ultrasound (IVUS) provides additional information that may assist stent implantation [2].

Coronary heart disease is treated in a number of ways, which depending on the seriousness of the disease. The goal of a therapy for patients with coronary heart disease is a restoration of the working order of the heart muscle to minimise the risk of a heart attack and death. For non-serious patients, coronary heart disease is managed with lifestyle changes (e.g. stop smoking, reducing weight, sports, reduction of stress) and medications (e.g. to improve the blood circulation by increasing the vessel diameter or prevention of blood clot). Others with severe coronary heart disease may need an operation.

1.3 Arterial Bypass Surgery

Several techniques have been developed to treat coronary artery disease during the last decades. From 1967 to 1977 the only method of treatment has been the arterial bypass surgery [3].

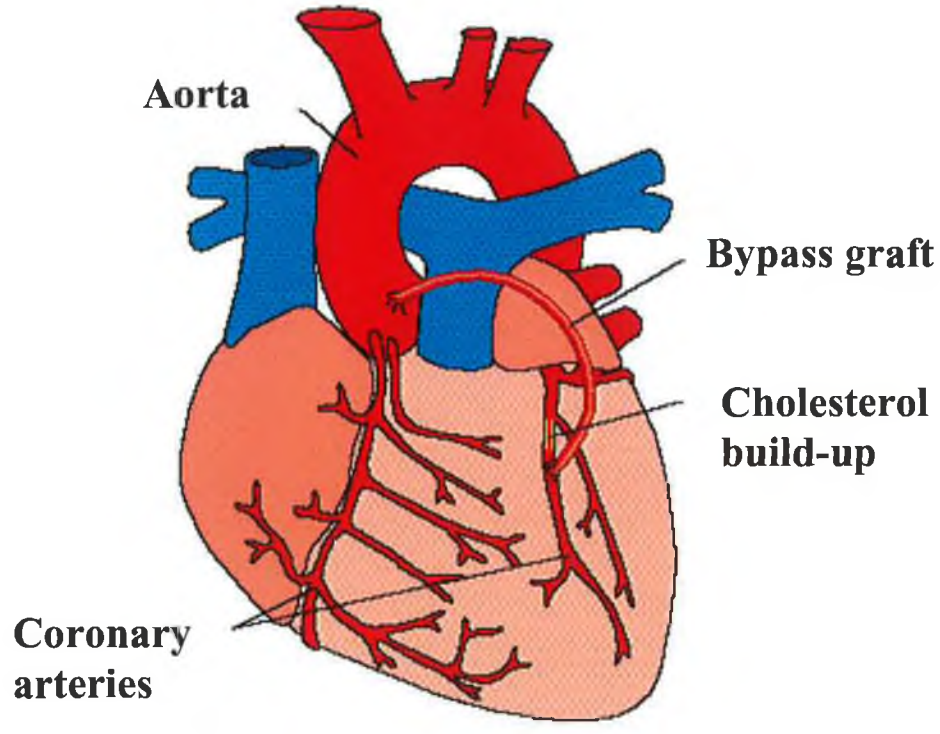

Figure 1.2: Coronary artery bypass [3]

In this procedure, the sternum (breastbone) is actually opened to allow direct access to the heart and all of the major arteries surrounding it. After the lesion is located, the heart is iced down to stop activity within the heart itself. A graft of a vessel from another part of the body (usually taken from the leg or chest) is connected to the artery in front of and behind the blocked area (Figure 1.2). This procedure is generally successful, however it is the most invasive method and is used only as an alternative to balloon angioplasty or stent deployment [4]. Coronary artery bypass graft surgery is advised for selected groups of patients with significant narrowings and blockages of the heart arteries (coronary artery disease). It is performed to relieve angina (chest pain) in patients who have failed medical therapy and are not good candidates for balloon angioplasty.

1.4 Percutaneous Transluminal Coronary Angioplasty (PTCA)

Despite the surgical procedure for correction of arterial stenosis, there are non-surgical alternatives that open blocked arteries with less risk and less initial cost than surgery. Coronary angioplasty with a balloon, stent or other devices is probably the most common alternative. Percutaneous transluminal coronary angioplasty (PTCA) or better known as "Balloon Angioplasty" of the coronary artery is a relatively new procedure introduced in the late 1970's [5]. Since the introduction of the balloon angioplasty in 1977, the era of the minimal invasive cardiology methods began and won increased significance over recent years. Percutaneous means "through the skin", transluminal means "inside the blood vessel", coronary means "relating to the heart" and angioplasty means "blood vessel repair". During PTCA, a local anaesthetic is injected into the skin over the artery in the groin or less frequently arms. The artery is punctured with a needle and a plastic sheath is placed into the artery to protect it during the procedure. Under x-ray guidance (fluoroscopy), a long, narrow, hollow tube (guiding catheter) is advanced through the sheath to the origin of the coronary artery from the aorta. A dye (contrast medium) containing iodine is injected through the guiding catheter so that x-ray images of the coronary arteries can be seen on a special TV screen. Afterwards, a second thinner catheter (guide wire) which is tipped with a miniature and deflated balloon is inserted into the first one. The balloon catheter over the guide wire is then pushed forward through the guiding

catheter to the area with the plaque. Once in the proper position, the balloon is inflated to enlarge the narrowing in the artery and the widening of the artery improved the flow of blood through the narrowed area (Figure 1.3).

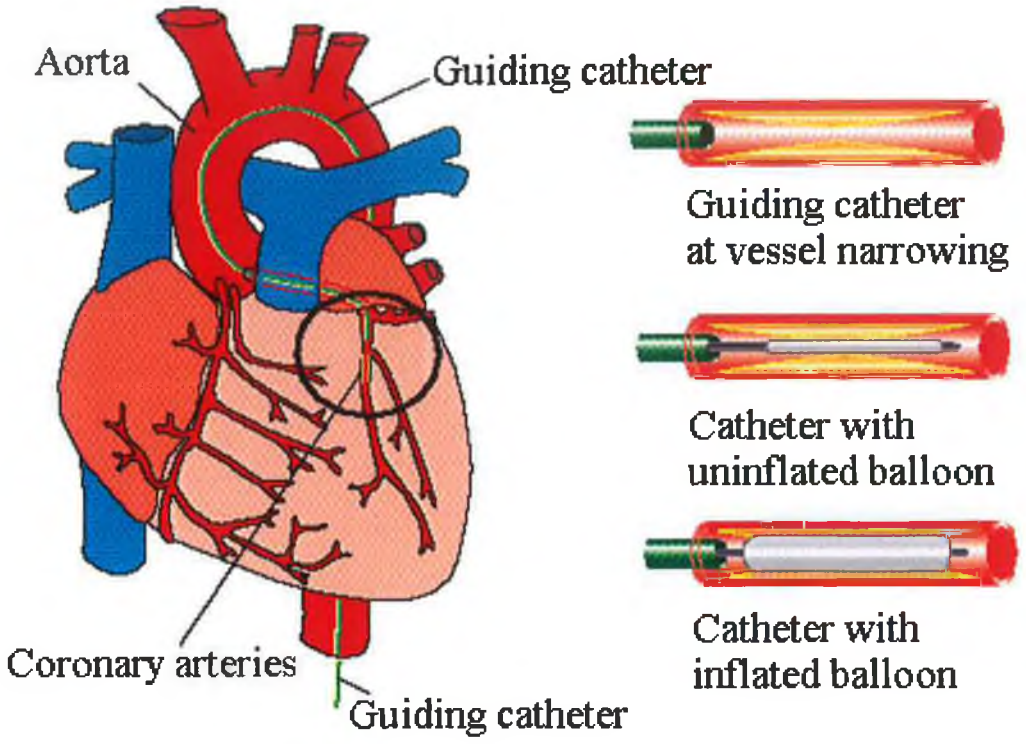

Figure 1.3: Balloon angioplasty [5]

1.5 Stent Implantation

Stent implantation is another non-surgical method to treat the coronary artery disease. A stent may be used as an alternative or in combination with angioplasty. Stenting is a catheter-based procedure in which a stent is inserted into a diseased artery to hold it open [6]. Stenting is often used in conjunction with a balloon angioplasty to treat coronary artery disease. In about one-third to one-half of the successful angioplasty procedures performed, a blockage recurs later at the same site [7]. This kind of recurrence is called a restenosis (re-narrowing of artery). In order to minimise the chances for restenosis, implantation of a coronary stent after balloon angioplasty is always recommended [8]. A coronary stent is a small, metallic, slotted tubular device that mounted on a balloon catheter. It is introduced into the artery just

after balloon angioplasty and is positioned at the site of the obstruction. When the balloon is inflated, the stent expands and is pressed against the inner walls of the artery. After the balloon is deflated and removed, the stent remains in place, keeping the artery open (Figure 1.4). The stent remains in the artery permanently, holds it open, improves blood flow to the heart muscle and relieves symptoms of coronary artery disease such as chest pain.

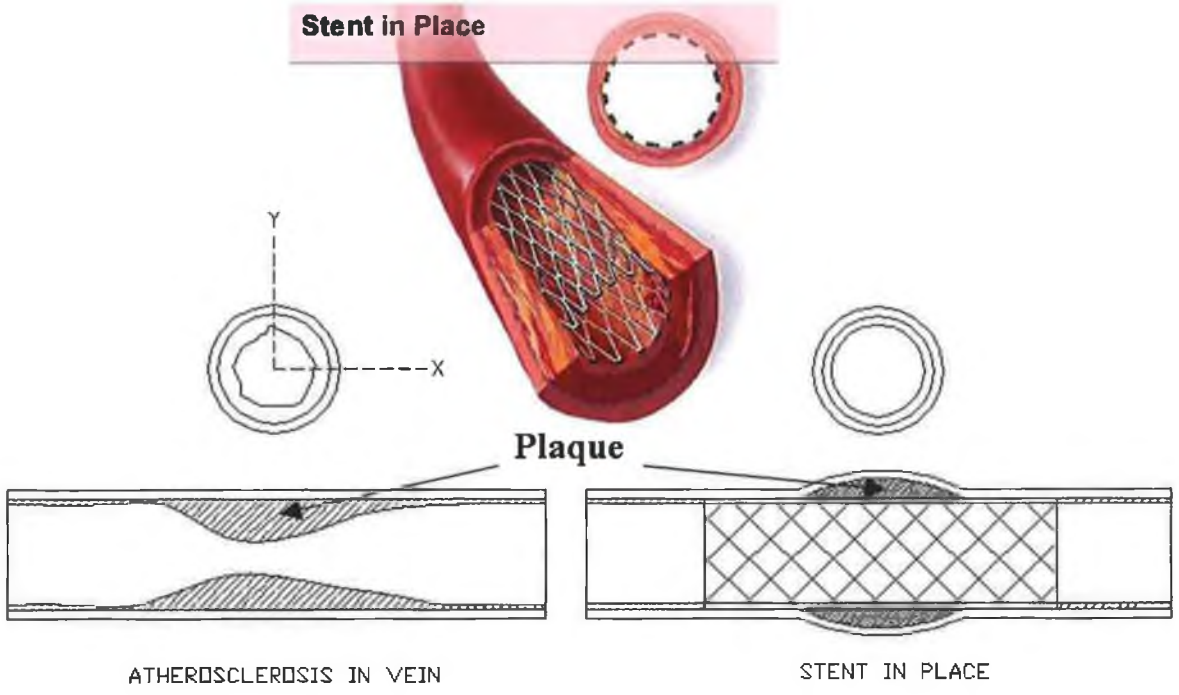

Figure 1.4: Stent in place

1.6 Atherectomy

Other sorts of techniques by means of catheter are atherectomy [9] and laser angioplasty [10]. Coronary atherectomy was introduced in 1993. It is often used in addition to, or instead of, the more traditional balloon angioplasty when plaque is exceptionally hard (due to calcification) or presents other challenges [11]-[12]. There are several types of atherectomy as shown in Figure 1.5. The procedures for implementing the atherectomy are very much the same as balloon angioplasty except that a special atherectomy catheter is threaded through the guiding catheter and over the guide wire to the site of obstruction. Once the catheter is in place, the plaque is cut away using either a sharp blade or abrasive material (like sandpaper) located at

the tip of the catheter. The shavings are collected in the catheter and removed when it is withdrawn from the body. By removing some of this plaque, blood flow is improved and the risk of having a heart attack is reduced.

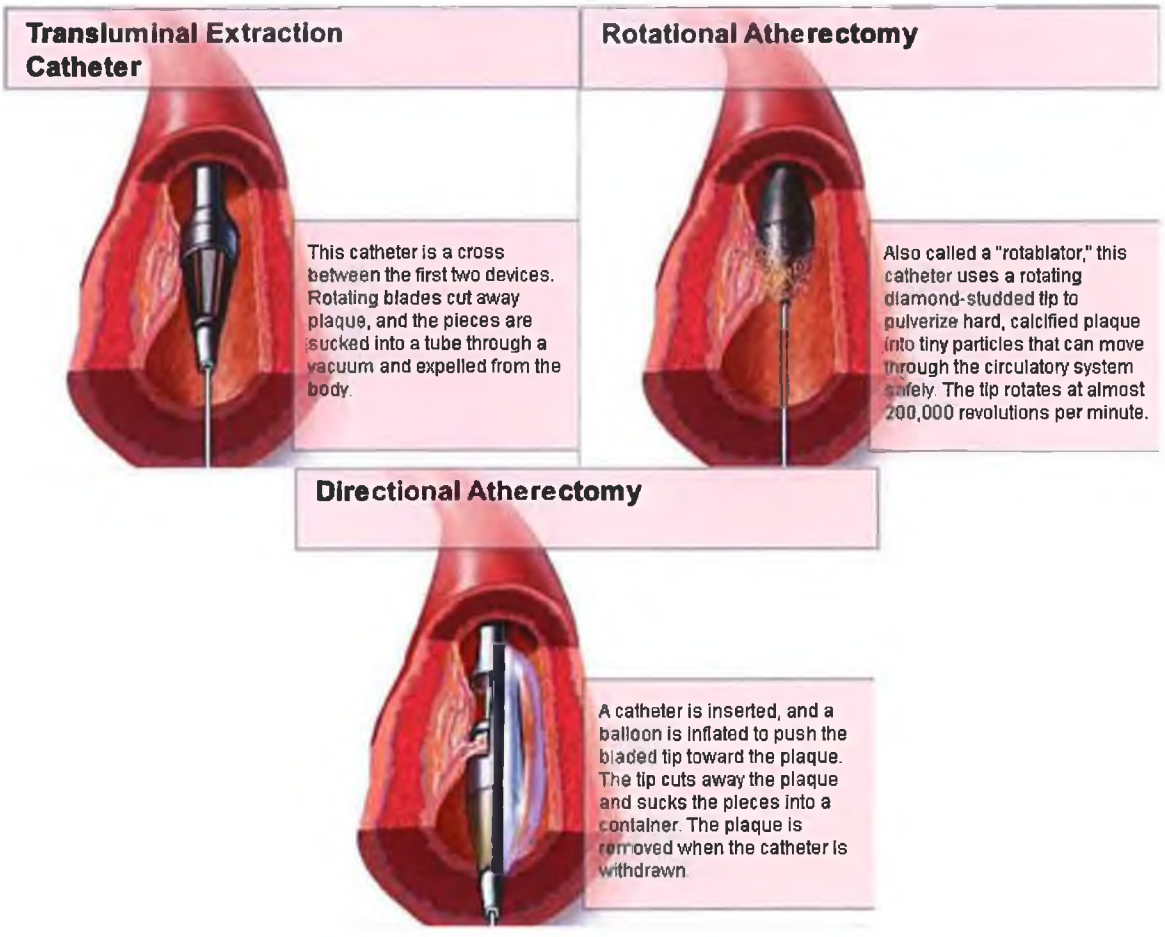

Figure 1.5: Transluminal extraction catheter, rotational, and directional atherectomy [9]

1.7 Laser Angioplasty

Laser assisted angioplasties are available but rarely used to remove plaque in the coronary arteries [13]. This procedure is normally reserved for treating areas that cannot be opened with balloon technology as it exists today. A laser-tipped catheter produces a high intensity light beam (ultraviolet light) that vaporises the obstructing plaque without damaging the surrounding tissues. This then allows the passage of a balloon system to further open the obstruction. Balloon angioplasty or stent procedure may be followed immediately afterward to ensure that the artery remains

open. However, atherectomy (31% restenosis) and laser angioplasty (50% restenosis) show a significant smaller rate of success than the PTCA or stent implantation (19% restenosis) [14].

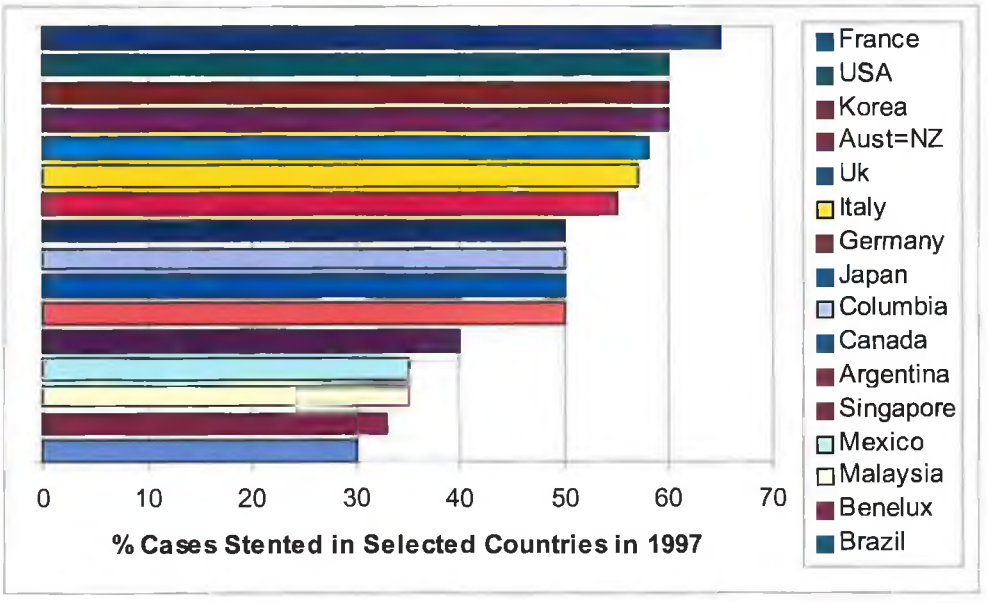

Figure 1.6: Procedural stent rates in selected countries for 1997

There were about 900 000 coronary operations throughout the world in 1995 [15]. Since 1994 the amount of stent implantation has constantly growing each year. In 1997, in countries with interventional cardiology programs, procedural stent rates ranged from 30% to 65% and tended to be highest in southern Europe (Figure 1.6)[16]. It is expected that the rate of stent implantation will be further increasing over the coming years. One of the reasons for this is that the use of stents has proved more effective in the treatment of coronary stenosis than balloon angioplasty [17]-[18]. Nevertheless, difficulties and questions remain, and the outcome is never 100 % successful.

Despite the fact that thrombosis has been the major problem in the first years of stenting due to the changes in blood stream, rapid developments in interventional cardiology have permitted this to be treated by medication [19]-[21]. However, there is evidence that the success of the stent implantation is limited by restenosis [22]. To date, although the application of a stent reduces the restenosis occurrence to approximately 20-30% [23], it has not yet been eliminated altogether. The detailed

event of restenosis and the main reasons remain dubious up to date and are discussed almost solely in the medical and biological area [24]-[25], while the mechanical aspects have received little attention. Some practitioners have reported problems such as migrations [26]-[27], collapses [28]-[31] or difficulties in the positioning due to the engineering of products. But, still a lot of questions remain to be answered. Perhaps, this is due to the current lack of research on the mechanical properties during and after the dilatation of the stent, despite the increasing number of publications underlying the necessity [32]-[34].

The understanding of the mechanism may be best investigated by finite element modelling and simulations whereby the expansion behaviour of stents, elastic recoil, stress, strain etc. can be fully investigated. Accurate and reliable structural analysis provides essential information in an environment where in vivo experimentation is extremely expensive or impossible. Realistic experimentation on stent expansion is difficult to carry out and manage due to the nature of the structure and material of the slotted tube, experimental set up, cost, accuracy etc. Finite element analysis provides a solution in which accurate and reliable results can be obtained. However, a realistic modelling of the deployment mechanism is very tricky to manage as well. It is not only the accuracy of the results that has to be considered but also the computation time. The premise is that, if the underlying situation can be simulated with variable conditions that may not be done by experimental tests, this could therefore, provide detailed analyses that would lead to a good understanding of failure or success of the design and be extremely useful. Appreciating that the stress, strain and magnitude of stent expansion etc. are functions of altering such variables, the risk of stent implantation and failure of the stent may be reduced accordingly. Apart from that, perhaps mechanical aspects that had received little attention may play an important role or may have major effects on stent deployment.

The objective of this work is to investigate the slotted tube stent expansion process theoretically (FEM) and experimentally, which can be outlined as follows:

- Investigate the expansion behaviour of stent under internal pressure only.
- Investigate the effect of manufacturing defects on stent.
- Investigate the effect of change of material fraction (gap density)

- Factor of scaling down the size of stent on deformation characteristic.
- Investigate the expansion behaviour of combined balloon, stent, plaque and artery.
- Investigate the expansion behaviour of the slotted tube experimentally using a purpose-built machine.

Chapter 2

LITERATURE SURVEY

2.1 History of Stent

Percutaneous stenting of vascular stenoses was first conceived in 1969 by Charles Dotter [35]. He published a new technique to percutaneously place tubular coilspring endovascular prosthesis into peripheral vessels and attempted to keep the vessels open by scaffolding the inner surface. The experiments performed on animals at that time were unsatisfactory because of the resulting stenoses and dislocations took place. Due to the technical limitations at that time, however, further research was not revived until the early 1980s when Charles Dotter [36] and Cragg [37] reported on new experiments with the implantation of spiral coils using the memory-alloy technique. At the same time, Maass et al. [38]-[40] started to experiment and published data in 1983 and 1984 with a self-expanding spring coil implanted in peripheral arteries of animals at the surgical clinic of the University of Zurich. The history of endovascular stents is begun with the Maass double helix spiral prosthesis. This stent is first used in human clinical trials in the early 1980s and it was the first expandable prosthesis developed from an earlier simple coil design [38]-[39]. In animal experiments the double helix spiral stents were completely endothelialised (the healing of the inner surfaces of vessels or grafts by endothelial cells) within 6 weeks and intimal reaction was largely insignificant. However, an important finding

was that side branches of the arteries that were crossed by the stents remained patent [39]. The double helix spirals, however, are no longer manufactured [41].

2.2 Basic Initial Designs of Stent

The following are three basic initial designs of stent:

2.2.1 Self-expanding mesh

Stainless steel self-expanding mesh stents were amongst the first stents [42] to undergo clinical evaluation and they are made from overlapping wire. Self-expanding stents expand by their inherent expanding force to a certain predetermined diameter. This stent class grew out of the need to address special coronary conditions such as large vessels, aneurysmal dilatation and saphenous vein graft. These stents are also well suited for long lesions as they can accommodate different diameters within the same vessel due to their self-expanding mechanism. The lesion to be stented is usually predilated and to accelerate complete stent expansion the stented segment may be dilated with an angioplasty catheter. Foreshortening (Wallstent) on deployment is the major drawback of self-expanding stent. Precise positioning is less predictable. The other drawbacks of this stent are limited sidebranch access and it is suboptimal for small vessels. Examples of self-expanding mesh stents are Gianturco Expandable Wire Stent (Cook), Magic Wallstent (Schneider), Radius Stent (Scimed), etc.

2.2.2 Coil stent

The main feature of coil stent is that it is fabricated out of continuous single strand of wire formed into a repeating pattern. The original design of coil stent is to provide flexibility and allow access to tortuous vessels. Coil stents are highly flexible that have improved its trackability (manoeuvring the stent within coronary arteries). However, coil stents do not expand uniformly in areas of increased resistance. Therefore, attaining a smooth arterial lumen by predilating with balloon angioplasty [5] or debulking with atherectomy [9] devices is important prior to placing a coil stent. Coil stents have also been particularly attractive choices for stenting long and

soft lesions associated with significant dissection after balloon angioplasty. In the case of complex bifurcation lesions, coil stent designs are often favoured because of their flexibility and greater potential for side-branch access and dilatation. Despite the several theoretical advantages of coil stents, it has drawbacks such as problems of tissue prolapse, weak radial strength (recoil) and an increase in subacute thrombosis. Examples of coil stents are Crossflex Stent (Cordis), GR II (Cook), Wiktor Stent (Medtronic), etc.

2.2.3 Slotted tube stent

The original slotted tube stent is fabricated from stainless steel slotted tubes. These first generation stents set the standard for performance and procedural success. The Johnson & Johnson Palmaz-Schatz stent is the prototype for slotted tubular stent designs. The slotted tubular design stents generally provide greater surface coverage of the stented lesion and less likely to recoil. Nevertheless, their rigidity and suboptimal trackability especially in tortuous vessels represent the major shortcomings of this class.

By virtue of the weaknesses on design of the first generation slotted tube stents, the improved second generation of tubular stents with design innovations have come in with intention to correct the relatively poor flexibility and trackability of the first generation. As a result, they also feature better side branch access and a greater variety of diameters and lengths. Examples of second generation tubular stents are Crown Stent (Cordis), BX Stent (Cordis), Multilink Stent (Guidant), BeStent (Medtronic) [43], etc.

Development of new stents is evolving rapidly. In spite of the three basic designs of stent mentioned above, Charles et al. [44] categorised the stent design into five distinct classes based on their structure. These five classes of stent design are a) original slotted tube design, b) second generation tubular design, c) self-expanding design, d) coil design, and e) modular zigzag design. Modular zigzag design is similar to a train since it is composed of individual modules welded together, much like the coupled cars of a train. In January 1998, Charles [44] and his colleagues visited 10 prestigious interventional centres in six Europeans countries. They

compared 23 of the most commonly used stents and provided a conceptual framework for classifying the stent design, recognising the advantages and disadvantages of each, and defined the particular stent for specific coronary condition or lesion. Table 2.1 summarised the advantages and disadvantages of each class of stent made by Charles and his colleagues.

Class	Advantages	Disadvantages
Original Slotted-Tube Stent (Stainless steel 304/316 L)	• Maximum radial support • Very little plaque prolapse • Very little recoil	• Quite rigid • Not flexible • Poor visibility • Shortening • Suboptimal conformability • Suboptimal trackability • Limited sidebranch access • Difficult to retrieve
Second-Generation Tubular Stent (Stainless steel 304/316 L)	• Good to excellent radial support • Moderate trackability • Good to excellent conformability • No significant recoil • Good sidebranch access	• Variable visibility (Multilink) • Variable flexibility depending on strut design • Difficult to retrieve
Self-Expanding Stent (Nitinol, platinum and cobalt alloy)	• Moderate to good visibility • Good support • Quite flexible • Good trackability • Tapering with vessel • Little plaque prolapse	• Significant shortening (Wallstent) • Limited sidebranch access • Suboptimal for small vessels
Coil Stent (Stainless steel, tantalum and platinum)	• Good to excellent flexibility • Good trackability • Moderate to high visibility • Good sidebranch access • Good to excellent conformability	• Variable recoil • Plaque prolapse • Variable crossability • Possibility of subacute thrombosis (Wikto/GR II) • Suboptimal radial support • Difficult to retrieve monofilament
Modular Zigzag Stent (Stainless steel 304/316 L)	• Excellent trackability • Good flexibility • Good conformability • Access to sidebranch • Moderate radial strength • No significant shortening • Good visibility	• Micro I and II variable rigidity • Plaque prolapse possible in between modules • Difficult to retrieve

Table 2.1: Advantages and disadvantages of each class of stents [44]

2.3 Stent Techniques

There are three main groups of stent techniques:

2.3.1 Shape memory alloy

Dotter et al. [36] and Cragg et al. [37] were the first to apply the stent design contained the feature of shape memory properties of nitinol in animal experiments. Nitinol is a nickel titanium alloy with unique termal recovery properties. The alloy is first constrained to a desired shape and annealed at 500°C. This unique properties will memorise that shape. When nitinol wire is cooled down to 0°C, it becomes soft and can be deformed without destroying its memory. If the straightened wire is then warmed to its transition temperature (30-60°C depending on the alloy), it rapidly resumes its original annealed stage. By using the advantage of shape memory properties, Dotter [36] reshaped the nitinol wire coil stent into a temporary configuration that made it more suitable for transluminal placement. When heated to a transition temperature of 54-60°C, the stent loses its malleability and forcibly reverts to its initially imparted configuration.

2.3.2 Balloon expandable

This stent technique is applied when a balloon is used as a medium to expand the stent. The stent is mounted on the balloon catheter and are expanded passively by balloon inflation to the desired diameter. It is expanded in a controlled manner. The expansive force of the balloon dilates the stenosis and the stent simultaneously. Ziad et al. [45] reported their experience with balloon-expandable stent implantation for coarctation of the aorta in six patients. A mounted 30 mm long 3.4 mm nominal diameter stent (Palmaz P308, Johnson and Johnson Interventional System, Somerville, NJ) was utilised and manually crimped onto a 12, 16, or 18 mm balloon catheter. The medical device was advanced over the guide wire to the stenotic area. Once in position, the balloon was inflated up to the recommended inflation pressures of the balloon catheter. Ariel Roguin et al. [46] also used the same mode of action. The stent used in their studies was beStent. Three different lengths of stent mounted on three different lengths of balloon were studied i.e. a 15-mm stent is mounted on a

20-mm balloon, a 25-mm stent on a 30-mm balloon and a 35-mm stent is mounted on a 40-mm balloon.

2.3.3 Self-expanding

This technique uses inherent expanding force of the stents to expand itself. They are elongated and constrained on a delivery catheter by a rolling membrane sheath [42]. Retraction of the sheath results in stent self-expansion. The stent will reach its equilibrium state when released. The stent is said to have reached its equilibrium state when the elastic recoil of the vessel wall and residual elastic load of the stent is equalled. If the elastic recoil of the vessel wall overcomes the outward force of the stent and causes stent under-expansion, thrombosis may result. Conversely, if the stent is too strong for a given vessel, it may overdilate. Over-expansion of this type of stent has been related to thrombosis and excessive intimal proliferation [47]-[48].

2.4 Overview of the first clinical stent applications

Stent	Design	Deployment	First clinical implantation	Arteries	Reference
Maass double helix spiral	Spring coil	Self-expanding	1982-1986	Vena iliaca, Vena cava, Aortic dissection	[38][39]
Gianturco stent	Wire bent in zigzag pattern	Self-expanding	1986	Vena cava	[49]
Wallstent	Wire mesh	Self-expanding	1986	Peripheral arteries, Coronary arteries	[42][45]
Palmaz stent	Slotted tube	Balloon expandable	1988	Iliac arteries	[51]-[57]
Palmaz-Schatz	Slotted tube	Balloon expandable	1988	Coronary arteries	[58]-[60]
Strecker stent	Wire knitted in loosely connected loops	Balloon expandable	1988	Iliac arteries	[41]
Gianturco-Roubin	Incomplete coil, clam shell loop	Balloon expandable	1989	Coronary arteries	[61]
Wiktor	Sinusoidal helical coil	Balloon expandable	1991	Coronary arteries	[62]
Multilink	Multiple rings with multiple links	Balloon expandable	1993	Coronary arteries	[63]

Cordis	Sinusoidal helical coil	Balloon expandable	1994	Coronary arteries	[64]
AVE Micro	Zigzag axial struts, 4 mm units	Balloon expandable	1994	Coronary arteries	[64]

Table 2.2: Overview of the first clinical stent applications

In 1997, a group representative of the medical and scientific community expressed a consensus opinion about a number of regulatory issues with the aim of promoting new developments and research in the application of stents. It was also their intentions to protect patients from hazards that could result from the premature or uncontrolled dissemination of unsafe devices. They proposed formalising an evaluation scheme of coronary stents. This evaluation scheme consists of four phases i.e. in vitro testing, animal studies, clinical evaluation and clinical application [65]. The legal context of these guidelines became compulsory application of the 'Medical Devices Directives' of Endovascular Graft Committee from June 1998. Intracoronary stents fall into category III, that is the group of devices considered to be at the highest level in terms of risk of use [66]-[67].

2.5 Mechanical Considerations

According to Julio C. Palmaz [68], the mechanical characteristics of a stent are a compromise among five critical requirements.

a) A stent must have high expandability or a high ratio between collapsed and expanded diameter to allow for the smallest possible diameter of the delivery system.
b) The wall thickness should be as small as possible to offer the lowest profile after deployment.
c) The postimplant metal surface should be as small as possible because it determines the degree of thrombus formation.
d) Due to the fact that the degree of residual elasticity or hoop stress of an artery following balloon dilatation cannot be anticipated, the circumferential

strength of a stent must be calculated with a wide margin of excess to prevent collapse after deployment.

e) Radiopacity is essential for precise manipulation and positioning under fluoroscopy (examination of body structure using fluoroscope).

G. David Jang and Paulo A. Ribeiro [69] outlined the ideal characteristics of a coronary stent. They defined that a coronary stent has three metamorphoses in its life cycle and an ideal stent should have incorporated the ideal features in each of the three phases of a stent life cycle. The first phase is the 'Neutral Phase' as it is engineered and manufactured. The second phase is the 'Delivery Phase' as it is crimped on a balloon catheter. The third phase is the 'Final Deployed Phase' as it is permanently implanted in the coronary vessel. A stent that is well designed and ideal in its deployed state may not be an ideal stent if it is very difficult or unreliable to deliver in the coronary tree site. If the features of an ideal stent were not present in the neutral stent design, the deployed stent would not have the ideal characteristics. Similarly, a deployed stent with ideal characteristics does not necessarily have ideal delivery features. A stent that is ideal in its deployed state may not be a user-friendly stent, if it is very difficult to deliver to the vessel site. A neutral stent should have all the ideal delivery and deployed elements built into the design in order to become a truly ideal stent.

2.6 Stent Features

2.6.1 Flexibility

Flexibility is one of the most desirable features in a coronary stent [30]. Flexibility is certainly needed when it comes to delivery of catheters through tortuous vessels to the target area. Some investigators working with intravascular stents have stressed the need for stent flexibility to ease deployment and to allow vessel movement when placed in segments subjected to bending [70]. It is most appreciated by a stent user during delivery phase of a stent life. Flexible stents are generally easier and faster to use. Even though flexibility is very desirable during delivery, it may not be desirable after deployment [71]-[72]. J. C. Palmaz [68] believes that stents should be rigid

after placement to provide a stable, nonshifting surface for endothelial growth and stability. Flexibility after deployment is not desirable, as they may not have the same fatigue tolerance compared to the stent that is flexible during delivery but transforms into a more rigid frame after deployment. As a result, designing a stent that is flexible during delivery but transforms into a relatively rigid form after deployment is more difficult and challenging that designing a stent that is flexible both in the delivery and deployed states. Stent can be designed to be flexible during delivery phase but be transformed into a relatively rigid state after deployment by balloon expansion.

2.6.2 Radial (Hoop) Strength

Radial strength is one of the fundamental characteristics in a stent. It defines the ability of a stent to withstand the elastic recoil or collapsing force of a vessel wall [73]. Radial strength is needed for scaffolding the vessel in the deployment phase of a stent life cycle. A stent would fail to scaffold the internal lumen of the target vessel without a sufficient radial strength. A stent of any design variety should have a sufficient radial strength to prevent the elastic recoil and keep the vessel wall wide open.

2.6.3 Foreshortening

Foreshortening is an inherently common problem in stents. Foreshortening happens when a stent is expanded and transformed during deployment. It is regarded as the contraction of a stent from its original length after the expansion. In a general, foreshortening is not desirable as accurate placing and optimum longitudinal vessel coverage suffers proportionally with the degree of foreshortening with a stent. The more a stent foreshortens the more undesirable a stent. In the current state of the art, no foreshortening would be ideal. G. D. Jang and P. A. Ribeiro [69] have quoted that foreshortening of less than 5% when it is expanded to 4.0 mm in internal diameter with a regular vessel coronary stent may be acceptable. If foreshortening were less than 5% with a 4.0 mm internal expansion, accurate placing and deployment of a stent would not be compromised. The larger an expansion the greater the foreshortening due to the physics of expanding a crimped low profile to an expanded large profile in a stent with a fixed length.

2.6.4 Expansion Rate

Expansion rate is defined as a potential diameter increase of a stent from the crimped state of delivery phase to the optimal or maximum expanded deployed state. A stent should have a good expansion rate to allow for the smallest possible diameter during the delivery phase and greatest possible diameter after the deployment phase. Nevertheless, expansion rate is somehow somewhat effected the foreshortening of a stent. There is one common down side of high expansion rate. High expansion rate might cause an excessive foreshortening of stent. Thus, during the designing of stent these two factors have to be reconciled to ensure that the stent has highest expansion rate possible and at the same time has the smallest foreshortening as possible.

2.6.5 Vessel Coverage

Vessel coverage is one of the most important features of stent. This factor is extremely crucial when the stent permanently implanted in a coronary vessel. Vessel coverage defines on how well the stent struts are inter-woven to prevent tissue prolapse when it is expanded inside the vessel lumen. Vessel coverage is associated with the geometric size of the cells. Different stents have different vessel coverage. Hugh vessel coverage does not promise the feasibility of a stent as too many struts have been incorporated. Inevitably, the stent becomes too rigid and loses its flexibility. On the other hand, low vessel coverage does not form an ideal stent too. This is because of the stent cells are too large and the vessel wall is not covered well. The tissue of the vessel wall would prolapse through the space between the stent struts or the stent cells.

2.6.6 Metal Fraction

Metal fraction is the ratio of stent metal surface area that is constant prior to and after expansion to the total internal vessel surface area that varies according to the expanded stent diameter. Theoretically, the higher the metal fraction the higher would be the rate of acute thrombosis or late restenosis due to the deterioration of radial strength and vessel coverage. However, there is no good clinical data that correlates the metal fraction to the rate of stent thrombosis or restenosis. For an ideal stent, the metal fraction of an expanded stent may have to be less than 15% at a 3.0

millimetre internal expansion with a regular size vessel stent. In a small diameter vessel, the ideal metal fraction may have to be below 10% with an internal expansion of 2.5 millimetres [69].

2.6.7 Radiopacity

Radiopacity is an important stent feature that contributes to optimal clinical result and fewer complications. Radiopacity is essential to properly place the stent inside the coronary lesion [27]. The precision required in correctly placing the stent in the coronary lesion for deployment can be very demanding. A poorly visible stent is harder to use optimally when precision is demanded.

2.6.8 Fatigue Tolerance

Fatigue tolerance defines how well the structural integrity of a stent is preserved after the stent is permanently implanted in a constantly beating heart. A stent that is transformed into rigidity after deployment would give a better fatigue tolerance than a stent that remains flexible after deployment, when other structural factors being equal [69].

2.7 Material Composition and Surface Characteristic

A device or implant can fail simply because the material components do not have the requisite physical or chemical properties for a particular application. Physical characteristics of the surface, such as roughness, electrical charge, free surface energy and wettabbility are important determinants of thrombogenicity and tissue incorporation [74]. A number of intravascular stents that have been in clinical use for years provide useful knowledge on basic biocompatibility of certain alloys and metals. Table 2.3 indicates the composition of some of the most popular intravascular stents [64],[75].

Stent	Composition
Z stent	304 stainless steel
Palmaz-Schatz stent	316 L stainless steel
Medinvent stent	Mediloy (unknown composition)
Strecker stent	Tantalum
Nitinol stent	Nitinol (Nikel Titanium Alloy)
Gianturco coils	304 stainless steel
Wallstent	Cobalt-based alloy
AVE Micro	316 L stainless steel
Wiktor	Tantalum

Table 2.3: Metallic composition of intravascular stent

The finishing process during manufacturing influences the biocompatibility of stent because the process may determine the chemical composition of the surface [76]. Electropolishing removes most of the elements from the metal surface and leaves a high concentration of chromium. After exposure to air and sterilisation, a layer of chromium oxide with few nanometers thick forms, stabilising the surface by preventing further oxidation. I. E. Scheerder et al. [77] used an electrochemical polishing system to improve surface characteristics of stainless steel stents. They found that electrochemical polishing of coronary stents results in both decreased trombogenicity and neointimal hyperplasia after stent implantation in different animal models. If the surface finish is provided by abrasive polishing, the surface contains all the elements of the bulk material and consists of a mosaic of randomly oriented crystals or grains. Surface defects and trace elements at grain boundaries may cause protein alteration and influence cellular reaction [78].

2.8 An Experimental Approach

2.8.1 Stent Geometry

A considerable amount of experiments have been carried out in vivo to detect the influence of stent design towards the clinical outcomes in patients undergoing coronary stent placement. A. Kastrati et al. [79] have randomly assigned patients to receive five different types of stainless steel stents. They concluded that stent design has a significant impact (restenosis varied between 25.3% and 35.9%) on the long-term results after coronary stent placement. A number of experimental data support the concept that stent designs have a crucial impact on thrombosis and hyperplasia [80]-[81]. J. C. Squire et al. [82] were sought to determine whether intimal hyperplasia (abnormal increase in number of cells) provoked by stents stem from injury imposed by stent expansion characteristics. They concluded that stent expansion is nonuniform, which produces vascular injury that varies with stent geometry and this mechanism of injury is a determinant of stent restenosis.

2.8.2 Pressure Deployment

High-pressure stent dilatation has virtually reduced the risk of subacute stent thrombosis [83]-[84] but it can increase wall damage due to enhancement of the expanded geometry of coronary stent. High-pressure stent dilatation has been associated with a higher risk of late restenosis. To test this hypothesis, T. Akiyam et al. [85] have categorized 1181 lesions into two groups to distinguish between "low-pressure" and "high-pressure". They concluded that the restenosis rate after stenting is not affected by high-pressure stent expansion. High-pressure dilatation is considered a better stent placement strategy, but this has not yet been proved by appropriately designed studies. J. Dirschinger et al. [86] therefore, assessed the role of high-pressure dilatation in the early and late outcome of patients undergoing coronary stent placement. They concluded that the systematic use of high balloon pressure inflation (15 to 20 atm) during coronary stent placement is not associated with any significant influence on the 1-year outcome. Goldbery et al. [87] however tested whether the use of aggressive stent dilatation lead to more late lumen loss and restenosis. Their results suggested that aggressive stent expansion did not increase

late lumen loss but was associated with a lower rate of restenosis. Savage et al. [88] reported on the longer term effects of high pressure inflations on vascular healing and neointimal proliferation. It was found that stented lesions treated with high-pressure inflations demonstrated significantly smaller minimal luminal diameter than lesions treated with lower pressure inflations. They concluded that high distending pressure has a deleterious effect on late lumen loss presumably due to increased neointimal proliferation within the stent.

2.9 A Finite Element Analysis Approach

Implantation of coronary stent in a human artery to treat coronary artery decease is a complicated process. Apart from the current state of art play on stent technology, a highly skilled and experienced cardiologist is needed to perform the task. The behaviour of the stent expansion during the stent deployment in an artery is complicated and difficult to perform. There is no established procedure to ensure full stent deployment. Despite the numerous of software tools available, published works on behaviour of stent expansion by computer simulation are extremely rare and the current knowledge is mostly empirical.

A number of simulation works concerned with analysis of stent expansion have been reported. Borgersen and Sakaguchi [89] simulated the inflation of a vascular stent using three dimensional non-linear finite element contact analysis. The catheter balloon, stent and arterial wall were modelled as separate structural components. The polymer material was assumed to represent the catheter balloon. The stainless steel stent alloy is also represented as a non-linear material with a linear elastic modulus. Material characteristics of the arterial wall were assumed to be linear elastic and full contact algorithm approach was used to simulate contact between component surfaces. Teo et al. [90] reported on design optimisation of coronary stent using finite element method. They modelled the stent using computer aided design software (Pro-Engineer) and imported the IGES data to ANSYS 5.5 to generate the finite element model. The displacement and stress distributions over the stent were then computed.

Dumoulin and Cochelin [91] simulated a balloon-expandable stents (P308 Palmaz stent) to evaluate its mechanical properties by using the program package ABAQUS. The structure expansion of the stent and its long-term behaviour were analysed. Stress and strain fields in its wall were investigated during the dilatation of the stent. It was found that the major equivalent plastic strains were localised in the corners while the major stresses were located in the middle of the cells junctions. The sensitivity of the critical pressure to geometric imperfections was also studied and the fatigue life was tested. The results shown P308 Palmaz stent was insensitive to geometric imperfections and the stent could withstand an indefinite number of cardiac cycles.

Tseng et al. [92] reported the effects of stent geometry, balloon compliance and deployment pressure on balloon-artery interactions during stent placement by using FEA approach. It was found that the contact area of balloon and artery increased linearly with increasing inter-strut distance and with increasing balloon compliance. Rogers et al. [93] used finite element analysis to model how balloon-artery contact stress and area depended on stent-strut geometry, balloon compliance and inflation pressure. It was found that higher inflation pressures, wider stent-strut openings, and more compliant balloon materials had caused markedly larger surface-contact areas and contact stresses between stent struts.

Brauer et al. [94] carried out the experiments and numerical simulations to examine the dilatation properties of metallic stents. The dilatation behaviour of stents out of different materials was also investigated. Only the ends of the stent were modelled and an elastic-plastic model was chosen for the material of the stent. The material of the balloon was modelled in such a way that this material had a very low (0.001-0.1 GPa) Young's modulus in the circumferential direction and a normal value (3 GPa) in the radial direction. The friction between the two bodies was neglected due to the fact that simulation of the dilatation would need too much time for calculation. It was found that the behaviour of the balloon/stent systems at dilatation was related to both the properties of the stent and balloon. They concluded that the burst open pressure and recoil of the stent were depended on the stent design and material.

Whitcher [95] simulated a nitinol vascular stent (Symphony stent) to estimate its in vivo structural behaviour and fatigue properties. Al-Hassani et al. [96] illustrated a potential technique to study stent behaviour by using ABAQUS and Etave et al. [97] performed a series of finite element analyses to determine the exact mechanical characteristics of tubular stents and coil stents.

2.10 Summary of Literature Survey

From the literature cited and reviewed the following points can be noted:

- Many experimental studies have been carried out on different designs of stents. These studies have examined the effect of stent design and deployment pressure on the clinical outcomes in patients undergoing stent implantation.
- A considerable amount of analytical studies are available concerning expansion characteristic of stents but most do not take important parameters such as balloon length, balloon thickness and friction into account.
- No work on three-dimensional finite element simulations was found on stent production defects, which is important especially when the stent is implanted permanently inside blood vessel.
- The cost of experimental investigation with real size stent has long been an issue of concern. The finite element simulations on scaled up stent and then application to a normal stent size by scaling down have not been conducted before.
- It appears that no simulation studies with the presence of balloon, stent, plaque and artery have been performed to investigate the expansion characteristic of the stent after deployment.

Chapter 3

BRIEF INTRODUCTION ON FEA

3.1 Introduction

This chapter presents a basic theoretical outline of the numerical methods used to solve the problems as described in later chapters. It is not intended as a text on the finite element method but rather as a description of how the method was utilised here. The method presented was mostly extracted from the references [98]-[102]. Therefore, the reader unfamiliar with the method is referred to the reference section.

3.2 The Finite Element Method

The finite element method is a numerical analysis technique for obtaining approximate solution to a wide variety of problems. There are few basic steps in finite element method. These basic steps are involved in any finite element analysis and it consists of the following:

1. Discretization

The problem domain is divided into a number of subdomains called finite element. Each element contains a number of nodal points that given in coordinates relative to global coordinate system of the problem. The shape of each element is defined in terms of nodal coordinates by interpolation or shape functions.

2. Determination of Element Behaviour

An interpolation function is assumed for the variation of the unknown (i.e. displacement, temperature etc. depending on the analysis) that characterize the response of the system across each element. For each element, coefficient matrices which describe the response characteristics of the element are determined. In the case of stress analysis this matrix corresponds to the element stiffness matrix.

3. Transformation of Element Behaviour to Global Axis

The element stiffness matrices naturally lie parallel to the element local coordinate system. In order to solve the entire problem these matrices have to be transformed to align with the global coordinate system.

4. Element Assemblage

Assemble the elements to present the entire problem. The transformed stiffness matrix for each element is now combined in order to determine the stiffness matrix (global stiffness matrix) for the entire problem domain. This forms a matrix equation defining the behaviour of the entire solution domain.

5. *Apply Boundary Conditions*

Boundary conditions must be applied before a solution is possible. Some of the nodal unknowns must be restrained and will not be arbitrary in value.

6. *Solution for Nodal Unknowns*

The nodal unknowns are determined by solving a set of linear and non-linear algebraic equations. In most problems the number of equations to be solved is very large thus special solution techniques are employed. After solution the values (e.g. displacement values, temperature values etc.) of the dependent variable at each node are known.

7. *Calculation of Response*

Using the nodal values and interpolation functions, the response of each element is calculated. Parameters such as strain, stress etc. across each element may be determined.

3.2.1 General Theory

There are a number of methods available for determining the governing equations of equilibrium for the finite element method. One such method is to use the principle of virtual displacements to express the equilibrium of the body. This method is a basic relationship used for the finite element formulation. The principle of virtual displacements states that when a body in its state of equilibrium, the total internal virtual work in the body is equal to the total external virtual work acting upon that body due to external forces. The internal virtual work is equal to the actual stresses going through the virtual strains. The external work is given by the actual stresses going through the virtual displacements. The equilibrium of a general three dimensional body with body forces f^B, surface tractions f^S, and concentrated forces f^i, resulting in virtual displacements $\overline{U}$, actual stress $\boldsymbol{\sigma}$ and virtual strain $\overline{\varepsilon}$, the principle can be stated as:

$$\int_V \{\overline{\varepsilon}\}^T \{\sigma\} dv = \int_V \{\overline{U}\}^T \{f^B\} dv + \int_S \{\overline{U}\}^{T^S} \{f^S\} ds + \sum_i \{\overline{U}\}^{T^i} f^i \qquad (1)$$

where,

$$\{\overline{\varepsilon}\}^T = \left[\overline{\varepsilon}_{xx} \quad \overline{\varepsilon}_{yy} \quad \overline{\varepsilon}_{zz} \quad \overline{\gamma}_{xy} \quad \overline{\gamma}_{yz} \quad \overline{\gamma}_{zx}\right]$$

$\{\sigma\}^T = [\sigma_{xx} \quad \sigma_{yy} \quad \sigma_{zz} \quad \sigma_{xy} \quad \sigma_{yz} \quad \sigma_{zx}]$

$\{\overline{U}\}^T = [\overline{U} \quad \overline{V} \quad \overline{W}]$ and $\overline{U}$, $\overline{V}$ and $\overline{W}$ are displacements in global directions

$\{f^B\}^T = [f_x^B \quad f_y^B \quad f_z^B]$ where superscript ***B*** indicates body

$\{f^S\}^T = [f_x^S \quad f_y^S \quad f_z^S]$ where superscript ***S*** indicates surface

$\{f^i\}^T = [f_x^i \quad f_y^i \quad f_z^i]$ where superscript ***i*** indicates points

In finite element analysis the problem domain is approximated by an assembly of finite elements which interconnected at nodal points on the element boundaries. The displacements measured in a local coordinate system *x, y, z* in each element are assumed to be a function of the displacements at the nodal points within that element. Thus, for element ***m***

$$u^{(m)}(x,y,z) = H^{(m)}(x,y,z)\hat{U} \tag{2}$$

where, $H^{(m)}$ is the displacement interpolation matrix or shape function for element m. $\hat{U}$ is a vector of the three global displacement components U_i, V_i and W_i at all nodal points. If there are ***N*** nodal points in the element then $\hat{U}$ will be of dimension 3***N***. It is expressed generally as:

$$\hat{U}^T = [U_1 V_1 W_1 \quad U_2 V_2 W_2 \quad .... \quad U_N V_N W_N] \tag{3}$$

From the assumption on displacements in equation (2), the corresponding element strains can be evaluated as:

$$\varepsilon^{(m)}(x,y,z) = B^{(m)}(x,y,z)\hat{U} \tag{4}$$

where $B^{(m)}$ is the strain-displacement matrix for element ***m***. The rows of $B^{(m)}$ are obtained by appropriately differentiating and combining rows of matrix $H^{(m)}$.

The stresses within a finite element are related to the element strains and the element initial stresses by

$$\sigma^{(m)} = E^{(m)}\varepsilon^{(m)} + \sigma^{I(m)} \tag{5}$$

where $E^{(m)}$ is the elasticity matrix (stress-strain material matrix) of element ***m*** and $\sigma^{I(m)}$ is the element initial stresses. The material law specified in $E^{(m)}$ for each element can be that for an isotropic or anisotropic material and can vary from element to element.

Using the assumption on the displacements within each finite element (equation 2), equilibrium equation that correspond to the nodal point displacements of the assemblage of finite elements can be constructed from equations (1):

$$\sum_m \int_{V^{(m)}} \bar{\varepsilon}^{T(m)} \sigma^{(m)} dV^{(m)} = \sum_m \int_{V^{(m)}} \bar{u}^{T(m)} f^{B(m)} dV^{(m)} + \sum_m \int_{S^{(m)}} \bar{u}^{T^S(m)} f^{S(m)} dS^{(m)} + \sum_i \bar{u}^{T^i} f^i \tag{6}$$

Substituting equation (2), (4) and (5) into (6), the equilibrium equation can be written as:

$$\bar{\hat{U}}^T \left[\sum_m \int_{V(m)} B^{(m)T} E^{(m)} B^{(m)} dV^{(m)} \right] \hat{U} = \bar{\hat{U}}^T \left[\begin{array}{l} \left\{ \sum_m \int_{V(m)} H^{T(m)} f^{B(m)} dV^{(m)} \right\} + \\ \left\{ \sum_m \int_{S(m)} H^{T^S(m)} f^{S(m)} dS^{(m)} \right\} - \\ \left\{ \sum_m \int_{V(m)} B^{(m)T} \sigma^{I(m)} dV^{(m)} \right\} + f \end{array} \right] \tag{7}$$

where $H^{S(m)}$ is the surface displacement interpolation matrices that is obtained from the volume displacement interpolation matrix $H^{(m)}$ in equation (2) by substituting the element surface coordinates. Letter ***f*** denotes the vector of concentrated loads applied to the nodes of the element assemblage. It is noted that in equation (7), the nodal point displacement vector $\hat{U}$ is outside the summation sign, as it is independent of the element ***m***.

In order to obtain the equations for the unknown nodal point displacements from equation (7), the virtual displacement theorem is utilised by imposing unit virtual displacements in turn at all displacement components. As a result $\overline{\hat{U}}^T = I$ (where $\boldsymbol{I}$ is the identity matrix) and it is not shown in equation (8) due to the virtual displacements on each side of the equation. By denoting the nodal point displacements $\hat{U}$ by $\boldsymbol{U}$, the equilibrium equation of the element assemblage corresponding to the nodal point displacements is:

$$KU = R \tag{8}$$

where $\boldsymbol{K}$ is the global stiffness matrix of the element assemblage and is given by:

$$K = \sum_m \int_{V(m)} B^{(m)T} E^{(m)} B^{(m)} dV^{(m)} \tag{9}$$

$\boldsymbol{R}$ is the load vector where,

$$R = R_B + R_S - R_I + R_C \tag{10}$$

where, R_B is the effect of element body force,

$$R_B = \sum_m \int_{V(m)} H^{(m)T} f^{B(m)} dV^{(m)} \tag{11}$$

R_S is the effect of the element surface forces,

$$R_S = \sum_m \int_{V(m)} H^{S(m)T} f^{S(m)} dS^{(m)} \tag{12}$$

R_I is the effect of the element initial stresses,

$$R_I = \sum_m \int_{V(m)} B^{(m)T} \sigma^{I(m)} dV^{(m)} \tag{13}$$

and the nodal concentrated loads, $R_C = f$.

Equation (8) is a statement of the static equilibrium of the element assemblage. In equilibrium considerations, the applied forces may vary with time, in which case the displacements also vary with time. In such a case, equation (8) is a statement of equilibrium for a specific point in time. Nevertheless, if in actuality the loads are applied rapidly, inertia forces need to be considered and a truly dynamic problem needs to be solved. This may be done by using d' Alembert's principle which the element inertia forces are simply included as part of the body forces. In such a case equation (11) becomes:

$$R_B = \sum_m \int_{V(m)} H^{(m)T} \left[f^{B(m)} - \rho^{(m)} H^{(m)} \ddot{U} \right] dV^{(m)} \tag{14}$$

where $f^{B(m)}$ no longer includes inertia forces, $\ddot{U}$ gives nodal point accelerations and $\rho^{(m)}$ is the mass density of element ***m***. In this case, the equilibrium equations are:

$$M\ddot{U} + KU = R \tag{15}$$

where ***R*** and ***U*** are time-dependent. The matrix ***M*** is the global mass matrix and is given by:

$$M = \sum_m \int_{V(m)} \rho^{(m)} H^{(m)T} H^{(m)} dV^{(m)} \tag{16}$$

In a dynamic analysis some energy is dissipated during vibration. This in vibration analysis is usually taken account of by introducing velocity dependant damping forces. Therefore, damping forces as additional contributions are introduced to the body forces R_B ,

$$R_B = \sum_m \int_{V(m)} H^{(m)T} \left[f^{B(m)} - \rho^{(m)} H^{(m)} \ddot{U} - k^{(m)} H^{(m)} \dot{U} \right] dV^{(m)} \tag{17}$$

where $\dot{U}$ is a vector of the nodal point velocities and $k^{(m)}$ is the damping property parameter of element ***m***. In this case, the equilibrium equations become:

$$M\ddot{U} + C\dot{U} + KU = R \tag{18}$$

where ***C*** is the global damping matrix and can be written as:

$$C = \sum_{m} \int_{V(m)} k^{(m)} H^{(m)T} H^{(m)} dV^{(m)} \tag{19}$$

3.2.2 Non-linearities

In the above formulation it is assumed that the displacements of the finite element assemblage are small and that the material is linearly elastic. It is also assumed that the nature of the boundary conditions remains unchanged during the application of the loads on the finite element assemblage. These assumptions have entered the equilibrium equation in the following manners:

(a) the fact that the displacement must be small has entered into the evaluation of the matrix ***K*** and load vector ***R***, because all integrations have been performed over the original volume of the finite elements.

(b) the strain-displacement matrix ***B***, of each element was assumed to be constant and independent of element displacements.

(c) the assumption of a linear elastic material is implied in the use of a constant stress-strain matrix ***E***.

(d) the unchanged boundary conditions is implied by keeping constant constraint relations for the complete response.

The above observations point to different types of non-linearity that may arise in finite element analysis. They are categorized as:

(i) Non-linearity due to large displacements, large rotations, but small strains.

(ii) Non-linearity due to large displacements, large rotations and large strains.

(iii) Material non-linearity.

(iv) Non-linearity due to contact.

3.2.3 Solution Methodology

There are many solution methods available for use with the finite element method. However, as the analysis in this work is primarily concerned with non-linear analysis, this section will concentrate on solution methodology for non-linear problems. The basic problem in a general non-linear analysis is to determine the state of equilibrium of the body corresponding to the applied loads. Assuming that the external loads are described as a function of time, the equilibrium conditions of the finite element assemblage can be written as:

$$ {}^{t}R - {}^{t}F = 0 \tag{20}$$

where ${}^{t}R$ gives the externally applied nodal point forces at time t and the vector ${}^{t}F$ gives the nodal point forces that correspond to the element stresses. From equation (10) ${}^{t}R$ and ${}^{t}F$ may respectively be expressed as,

$$ {}^{t}F = {}^{t}R_B + {}^{t}R_S + {}^{t}R_C \tag{21}$$

and by identifying the current stresses as initial stresses, $R_I = {}^{t}F$

$$ {}^{t}F = \sum_{m} \int_{{}^{t}V(m)} {}^{t}B^{(m)T} \, {}^{t}\sigma^{(m)} \, {}^{t}dV^{(m)} \tag{22}$$

In reference to equation (22), it may be noted that in a large deformation analysis the stress and volume of the body at time t are unknown. Since this is a dynamic analysis, the inertial and damping forces would be included in vector ${}^{t}R$.

Considering the solution of the non-linear response, equation (20) must express the equilibrium of the system in the current defined geometry by taking account of all non-linearities and must be satisfied throughout the complete history of load application. The solution process is carried out using a step-by-step incremental analysis. The basic approach in an incremental step-by-step solution is to assume that the solution for the discrete time ***t*** is known and that the solution for the discrete time $t+\Delta t$ is required, where Δt is a suitable chosen time increment. Therefore, at time $t+\Delta t$ equation (20) can be written as:

$$^{t+\Delta t}R - {}^{t+\Delta t}F = 0 \tag{23}$$

Since the solution at time ***t*** is known, it can be written that:

$$^{t+\Delta t}F = {}^{t}F + F \tag{24}$$

where, ***F*** is the increment in nodal point forces corresponding to the increment of element displacements and stresses from time ***t*** to time $t+\Delta t$. This vector can be approximated using a tangent stiffness matrix, ^{t}K, which corresponds to the geometric and material condition at time ***t***,

$$F \cong {}^{t}KU \tag{25}$$

where ***U*** is the vector of incremental nodal point displacements. By substituting equation (24) and (25) into (23), it becomes:

$$^{t}KU = {}^{t+\Delta t}R - {}^{t}F \tag{26}$$

and by solving for ***U***, an approximation to the displacements at time $t+\Delta t$ can be calculated:

$$^{t+\Delta t}U \cong {}^{t}U + U \tag{27}$$

Having evaluated an approximation to the displacements corresponding to time $t+\Delta t$, an approximation for stresses and corresponding nodal point forces at time $t+\Delta t$ can be obtained and could then be proceeded to the next time increment calculations. Nevertheless, because of the approximation expressed in equation (25), such solution may be subject to significant errors and, depending on the time or load step sizes used, may be unstable. In practice, it is therefore frequently necessary to iterate until the solution of equation (23) is satisfied to sufficient accuracy.

There are different solution procedures available for the solution of equation (26). In this work, the explicit time integration method was used and will be briefly outlined. The most common explicit time integration operator used in non-linear dynamic analysis is probably the central difference operator. The equilibrium of the finite element system is considered at time ***t*** in order to calculate the displacements at time $t+\Delta t$. Solution is sought for each discrete time step for the equilibrium equation neglecting the effect of damping which may be expressed as,

$$M\,{}^{t}\ddot{U} = {}^{t}R - {}^{t}F \tag{28}$$

where the nodal point force vector ${}^{t}F$ is evaluated on the basis of the methods used to formulate the material and geometric non-linearities. This involves the choice of element type, kinematics and kinetic descriptions in which of all are problem dependent. The solution for the nodal point displacements at time $t+\Delta t$ is obtained using the central difference approximation for the accelerations. In this approximation it is assumed that,

$${}^{t}\ddot{U} = \frac{1}{\Delta t^{2}}\left[{}^{t-\Delta t}U - 2\,{}^{t}U + {}^{t+\Delta t}U\right] \tag{29}$$

By substituting equation (28) into (29), it gives:

$$\frac{M}{\Delta t^{2}}\left[{}^{t+\Delta t}U\right] = {}^{t}R - {}^{t}F - \frac{M}{\Delta t^{2}}\left[{}^{t-\Delta t}U - 2\,{}^{t}U\right] \tag{30}$$

Therefore, if ${}^{t-\Delta t}U$ and ${}^{t}U$ are known then ${}^{t+\Delta t}U$ can be determined from equation (30). The drawback in the use of this method is that for stability, the time step size Δt must be smaller than a critical time step size, Δt_{CR}, which is equal to T_n/π where T_n is the smallest period in the finite element assemblage.

3.3 LS-DYNA3D Theoretical Methods

3.3.1 Solution Methodology

LS-DYNA3D is a general purpose, explicit three-dimensional finite element program used to analyse large deformation dynamic response and highly non-linear transient dynamic problems. The complex contact problems during the expansion of stent by using a balloon as a medium can be very complicated and high computer solution time consumption. The explicit method of solution used by LS-DYNA3D provides fast solutions for short-time, large deformation dynamics, quasi-static problems, non-linearities, and complex contact problems. This section briefly presents the relevant theoretical methods for LS-DYNA3D analysis.

The equilibrium equation of a dynamic problem and the solution process using the central difference method was given above in equation (28), (29) and (30). As mentioned above, the time step size Δt plays a decisive role in reaching stability and therefore must be smaller than the critical time step Δt_{CR}. LS-DYNA3D calculates the critical step size from,

$$\Delta t = \frac{I}{C} \tag{31}$$

where $\boldsymbol{I}$ is the characteristic length of the smallest element and $\boldsymbol{C}$ is the sonic wave propagation velocity through the element material. For stability reasons a scale factor of 0.9 is used to decrease the time step in equation (31). The formula used by LS-DYNA3D to estimate the time step is therefore,

$$\Delta t = 0.9 \frac{I}{C} \tag{32}$$

It is noted that ***I*** and ***C*** are calculated in a different manner depending on the element type concerned. For eight node solid elements ***I*** is the smallest distance between two neighbouring nodes of the smallest element in the model. The sound wave propagation speed, ***C*** is determined by using the formula as bellow:

$$C = \sqrt{\frac{E(1-\nu)}{(1+\nu)(1-2\nu)\rho}} \tag{33}$$

where ***E*** is the Young's modulus of the material, ν is the Poisson's ratio and ρ is the specific mass density.

3.3.2 Element Formulation

There are numbers of explicit dynamic elements available from LS-DYNA3D element library. In this work an eight-node solid hexahedron element was used for the analyses. Volume integration of the elements is carried out using Gaussian quadrature principle. Both reduced (one point) and full integration options are available. Reduced integration means that the number of points for numerical integration in the element formation process is less than that necessary for exact integration. A reduced integration brick element will have one integration point at its centre whereas fully integrated brick will have eight integration points.

Since the number of integration points is directly proportional to CPU time, one-point integration elements save a lot of computation time and extremely robust in the case of large deformations. In spite of being robust for large deformations and saving extensive amounts of computer time, one-point integration solid elements leads to modes of deformation which have zero strain energy, called zero energy. These modes are commonly referred to as hourglassing modes. Undesirable hourglass modes tend to have periods that are typically much shorter than the periods of the structural response. They are often observed to be oscillatory. Hourglassing modes result in stable mathematical states that are physically unrealistic because the single

integration point does not capture any strain energy in the element (Figure 3.1). They typically have no stiffness and give a zigzag deformation appearance to the finite element mesh. The zero energy or hourglass deformation mode in a two dimensional element is shown in Figure 3.1.

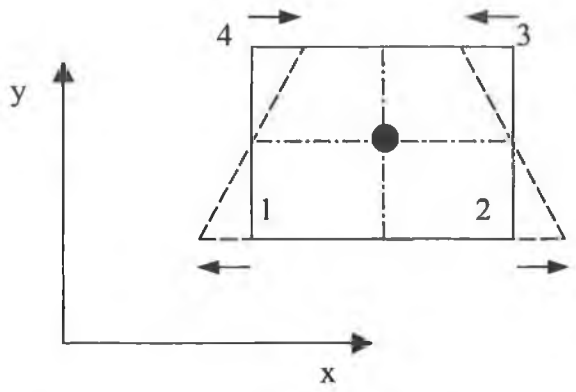

Figure 3.1: Hourglass deformation mode

The origin and consequent implication of the hourglass deformation mode is described in elementary form, with reference to the above figure, by Halliquist and Benson [100]. As illustrated in Figure 3.1, hourglass mode is generated when node 1 and 3 are given a velocity of +1 in the x direction and nodes 2 and 4 are given a velocity of -1 in either x or y direction. The element deforms but the velocity gradient of the element is zero. The element does not develop stresses to oppose the velocities due to zero in the velocity gradient. As a result, the element may continue to deform in this mode without resistance.

One way of resisting hourglassing modes is to use a viscous damping or a small elastic stiffness capable of stopping the formation of the hourglass modes but having a negligible effect on the stable global nodes. The hourglassing resisting force for a particular node in a particular co-ordinate direction is subject to the nodal velocity in that direction. The resisting force in solid elements is defined as,

$$f_{i\alpha}^{k} = a_h h_{i\alpha} \Gamma_{\alpha k} \tag{34}$$

where,

$$a_h = Q_{hg}\rho v_e^{2/3}\frac{c}{4} \tag{35}$$

$$h_{i\alpha} = \sum_{k=1}^{8} x_i^k \Gamma_{\alpha k} \tag{36}$$

in which:

α = number of hourglass mode

$\Gamma_{\alpha k}$ = hourglass shape vectors

x_i^k = velocity of node k in i direction

v_e = element volume

c = speed of sound in material

Q_{hg} = a constant usually set between 0.05 to 0.15 [100]

Fully integrated elements do not experience hourglassing modes. However, these options are more costly (in CPU time) than other element formulations. Fully integrated elements used in the solution of plasticity problems and other problems where Poisson's ratio approaches 0.5 lock up in the constant column bending modes. An average pressure is used over the elements to preclude locking and consequently the zero energy modes are resisted by deviatoric stresses. In other word, spurious pressure stresses develop in the element, which cause the element to have an over-stiffness for deformations that will not cause any volume change. In certain situations it has been noted [100] that the cost of using fully integrated elements can be justified by increased reliability and if used sparingly may actually increase the overall speed.

3.3.3 Material Model

LS-DYNA3D has an extensive library of material models that can be used to represent a wide range of material behaviour. In this work, two material models were used. The first one is the bilinear isotropic hardening plasticity model with no strain rate dependence for all simulations of the stent. The yield stress is defined as:

$$\sigma_y = \sigma_o + E_p \varepsilon_p^{eff} \tag{37}$$

where,

σ_o is the initial yield stress

E_p is the plastic hardening modulus and is given by $E_p = \frac{(E_{\tan} E)}{(E - E_{\tan})}$

ε_p^{eff} is the effective plastic strain

$E_{\tan}$ is the tangent modulus

E is Young's modulus

The second one is a material model of incompressible Mooney-Rivlin Rubber. The Mooney-Rivlin option is suitable for incompressible materials such as rubber-like materials. Incompressible materials can undergo large deformations and strains without an appreciable change in volume. The stresses for the Mooney-Rivlin Rubber material models are derived from strain energy density functions. For LS-DYNA3D the strain energy density function (W) is defined in terms of input constants C_{10}, C_{01} and ν as:

$$W = C_{10}(I_1 - 3) + C_{01}(I_2 - 3) + C\left(\frac{1}{I_3^2} - 1\right) + D(I_3 - 1)^2 \tag{38}$$

where:

$$C = \frac{C_{10}}{2} + C_{01} \tag{39}$$

$$D = \frac{C_{10}(5\nu - 2) + C_{01}(11\nu - 5)}{2(1 - 2\nu)} \tag{40}$$

ν = Poisson's ratio

$G = 2(C_{10} + C_{01})$ = shear modulus of linear elasticity

I_1, I_2, I_3 = strain invariants

It is noted that the recommended values for Poisson's ratio are between 0.490 and 0.495 or higher [100]. Lower values may lead to instabilities.

3.3.4 Contact Algorithm

Contact is represented differently in an explicit dynamic analysis than in other types of implicit analyses. In other analyses, the contact is represented by actual contact element. For explicit dynamics, the contact is defined using contact surfaces. Contact occurs when one segment of a model outer surface penetrates another segment. LS-DYNA3D incorporates eighteen different contact types to adequately characterise the complex interaction between surfaces. To properly select a contact surface for a given model it is important to understand the different contact algorithms available. The are three different contact algorithms available in the LS-DYNA3D program: Single surface contact, Nodes to surface contact and Surface to Surface contact. In this work the surface to surface contact algorithm was used for all simulations and will be briefly described.

The surface to surface contact algorithm establishes contact when the surface of one body penetrates the surface of another. Surface to surface contact is fully symmetric so that the choice of contact and target surfaces are arbitrary. In order to define surface to surface contact, nodal components or part numbers are required for the contact and target surfaces. The surface to surface contact algorithm is generally used for bodies that have large contact areas and the contact surfaces are know.

In LS-DYNA3D, contact searching is performed in two steps: global and local searching. In a global search the bucket sort method contact search algorithm is used by an automatic surface to surface contact option. This method is used to determine which target surface is being contacted by which contact surface. The bucket sort algorithm divides the target surface region into cubes (buckets). Contacting nodes can contact any segment of the target surface in the same bucket or adjacent buckets. After the global search has located possible contact, the penetration is checked by the local search. A node to segment algorithm is used to find the penetration.

The surface to surface contact algorithm is based on the penalty method. The penalty method is used for the calculation of the contact forces. This method consists of placing normal interface springs between all penetrating nodes and the contact surface as illustrated in Figure 3.2.

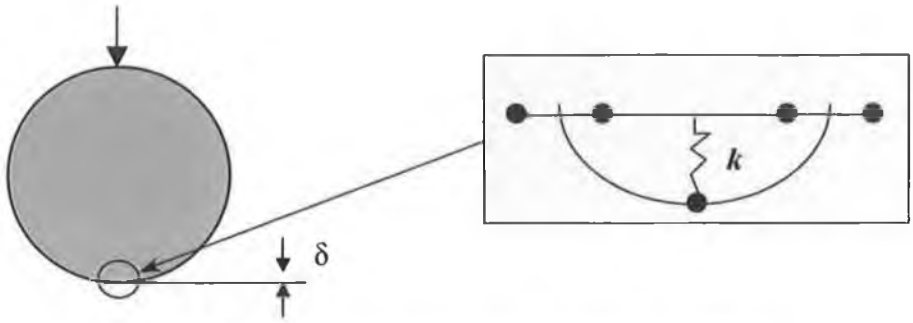

Figure 3.2: Contact algorithm with penalty method

In applying the penalty method, each slave node is checked for penetration through the master surface. An interface force is applied between the slave node and its contact point during the penetration. The interface force acts like a restoring force to restore the node to the contact surface in the normal direction. The magnitude of this force is proportional to the amount of penetration and is given by:

$$F = k\delta \tag{38}$$

where,

F = contact interface force

k = contact interface stiffness

δ = penetration depth

The LS-DYNA3D program calculates the contact stiffness based on the material properties and size of the contacting segments. The contact stiffness that is used depends on the relative stiffness of the bodies in contact. The contact stiffness $\boldsymbol{k}$, is expressed as:

$$k = \frac{(SFSI)A^2K}{V} \tag{39}$$

where,

A = area of contact segment

K = bulk modulus of contacted element

$SFSI$ = contact stiffness scale factor (0.1 by default)

V = volume of the contacted element

As mentioned earlier, the penalty method is implemented in a symmetric manner. When the mesh grading varies along the contact surfaces, or the surfaces are subject to large distortions, the best choice of master surface may vary along the contact surfaces. The symmetry greatly increases the robustness of the contact algorithm by allowing each surface to act as both the master and slave surfaces.

Chapter 4

SIMULATION AND ANALYSIS OF STENT

The most important step in any finite element simulation is to ideally model the problem. In order to achieve this, a great understanding of the software is essential to correctly approach the problem and simulate the particular problem as closely as possible. In the case of stent expansion analysis good modelling of the deforming body is of most importance in order to achieve an accurate solution. Expansion of stent is a complicated process. A three dimensional analysis is required in order to properly represent the problem and to be able to detect unusual deformations. The analyses were performed using finite element packages ANSYS as a pre- and post-processor and LS-DYNA3D explicit solver for the solution of the problem.

4.1 Stent Expansion without Balloon

Inflation pressure plays an important role in the dilatation of stent to its maximum distension limits. The variation of pressure loads has been recognised as one of the key points to achieve the ultimate stent geometry in the expansion of the stent. The alteration of stent geometry due to the inflation pressure therefore has become a decisive factor in the risk of subacute stent thrombosis [85]. That leaves a wide variety of areas to delve into. Application of pressure speed is one of the factors that should not be neglected. In this section, Finite Element (FE) simulation is used to simulate the expansion of a stent with pressure applied on the inner surface of the

stent. The analysis presented in this paper addresses the effect of the speed of pressure on the stress distribution, degree of expansion and foreshortening of the stent.

4.1.1 Modelling

The ANSYS Finite Element Package was used to develop the geometric models. The simulations were carried out to expand a stainless steel 304 stent of 3.0 mm outer diameter and 2.9 mm inner diameter with 20 mm in length. The model contains 66 slots (cells) which are equally spaced throughout the entire model. The dimensions of the model are simply described in Table 4.1 below:

Category	**Stent before Expansion**
Number of Cells	66 (33 x 2)
Cell Size	1.1128 mm^2
Cell Areas	73.4448 mm^2
Metal Surface Area	41.606 mm^2
Stent Surface Area	115.0508 mm^2
Outer Diameter of Stent	3 mm
Inner Diameter of Stent	2.9 mm
Length of Stent	20 mm

Table 4.1: Dimensions of the stent

By taking advantage of symmetry it was possible to model half of the problem. The finite element model of half of the stent used is shown in Figure 4.1. In this case the stent is particularly difficult part to model satisfactorily especially at the region where the slots are located. The slots have to be placed accurately in order to obtain the symmetrical geometry throughout the stent. Even though the stent could be created by computer aided design packages (e.g. Mechanical Desktop), meshing the stent would be the most difficult step since hexahedron solid brick elements were preferred for analysis reasons. Owing to this reason, the stent was first created in one volume and then the entire volume was meshed without the present of any slots. The stent elements were then detached from each other using a function provided by

ANSYS finite element package. The elements could be deleted once the constitution of elements was broken. The slots of the stent were then created by eliminating the detached elements.

Figure 4.1: Finite element model of half of the stent

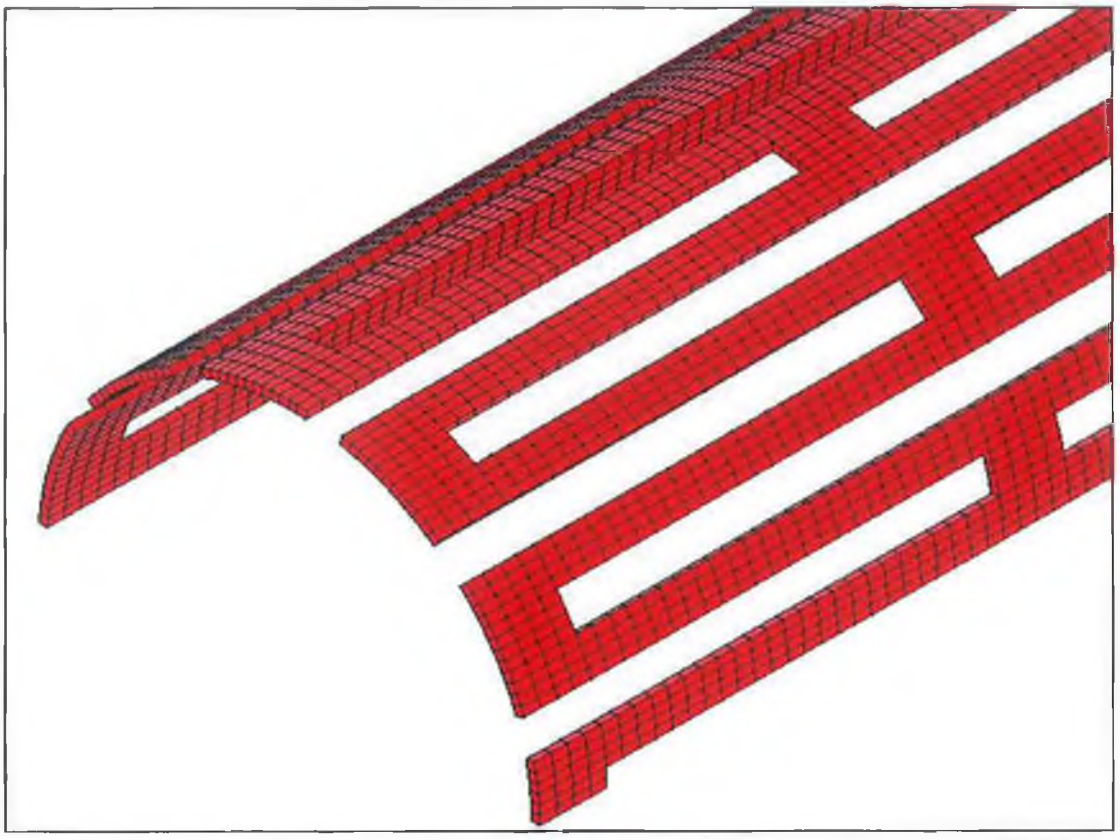

Figure 4.2: Selected discretised geometry

The individual stent strut width is 0.214 mm in circumferential direction and the length of the bridging strut connecting between the two adjacent cells is 0.4 mm. Figure 4.1 shows the discretised model of the stent and Figure 4.2 shows a close up of the mesh used. The finite element model consists of a total of 9504 elements. The stent was discretised by 200 elements along its modelled length and 88 elements in circumference with 1 element across the thickness.

The stent was modelled using eight node three dimensional explicit dynamic solid brick elements. A bi-linear elasto-plastic material model was assumed for the stent material. This model uses two slopes (elastic and plastic) to represent the stress-strain behaviour of the material as shown in Figure 4.3. These two slopes were calculated by using Young's modulus as for elastic region and a Tangent modulus for plastic region. The material properties were chosen to approximately represent Stainless Steel 304 [103] and are shown in Table 4.2.

Stainless Steel 304	**Material Properties**
Young's Modulus	193 GPa
Tangent Modulus	692 MPa
Shear Modulus	75×10^{6} MPa
Poison's Ratio	0.27
Density	7.86×10^{-6} Kg/mm^3
Yield Strength	207 MPa
Failure Stress	517 MPa
Failure Strain	0.45

Table 4.2: Material data used for material model

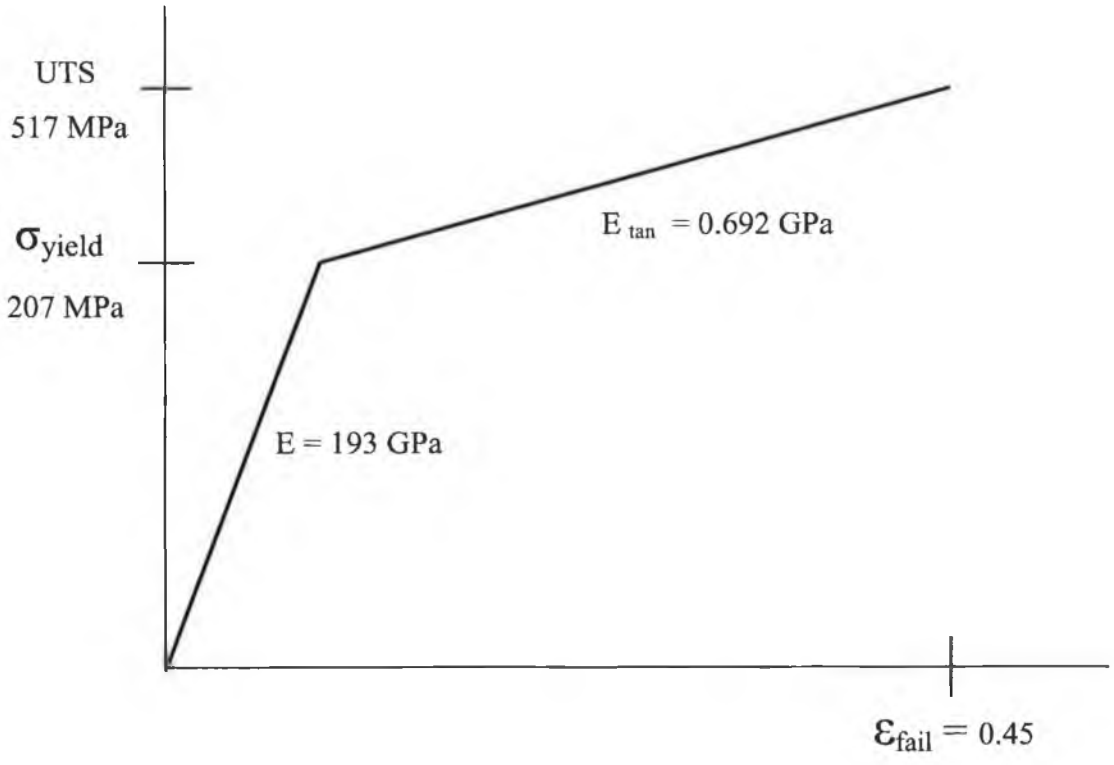

Figure 4.3: Material model used for tube material

4.1.2 Boundary Conditions, Loading and Solution

Due to the symmetry of the stent only half of the model was developed to simulate the expansion process. By utilising the correct boundary conditions, the stent nodes at the symmetry edges were restrained in the appropriate directions. Symmetric

boundary conditions were imposed on the nodes of the stent in the plane of symmetry. Both ends of the stent were free from any constraints so that expansion and foreshortening behaviour of the stent would be observed.

The pressure load was applied as a surface load on the inner stent surface, expanding the stent radially past its elastic limit to a maximum diameter before failure stress was reached. Extra precaution was taken to make sure that the pressure load was applied on the right face of the elements. A problem could be encountered if the pressure loading was wrongly placed.

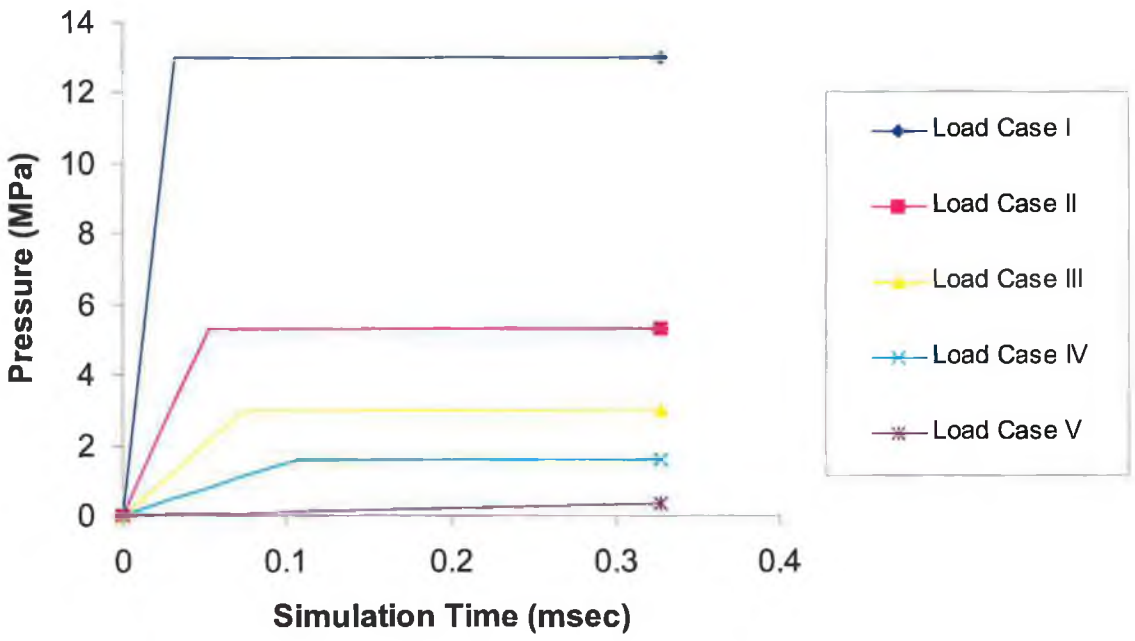

Figure 4.4: Five different load cases

As illustrated in Figure 4.4 five simulations with different load speeds were investigated during the analysis. A wide range of load speeds was carried out but only these five load speeds were selected as a probe to investigate the effect of loading speeds on the deformation of the stent. This is due to the fact that too high of the load speed may only cause the stent to damage and too low of the load speed may result in buckling. Apart from that it was believed that the relation between the load speed and the deformation of the stent could easily be established with the load range

presented. The five different load cases as illustrated in Figure 4.4 could be summarised in Table 4.3 as below:

Load Case	**Load Speed (MPa/Msec)**
I	400
II	100
III	40
IV	15
V	1

Table 4.3: Five different load cases with different load speeds

4.1.3 Results and Discussion

Generally speaking, the model of stent used in these analyses has the same behaviour of deformation regardless of the speed of the pressure applied. All the simulations showed that the stent started distending from both ends and then gradually developed towards the centre of the stent.

In order to determine the value of maximum radial displacement, the stent was radially expanded until the onset of plastic deformation was observed and the ultimate tensile strength of the material was reached. For the stent, maximum equivalent stresses were used for the direct comparison with the ultimate tensile strength of the material. All maximum radial displacements were measured by taking the displacement values of the nodes in radial direction and they were located in the middle of the stent. The shape of stent changed according to the pressure speeds applied.

The regions of high stress are concentrated on the four corners of the cells rather than in the middle of the struts or the bridging strut itself. This was because the struts pulled apart from each other to form a rhomboid shape of cells during the expansion. This also resulted in shortening of the stent. As the stent is expanding, the bridging struts move closer and close to each other until the maximum applied pressure is reached.

4.1.3.1 Load Case I

For load case I, the stent was subjected to a uniform internal pressure increasing at a constant rate of 400 MPa per millisecond. Amongst the five different load cases, this simulation was run with the highest pressure and implemented by the fastest load speed. The development of the expansion process is detailed in Figure 4.5 to Figure 4.8, which show the distribution of stress at various times during the simulation.

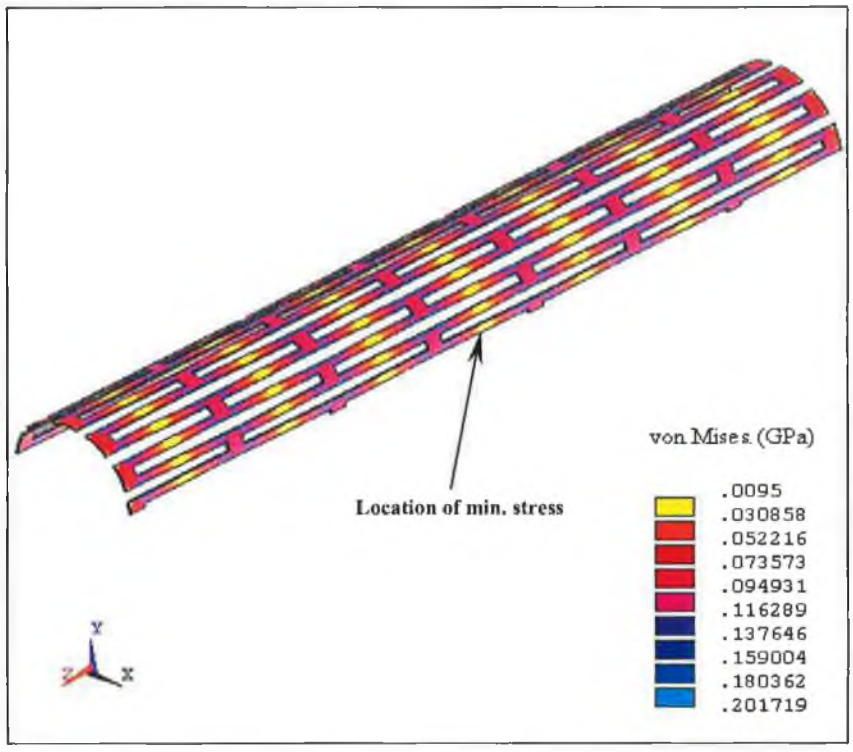

Figure 4.5: Distribution of stress in the stent at 25% of final load by load case I

It is evident from these figures that the region of maximum stress is always concentrated at the corner of the cells. However, the lower stress region is always changing. The distribution of stress shown in Figure 4.5 indicates that the lowest stress region is located very much in the same area and they are equally placed in the body struts throughout the entire stent. As the pressure increases the region becomes smaller. Somehow, it is very obvious from Figure 4.6 that the development of stress in body struts near the two ends of the stent are much slower compared to the rest of the body struts near the centre of the stent. As the pressure increases to 75% of final

load, most of the stresses on the body struts are within the region of 183 MPa to 286 MPa.

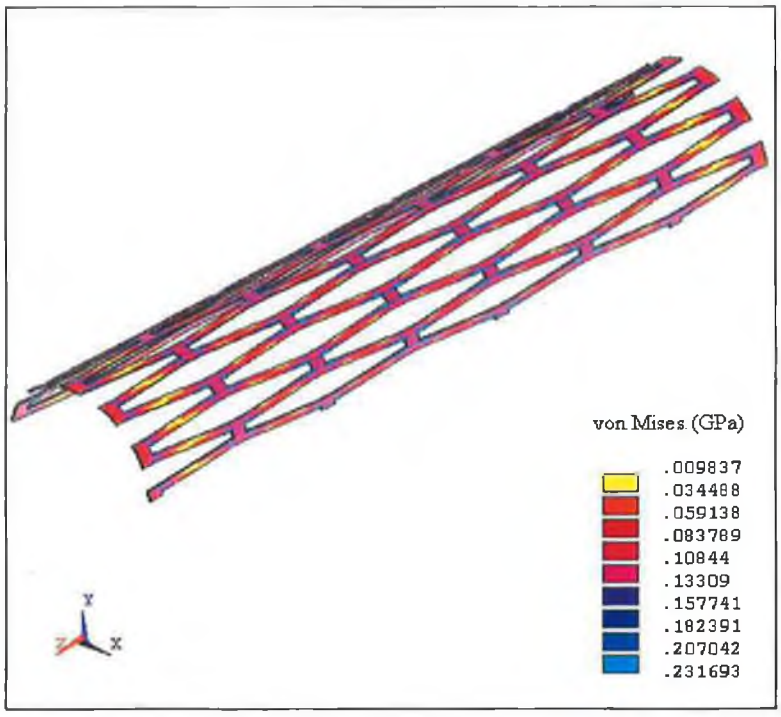

Figure 4.6: Distribution of stress in the stent at 50% of final load by load case I

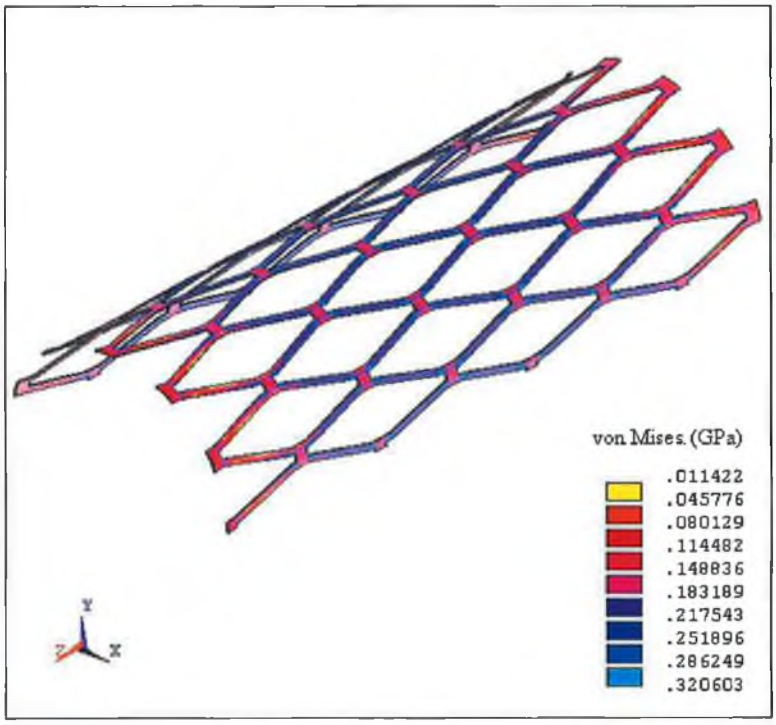

Figure 4.7: Distribution of stress in the stent at 75% of final load by load case I

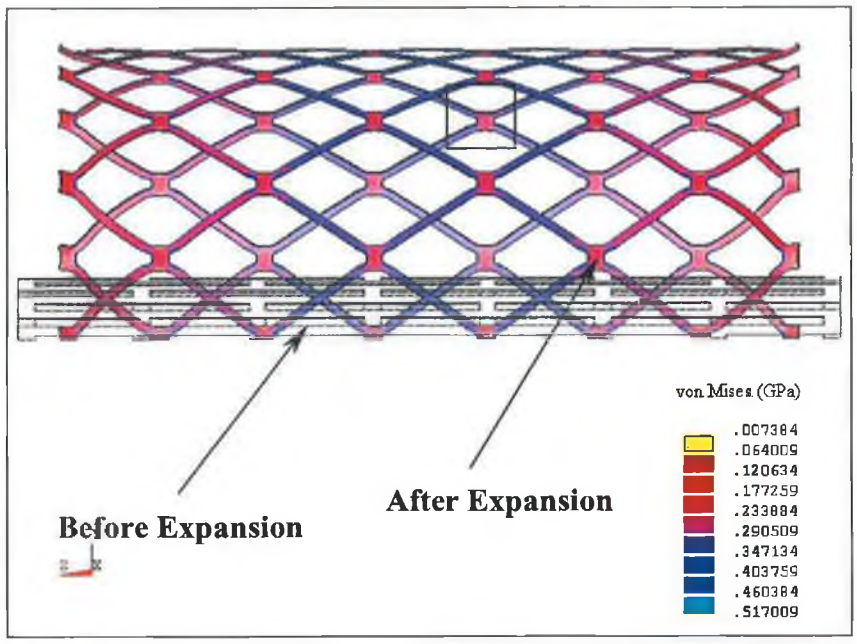

Figure 4.8: Distribution of stress in the stent at final load by load case I

Figure 4.9 shows some parts of the structure in the stent are being loaded to their yield point. The highest stress region will first experience the plastic deformation. This region is located at the inner and outer corners of the cells. At this stage, some parts of the stent are going through the elastic deformation. It tends to remain its shape. As the pressure increases, this region no longer able to store the applied forces and cause the neighbouring parts to deform plastically. The pressure at this point is found to be 4.48 MPa.

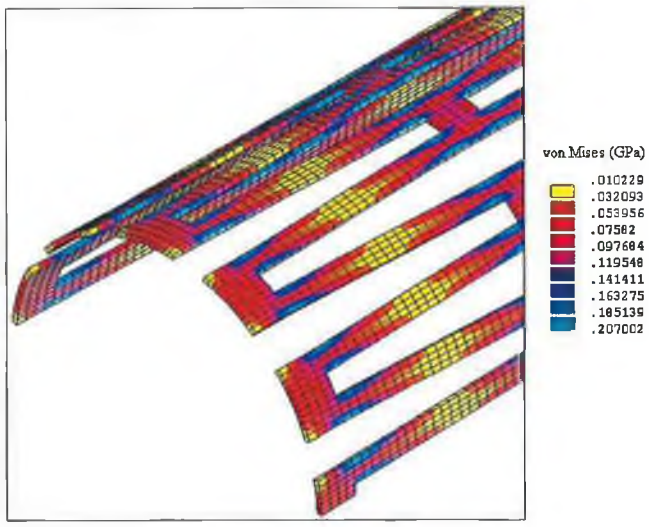

Figure 4.9: Distinct local plastic deformation by load case I

Figure 4.10 shows a close up of the deformed mesh in the centre part of the stent (as indicated in Figure 4.8) after enlargement. Although the maximum stress was located at the corners of the stent struts, it is observed that the regions of most of the higher stresses are concentrated on the body of the stent struts. On the contrary, the lowest stressed region is located at the bridging struts itself.

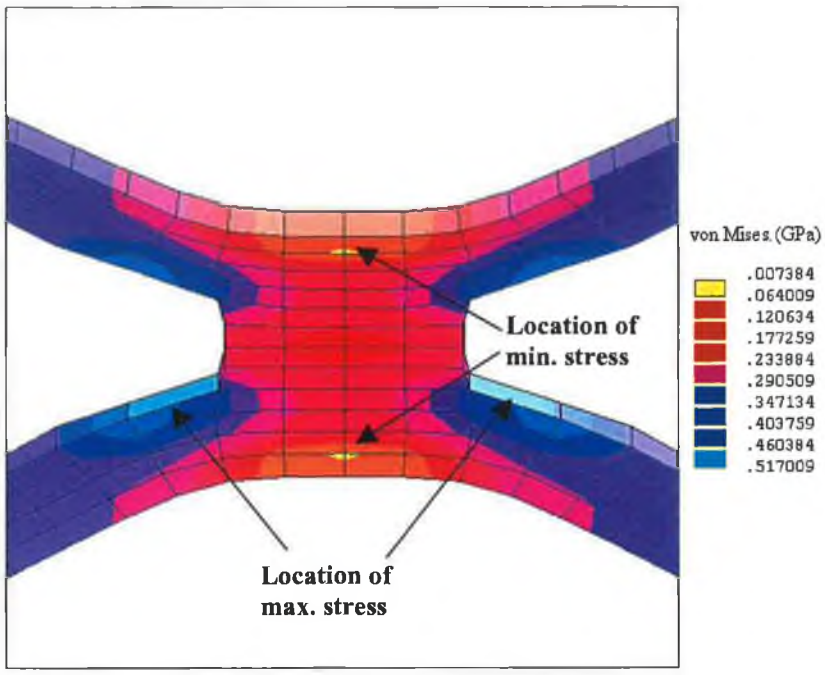

Figure 4.10: Closer view of the central stent strut by load case I at final load

Figure 4.11 shows the stress level along the stent in z-direction at maximum expansion. This figure depicts the integration of stress levels at three locations of the stent respectively. There is no doubt that the stress level is getting higher when approaching to the centre of the stent. Nevertheless, three specific locations of the stent can be easily recognised from the graph. These three regions in the stent experience the paramount differences in stress level and they are found to be at the corner of the cell, body strut and the bridging strut.

The maximum peaks of the graph represent the corner of the cell and the highest peak point is found to be at 343.6 MPa. The bridging strut of the stent is represented by the minimum peaks of the graph and the highest peak point is found to be at 196 MPa. As can be seen from the graph that the maximum stress sustained by the peak

point of the bridging strut is still lower than the yield stress. This indicates that at some points of the bridging strut remain in the elastic region despite the fact that the stent is experiencing the maximum expansion. The body strut is represented by intermediate lines that are located between maximum and minimum peak points. The highest stress that the body strut could achieve is 303.3 MPa. A conclusion that can be drawn from these intermediate lines is that the differences in stress along the body struts are getting smaller near the centre of the stent. The highest stress occurs at the corner of the cell, follows by the body strut and then the bridging strut. On the contrary, the lowest stressed point is located near the ends of the stent and it is found to be 75.2 MPa as can be seen from the figure.

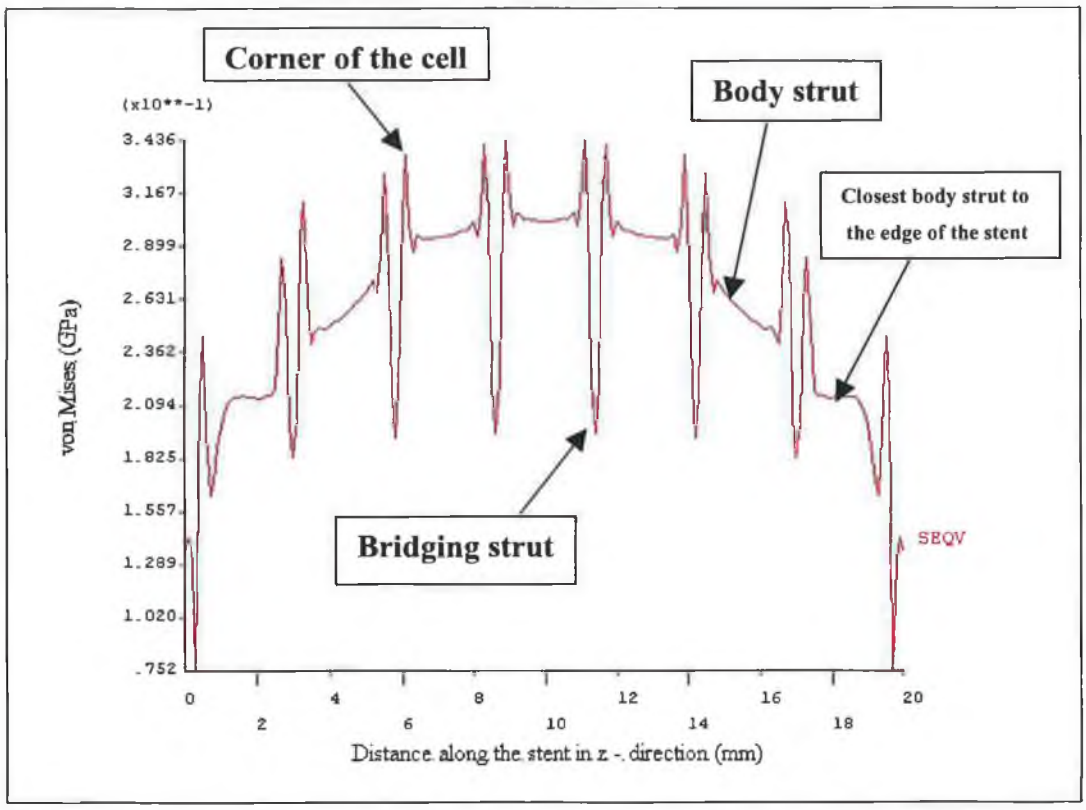

Figure 4.11: Stress level along the stent in z-direction at max expansion by load case I

The critical pressure was determined based on the ultimate stress or tensile strength of the material that was approximately 517 MPa [103]. The simulation time at this point was 0.032 ms. Figure 4.12 shows the development of radial displacement and foreshortening of the stent with respect to the pressure applied. The maximum pressure just before failure was 13 MPa. The maximum radial displacement obtained

was found to be 5.6 mm from the central axis of the stent. The maximum foreshortening of the stent in axial direction at that point was 2.06 mm. During the expansion process, the radial displacement and foreshortening increased gradually as the pressure increased to 13 MPa. It was observed that foreshortening of stent always occurs slower than radial displacement and it tended to go even slower when the pressure was approaching the critical value. The discrepancy between the radial displacement and foreshortening was found to be 3.54 mm when the maximum pressure was reached.

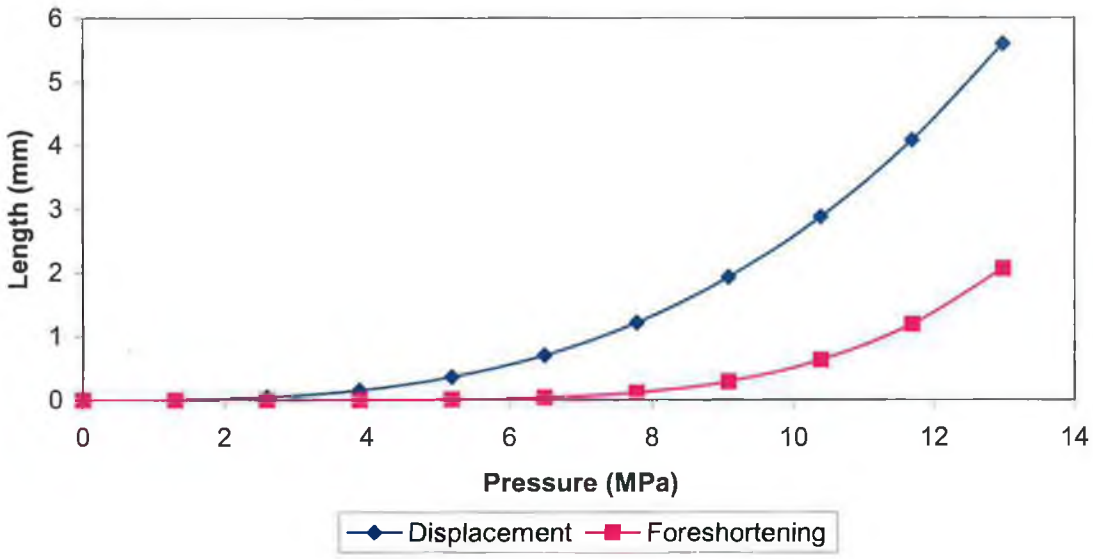

Figure 4.12: Development of radial displacement and foreshortening by load case I

4.1.3.2 Load case II

For load case II, the stent was subjected to a uniform internal pressure increasing at a constant rate of 100 MPa per millisecond. This simulation was run with the pressure speed that is four times slower than the pressure speed applied in load case I.The development of the expansion process is detailed in Figure 4.13 to Figure 5.2, which show the distribution of stress at various times during the simulation. As can be seen from the figures the location of maximum and minimum stress does not change as the expansion of stent continues. The distribution of stress in the stent does not show a huge distinction from load case I throughout the expansion process. The stress level sustained by the stent in load case II is somewhat lower here but the region where the higher stress occurs is more concentrated compared to load case I. At maximum

expansion, most of the stresses on the body struts are within the region of 232 MPa to 289 MPa.

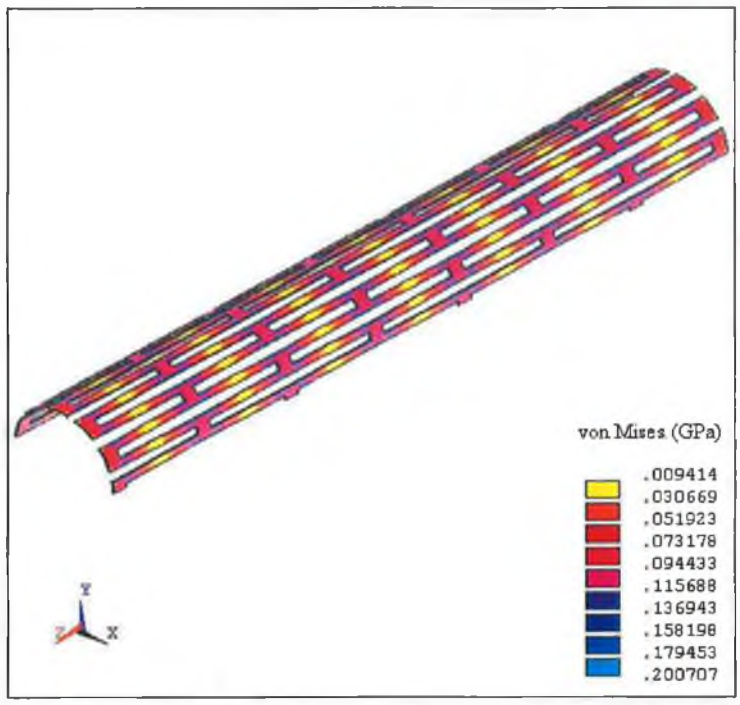

Figure 4.13: Distribution of stress at 25% of final load by load case II

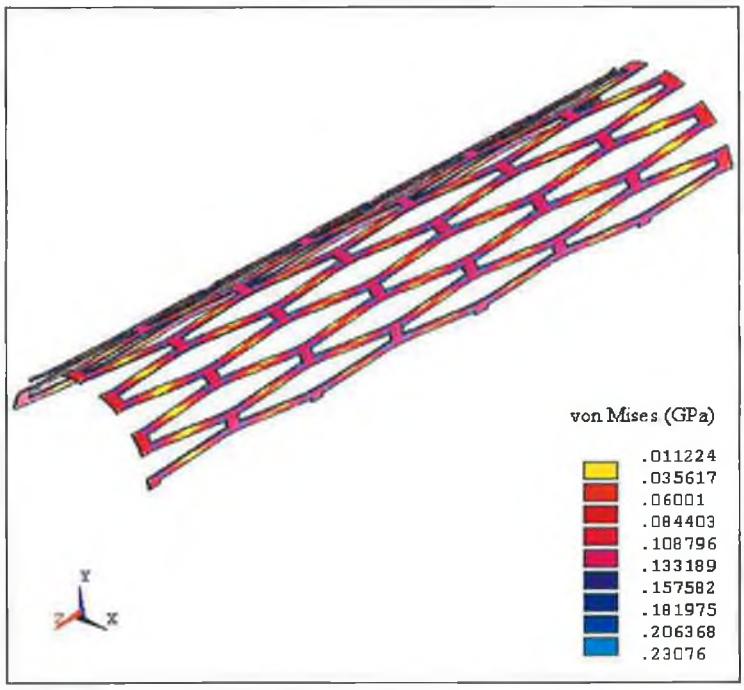

Figure 4.14: Distribution of stress at 50% of final load by load case II

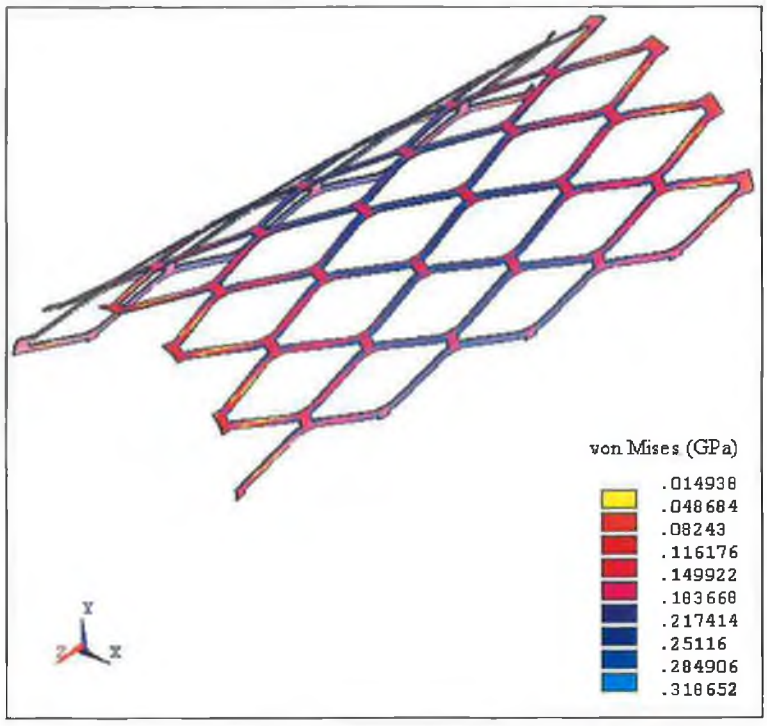

Figure 4.15: Distribution of stress at 75% of final load by load case II

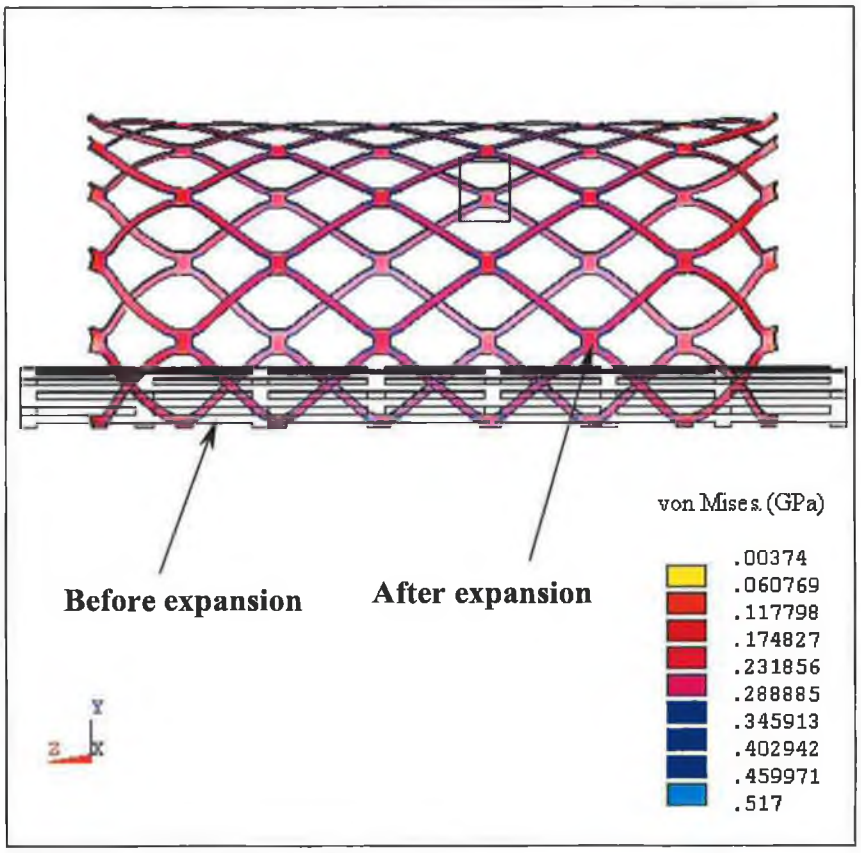

Figure 4.16: Distribution of stress at final load by load case II

Figure 4.17 shows the distinct local plastic deformation at the end of the stent by load case II. It can be clearly seen from the figure that the outer and inner corners of the cells will first go through the plastic deformation. The body strut experiences the least stress compare to the bridging strut. As the expansion going on, the lowest stressed region becomes smaller. This is due to the force that gradually transferred to the middle of the body strut. However, the figure shows no distinctions of stress allocation between load case I and load case II at the yield point. The pressure load at this point is found to be 1.83 MPa.

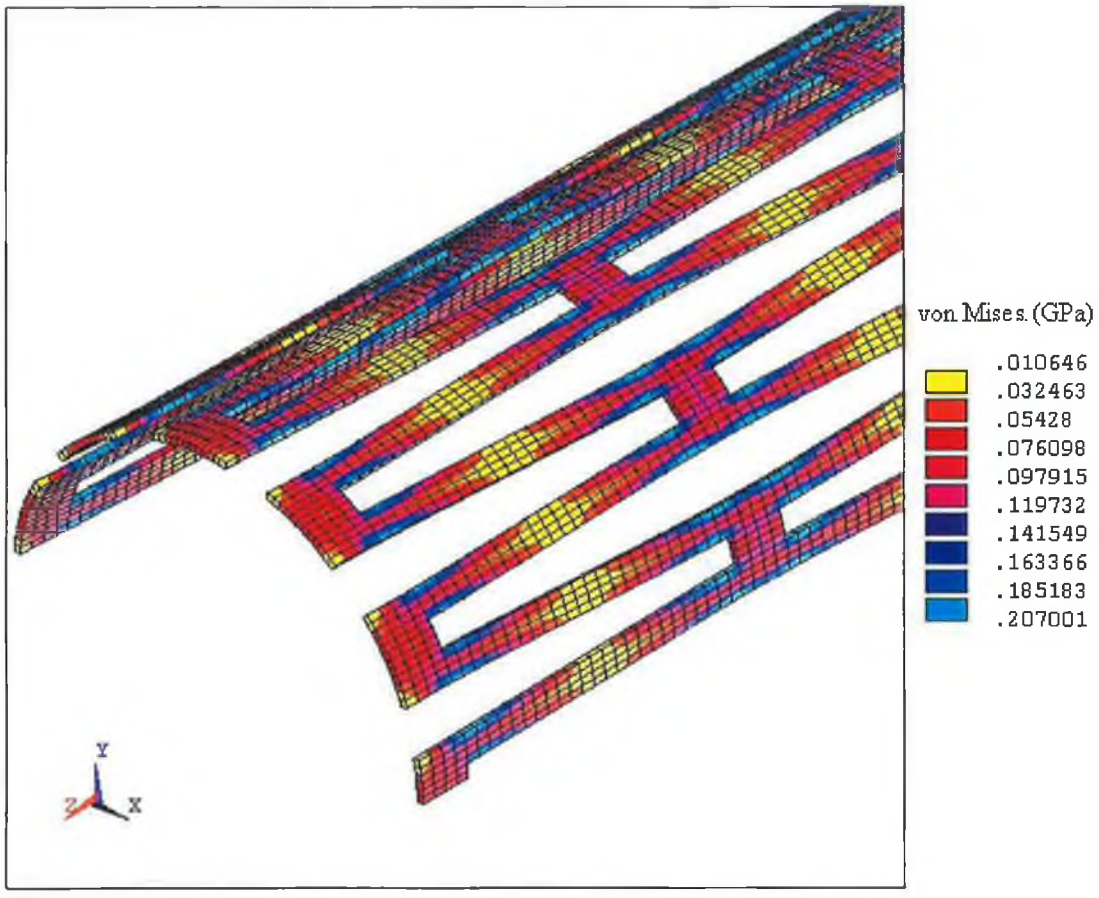

Figure 4.17: Distinct local plastic deformation by load case II

Figure 4.18 shows a close up of the deformed mesh in the centre part of the stent (as indicated in Figure 4.16) after enlargement. From this figure, it can be seen that the distribution of stresses are mostly concentrated on four corners of the cells rather than in the middle of the struts or the bridging strut itself. Unlike load case I, the

stress levels over the entire body of the stent struts were much lower in load case II. They were approximately within the range of 232 and 289 MPa.

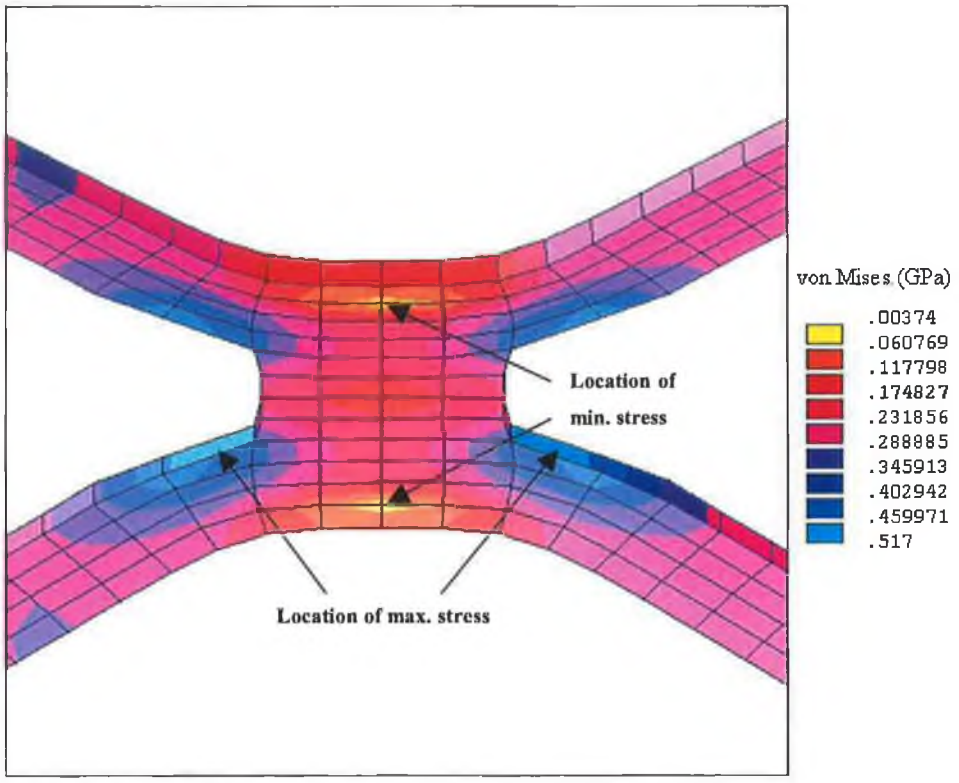

Figure 4.18: Close view of the central stent strut by load case II at final load

Figure 4.19 shows the stress level along the stent in z-direction at maximum expansion by load case II. The stress levels of the stent are getting higher as in the load case I when approaching to the centre of the stent. The highest peak point of the corner of the cell and the bridging strut is found to be at 331.4 MPa and 191.6 MPa respectively. The discrepancy of these two peak points is smaller comparing to load case I. The highest stress occurs in the body strut is found to be 287.5 MPa. The lowest stress point is located near the edge of the stent which is found to be 51.8 MPa. The stress level of the closest body strut to the edge of the stent in load case II is slightly different from load case I. The stress increases along the first half of the body strut in both load cases but they experience a different trend in the second half of the body strut. The stress occurs in the load case II tends to lower down in second half of the body strut whereas it remains constant in load case I.

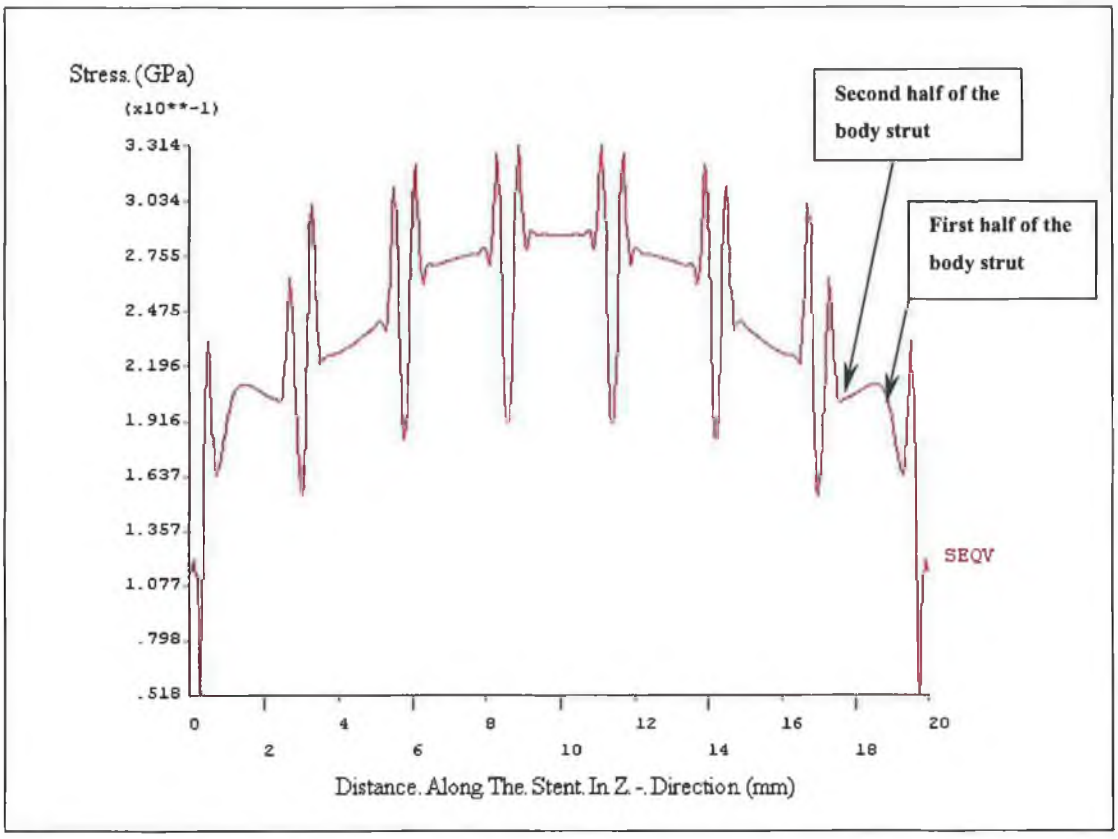

Figure 4.19: Stress level along the stent in z-direction at max expansion by load case II

Figure 4.20 shows the development of radial displacement and foreshortening of the stent with respect to the pressure applied. The maximum pressure achieved just before failure was 5.33 MPa and the simulation time at that point was 0.053 ms. The magnitude of displacement and foreshortening were found higher in load case II. The maximum radial displacement obtained in load case II was 6 mm whereas the maximum foreshortening obtained was found to be 3.45mm.

Like load case I, the foreshortening in load case II always occurs slower than radial displacement. However, the foreshortening tended to reduce its length at same rate as diameter expanded when the pressure was approaching the critical value. The discrepancy between the foreshortening and radial displacement at that stage was 2.55 mm.

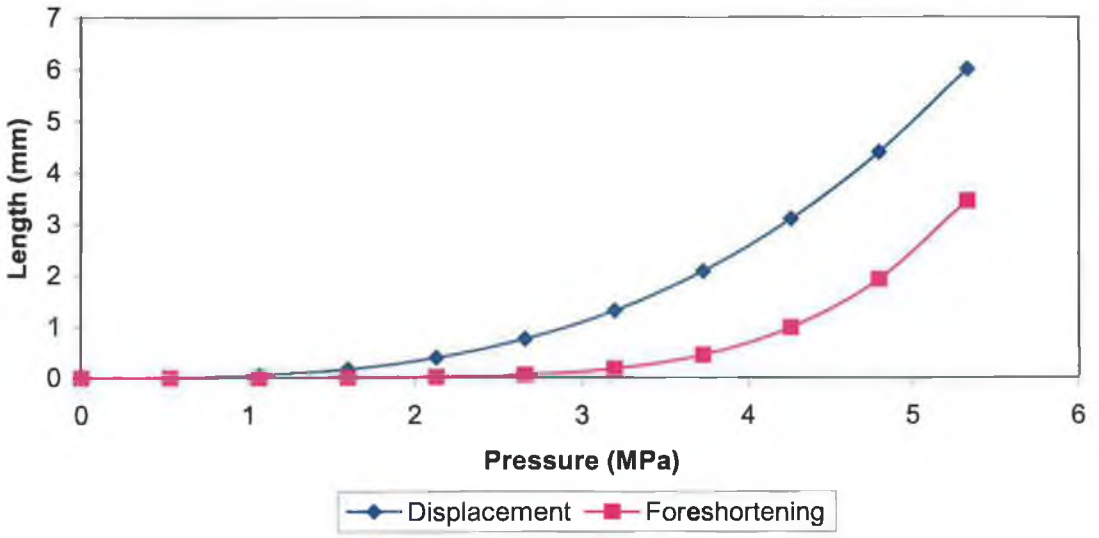

Figure 4.20: Development of radial displacement and foreshortening by load case II

4.1.3.3 Load Case III

For load case III the stent was subjected to a uniform internal pressure increasing at a constant rate of 40 MPa that is ten times slower than the pressure speed utilised in load case I. The development of the expansion process is detailed in Figure 4.21 to Figure 4.24, which show the distribution of stress at various times during the simulation.

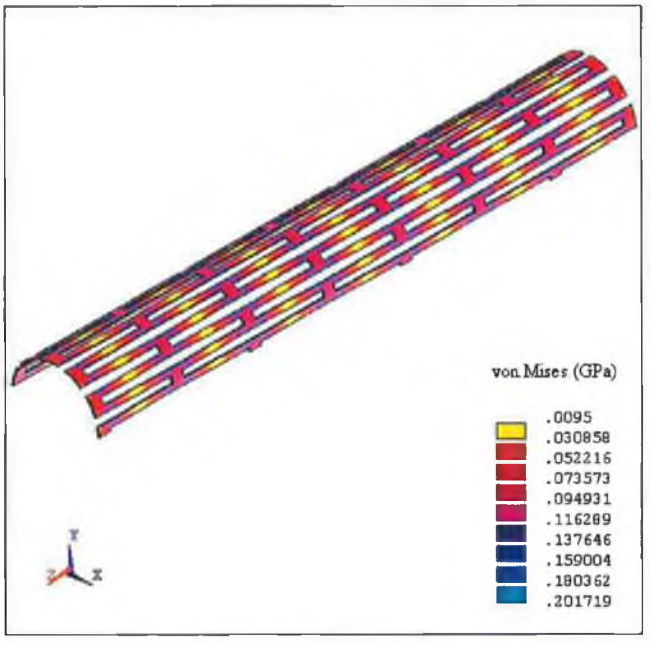

Figure 4.21: Distribution of stress at 25% of final load by load case III

The distributions of stress in the stent before 50% of the final load in load case III resemble the first two load cases. The distribution of stress begins to change at 75% of the final load. The stress in the body struts are lower especially in the middle of the stent compared to the load case I and II. Most of them are within the region of 150 to 184 MPa.

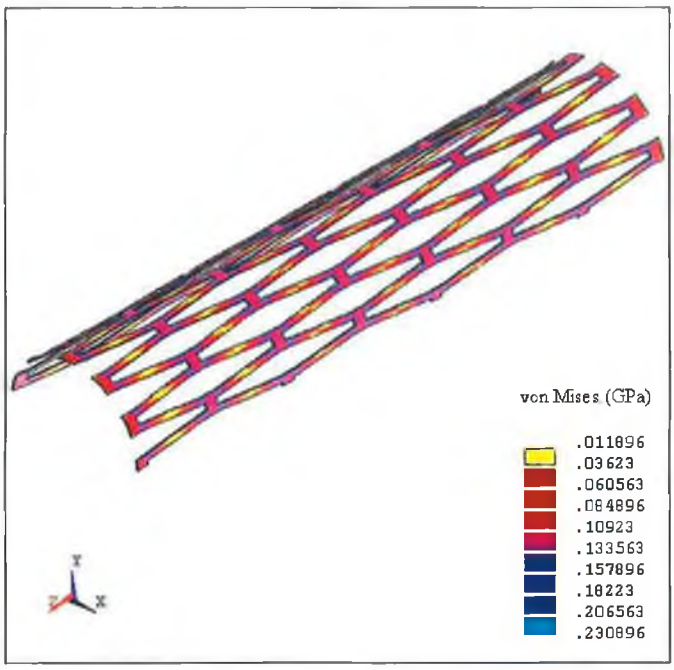

Figure 4.22: Distribution of stress at 50% of final load by load case III

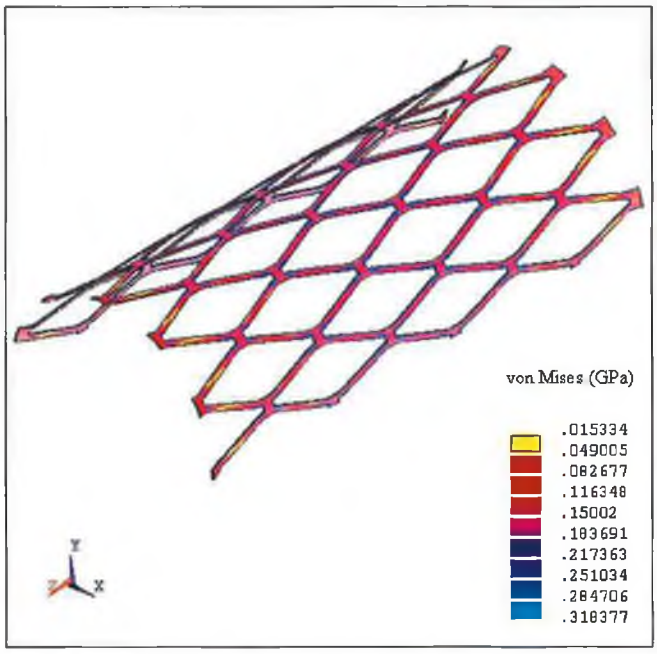

Figure 4.23: Distribution of stress at 75% of final load by load case III

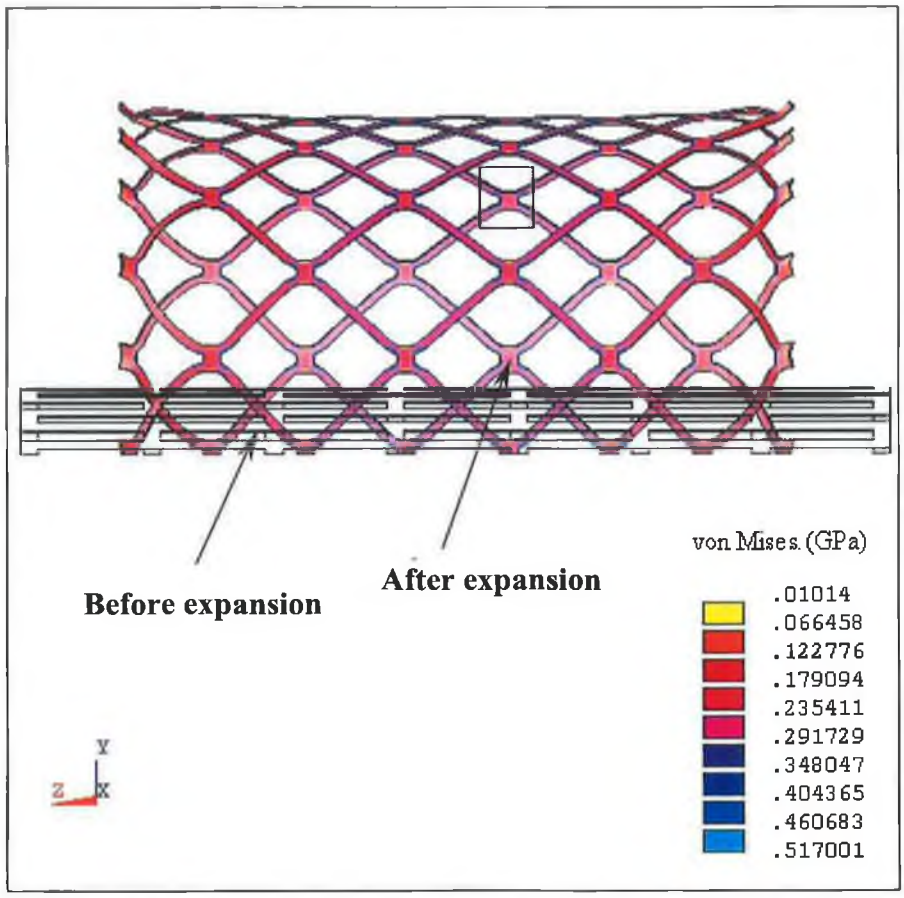

Figure 4.24: Distribution of stress at final load by load case III

Figure 4.25 shows the distinct local plastic deformation at yield point by load case III. Once again this figure shows no differences on the allocation of stress from the first two load cases. The region of lower and higher stresses remain at the same location as in load case I and II. The pressure load at this point is found to be 1.02 MPa. Figure 4.26 shows the close up of the deformed mesh in the centre part of the stent as indicated in Figure 4.24 after enlargement. It can be seen from this figure that the distribution of stresses over the entire body of the stent was resembled to the stent under load case II. However, the compilation of stresses at the four corners of the cells were more prominent in this load case. The regions of higher stresses were smaller and stress levels on the stent struts were lower as well compared to load case II. At maximum expansion the stress levels under load case III was approximately within the range of 235 to 292 MPa.

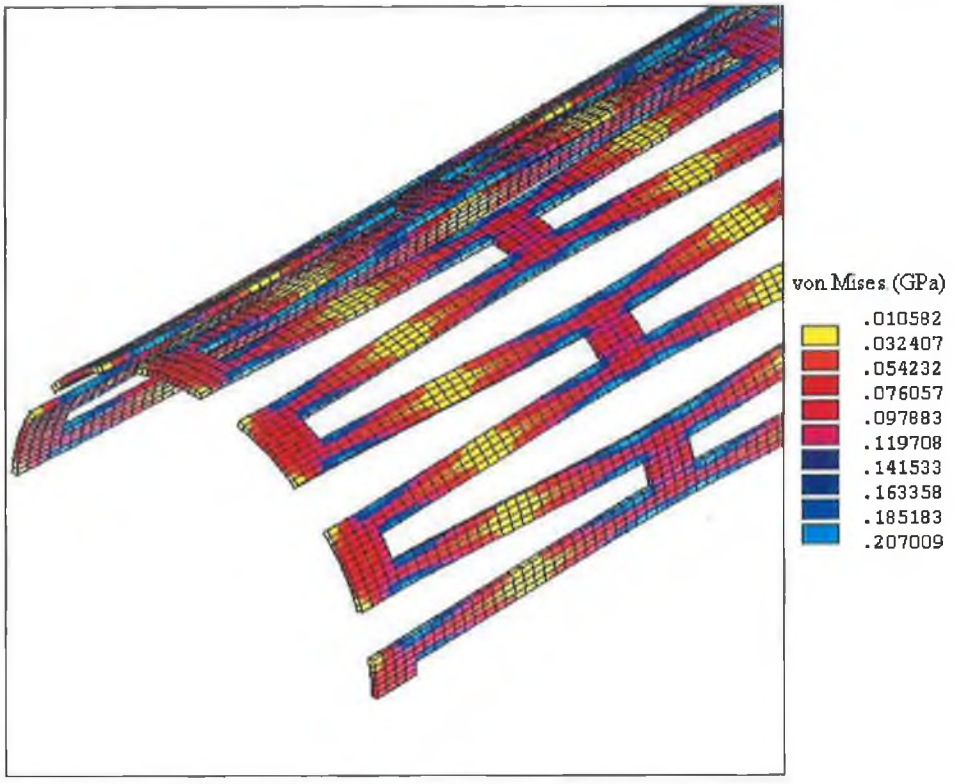

Figure 4.25: Distinct local plastic deformation by load case III

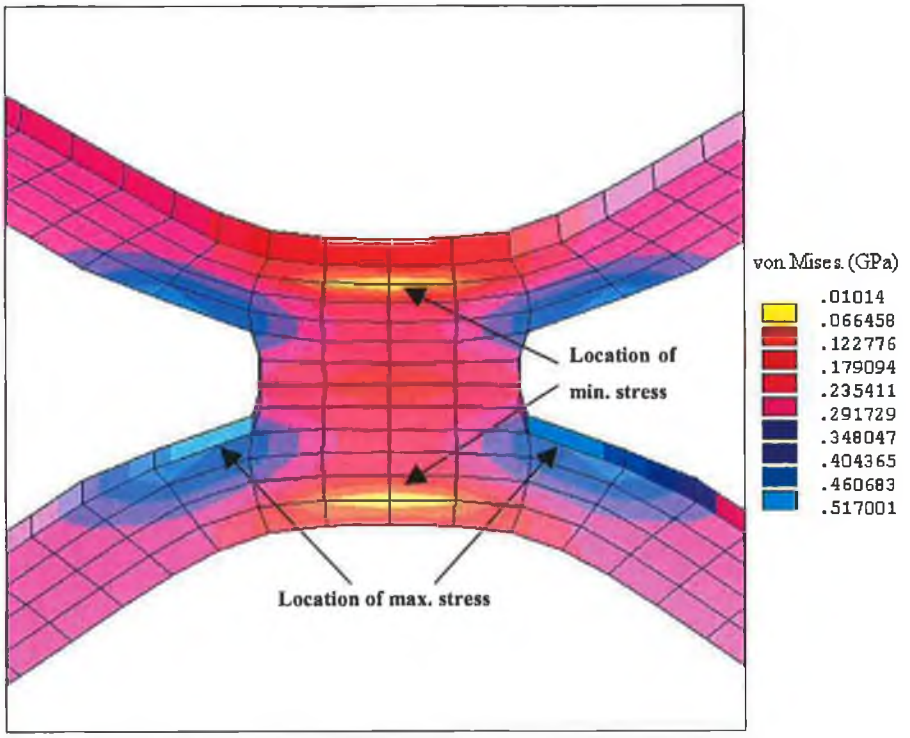

Figure 4.26: Close view of the central stent strut by load case III at final load

Figure 4.27 shows the stress level along the stent in z-direction at maximum expansion by load case III. It is found that the path of the stress along the stent in this load case is similar to the path of stress engendered in load case II. However, the stress occurs at the corner of the cell, body strut and bridging strut here is lower than load case II. The maximum stress obtained at the corner of the cell and bridging strut is found to be 319 MPa and 178.5 MPa respectively. The body strut, which is represented by the intermediate lines that are located between maximum and minimum peak points is found to be 265.1 MPa. The lowest stress point where is located in the vicinity of the end body strut is measured as 49.5 MPa.

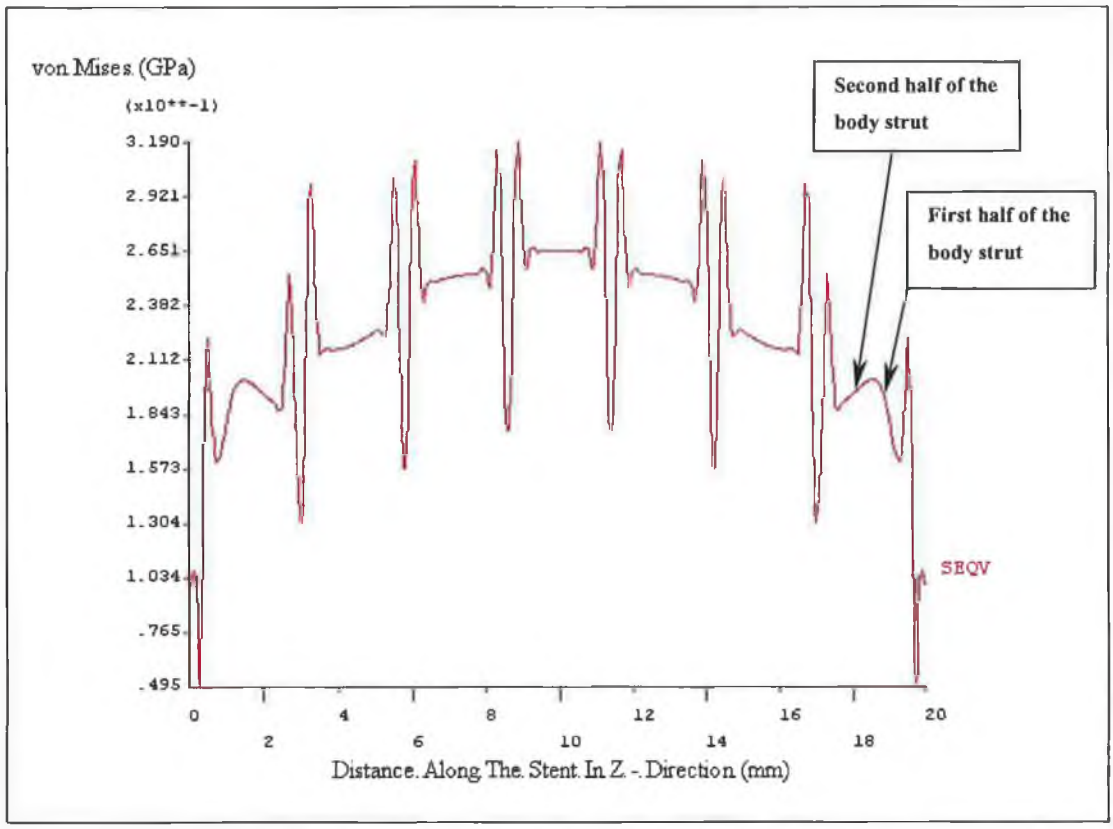

Figure 4.27: Stress level along the stent in z-direction at max expansion by load case III

Figure 4.28 shows the maximum radial expansion and foreshortening achieved under load case III. The maximum pressure achieved just before failure was 2.97 MPa and the simulation time at that point was 0.074 ms. The maximum radial displacement and foreshortening achieved were found to be 6.3 mm and 4.63 mm respectively. Although the amount of foreshortening was smaller than diameter expanded the

foreshortening reduced its length at a quicker rate when the pressure of 2.68 MPa was reached. The discrepancy between the foreshortening and radial displacement at full load was 1.67 mm.

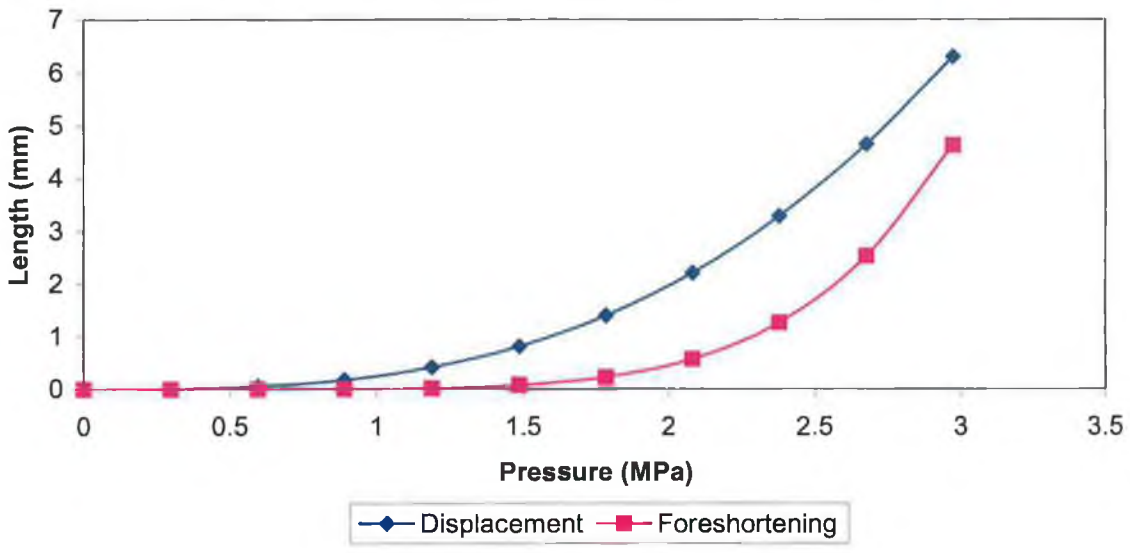

Figure 4.28: Development of radial displacement and foreshortening by load case III

4.1.3.4 Load Case IV

The fourth simulation was run with the internal pressure increasing at a constant rate of 15 MPa/Msec. Obviously, the pressure speed utilised in this simulation was much slower than the previous simulations.

Figure 4.29 to Figure 4.32 shows the development of the expansion process with the distribution of stress at various times during the simulation. As can be seen from the figures that the location of maximum stress does not change as the expansion of stent continues. In spite of a slight difference in the magnitude of displacement, the distributions of stress over the entire body of the stent at 25% of final load in load case IV are resembled to previous three load cases. As the pressure increases to 50% of final load, the region of the lowest stress becomes more prominent and more concentrated. In this load case, the magnitude of stress in most of the body struts is lower than 150 MPa at 75% of final load and 250 MPa at final load.

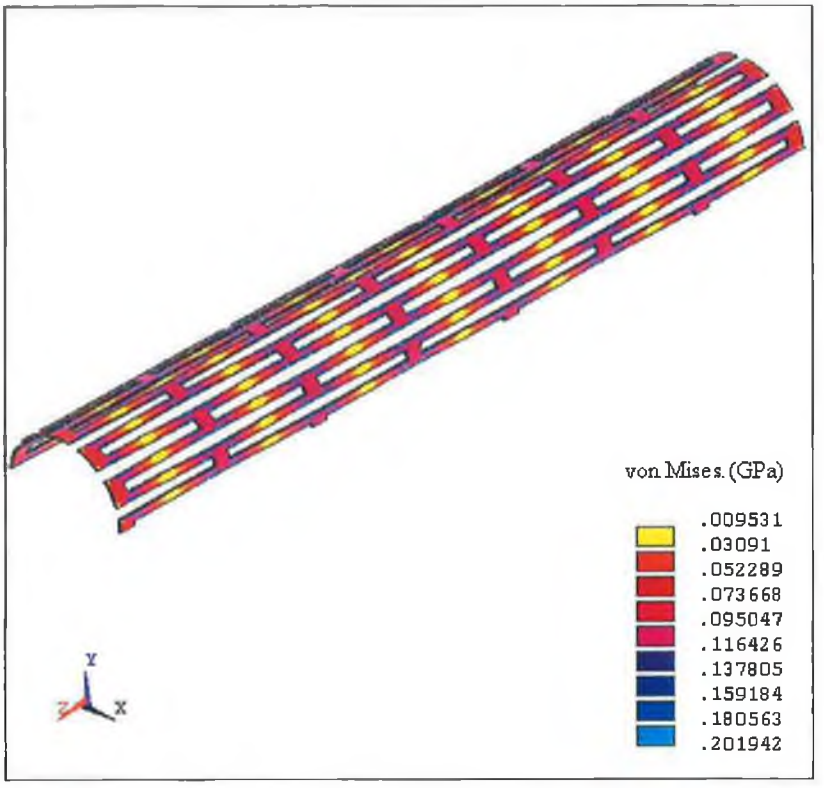

Figure 4.29: Distribution of stress at 25% of final load by load case IV

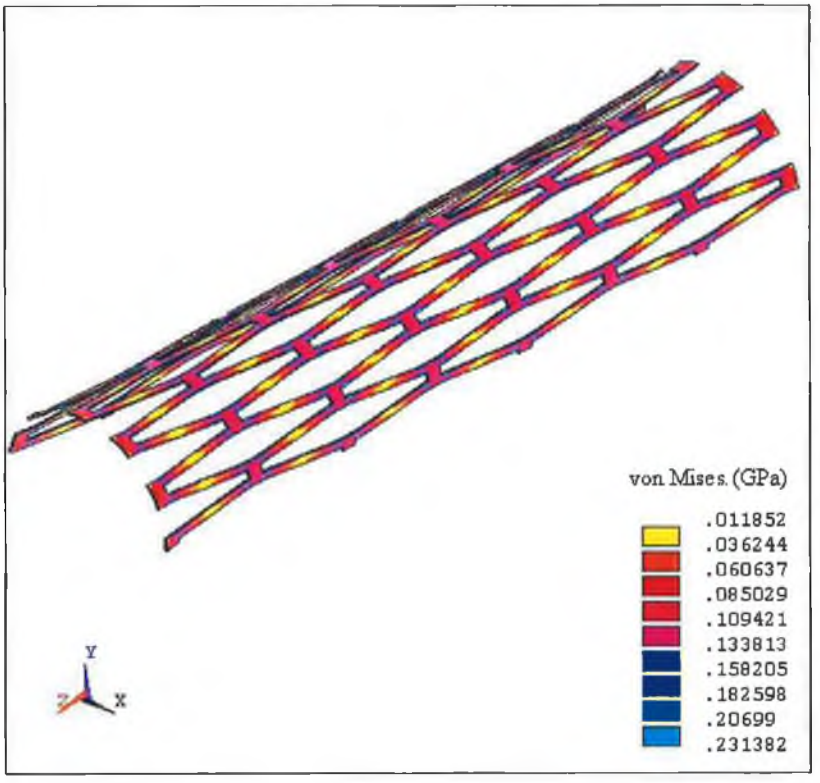

Figure 4.30: Distribution of stress at 50% of final load by load case IV

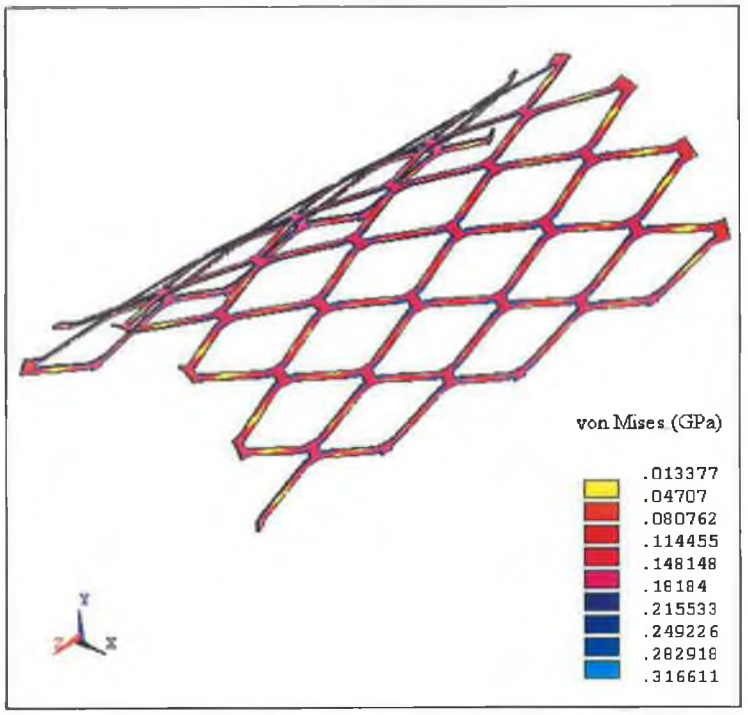

Figure 4.31: Distribution of stress at 75% of final load by load case IV

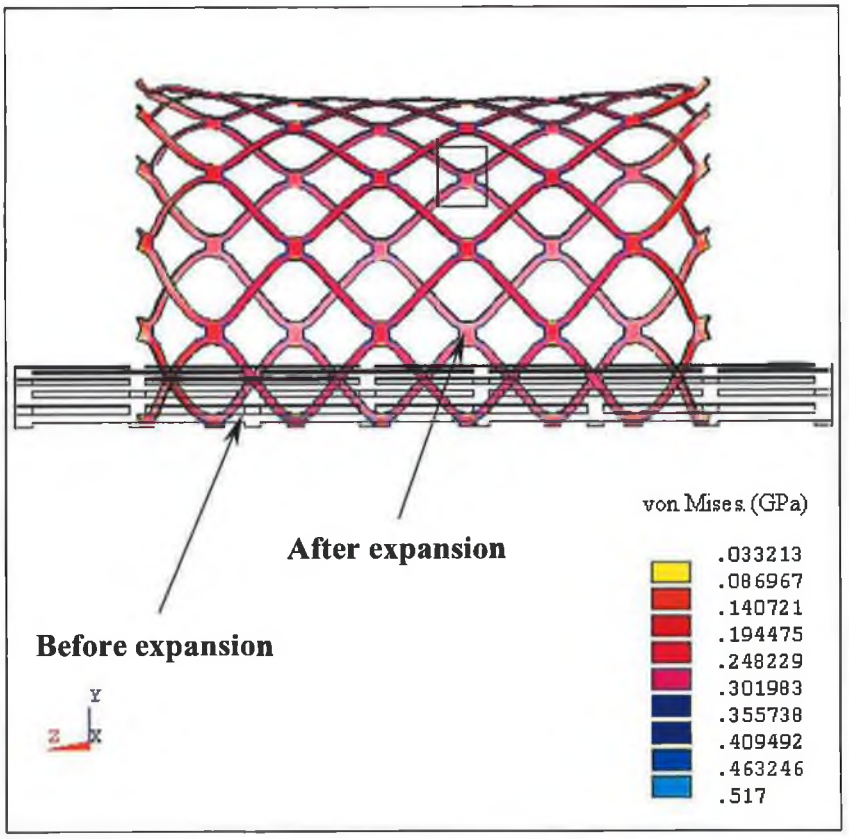

Figure 4.32: Distribution of stress at final load by load case IV

The stress levels shown at the body of the struts in Figure 4.32 were much lower compared to the previous three simulations. They were within the range of 194 MPa to 248 MPa. However, the stress level in the bridging struts itself was found to increase significantly as can be seen in Figure 4.33. The regions of lower stress in bridging struts have become wider and higher. But, the stent under this load case has one similarity with load case I, II and III that is the higher stresses accumulated at the four corners of cells and became more concentrated.

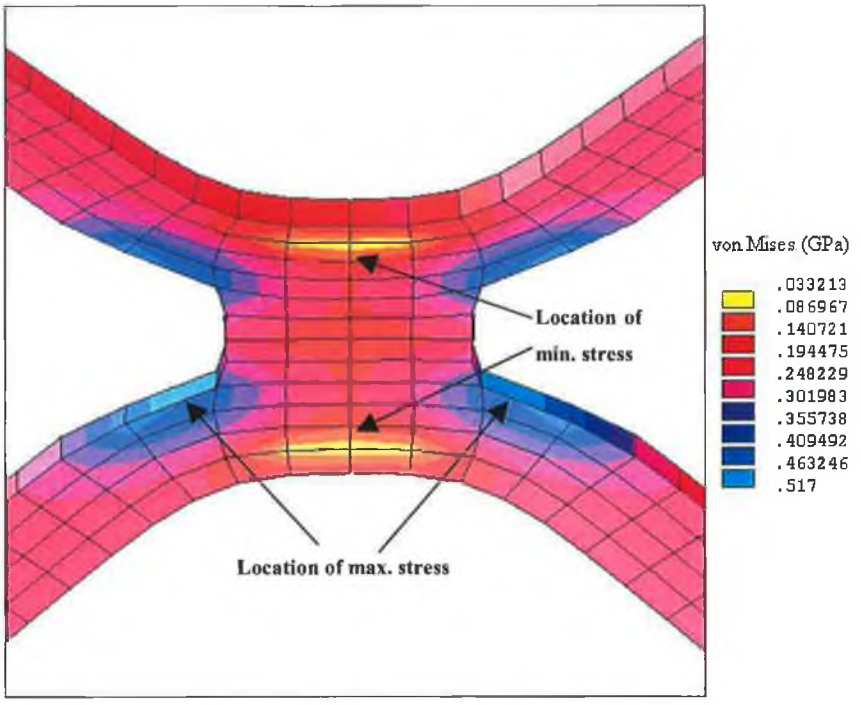

Figure 4.33: Close view of the central stent strut at final load by load case IV

The stress level along the stent in load case IV at maximum expansion is shown in Figure 4.34. As can be seen from the figure that all the intermediate lines are flatter than the previous three load cases. This indicates that the differences in stress along each body strut are getting smaller. Besides that the discrepancy of stress at the body strut in the vicinity of stent edge and centre of stent are lower. The highest peak point of the corner of the cell and the bridging strut is found to be 302.9 MPa and 143 MPa respectively. The highest stress that occurs in the body strut is found to be 241.1 MPa. As previous three load cases, the lowest stressed point is located in the middle of the bridging strut at the end of the stent. The magnitude of the lowest stress point is measured as 48.5 MPa.

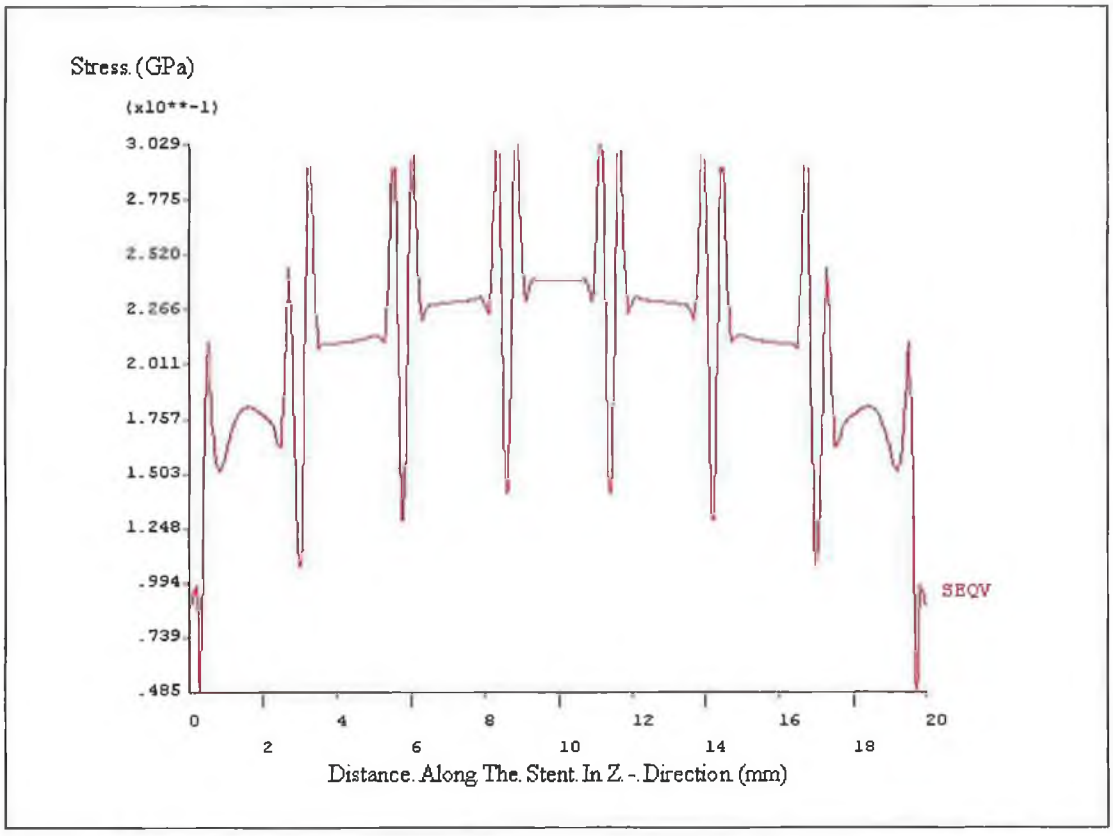

Figure 4.34: Stress level along the stent in z-direction at max expansion by load case IV

Figure 4.35 shows the development of radial displacement and foreshortening of stent with respect to the pressure applied. The maximum pressure achieved was 1.61 MPa and the simulation time at that point was 0.107 ms. The maximum radial displacement and foreshortening obtained were found to be 6.66 mm and 6.12 mm respectively.

It was noticed that the stent reduced its length at a quicker rate much earlier than the stent in previous load cases throughout the expansion process. The amount of length reduced was found to be higher than the amount of diameter expanded when the pressure of 1.45 MPa was reached. At the maximum pressure, the total magnitude of the foreshortening and the radial displacement were nearly equal. The discrepancy between the diameter expanded and the foreshortening at maximum pressure was 0.54 mm.

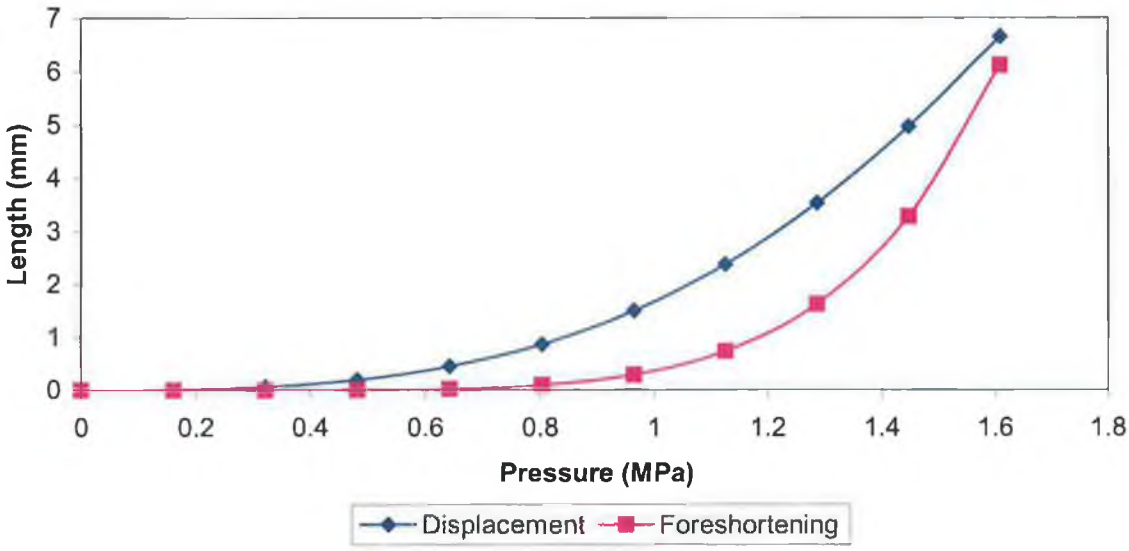

Figure 4.35: Development of radial displacement and foreshortening by load case IV

4.1.3.5 Load Case V

This simulation was run with the lowest pressure and utilised by the slowest load speed. The pressure speed used in this load case was 1 MPa/Msec. Although this simulation could have used pressure speeds lower than 1 MPa/Msec, it would seem like a good idea to know the ultimate shape the stent takes up at this stage. Since the outcome of this simulation was not impressive and the shape of the stent became concave, simulations slower than this pressure speed are not necessary.

The development of the stent expansion process is detailed in Figure 4.36 to Figure 4.39, which show the distribution of stress at various times during the simulation. At the outset of the stent expansion the allocation of stress show commensurate with the previous four load cases regardless of what pressure speed was being applied. As the pressure increases to 50% of the final load, the location of lowest stress where resided in the middle of the body struts becomes more concentrated compared to the load case I, II, III and IV. A slight bending has taken place at both ends of the stent. The middle of the stent has bulged a little bit more than the neighbouring struts as well. As the pressure increases the bending becomes more obvious while the body struts have developed into a concave shape. The lowest stress region at this stage is still clearly seen as in Figure 4.38. By the time the final load is reached the stent has shorten into 1/3 of its original length.

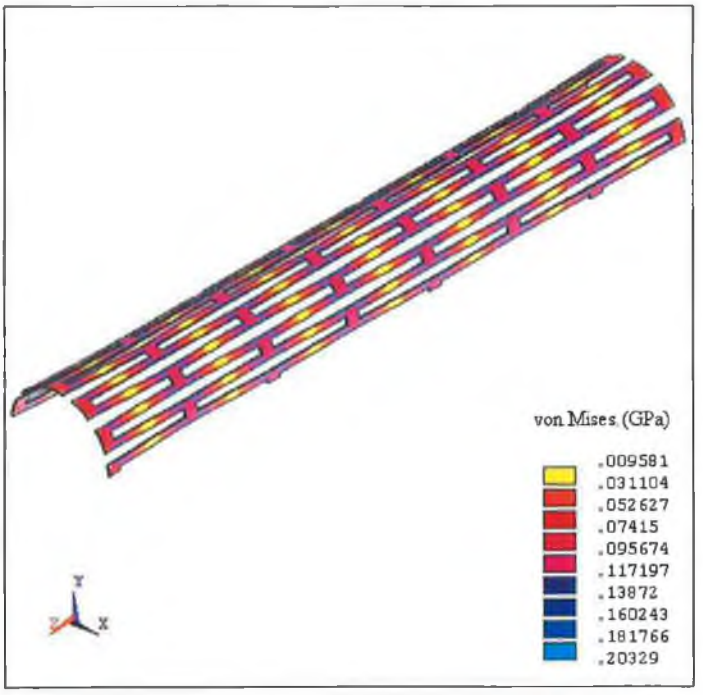

Figure 4.36: Distribution of stress at 25% of final load by load case V

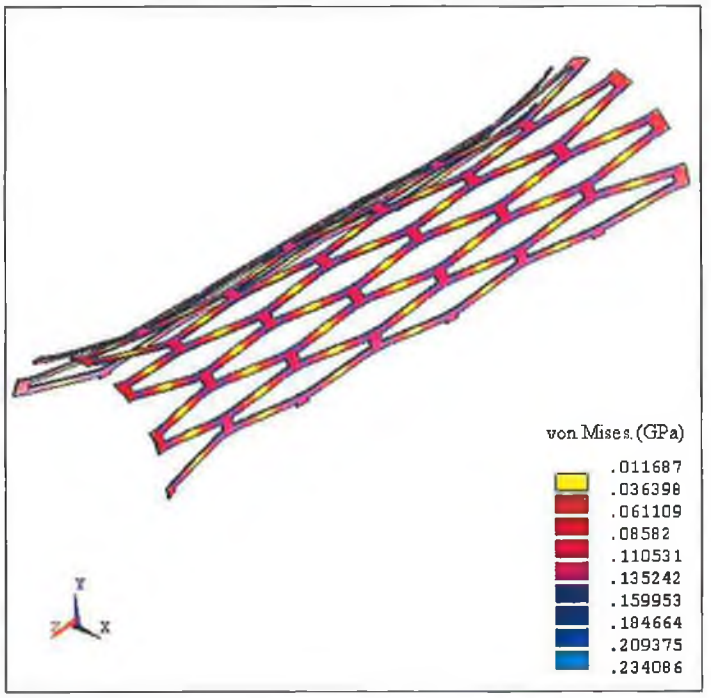

Figure 4.37: Distribution of stress at 50% of final load by load case V

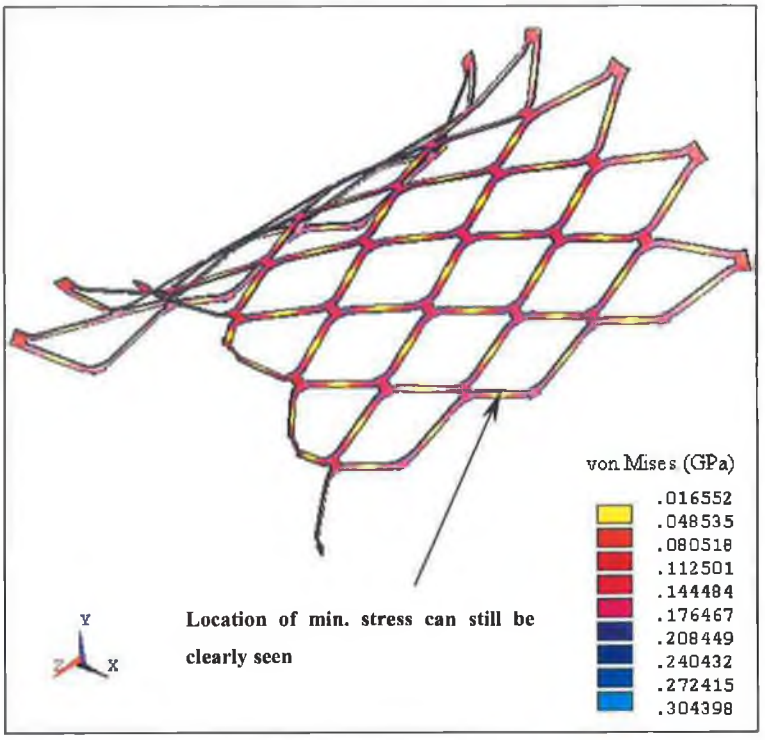

Figure 4.38: Distribution of stress at 75% of final load by load case V

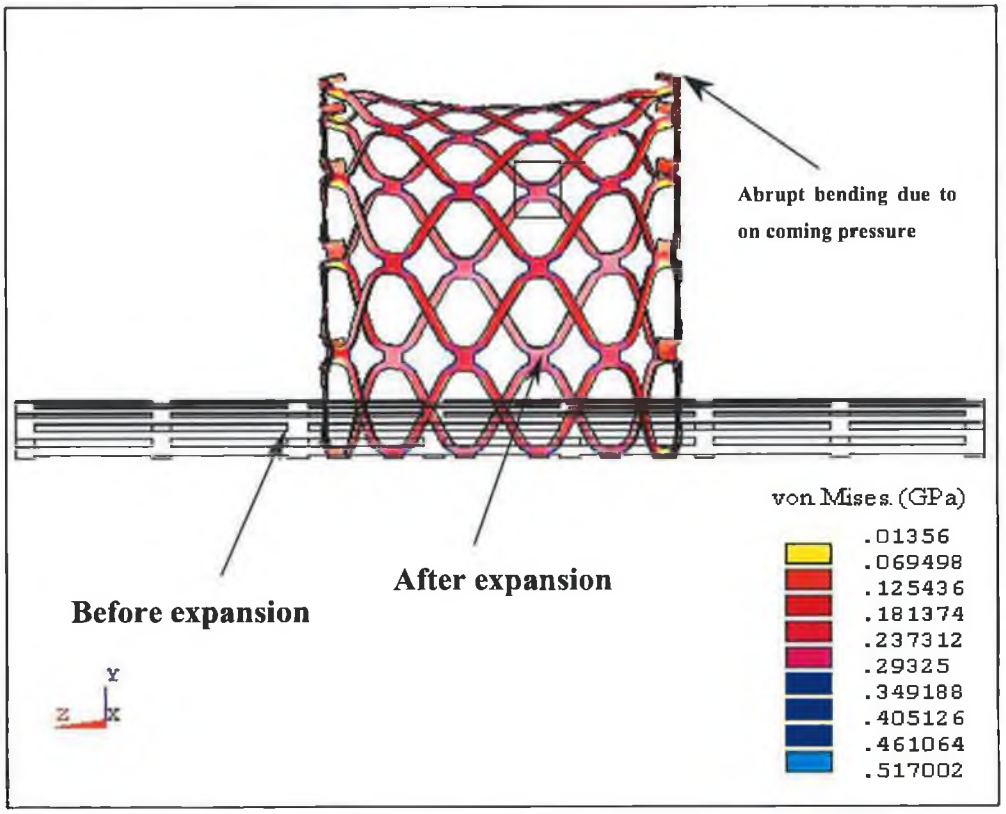

Figure 4.39: Distribution of stress at final load by load case V

Figure 4.40 shows the elastic plastic region of the stent at material yield point by load case V. As can be seen from the figure that the location of the maximum and minimum stress at the yield point does not change as in the previous four load cases. The stress level at different elastic regions is similar to the previous load cases as well. However, the slight bending at the end of the stent is clearly seen from this figure.

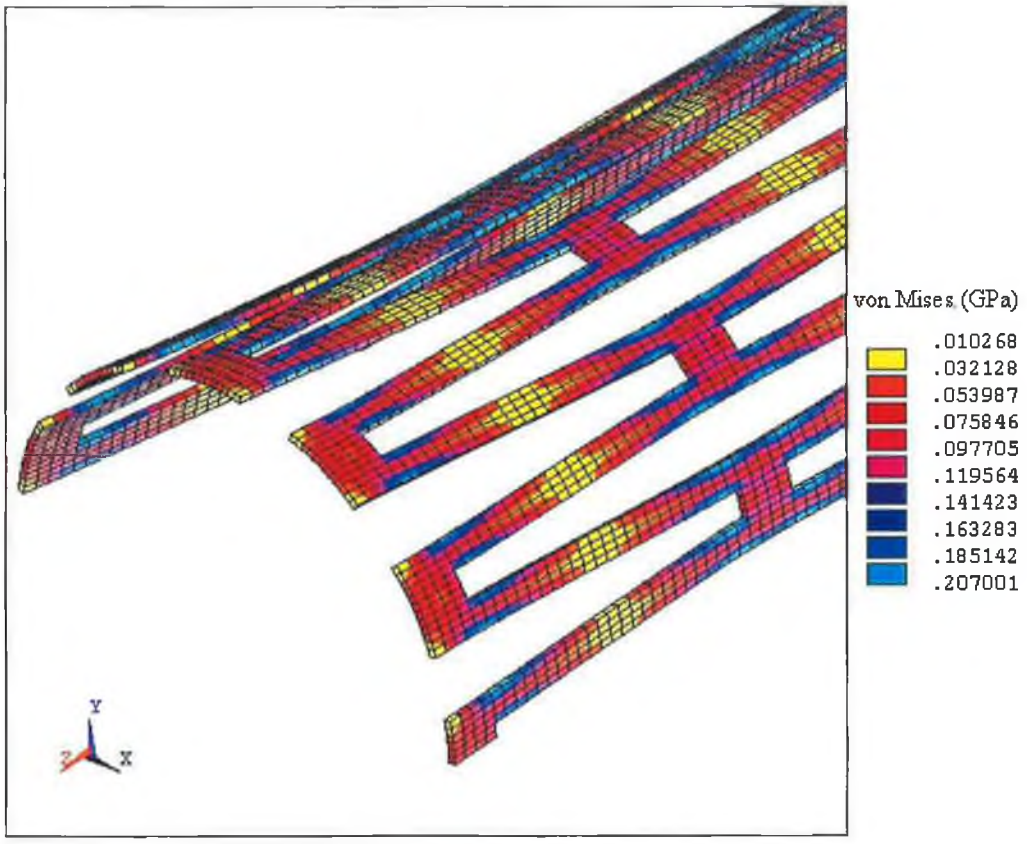

Figure 4.40: Distinct local plastic deformation by load case V

Figure 4.41 shows a close up of the deformed mesh in the centre part of the stent as indicated in Figure 4.39 after enlargement. It was noticed that the regions of lower stress have switched from the bridging struts to the outer corners of the bridging struts itself. Nevertheless, regions of higher stress are still accommodated in the same place as the previous four load cases (i.e. at the four corners of the cells). The average stress levels experienced by the stent struts were approximately within the range of 125 MPa to 237 MPa.

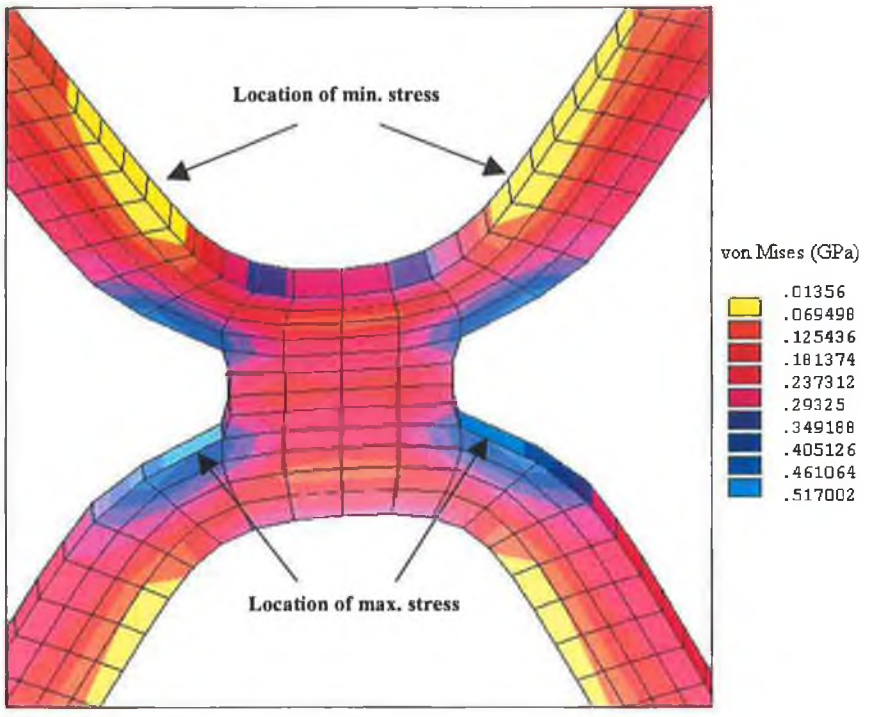

Figure 4.41: Close view of the central stent strut at final load by load case V

Figure 4.42 shows the stress level along the stent in z-direction at maximum expansion by load case V. The stress level in this load case is very different to those obtained in previous simulations. There is an abrupt dropping of stress between the corner of the cell near the edge of the stent and the centre of the stent. The body struts near the centre of the stent lay in the same line of stress level but they are no longer in the same level within itself. This is typically unlike the previous four load cases, which the stress level in the specific body strut is very much in the same magnitude. This could be the cause of the localised deformation of stent struts into a concave shape in this load case. The highest stress that occurred in the body strut is measured as 141.2 MPa.

As can also be seen from this figure that, the lowest stress point is not located at the edge of the stent anymore, but at the second bridging strut from the ends of the stent. At this point, the stress is measured as 31.1 MPa. The highest peak point of the corner of the cell and the bridging strut is found to be at 283.9 MPa and 67.2 MPa respectively. One point should be noted is that the discrepancy of stress between the corner of the cell and the bridging strut has become significantly large.

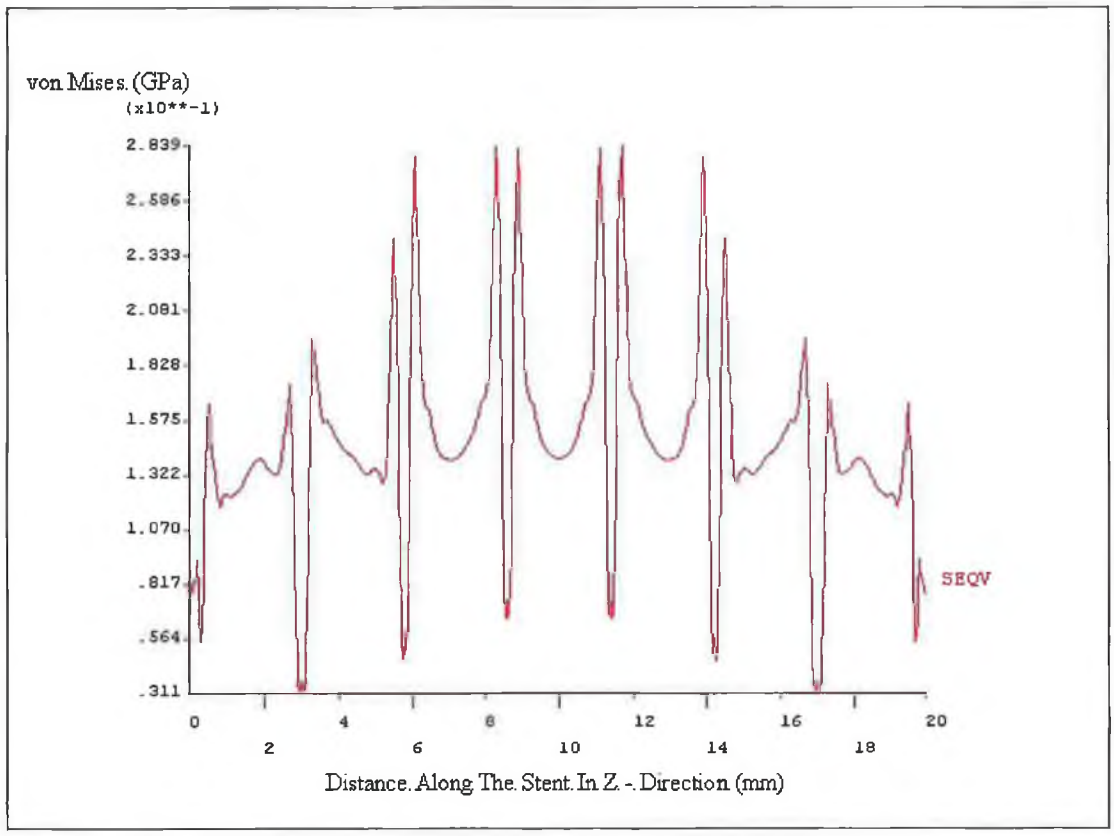

Figure 4.42: Stress level along the stent in z-direction at max expansion by load case V

The development of radial displacement and foreshortening of stent during the expansion is shown in Figure 4.43. The maximum pressure achieved just before failure was 0.327 MPa whereas the simulation time at that point was 0.327 ms. In this case, the maximum radial displacement and foreshortening achieved were found to be 7.56 mm and 13.57 mm respectively. It can be seen in Figure 4.43 that the amount of foreshortening tended to pick up rapidly when the pressure was reaching 0.229 MPa. Unlike the previous four load cases, the foreshortening in this simulation has completely overtaken the radial displacement and become dominant when the pressure of 0.262 MPa was reached. The discrepancy between the foreshortening and maximum radial displacement at maximum pressure was equal to 6.01 mm. In other words, the total length of the stent contracted was more than the diameter expanded by 6.01 mm when the maximum pressure was reached.

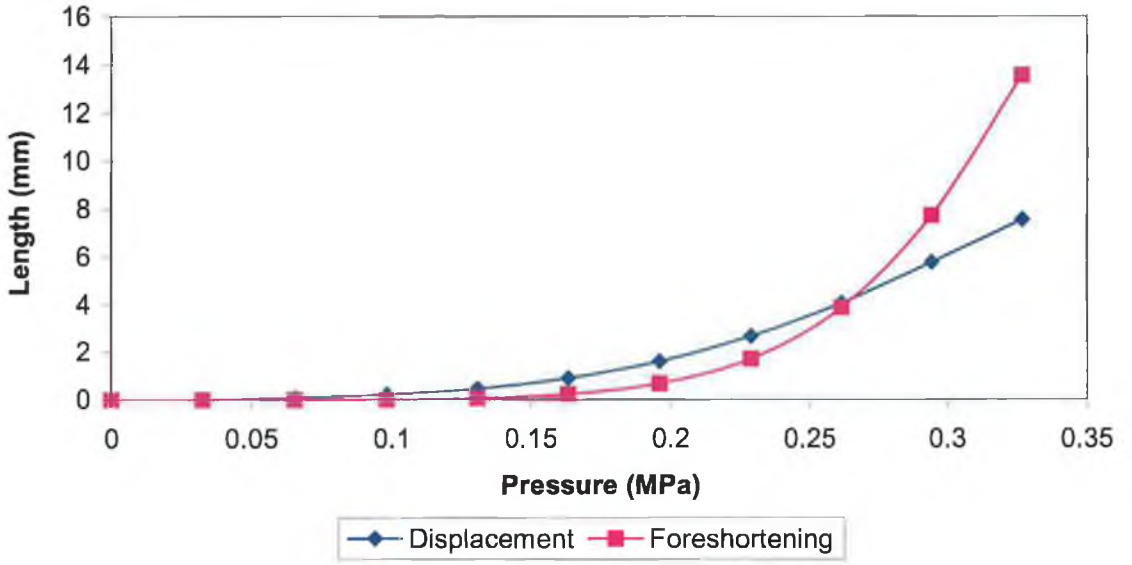

Figure 4.43: Development of radial displacement and foreshortening by load case V

4.1.4 Comparison of Results

In order to compare the results between the five load cases, the potential diameter of the distending stent was calculated from the deformed shape at each equal increment of pressure points.

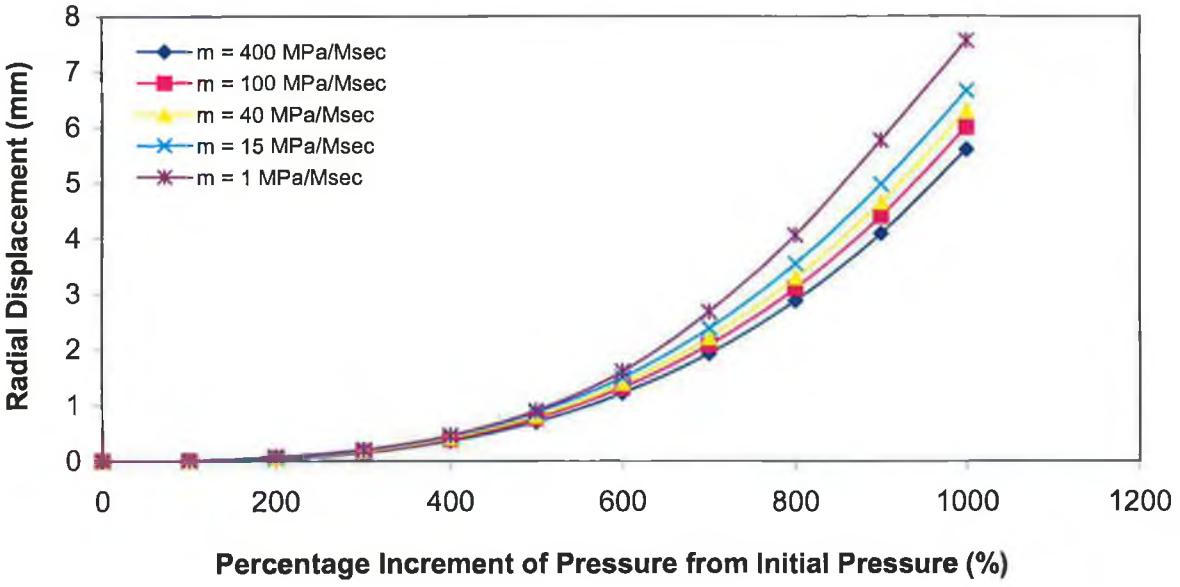

Figure 4.44: Displacement vs. percentage increment of pressure at equal intervals

It is clearly shown that the stent will experience the greatest expansion under load case V. On the contrary, the stent under load case I will experience the smallest expansion. The graph also shows that if higher-pressure speeds are applied smaller radial displacement can be achieved.

The amount of foreshortening at each equal increment of pressure points for five different load cases is shown in Figure 4.45. It can be seen that the development of foreshortening follows exactly the same sequence as in radial displacement that is when the pressure speed increases the total length of foreshortening decreases. However, it was noticed that the proportion of foreshortening to pressure speed applied is higher in load case V. The reduction in length of the stent has developed rapidly when the percentage increment of pressure from its initial pressure reached approximately 600% for load case V. It was assumed that there are four different ranges of pressure speeds between 1 MPa/Msec and 400 MPa/Msec, so, any pressure speed between 1 MPa/Msec and 15 MPa/Msec has a major effect on the foreshortening of stent. This indicates that a small increment of pressure speed will result in a large contraction of stent within that range. It was also evident that the pressure speeds ranging from15 MPa/Msec to 400 MPa/Msec have only a minor effect in terms of percentage increment in foreshortening.

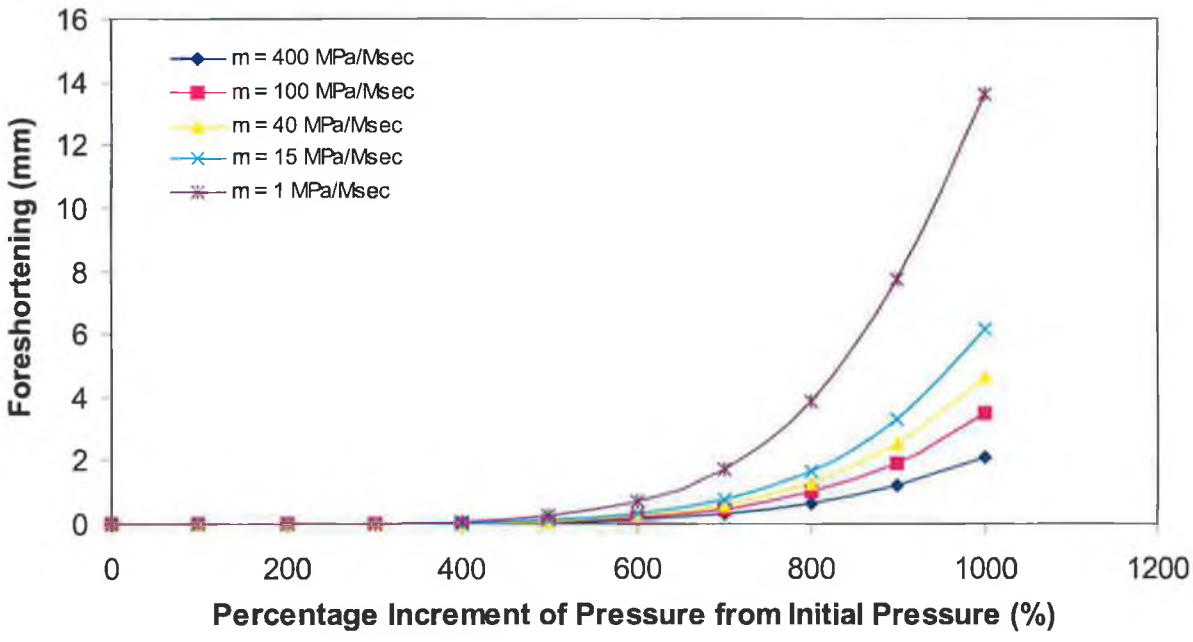

Figure 4.45: Foreshortening vs. percentage increment of pressure at equal intervals

Figure 4.46 shows the development of von Mises stress throughout the expansion process. It is clearly shown that the stresses in the stent developed at the faster rate within the first millimetre of radial expansion regardless of what pressure speeds were applied. However, the stresses in load case I seemed to develop quicker at every subsequent one millimetre of increment in radial displacement after the first millimetre of expansion. This graph again shows that the von Mises stress developed slower as the pressure speeds increased. It was again noticed that the stress levels of stent in the range of 1 MPa/Msec to 15 MPa/Msec tended to drop faster as the pressure speeds decreased. As a result the stent under load case V reached the failure point at a higher level of radial expansion than the other four load cases.

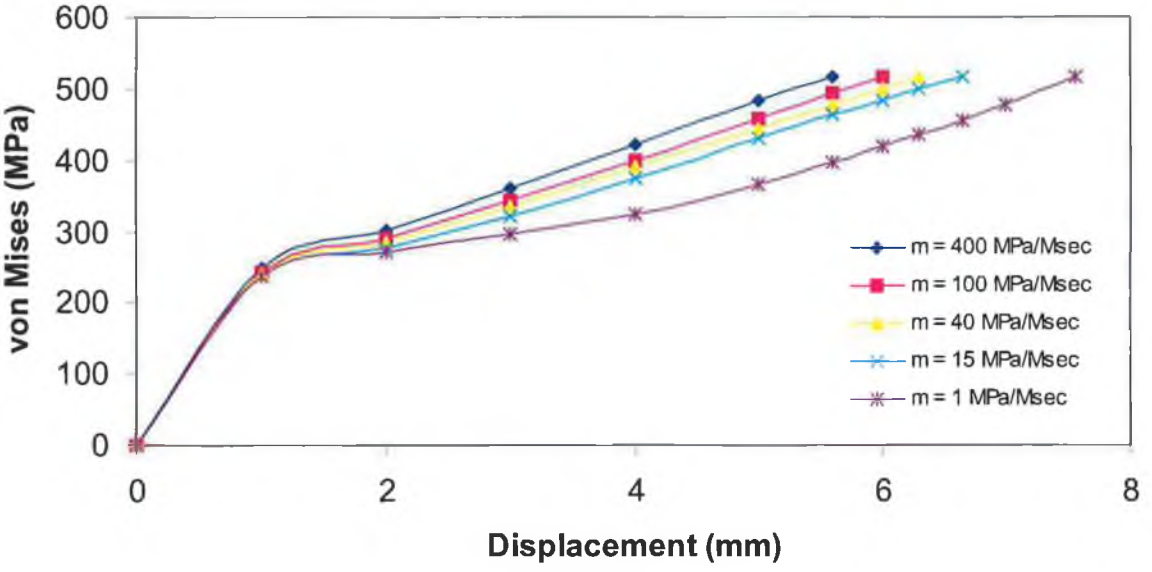

Figure 4.46: Development of stress in stent under five different load cases

Figure 4.47 shows the total length of foreshortening for every 1-millimetre increment of radial displacement. It is evident that the application of high speed pressure has a direct effect on the foreshortening of stent during the expansion. Therefore, slower speeds of pressure application imply greater foreshortening of stent. Load case I and II have the tendency of having a faster expansion in the radial direction compared to foreshortening in axial direction throughout the expansion process. However, for load case III and IV the stent reduced its length at a quicker rate after the fourth millimetre of radial displacement. The rate of foreshortening under load case V was

absolutely ample. It was found that the foreshortening has replaced the radial displacement in stent expansion after the second millimetre of radial displacement. Therefore, the stent was found shorter in axial direction compared to the diameter expanded in radial direction at the end of simulation under load case V.

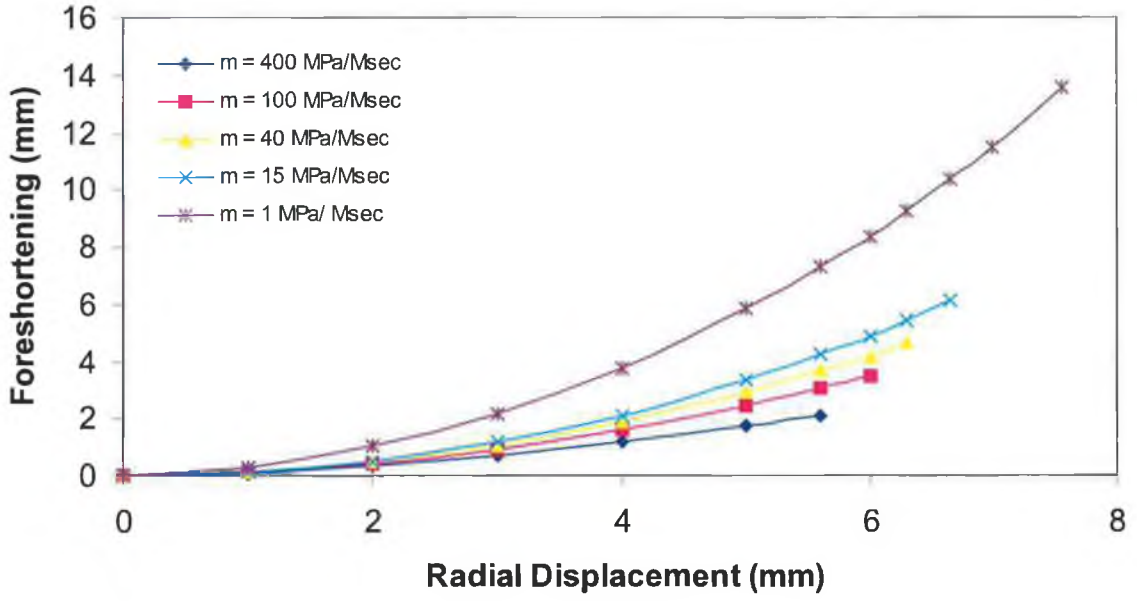

Figure 4.47: Comparison between the length of foreshortening and radial displacement

From the analyses a relationship between the maximum stent expansion diameter and pressure speed can be established, as shown in Figure 4.48. This figure indicates that the pressure speeds will have the major effect on the stent expansion in radial direction when the pressure speed is lower than 15 MPa/Msec. Although there was a dramatic drop of pressure speed from 400 MPa/Msec to 100 MPa/Msec, there was no indication that the stent will have a massive increment in stent diameter. Figure 4.49 shows the relationship between the foreshortening of stent and pressure speeds. From this graph, it is evident that the stent will experience greater foreshortening when the pressure speed is decreased. However, as in radial expansion, the pressure speeds will have a major effect on foreshortening when pressure speeds lower than 15 MPa/Msec are applied. Besides that, the magnitude of reduction in length of stent compared to radial expansion at pressure speed lower than 15 MPa/Msec was found extremely large. For example, the difference between the pressure speeds of 1

MPa/Msec and 15 MPa/Msec for the foreshortening and the diameter expanded were found to be 7.45 mm and 0.9 mm respectively. This implies that pressure speed has the major influence on the foreshortening rather than radial expansion of stent.

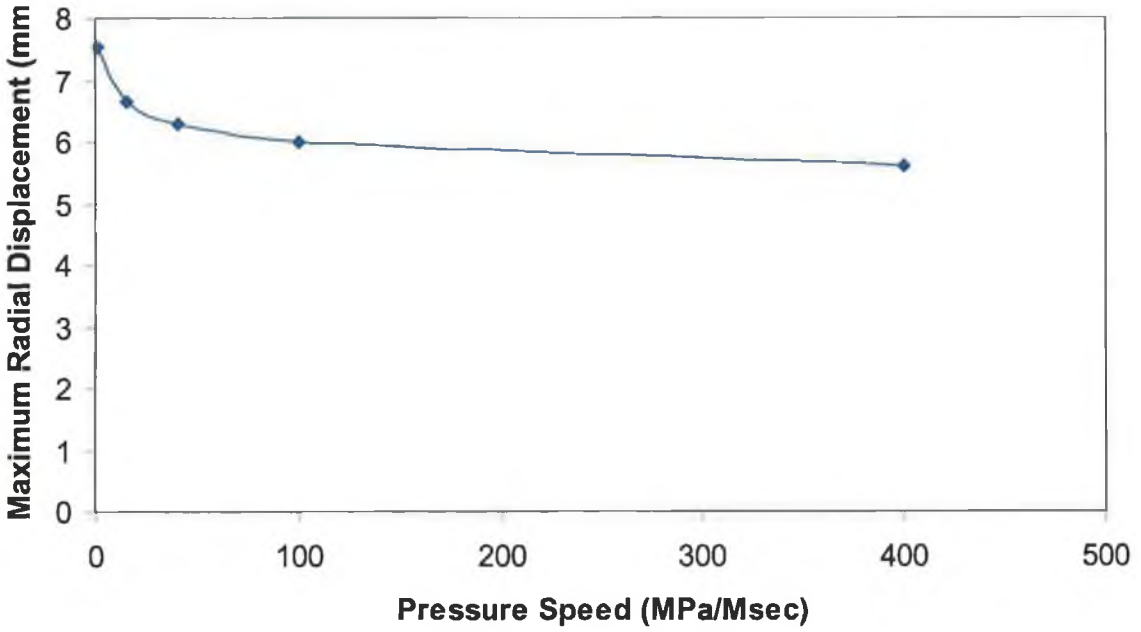

Figure 4.48: Plot of max radial displacement achieved with respect to pressure speed

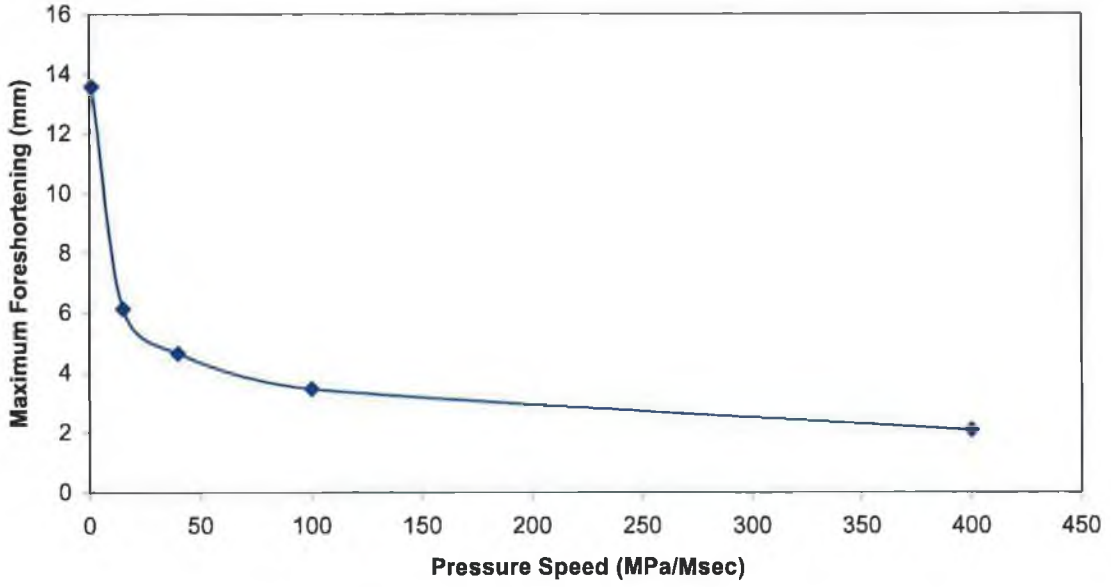

Figure 4.49: Plot of maximum foreshortening achieved with respect to pressure speed

4.1.5 Study Limitations

This study presents a finite element analysis of predicting the stent diameter and foreshortening under different speed of pressure application during the entire expansion process. The study is mainly concentrated on the expansion and foreshortening of the stent. The feasibility of stent will not be an issue here as in an ideal stent, the foreshortening should not be shorter than 1.5 mm [69]. In the actual situation, a balloon is used as the medium to distend the stent and the detail simulations will be explained in next section.

It should be noted that no experimental works are conducted. Validation of the results was simply based on the standard general validation checks of the finite element method such as smooth load development, similarity of stress-strain plot of the structure against material property data and smooth continuity of contour lines across element boundaries. Figure 4.50 shows the development of stress for each load case at a node in the corner of the cell where maximum stress areas are located. It is evident that the development of stress is closely resembled the bi-linear stress-strain relationship of the material, which indicates a reliable solution.

It was observed that the stent assumed a concave shape at maximum expansion and the end struts showing more concave shaped deformation. During stent deployment, it is not desirable to have such abrupt bending because it may cause injury and damage to the arterial wall [104].

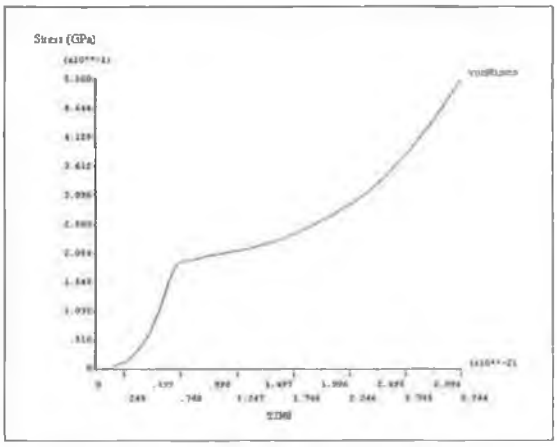

Load case I

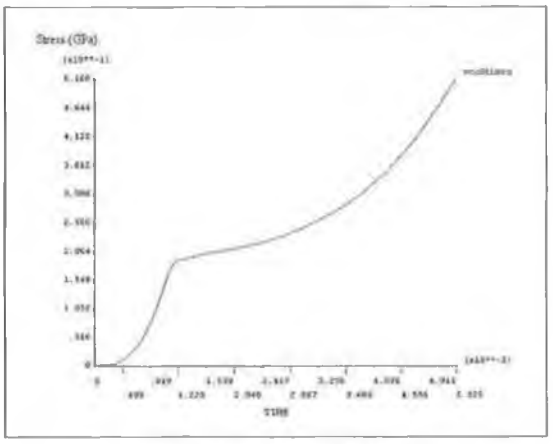

Load case II

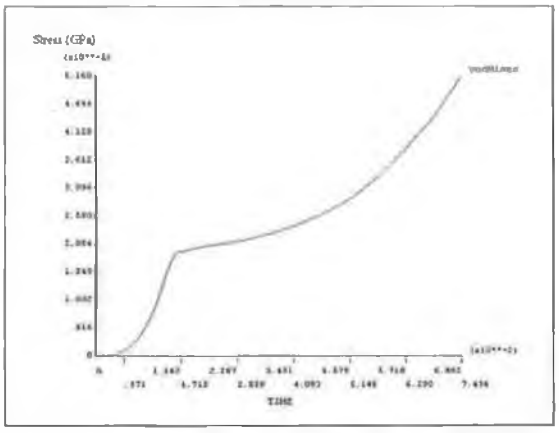

Load case III

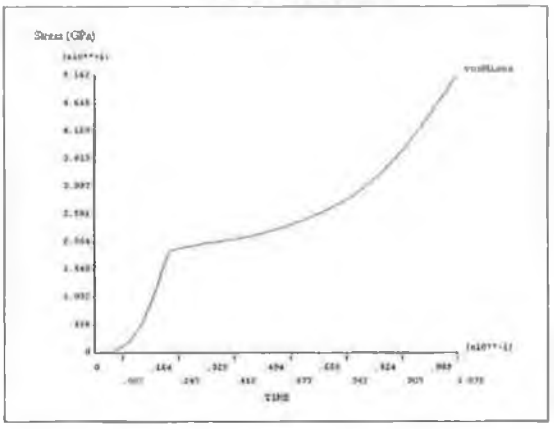

Load case IV

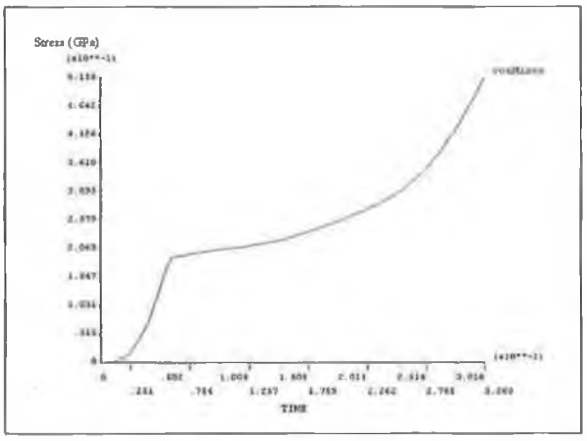

Load case V

Figure 4.50: Development of von Mises stress at corner node for each load case

Chapter 5

SIMULATION AND ANALYSIS OF STENT AND BALLOON

5.1 Stent Expansion with Balloon

The pressure load utilised in the stent expansion without balloon was applied on the inner surface of the stent itself. However, in the actual situation a balloon catheter is used as a medium to engender the stent expansion. Therefore, to obtain a more realistic insight into the expansion process and deformation behaviour, the balloon must be taken into consideration. In order to do that, the balloon has to be modelled with stent. In such a case, the analysis will be more complicated due to the fact that the balloon will have to be modelled and contact conditions between the balloon and stent will have to be considered. This section details the modelling procedures used to simulate the stent expansion by using a balloon as an expansion medium. The results from the simulations are presented and analysed.

5.1.1 Modelling

The ANSYS Finite Element package was used to design the geometric models of the stent and the balloon catheter. The simulation was carried out to expand a stainless steel 304 stent of 3 mm outer diameter and 2.9 mm inner diameter with 10 mm in length. The stent contains 84 slots (cells) which are equally spaced throughout the entire model. The dimensions of the stent are simply described in Table 5.1 below:

Category	**Stent before Expansion**
Number of Cells	84
Cell Size	0.416 mm^2
Cell Areas	35.25 mm^2
Metal Surface Area	59.00 mm^2
Stent Surface Area	94.25 mm^2
Outer Diameter of Stent	3 mm
Inner Diameter of Stent	2.9 mm
Length of Stent	10 mm

Table 5.1: Dimensions of the stent

Due to the symmetrical geometry of the stent it was possible to model just one quarter of the stent. The finite element model of a quarter of the stent is shown in Figure 5.1. One particular benefit gained from this symmetrical model is that the computation time of the problems was greatly reduced. The stent was first created as a partial cylinder. The volume was created from zero to ninety degrees, which generated a quarter of the stent. The slots were created as separate parts of volumes. It was created in such a way that the volume of the slots will intersect with the volume of the stent. Hence, the volume of the stent can be taken off separately by subtracting the volumes of the slots. When the subtraction was done, the remaining volume was the geometry of the stent.

The individual stent strut width is 0.1963 mm in circumferential direction and the length of the bridging strut connecting between the two adjacent cells is 0.29 mm. The finite element model of the stent was meshed with tetrahedral elements to properly model the geometry. Figure 5.2 shows the discretised finite element model of the entire assembly. The stent comprised of 7881 elements and 3473 nodes. A bi-linear elasto-plastic material model was assumed for the stent material. The material properties were chosen to approximately represent Stainless Steel 304 and are as used in previous section.

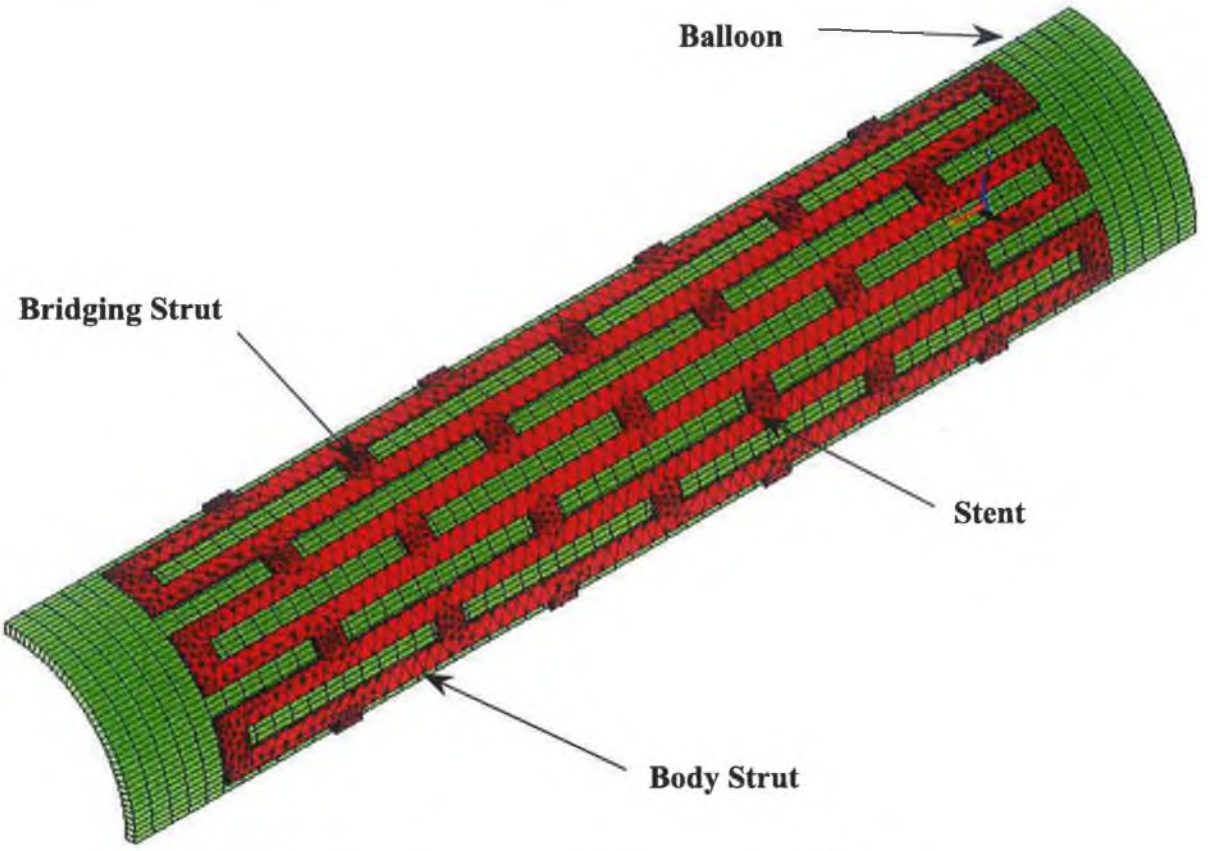

Figure 5.1: Finite element model of one quarter of the stent

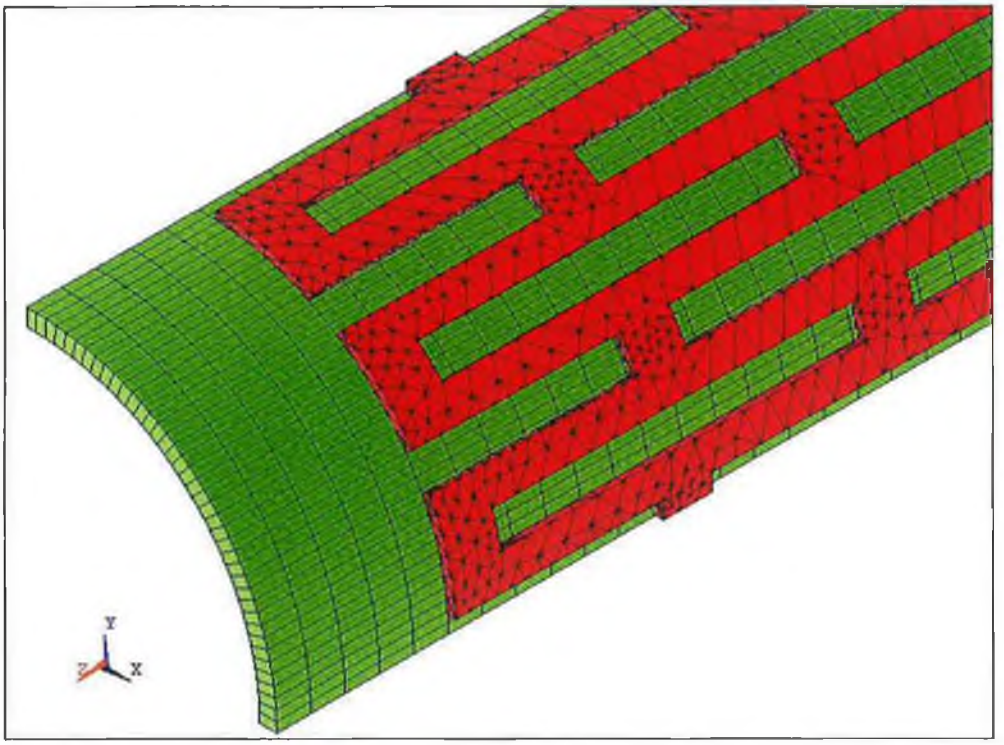

Figure 5.2: Selected discretised geometry

The balloon was modelled as a quarter cylinder placed inside the stent with the outside diameter of the balloon being equal to that of the inside diameter of the stent. A polyurethane rubber type material was used to represent the balloon. The balloon as a medium to expand the stent was modelled to be 12 mm in length. The outer diameter of the balloon was 2.9 mm and the thickness of the balloon was 0.1 mm. The balloon was modelled using eight node three dimensional explicit dynamic solid brick elements. The finite element model of the balloon consists of a total of 2400 elements. The balloon was discretised by 60 elements along its modelled length and 40 elements in circumference with 1 element across the thickness. The balloon was discretised with 40 elements in circumference in order to have better deformation result in circumferential direction.

A non-linear analysis approach and a hyperelastic material model were chosen to represent the balloon. A two parameter Mooney-Rivlin material model was used with the constants being derived using test data, which represented all modes of deformation, and strain ranges that the model will experience. One hundred and twenty two data points were taken from the test data. These data points were input into ANSYS for computing the two term Mooney-Rivlin series. The quality of the Mooney-Rivlin constants was evaluated to ensure that the curve fitted well with the experimental data provided. A graph of calculated stress-strain data versus the experimental stress-strain data was plotted to check the quality of the curve fit. This graph is shown in Figure 5.3.

The Mooney-Rivlin constants derived from ANSYS were then input to the LS-DYNA programme to assign for the material characteristic of the balloon. The two parameter Mooney-Rivlin constants used were C(10) = 0.106881E-02 and C(01) = 0.710918E-03. The density of the polyurethane rubber was determined experimentally to be 1.07×10^{-6} Kg/mm^3 and the Poisson's ratio was assumed to be 0.495 [99].

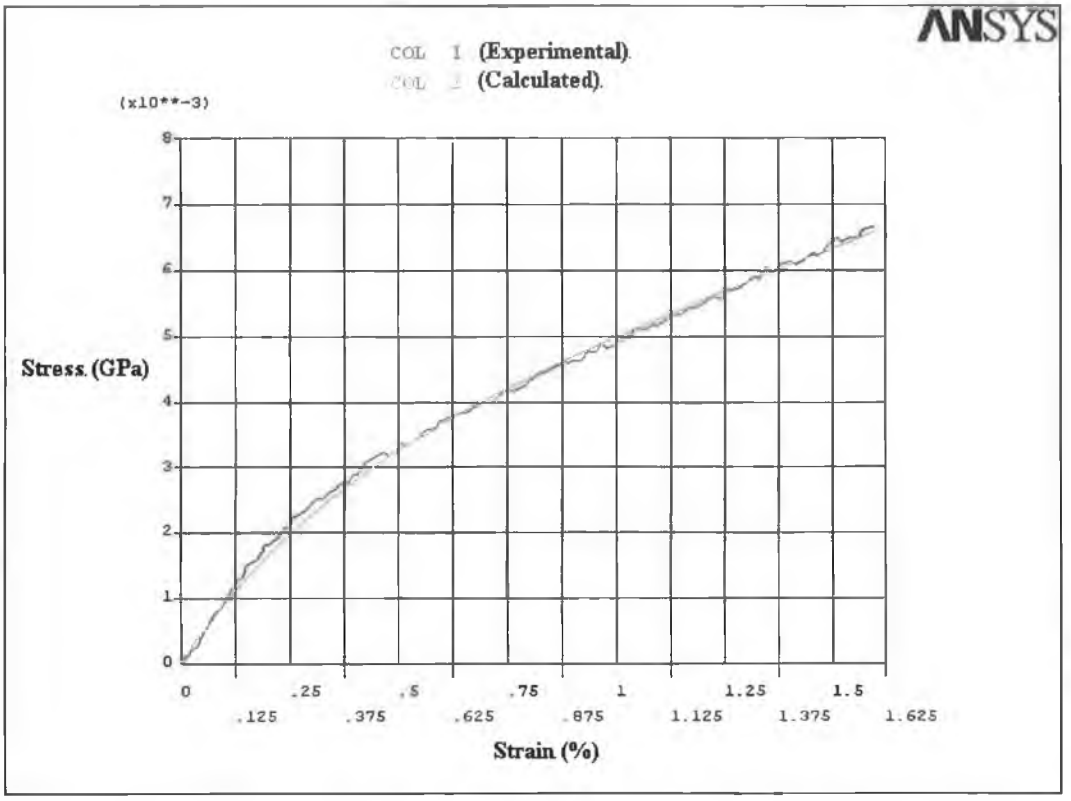

Figure 5.3: Graph calculated values versus experimental data

5.1.2 Boundary Conditions, Loading and Solution

By taking the advantage of symmetrical conditions, only a quarter of the stent and balloon was modelled. Symmetric boundary conditions were imposed on the nodes of the stent and balloon in the planes of symmetry where all the nodes perpendicular to y-axis were not allowed to move in y direction and all the nodes perpendicular to x-axis were not allowed to move in x direction. Both ends of the stent were free from any constraints so that the expansion and shortening behaviour of the stent would be observed. For modelling purpose, the balloon was assumed to be fully tethered at both ends and hence only the expansion in radial direction was permitted.

An automatic surface to surface algorithm approach was selected in order to cope with the non-linear contact problem between the two component surfaces. This algorithm was chosen because it is used for bodies, which have arbitrary shapes that have relatively large contact areas. Also, this type of contact is most efficient for bodies that experience large amounts of relative sliding.

The pressure load was applied as a surface load on the inner surface of the balloon, expanding the stent radially past its elastic limit to a maximum diameter before failure stress was reached. The loading pattern used for this simulation is shown in Figure 5.4. As illustrated in Figure 5.4, the balloon was subjected to a uniform internal pressure increasing from 0 to 0.409 MPa at a constant rate for 1.635 milliseconds. Ramp loading at a sufficiently slow rate that has small kinetic energy or small oscillations provides the opportunity to find the relationship of pressure level to ultimate tensile strength of the stent material. In order to eliminate or reduce the dynamic effects to the minimum, a few analyses with different values of system damping coefficient were carried out. It was found that the system damping coefficient of 10 produced satisfactory result.

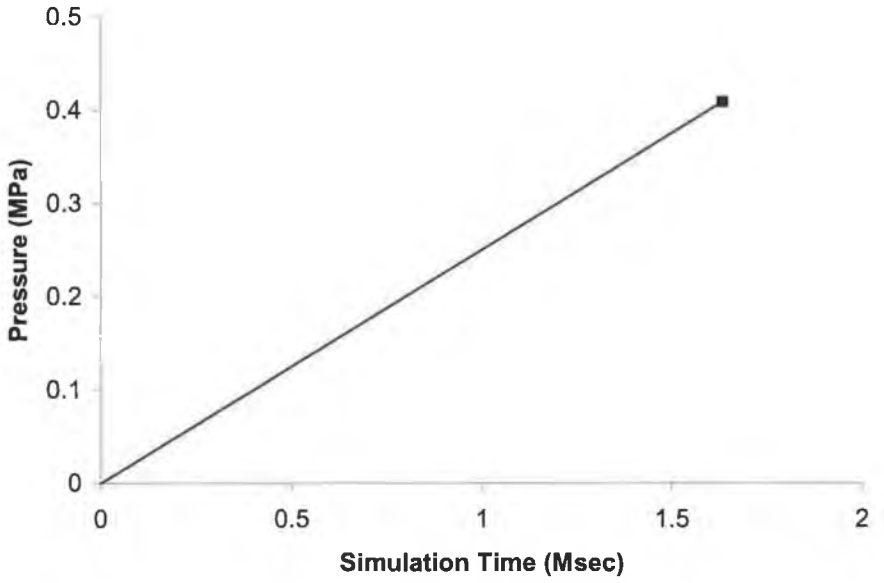

Figure 5.4: Loading curve

5.1.3 Results and Discussion

In order to determine the value of maximum radial displacement, the stent is radially expanded until the onset of plastic deformation is observed and the ultimate tensile strength of the material is reached. For the stent, maximum equivalent stresses are used for the direct comparison with ultimate tensile strength of the material. All maximum radial displacements are measured by taking the displacement values of the nodes in radial direction and they are located in the mid-section of the stent.

The dilatation of the stent with the balloon is a volume controlled process. At the very beginning, a certain amount of pressure is applied to the balloon which causes the balloon to open. This happens without any increase of the stent diameter and can be evidenced from Figure 5.5, which shows that there is almost no dilation of stent diameter from the start until the pressure has reached approximately 0.06 MPa. At this point, it is thought that the balloon actually starts to fit closely to the stent.

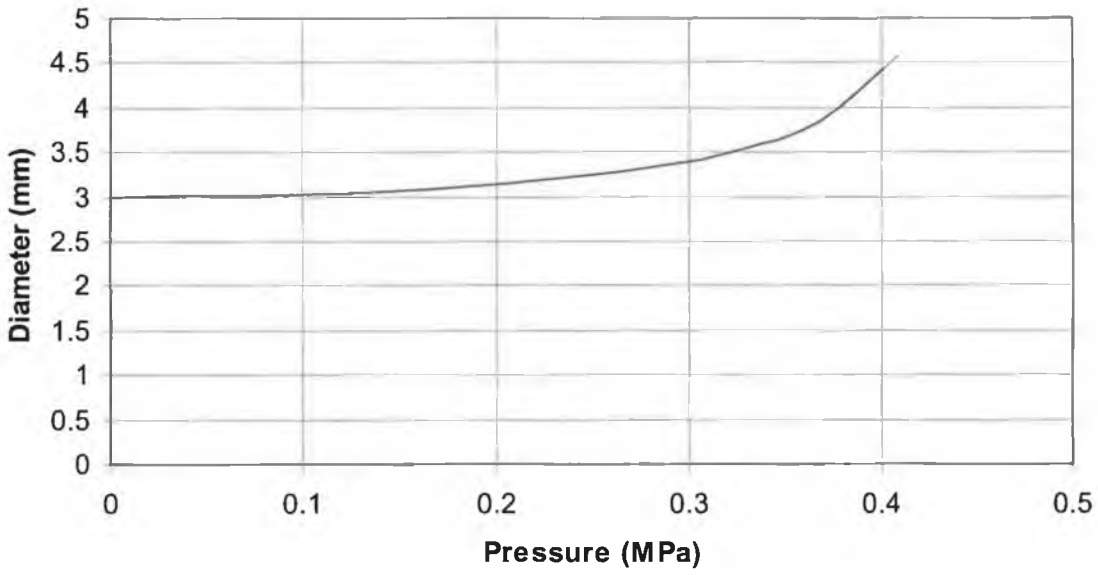

Figure 5.5: Stent diameter versus pressure

The balloon experiences bulging to the utmost at both ends as the pressure is increased and then slowly transmits its forces towards the central part to balance out its force through the entire model. It is understood that the balloon under uniform pressure begins to expand at both ends because of the differences in material properties between the balloon and the stent plus resistance from the stent itself. So, when the force required to further expand the balloon at both ends exceeds the resistant force from the stent, expansion of stent takes place. As the pressure increases, the reaction force of the stent is no longer able to hold the balloon back to its original state. Therefore, a small increase in the stent diameter takes place. During further dilatation, the diameter of the stent tends to pick up gradually.

As the stent is expanding, some parts of the structure in the stent are actually being loaded to their yield point as can be seen from Figure 5.6. As a result, the stress in the stent is gradually increased. However, the stress in some areas of the stent is typically high. These areas are found to be located at the four corners of the cells and in the middle of the cells or in the bridging struts. This is because of the struts being pulled apart from each other to form a rhomboid shape of cells during the expansion. The pressure load at this point is measured as 0.055 MPa. At this stage, some parts of the stent are actually going through the elastic deformation. When the stent structure is not able to store the applied forces anymore, the weakest part of the structure collapses. As a result, these parts are plastically deformed. The neighbouring parts follow through the deformation as the pressure increases. This deformation occurs in a chain reaction until the entire stent is plastically deformed into its new shape.

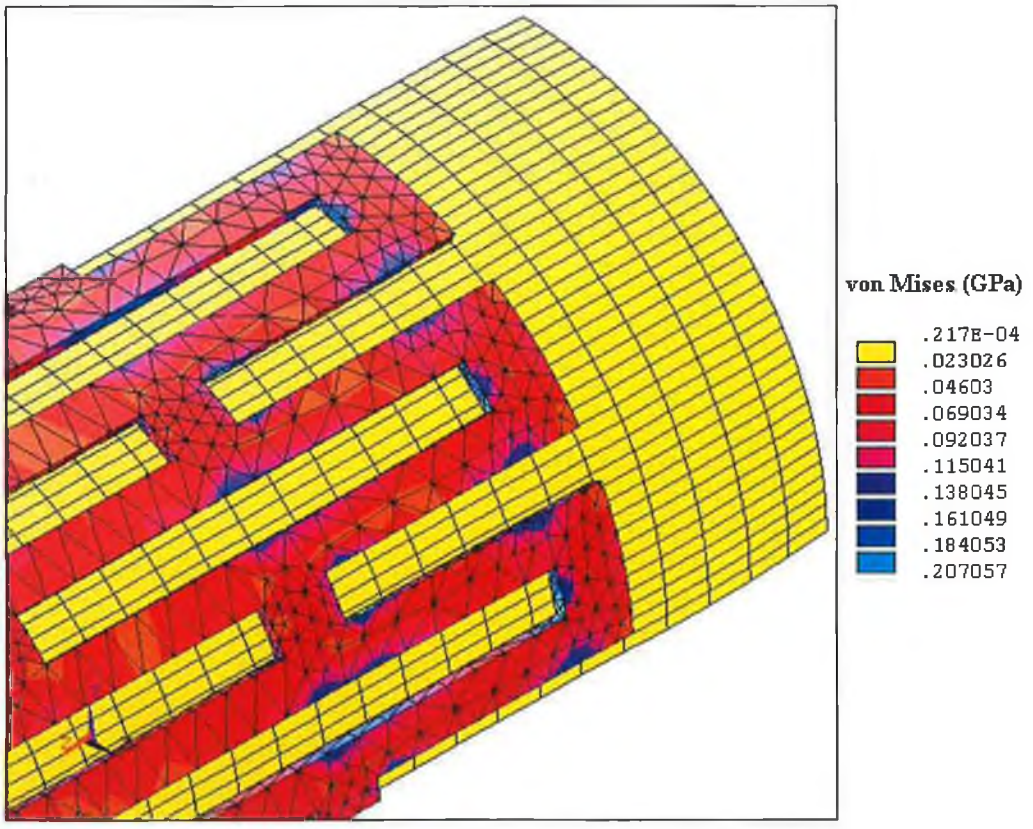

Figure 5.6: Distinct local plastic deformation

Figure 5.7 shows the distribution of von Mises stress in the expanded balloon and stent when the critical pressure is reached. At this point the pressure measured is

found to be 0.4 MPa. Figure 5.8 shows the geometry of the stent before deformation and the distribution of stress in the expanded stent after deformation. Apart from the critical stress at the corner of the cells, from Figure 5.8 it can be seen that the distribution of higher stresses is mostly concentrated in the middle of the struts or the body struts. This is unlike the distribution of stresses at the beginning or just before the yield point of the material strength (Figure 5.6), in which the major stresses are mostly concentrated around the cells. The average stress level in the body struts is approximately within the range of 243 MPa to 298 MPa.

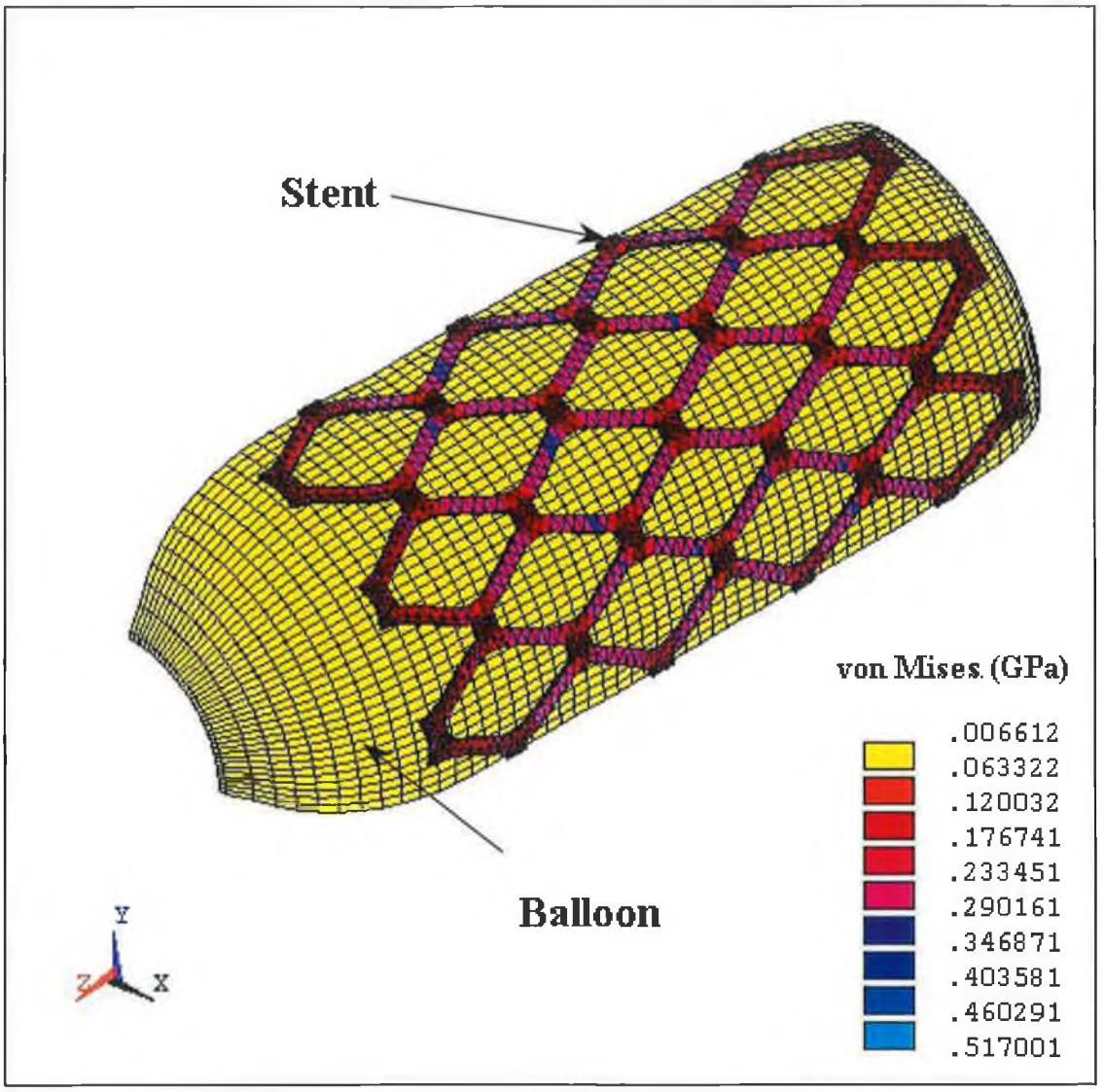

Figure 5.7: Distribution of stress at maximum expansion

One point to be noted here is that the average stress level in the region at both ends of the stent is rather lower compared to the central part of the stent. This is due to the forces being transferred to the central part of the stent by the balloon.

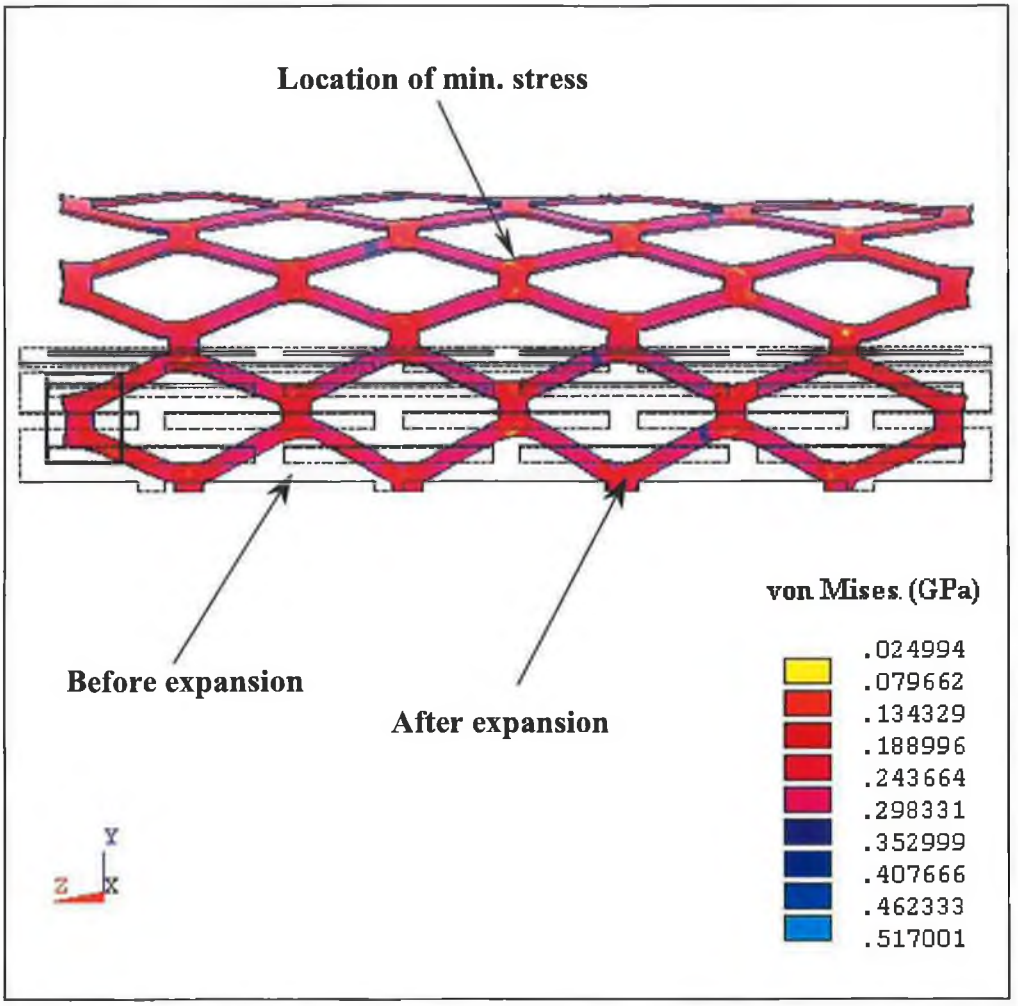

Figure 5.8: Distribution of stress in the stent at maximum expansion

Figure 5.9 shows a close up of the deformed mesh in the edge of the stent (as highlighted in Figure 5.8) after enlargement. This figure also shows the distribution of stresses around the corner of the cell at maximum expansion. As can be seen from the figure that the maximum stress is located around the junction of the cell. It is believed that the consecutive application of pressure after this point might result in a tear at the junction of the cell.

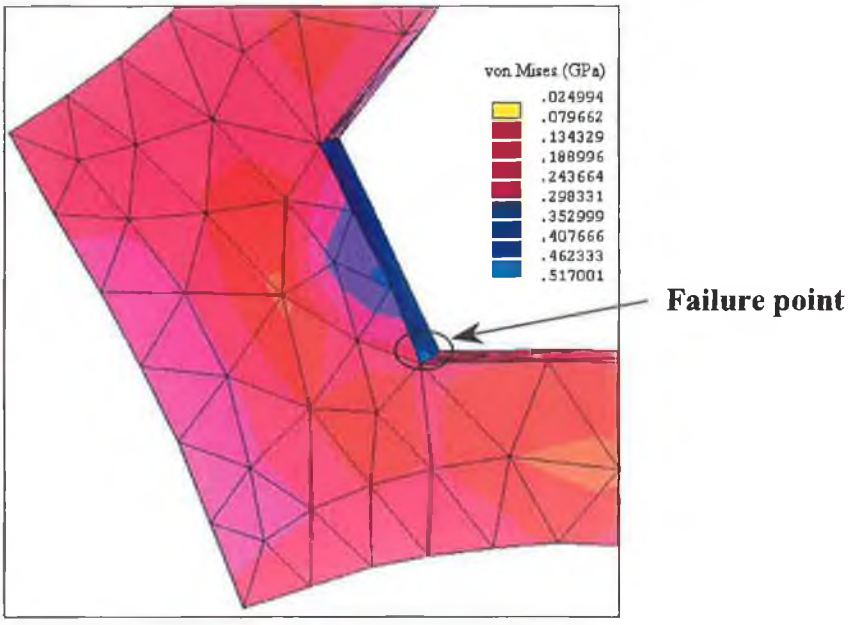

Figure 5.9: Closer view of the end strut as highlighted in Figure 5.8

Figure 5.10 shows the ultimate deformation at the end of the stent when the critical pressure is reached. It is noticed that there is no contact between the balloon and the ends of the stent when the maximum pressure is approached. This also explains the reason that the stress level is lower near the ends of the stent.

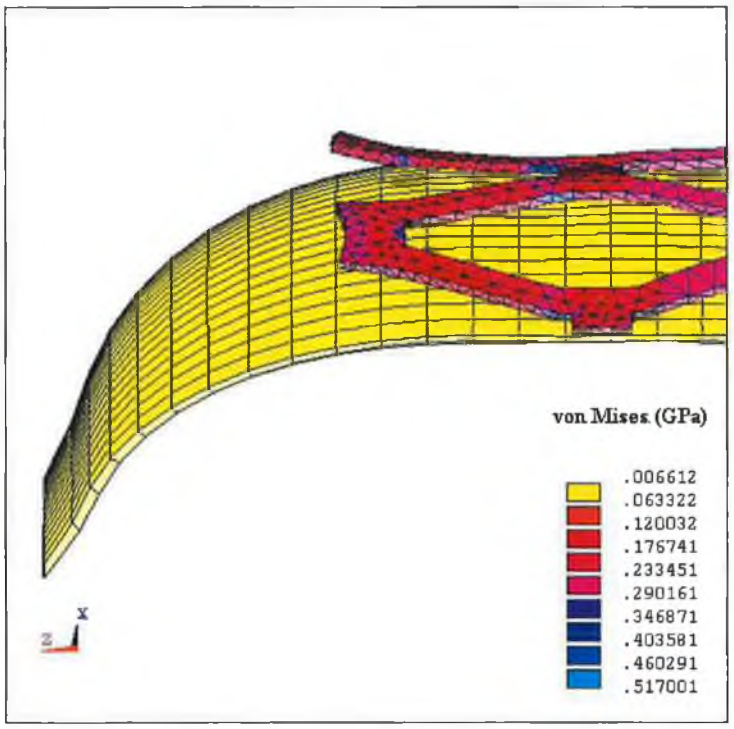

Figure 5.10: Closer view of the deformation at the end of the stent

Foreshortening is an inherently common problem in stents and is evident when a stent is expanded. In order to calculate the foreshortening of the stent, a node was picked from one edge of the stent and a graph was plotted to find out the displacement of that node in z-direction. The node was only taken from one of the two edges of the stent was because of the symmetrical geometry of the stent. Therefore, the magnitude of the foreshortening in the left-hand side should be identical to the right-hand side.

Figure 5.11 shows the development of the foreshortening at that node. As can be seen from the figure that the foreshortening develops in three stages. It is noticed that the foreshortening happens very slowly or almost negligible at the start of dilatation. At this stage, the stent is still awaiting for the balloon to make a proper contact. The stent is way too strong to deform just yet. As parts of the stent experiences an increasing stress, it is then that the foreshortening develops at a faster rate when the time of approximately 0.3 msec is reached. The foreshortening continues fairly at a constant rate until the time of 1.383 msec is reached. At this time, the foreshortening suddenly picks up very quickly due to the massive expansion in the radial direction.

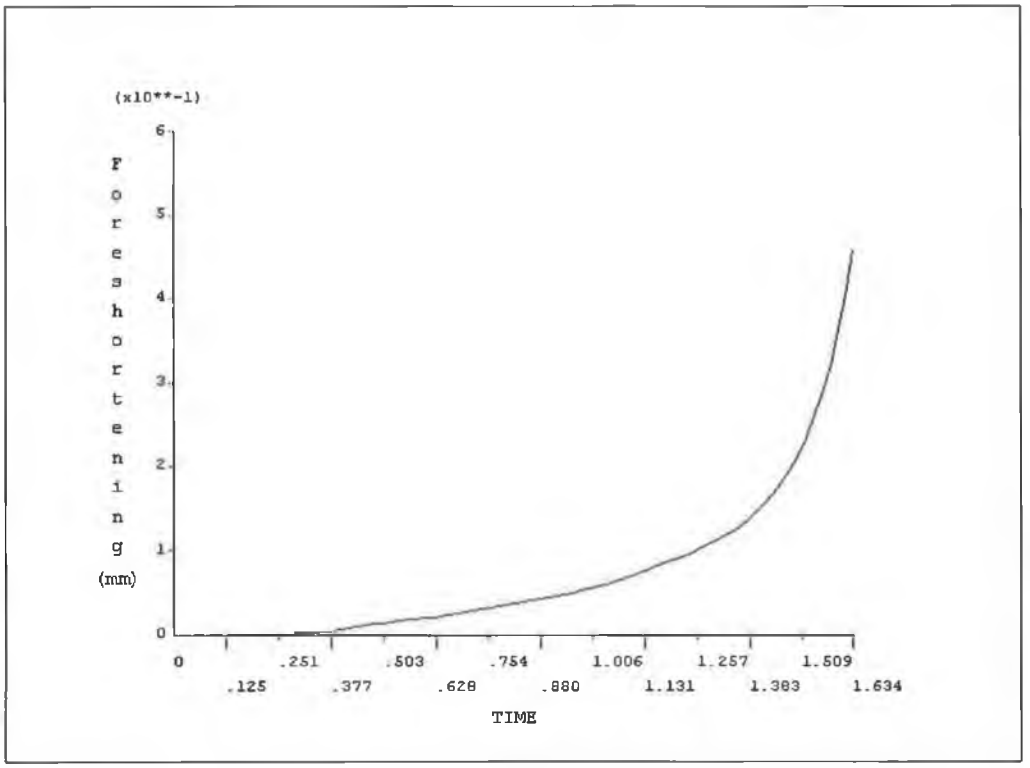

Figure 5.11: Foreshortening of the stent with time

5.2 Analysis of Deployment Pressure on Slotted Tube Stent Expansion

Deployment pressure is one of the major factors that will affect the stent dilatation. It is one of the subjects of considerable discussion and argument. Low deployment pressures can result in incomplete apposition of the stent struts against the vascular wall, which in turn can provoke thrombus (a clot in a blood vessel) formation leading to either subacute closure or late restenosis. Many physicians believed that high pressure dilatations have reduced the risk of thrombotic closure. They believe that the elimination of the risk of subacute stent thrombosis is due to the enhancement of the expanded geometry of coronary stents. However, high deployment pressures can also result in the penetration of the stent struts into the adventitia as well as an over-expanded vessel wall, promoting proliferative neointimal response [107]. This section will detail the effect of deployment pressure on the structure of the slotted tube stent from mechanical point of view. Also, how the alteration in deployment pressures reflects the changes in obtaining uniformity of the stent geometry are presented.

5.2.1 Modelling

Modelling was performed using ANSYS finite element package. The most important step in any finite element simulation is the idealisation and modelling of the problem. In the case of stent analysis, modelling could be very complicated. This is because of the complicated shape of the stent. Furthermore, the symmetrical geometry of the stent makes it even more complicated as all the slots have to be fitted in evenly. In order to properly represent the problem and to be able to observe the deformation of the stent a three- dimensional analysis is required. The ANSYS pre-processor was used to develop the finite element model and the LS-DYNA3D explicit solver was used to solve the problem. A fundamental part of the analysis process is the simplification of geometry to keep model size manageable while allowing sufficient element density. One way of doing this is to take advantage of symmetry. Consequently, only a section of the model is analysed. The idea behind symmetry is that if with proper boundary conditions, only one section needs to be modelled and at the same time obtain results that are representative of the entire geometry.

The simulations were carried out to expand a stainless steel slotted tube of 25.4 mm outer diameter and 23 mm inner diameter with 86.8 mm in length. The geometry of the slotted tube was developed in such a way that all the slots were equally spaced throughout the entire model. In order to do this several volumes had to be created. These volumes were combined together to form a complete geometry of the slotted tube. Since only a quarter of the problem will be modelled, it was understood that the slot and the solid part of the model (i.e. the body strut) had to be evenly placed within ninety degrees. The geometry of the slotted tube can be categorised into two groups, i.e. body strut and slot or bridging strut. The slot and the bridging strut were divided into the same group was because both of them laid in the same section or same portion within an angle. The volumes could be created once the numbers of slot were decided. In the case of this geometry model, they were divided into eight divisions. As a result, the angle for each slot and body strut was determined to be 11.25 degrees. The dimensions of the slotted tube are simply described in Table 5.2 below:

Category	**Stent before Expansion**
Number of Cells	40
Cell Size	62.748 mm^2
Cell Areas	2509.92 mm^2
Metal Surface Area	4416.41 mm^2
Stent Surface Area	6926.33 mm^2
Outer Diameter of Stent	25.4 mm
Inner Diameter of Stent	23 mm
Length of Stent	86.8 mm

Table 5.2: Dimensions of the slotted tube

To develop the body strut of the model, a partial cylindrical volume with 11.25 degrees was first developed in a three-dimensional plane. The subsequent volumes of the body strut were then constructed by adding up the angles. For example, the first body strut was created from starting angle 5.625 degrees to 16.875 degrees. The second body strut was created from 28.125 degrees to 39.375 degrees. The degree of

angles differences within the body strut and between the two body struts was identical, i.e. 11.25 degrees. The geometry of the bridging strut was fabricated by altering the workplane from left to right based on the length of the slot and bridging strut. Basically, the workplane was adjusted accordingly to facilitate the bridging struts. The individual slot and strut widths are equal to 2.49 mm in circumferential direction. The widths of an individual slot and strut were determined to be equal size since they both contained the same degree of angle. The length of the bridging strut connecting the two adjacent cells is 2.8 mm and the length of the slot is determined to be 25.2 mm long.

One obvious change from the previous model is that the current finite element model of the slotted tube is meshed with hexahedral elements. Apart from fitting all the slots in, the main difficulty in modelling the slotted tube is creating a mesh with hexahedral elements. To mesh with hexahedral elements a cube kind of volume is required. This is the reason why the separate volumes of the slotted tube had to be created in the first place. All the lines of the volumes were set appropriately before meshing so that the nodes generated could be merged in a later step of the meshing procedure. The nodes were merged in order to bond the elements together to form the final geometry of the slotted tube. It is important to ensure that the nodes were properly merged, as failure to do so will result in an inaccurate solution in which all the elements will be out of alignment. Basically, the nodes need to be linked together so that the elements could be recognised as part of a family during the solution.

Figure 5.12 shows the discretised finite element model of the one eighth of the entire assembly. The slotted tube consists of 1104 elements. The slotted tube was discretised by 31 elements along its modelled length and 32 elements in circumference with 2 elements across the thickness. The balloon was modelled as one eighth of a cylinder in this model. As the previous model, the balloon was placed inside the slotted tube with the outside diameter of the balloon being equal to that of the inside diameter of the slotted tube. The balloon as a medium to expand the slotted tube was modelled to be 52 mm in length. The outer diameter of the balloon was 23 mm and the thickness of the balloon was modelled to be 1.2 mm. The balloon was modelled using eight node three dimensional explicit dynamic solid brick elements. The balloon consists of 3360 elements. It was discretised by 35 elements along its

length and 32 elements in circumference with 3 elements across the thickness. The balloon was discretised in such a way that the density of the mesh was finer towards the end of the balloon. The purpose of this meshing was to better capture the bending near the end of the balloon. A total of 4464 elements describe the entire model.

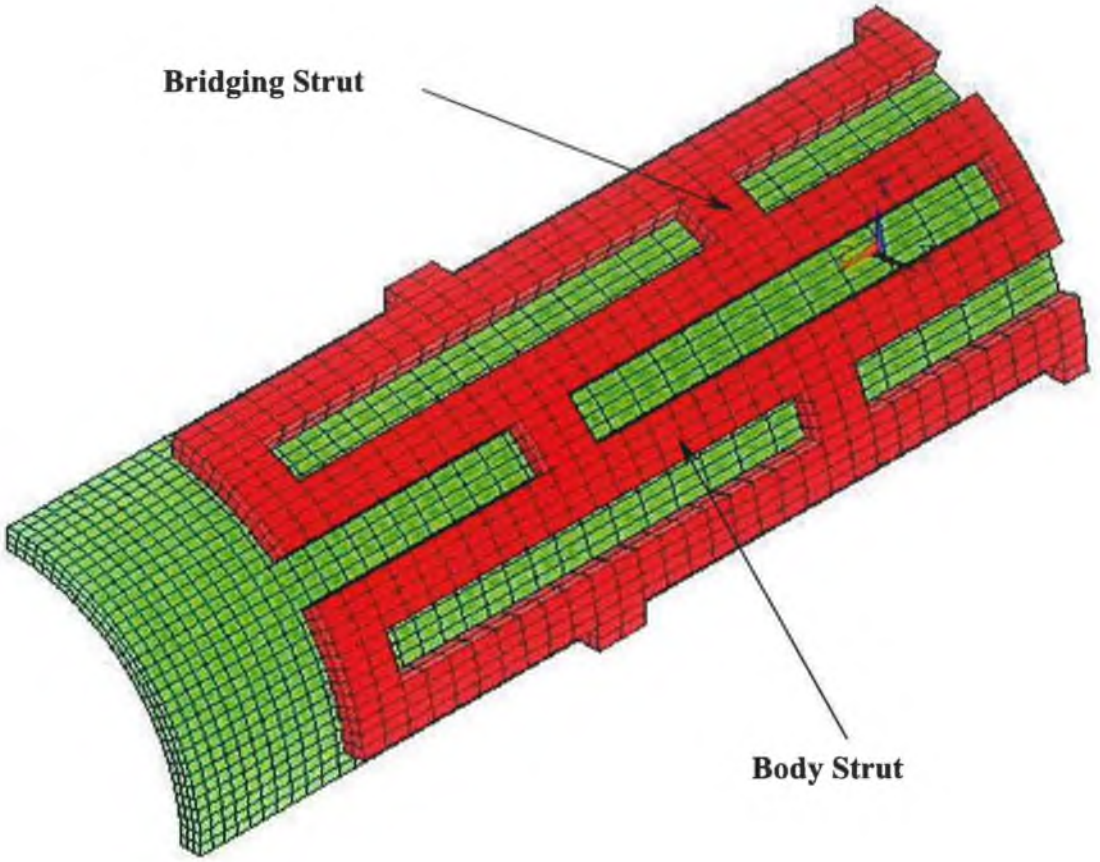

Figure 5.12: Finite element model of one eight of the slotted tube

A bi-linear elasto-plastic material model was assumed for the slotted tube material model. The material properties of Stainless Steel 304 as used in previous models were chosen for this simulation as well. As for the balloon, the material properties of a polyurethane rubber type material were used to represent the expanding medium. A non-linear analysis approach and a hyperelastic material model were chosen to represent the balloon. Although the derived Mooney-Rivlin constants can be used to evaluate the Mooney-Rivlin model outside of the range of the experimental data, it was thought that it was safer to have enough test data to cover the full range of strains that the balloon will experience. Therefore, higher strain ranges of the test data were taken to derive a new two parameter Mooney-Rivlin model. Twenty two

data points were taken from the test data in order to calculate for the Mooney-Rivlin constants. A graph of calculated stress-strain data by ANSYS versus the experimental stress-strain data was plotted to ensure that the two curves fitted well. The graph is shown in Figure 5.13.

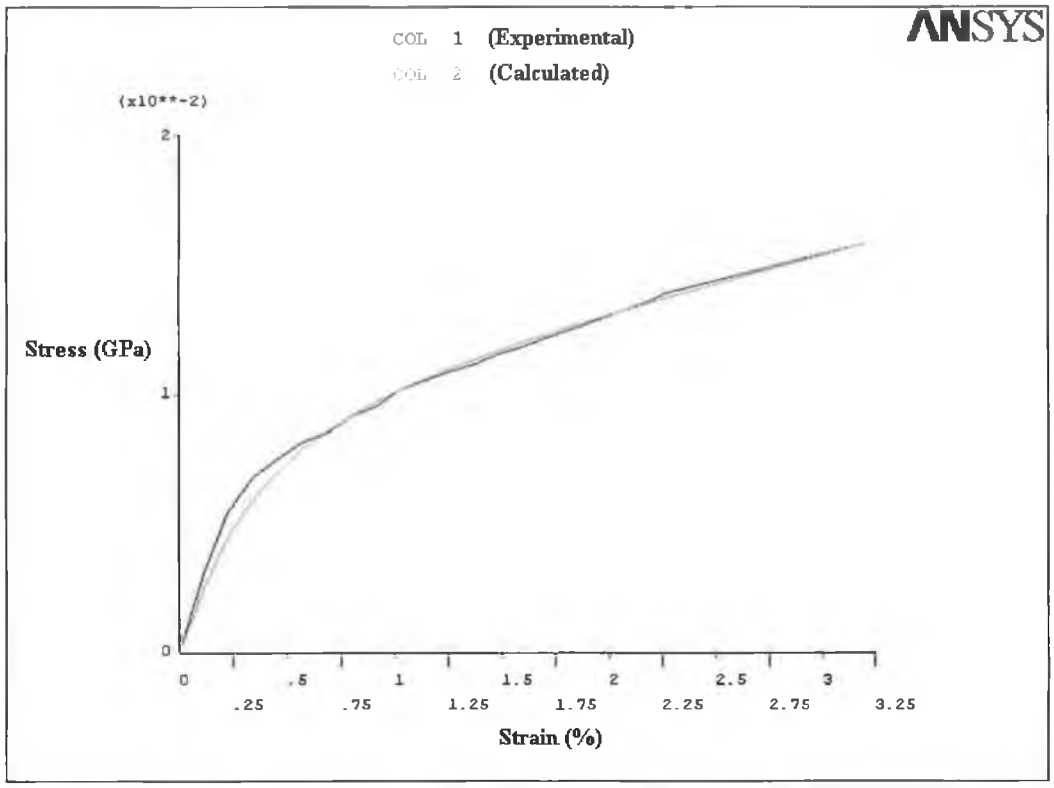

Figure 5.13: ANSYS calculated values versus experimental data

The two Mooney-Rivlin parameter constants were found to be C(10) = 0.103176E-02 and C(01) = 0.369266E-02. The density of the polyurethane rubber remained unchanged i.e. 1.07 x 10^{-6} Kg/mm^3 and the Poisson's ratio was assumed to be 0.495 [99].

5.2.2 Boundary Condition, Loading and Solution

Only one eighth of the model was developed by taking advantage of the symmetry, the slotted tube nodes and the balloon nodes at the symmetry edges were restrained in the appropriate directions. That is to say the symmetric boundary conditions were imposed on the nodes where all the nodes perpendicular to y-axis were not allowed to move in y direction and all the nodes perpendicular to x-axis were not allowed to

move in x direction. Since only half of the length of the slotted tube and balloon were modelled, symmetry constraints were applied to the corresponding nodes in the z direction. For modelling purpose, the balloon was assumed to be fully tethered at the left hand side and hence only the expansion in radial direction was permitted. An automatic surface to surface contact algorithm was chosen for interface modelling as large deformation and sliding were expected.

Three different levels of deployment pressures were carried out in these simulations. The pressure load was applied as a surface load on the inner surface of the balloon. The magnitude of the pressure was deployed in such a way that the geometry of the slotted tube will retain its shape after deflation of the balloon. The deployment pressure is therefore can be described, as the pressure required achieving plastic deformation of the material used. The loading patterns used for these simulations are shown in Figure 5.14. The three simulations of the expansion process were carried out with pressure loads varying in three stages i.e. pressure increasing, constant pressure and pressure decreasing. These three pressure stages were used to simulate the inflation and deflation of the balloon. The pressure was held constant for five milliseconds in order to give time for the slotted tube material to fully respond to the load.

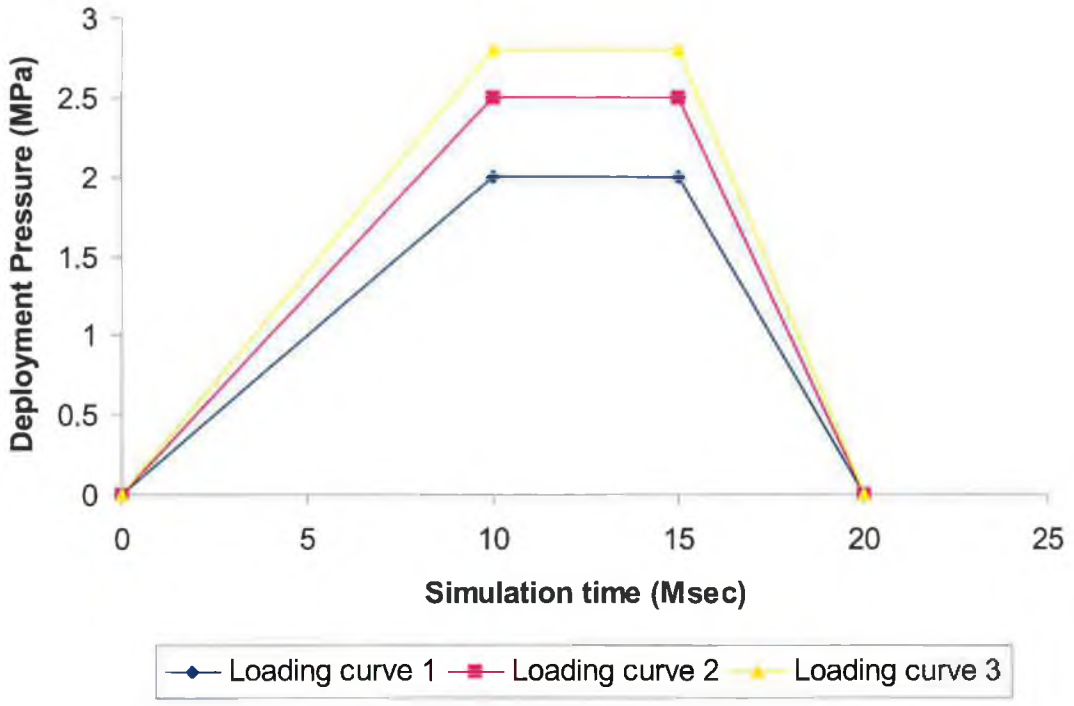

Figure 5.14: Three different deployment pressures

The first simulation of the expansion process was carried out with a pressure load increasing from 0 to 2 MPa. The total simulation time was set to be 20 milliseconds. The pressure stopped increasing when the simulation time of 10 milliseconds was reached. The pressure load was held constant for 5 milliseconds and then unloaded to zero pressure in which the simulation time of 20 milliseconds was finally reached. The second simulation of the expansion process was run with a pressure load increasing from 0 to 2.5 MPa within 10 milliseconds. The subsequent load history was just like first simulation, which the load was held constant for 5 milliseconds and then slowly reduced to zero pressure. The third simulation of the expansion process was carried out with a pressure load increasing from 0 to 2.8 MPa in 10 milliseconds. Obviously, this was the highest pressure level amongst the three simulations. Again, the pressure load was kept constant for five milliseconds and unloaded to zero pressure. The magnitude of the deployment pressures was determined based on the yield point and rupture point of the slotted tube material i.e. stainless steel 304. The deployment pressures were chosen in such a way that they were strong enough to achieve the plastic deformation at the same time without exceeding ultimate tensile strength of the slotted tube material.

5.2.3 Result and Discussion

5.2.3.1 Deployment pressure of 2 MPa

Loading curve 1 as can be seen from Figure 5.14 contains the lowest deployment pressure. The pressure deployed is just adequate to transform the slotted tube from its elastic limit to undergo the plastic deformation. A material is said to be undergone plastic deformation when it changes its shape permanently. It has gone through a changing phase of the material in which they will not recover to its original shape.

Figure 5.15 shows the slotted tube had experienced the plastic deformation. The simulation time at this point was 20 milliseconds. The balloon was totally deflated at this point in time but the slotted tube remained its shape after the expansion process. The expanded region has stressed considerably with a relatively uniform distribution albeit the highest stressed region could still be clearly seen. It is also very obvious that the location of the highest stressed region is located at the centre and at the four

corners of the slots. The maximum stress developed in this region is 272 MPa which exceeded the yield point. In comparison with the ultimate tensile strength of the material, the slotted tube was stressed only up to 52% of the ultimate tensile stress.

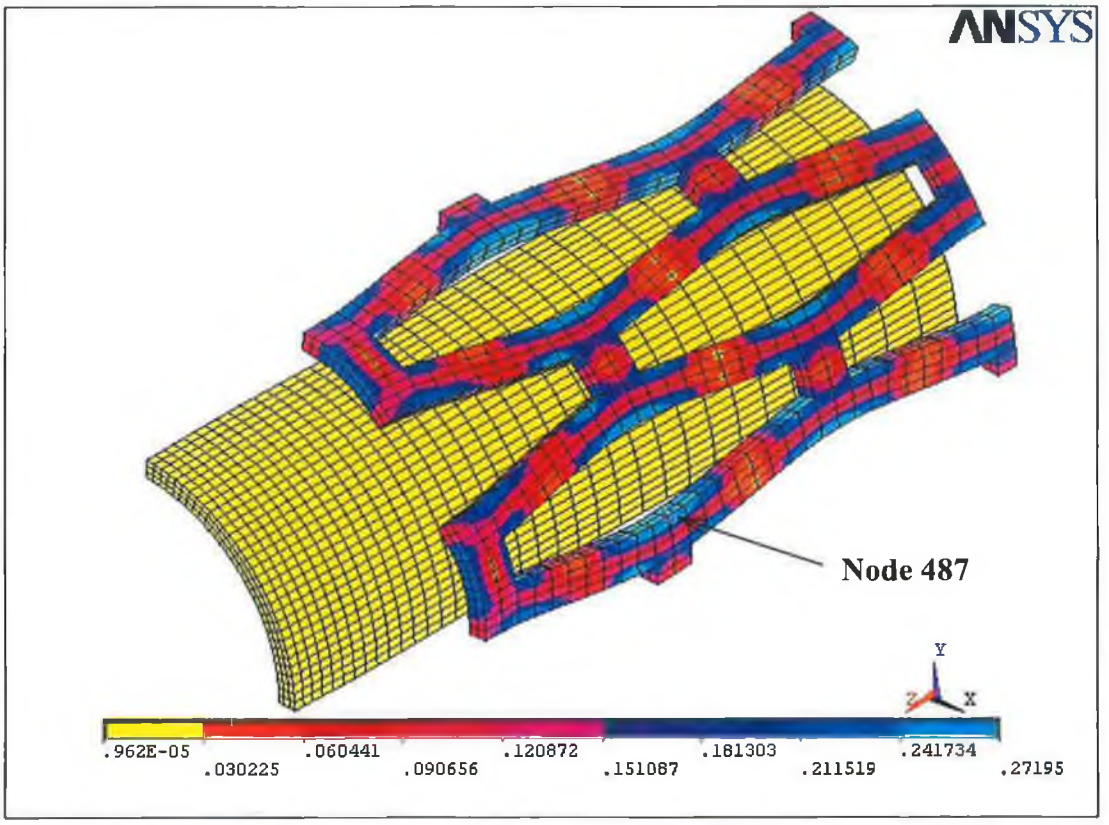

Figure 5.15: Residual stress in the deformed slotted tube by loading curve 1

Figure 5.16 shows the development of stresses in x, y, z direction and von Mises stress in the central node of the slot (node 487) top surface. The stress development was steady and relatively stable until the simulation time of 1.2 milliseconds, which corresponds to the beginning of the deformation. It can be seen that after the onset of deformation that the ratio of the stress in x and y directions was relatively constant in agreement with the pressure load which was raised uniformly throughout the dilatation process. When the maximum pressure is reached, the stresses remain uniform until the balloon starts releasing at the simulation time of 15 milliseconds. Apart from the beginning of the expansion process, it is evident from the graph that the stresses in x and y directions were always compressive. Nevertheless, this is not

the case for the stress in z direction as it switched from compression to tensile when the balloon was deflating.

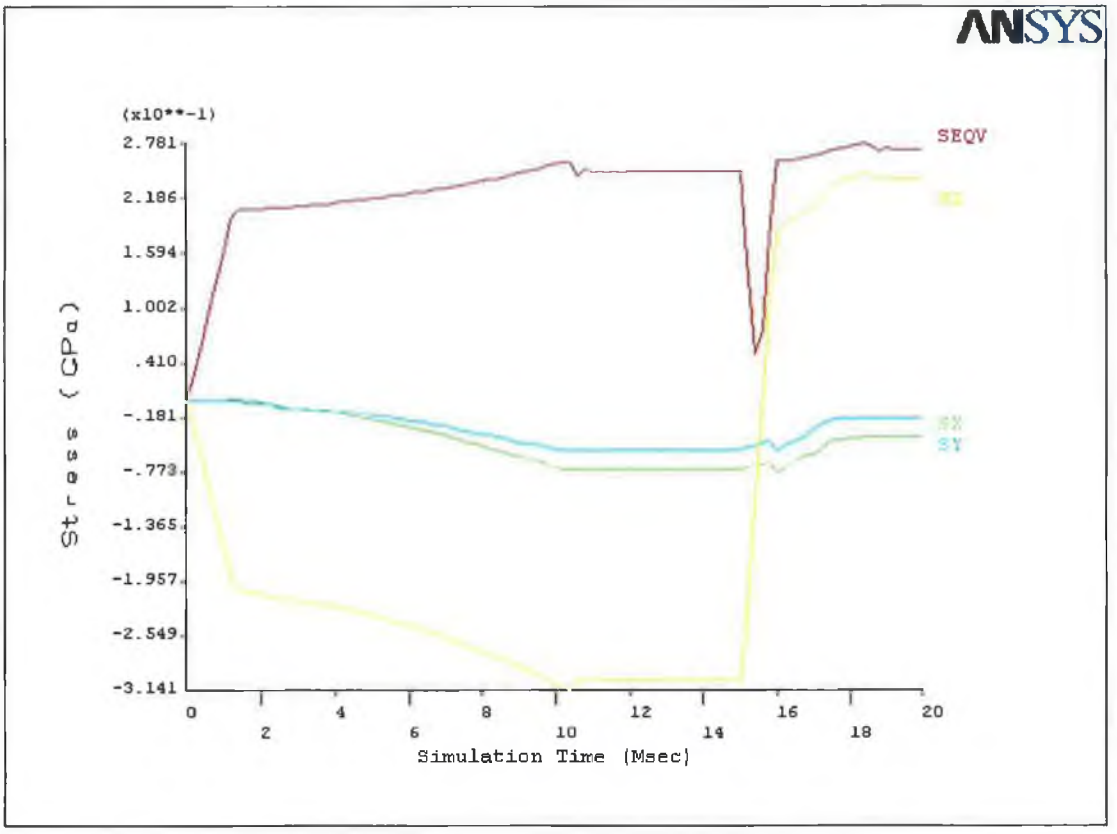

Figure 5.16: Development of stresses in node 487

Stresses in x and y directions developed in the same magnitude at the beginning of the dilatation process. As the pressure increases, the stress in x direction tends to develop quicker than the stress in y direction. This is inevitable, as the slotted tube tends to expand from the outer edge to the centre of the slotted tube. Higher stress was generated in the x direction as the edge of the slotted tube leaning outwards by the expansion of the balloon. The stress in x direction continued to dominant over stress in y direction until the balloon was deflated. The stress in z direction was always compressive until the deflation of balloon was begun and became tensile as soon as the slotted tube experienced a slight elastic recovery due to the material law being used. The simulation time at this point was approximately 15.4 milliseconds. The change from compression to tensile stress was because the slotted tube had been

pre-stressed and then released, a spring-back type condition was taking place once the pressure was released.

Figure 5.17 shows the equivalent plastic strain for node 487 throughout the simulation process. The time history illustrates the four stages in the response. The first stage was initial ramp loading as shown in the equivalent plastic strain from zero to ten milliseconds. The second stage was steady-state response i.e. from simulation time of 10 milliseconds to 15 milliseconds. The third stage was release of pressure that was indicated by the descending trend. The last stage was separation of rubber balloon from the slotted tube. The balloon was separated from the slotted tube at approximate time of 18.4 milliseconds. The time history of the curve was absolutely resembled the behaviour of the slotted tube from the beginning of inflation of the balloon to the deflation of the balloon.

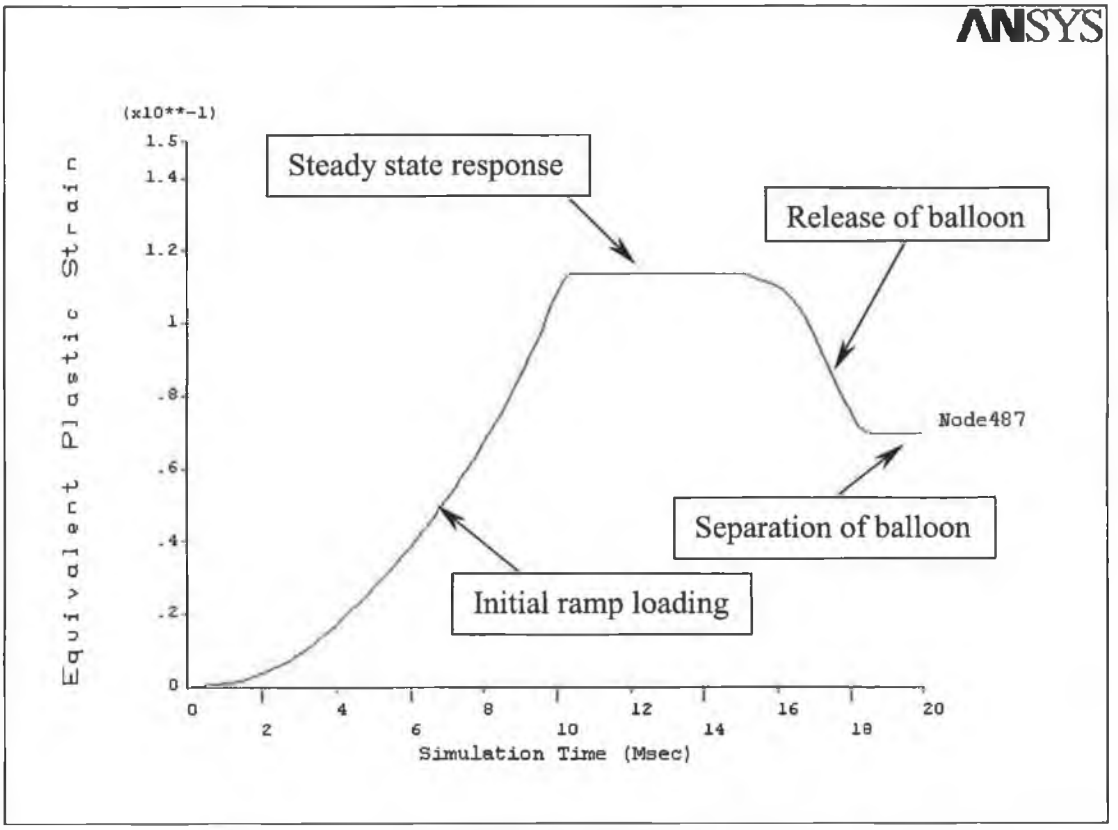

Figure 5.17: Equivalent plastic strain at node 487

The four different stages of response during the simulation were detailed in Figure 5.18 to Figure 5.21. Although only a quarter of the slotted tube was modelled the ANSYS post-processor contained a function, which allows duplication of the slotted tube at plane of symmetry for better visualisation. The picture was plotted in such a way that the four stages of response could be better seen and identified.

Figure 5.18 shows the distribution of stress at maximum deployment pressure. The highest stress achieved at that time was approximately 254 MPa. It was noticed that the maximum stress was slightly lower (Figure 5.19) when the slotted tube expansion process had reached the steady state response. This was due to the fact that the material of the slotted tube was responding to the pressure load. The stresses in the slotted tube reorganised amongst themselves to achieve the equilibrium state. As the pressure was releasing, the von Mises stress increased due to the increased and mode switched in the axial stress component. This explained why the stresses were higher right after the balloon lost contact with the slotted tube, which was approximately 277 MPa.

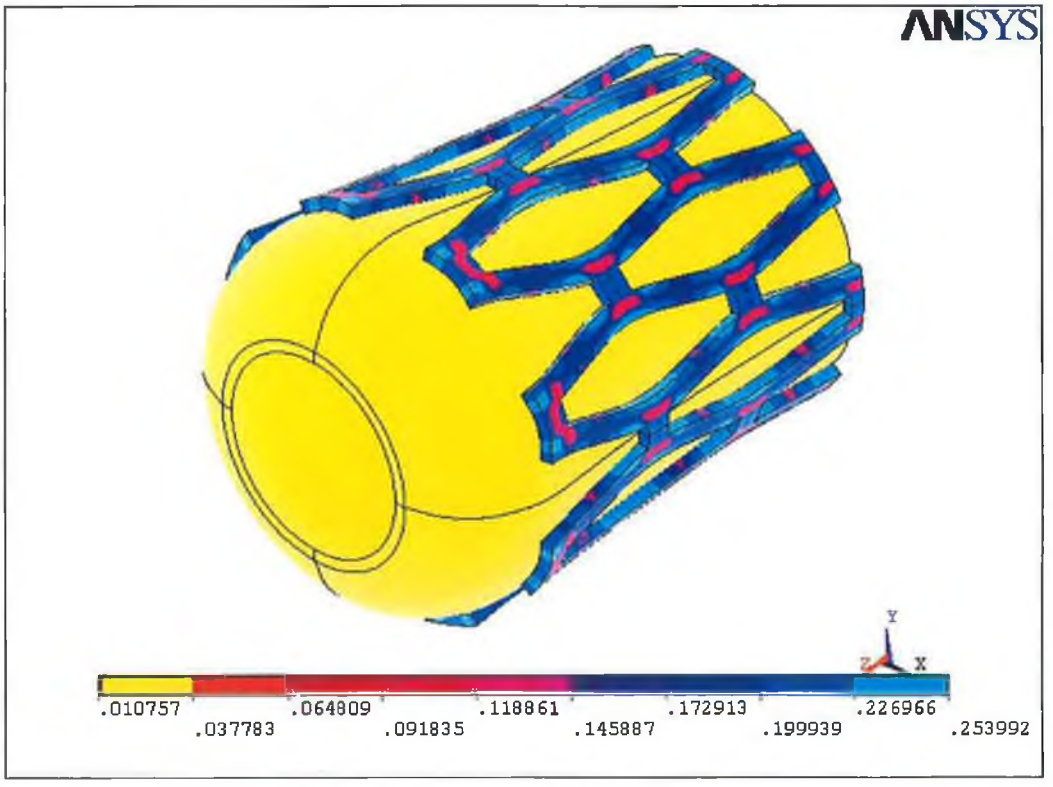

Figure 5.18: Deformation of the slotted tube by initial ramp loading at time 10 msec

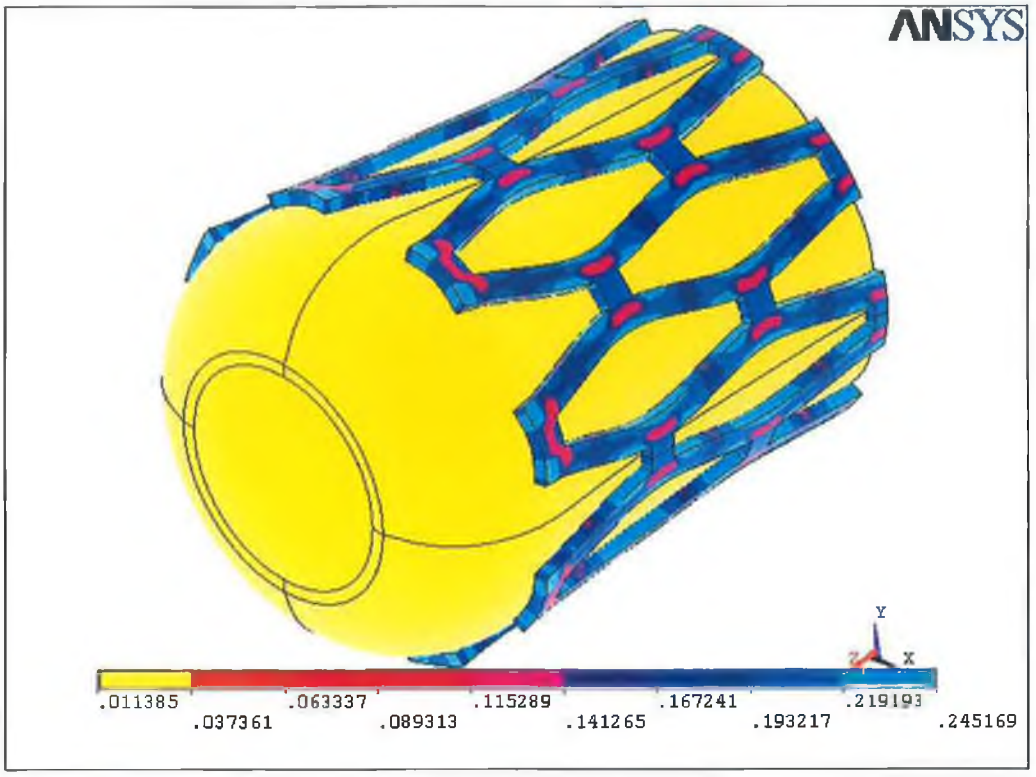

Figure 5.19: Deformation of the slotted tube in steady state response at 15 msec

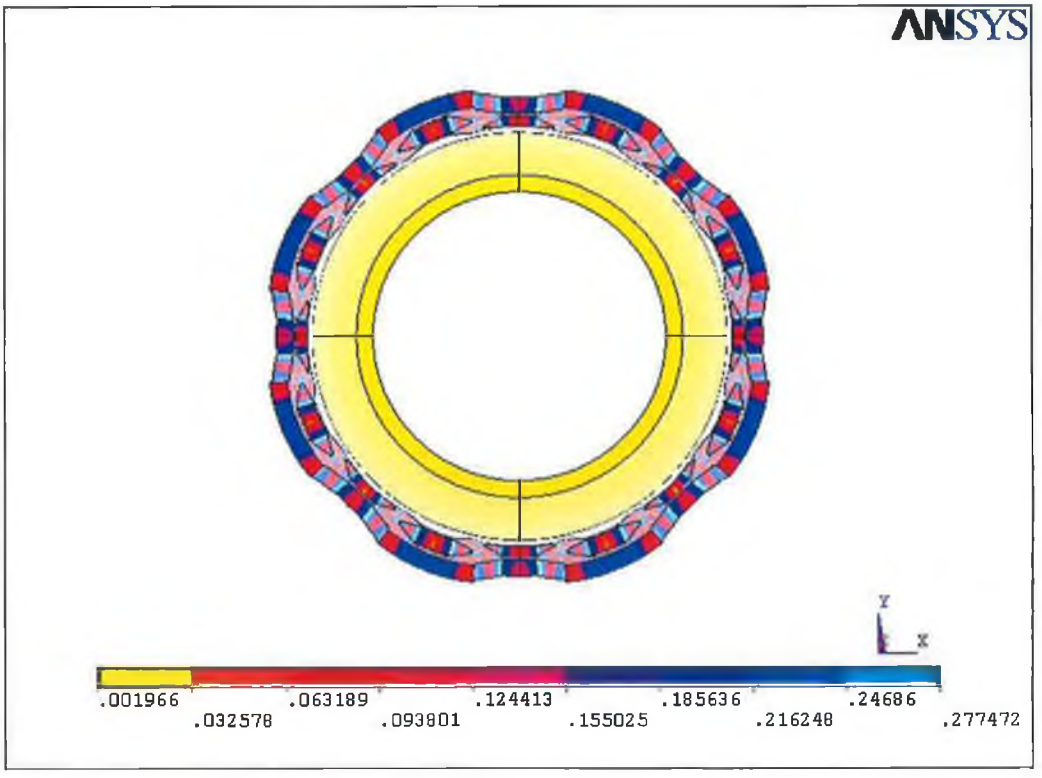

Figure 5.20: Deformation of the slotted tube at simulation time 18.4 msec

Figure 5.21 shows the residual stress distribution in the slotted tube when the balloon was completely separated from the slotted tube. After the pressure was completely deflated, the stress mapping shows higher residual stresses tend to be localised in the region at the centre of the slots as well as the corner of the slots. They ranged from 241 MPa to 272 MPa. This particular point plays an important role when it comes to designing a stent. It is also noticed that the stress levels in the end of the slotted tube were higher than the centre part of the slotted tube and the body struts when the pressure was released. They were within the range of 120 MPa to 151 MPa.

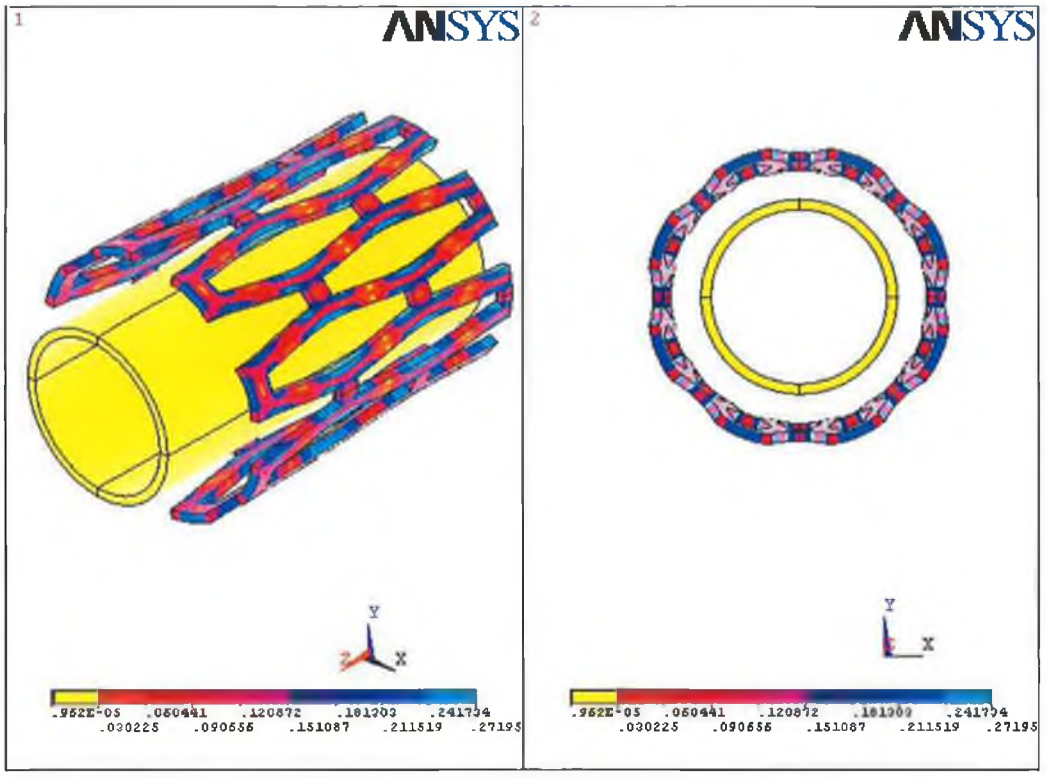

Figure 5.21: Deformation of the slotted tube at simulation time 20 msec

a) Deployment pressure vs. displacement

The slotted tube deployment pressure can be defined as the pressure required to obtain the required diameter after the expansion process. The pressure required to expand the slotted tube in this simulation was significantly lower than the other two simulations.

Figure 5.22 shows the magnitude of the slotted tube expansion in radial direction. This graph also illustrates the diameter of the slotted tube achieved when the maximum deployment pressure is reached. In order to calculate the diameter expanded, a node on the inner surface of the meshed slotted tube was taken for measuring the displacement in radial direction. The node was located in the edge where two symmetrical planes intersected. These two symmetrical planes were plane of symmetry parallel to y-axis and xy plane. They were perpendicular to each other.

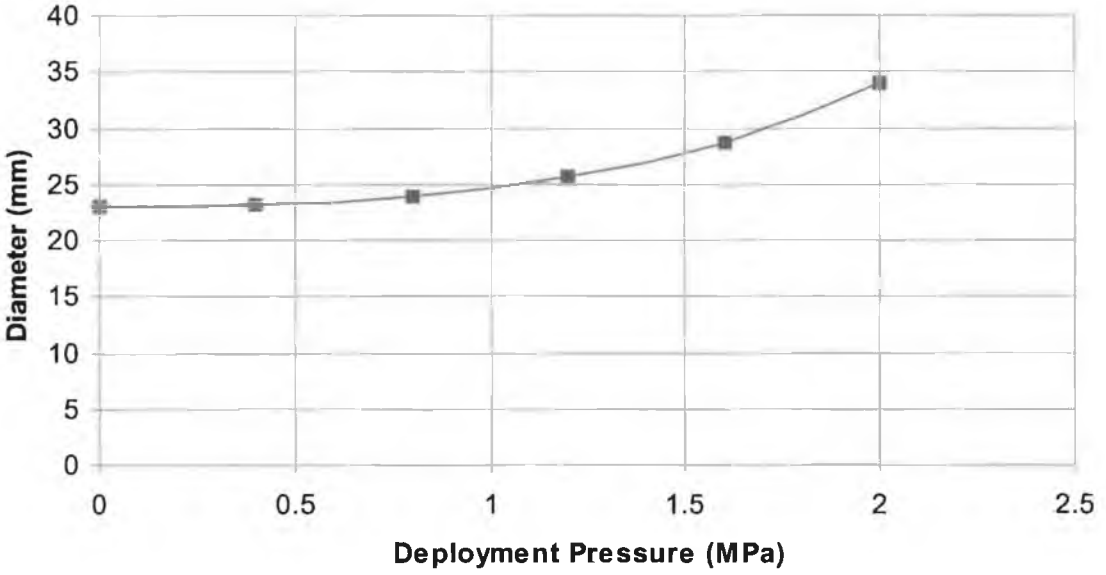

Figure 5.22: Expansion of slotted tube diameter with deployment pressure

The diameter of the slotted tube increased slowly as the pressure increased. The graph shows no difference with the past simulations that is the diameter expands slowly at the beginning of the dilatation process and then expands at a quicker rate when a certain pressure is reached. The maximum radial expansion of the slotted tube achieved was approximately 5.5 mm at simulation time of 10 milliseconds. This value was taken based on the lowest point of the displacement in radial direction where the node was located. The maximum diameter of the slotted tube achieved was 34.02 mm. The slotted tube has expanded up to 48% i.e. approximately 0.5 times from its original diameter.

b) Elastic recoil

Pressure was released to model the deflation of the balloon. This process also enables to detect the shrinkage of the slotted tube after the maximum pressure was deployed. After releasing the pressure, the diameter of the slotted tube was observed to have shrunk compared to the initial ramp loading stage which maximum radial expansion was observed at the end of inflation. This reduction in size is referred to as the elastic recoil of the slotted tube. The elastic recoil is a result of the elastic and plastic deformation of the material.

Figure 5.23 shows the reduction in the slotted tube diameter following the deflation of the balloon. The maximum diameter before the pressure was released was 34.09 mm. The diameter dropped after the pressure was completely released and it was found to be 29.94 mm. The slotted tube was calculated to have shrunk 12% from the maximum tube diameter obtained during the maximum deployment pressure.

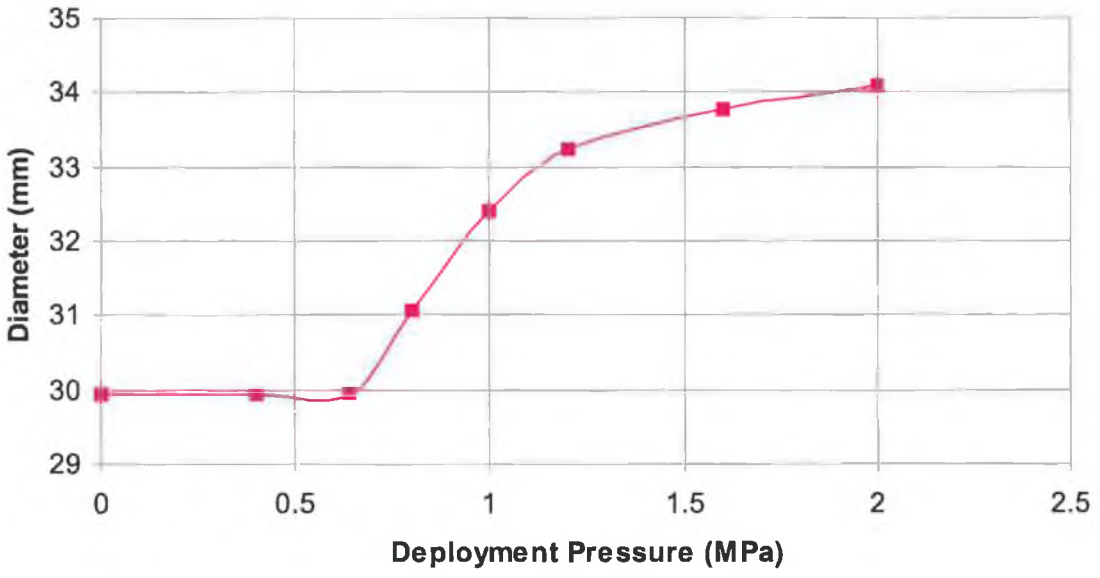

Figure 5.23: Elastic recoil of the slotted tube

c) Slotted tube foreshortening

The slotted tube foreshortening is defined as the contraction of the slotted tube from its original length. The foreshortening of the slotted tube was calculated from the longitudinal displacements of the node located at the end of the slotted tube.

Figure 5.24 shows the magnitude of foreshortening of the slotted tube with simulation time. It is evident form the graph that the amount of foreshortening was indirectly proportional to the deployment pressure. As the deployment pressure increases the foreshortening also increases. The total amount of foreshortening was found to be of 1.345 mm when the maximum pressure was applied. However, the foreshortening reduced to only 0.56 mm when the deflation pressure was completed. As can be seen from the graph that the foreshortening remained stable as the pressure was released. This indicated that the slotted tube material was fully responded to the load.

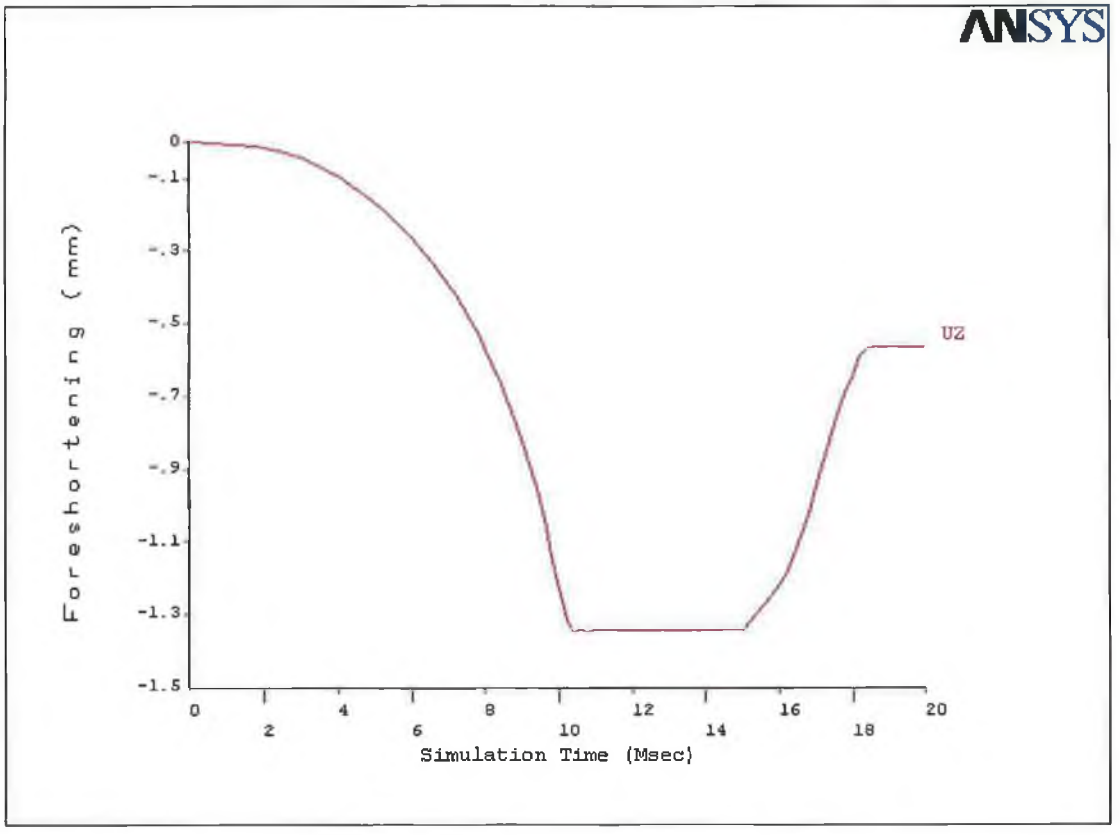

Figure 5.24: Foreshortening of the slotted tube with simulation time

Figure 5.25 shows the ultimate geometry of the slotted tube obtained after the deflation of the balloon. The slotted tube was found somewhat shorter than the original length before expansion. When the pressure was released the foreshortening also reduced. The pre-stressed slotted tube during the first phase of expansion process allows the stress in z stressed component to spring back. During the spring back action, the reduction in foreshortening occurred quicker than when the slotted tube was first expanded. The equilibrium state was reached when the balloon was separated from the slotted tube. As a result, the foreshortening remained constant and the magnitude of the foreshortening at that time was found to be 0.568 mm. The percentage of the foreshortening from the original length of the slotted tube after the deflation of the balloon was approximately 1.3%.

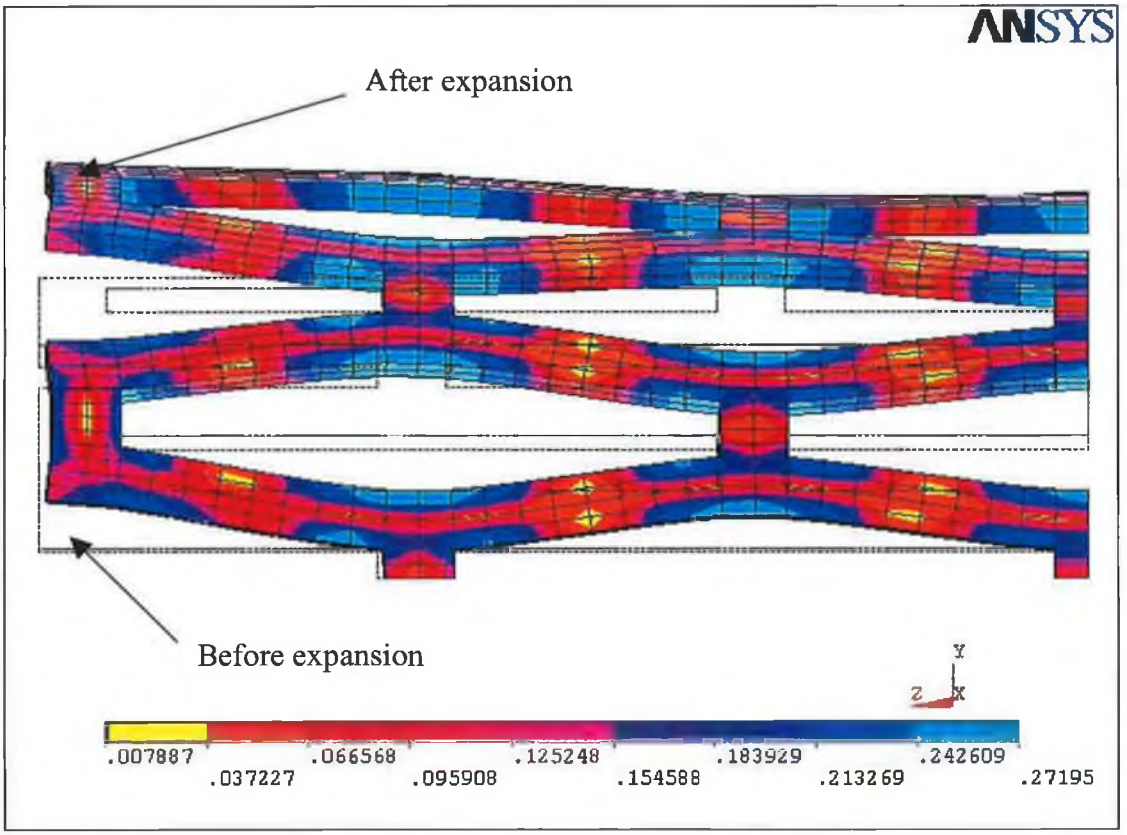

Figure 5.25: The geometry of the slotted tube before and after the expansion

5.2.3.2 Deployment Pressure of 2.5 MPa

This simulation was implemented with the intermediate pressure deployment that was 2.5 MPa. Load curve 2 as can be seen from Figure 5.14 totally explained the

load history of the pressure deployed. Figure 5.26 shows the residual stress distribution in the deformed slotted tube after deflation of the balloon by loading curve 2. The slotted tube experienced the plastic deformation under the deployment pressure. As can be seen from the figure that the stresses were well distributed over the entire slotted tube. Apart from that the region where the plastic deformation occurred was larger compared to the slotted tube under deployment pressure of 2 MPa. Nevertheless, the region where the maximum stresses occurred was considerably small. The higher stressed region had become more concentrated.

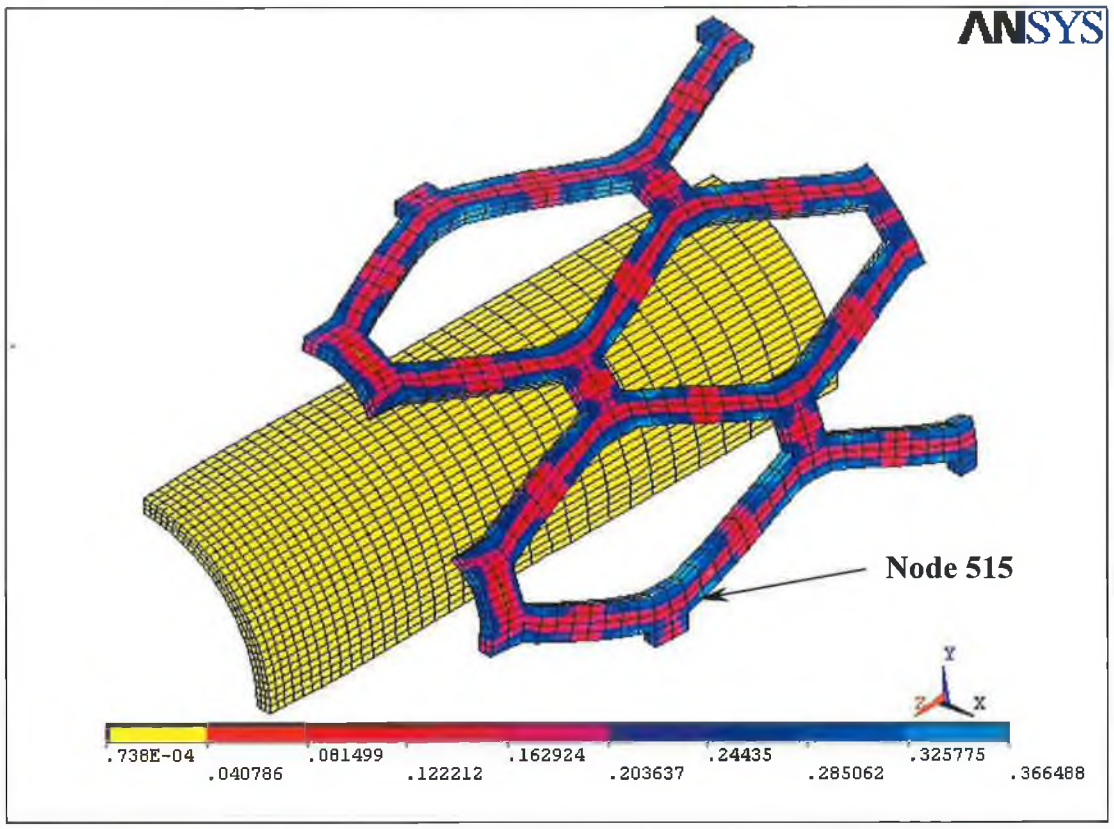

Figure 5.26: Residual stress in the deformed slotted tube by loading curve 2

As can be seen from the figure as well the maximum stressed regions were found slightly off the centre of the slots. This is unlike the slotted tube under pressure deployment of 2 MPa where the highest stressed regions were evenly distributed over the centre of the slots. In spite of the maximum stressed region somewhat off the centre of the slots the four corners of the slots remained as the main location where the highest stress occurred. The maximum stress developed in this region was

approximately 366 MPa. In comparison with the ultimate tensile strength of the material, the slotted tube was stressed up to 71% of the value i.e. 19% more than deployment pressure of 2MPa.

Figure 5.27 shows the development of stresses in x, y, z direction and von Mises stress at node 515 of element 1059. Element 1059 is representative of areas where maximum stresses occurred. Owing to the symmetry, other similarly located elements in the slotted tube could also yield maximum values very close or greater to that of element 1059. The choice of element 1059 was based on the maximum value over the total simulation time.

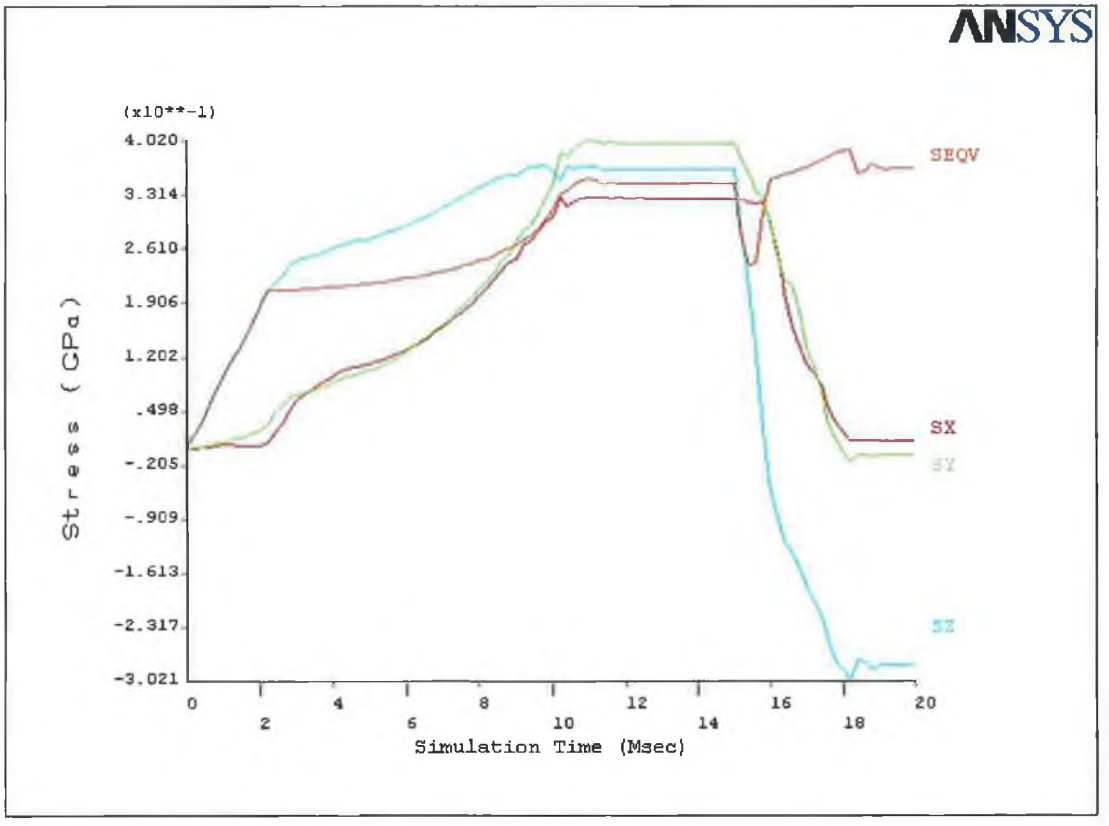

Figure 5.27: Development of stresses in node 515

The different history of deformation due to different deployment pressure can be seen more clearly by observing the development of stress at some nodes in the slotted tube. In this case the node 515 was selected since it was the location where the maximum stress occurred. It was noticed that the stresses in all three directions continued to be in tensile stress state throughout the inflation process. The stress in z

direction seemed to be developed a lot quicker than the other two directional stresses. It is also clearly seen that the influence of deployment pressure dominated the stress in z direction, which enormously affected the deformation of the slotted tube. The stress in axial direction that initiated the onset of the slotted tube deformation caused by the deployment pressure also triggered the yield point of the slotted tube material. Different location of node picked gives different information on the amplitude of the deformation based on that location. For node 515 the stress in z direction changed in mode from tension to compression when the pressure was released. This is unlike the selected node in the first simulation, which the stress in z direction changed mode from compression to tension when the pressure was released. Therefore it is fair to state that the axial stress switches mode either from tension to compression or from compression to tension without the interference of the location of the node. Stresses in x and y directions developed pretty much in the same magnitude throughout the dilatation process except that the stress in y direction settled on the higher stress level when the equilibrium state was reached.

Four different stages of response during the simulation of the slotted tube were detailed in Figure 5.28 to Figure 5.31. Figure 5.28 shows the distribution of stress at maximum deployment pressure by initial ramp loading. The simulation time at that time was 10 milliseconds and the pressure was 2.5 MPa. The stress achieved at that time was found to be approximately 312 MPa.

Figure 5.29 shows the distribution of stress in the slotted tube when the steady state response was reached. The maximum stress achieved at that point of time was approximately 349 MPa. Literally, the maximum stress should be obtained when the maximum pressure is reached in the initial ramp loading. Somehow, it was noticed that the stress kept increasing despite the fact that the maximum deployment pressure was reached. The von Mises stress achieved at that time was somewhat lower than in the steady state response. This may be due to dynamic effects as the LS-DYNA program provides the dynamics (inertia) term of the solution. It is usually difficult to reduce the value of inertia to exactly zero. It can, however, be reduced sufficiently to give good quasi-static solutions.

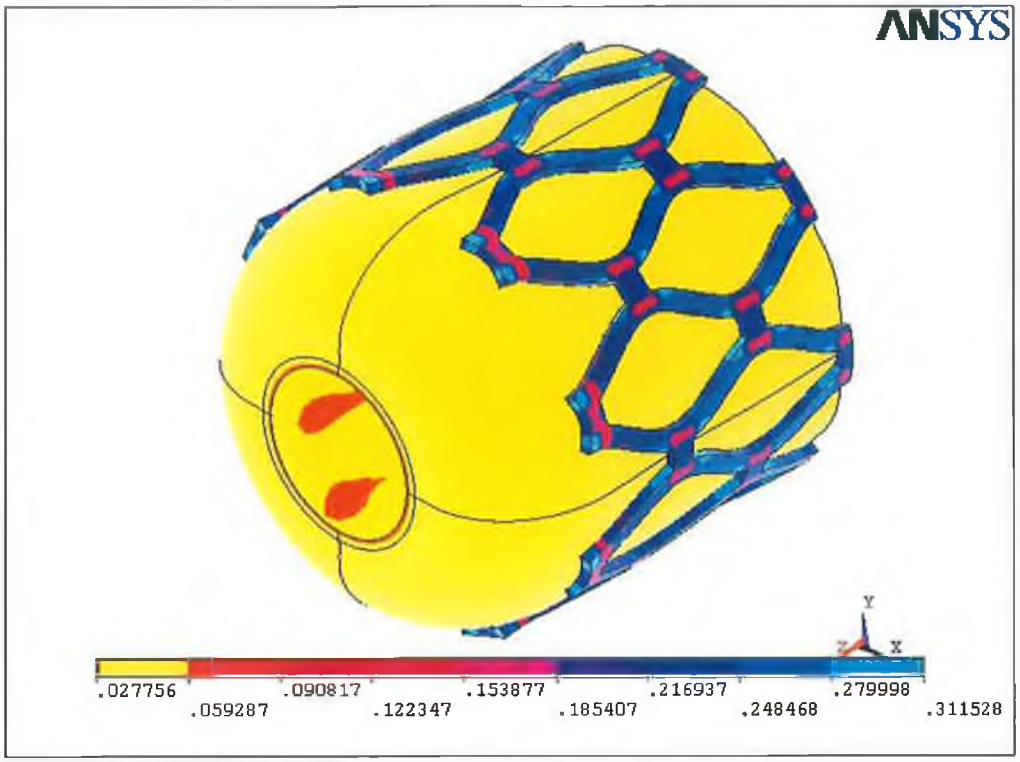

Figure 5.28: Initial ramp loading by deployment pressure 2.5 MPa at time 10 msec

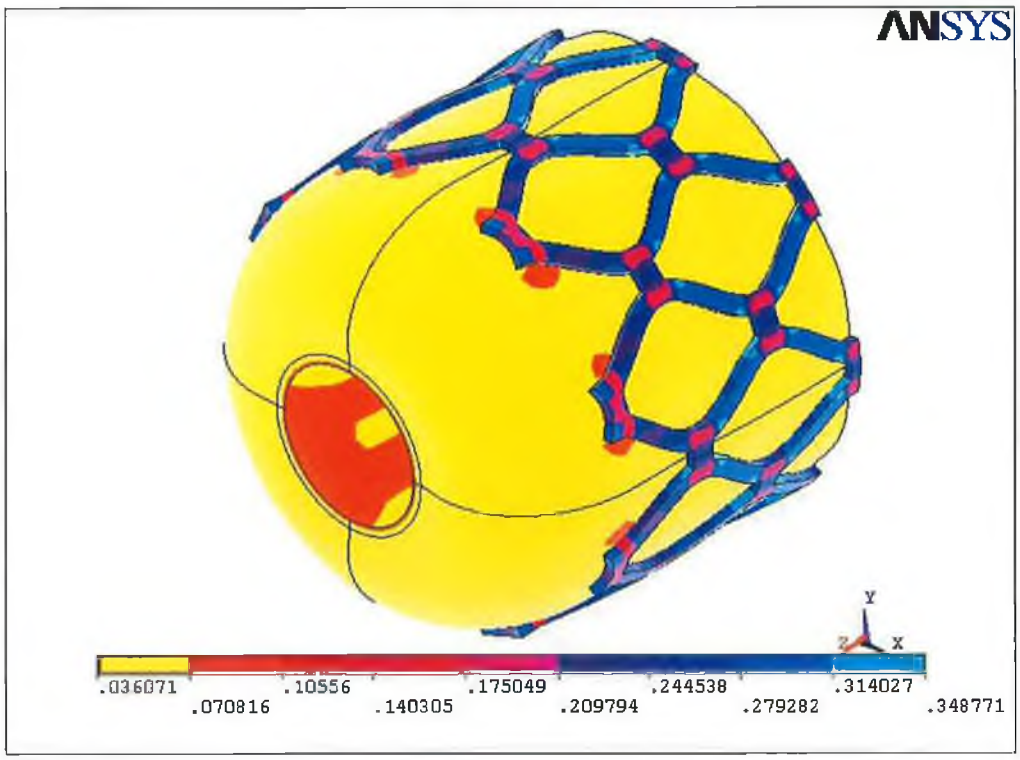

Figure 5.29: Steady state response of the slotted tube at time 15 msec

Figure 5.30 shows the residual stress in the slotted tube when the balloon was just losing contact with the slotted tube. The simulation time at this point was 18.01 milliseconds. As can be noticed that the residual stress at this point of time was the highest compared to the three other responses. The stress level at this time was approximately 388 MPa. As explained before higher stress level were expected here because the stresses were decreased for short period of time and then increased again as the pressure released due to the mode switched in the axial stress component. Once the pressure was released, a spring-back type condition (dynamic) exists whereby the slotted tube had been pre-stressed and then released.

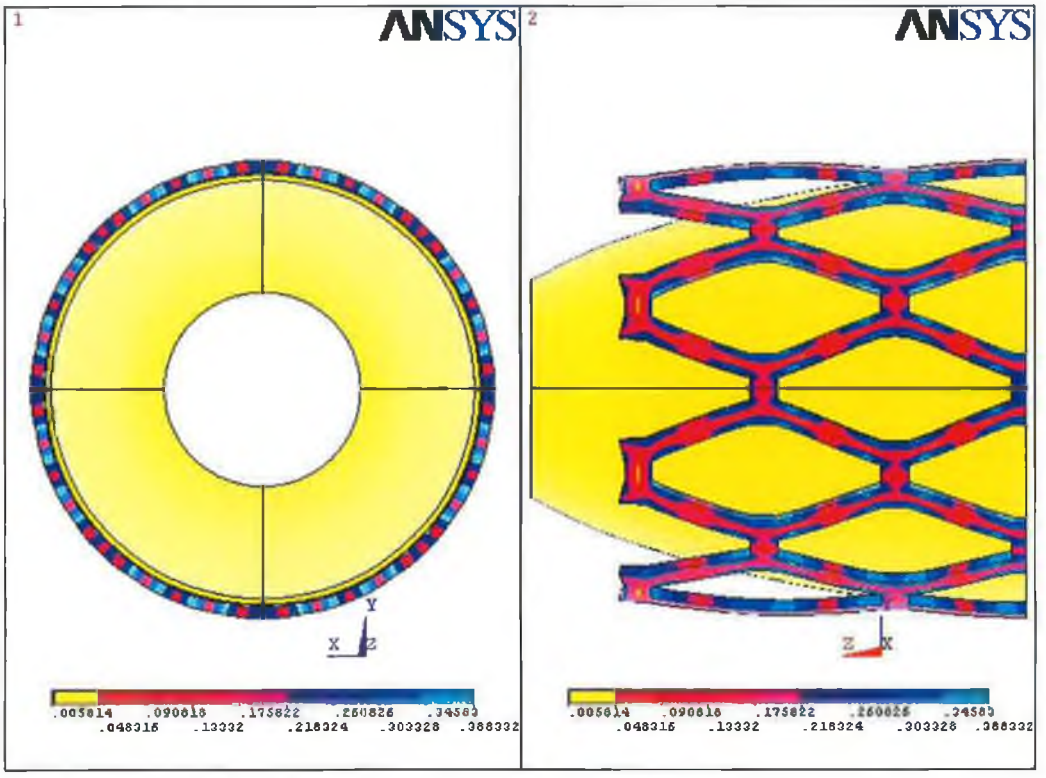

Figure 5.30: Separation of the balloon from slotted tube at time 18.01 msec

Figure 5.31 shows the residual stress in the slotted tube when deploying pressure was released to zero. The slotted tube was once again reached its equilibrium state when the balloon was completely separated from the slotted tube. This time the deployment pressure no longer affected the deformation of the slotted tube. The material of the slotted tube was fully responded to the deploying pressure and experienced plastic deformation. The highest residual stress remained in the slotted

tube at this stage was ranging from 326 MPa to 367 MPa. Once again, the higher stress regions were noticed to be located at the centre of the slots as well as the corner of the slots. One particular point was noticed different from the deployment pressure of 2 MPa was that the stress level at the end of the slotted tube was found lower than the centre part or the body strut of the slotted tube. This is unlike the lower deployment pressure whereby the stress level was rather higher near the ends of the slotted tube.

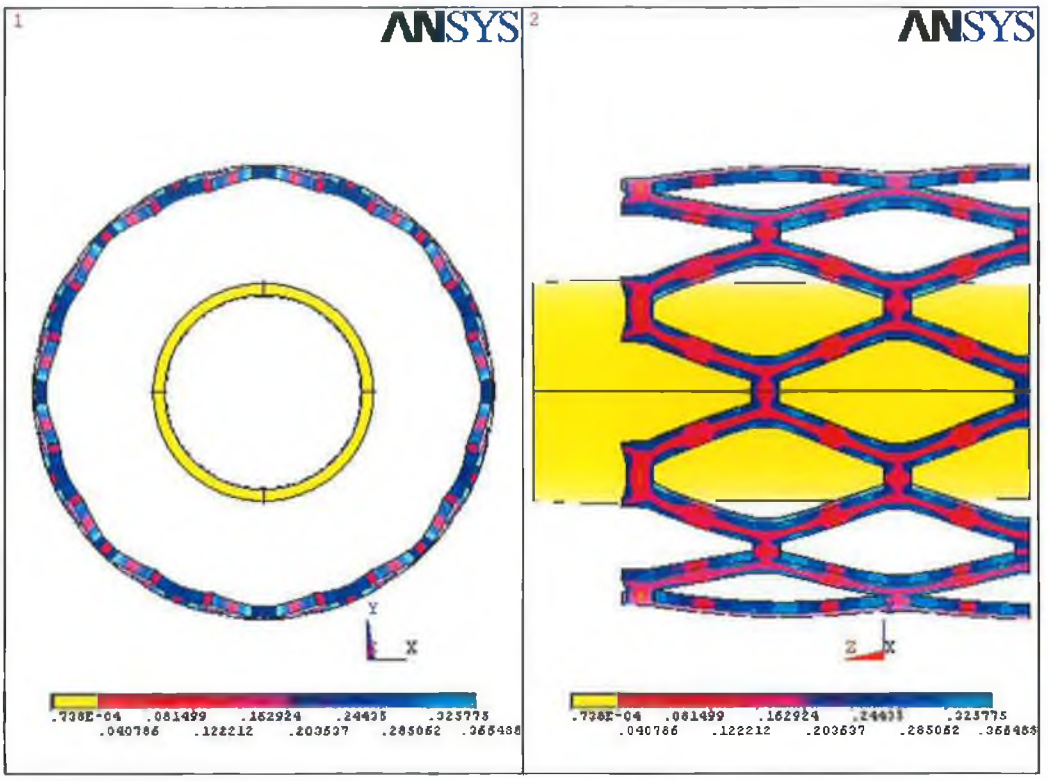

Figure 5.31: Deformation of the slotted tube at simulation time 20 msec

a) Deployment pressure vs. displacement

Figure 5.32 shows the magnitude of the slotted tube expansion in radial direction under deployment pressure of 2.5 MPa. This graph shows the expansion of slotted tube diameter with the deployment pressure in which greater deployment pressure generates greater diameter. It is noticed that the slotted tube expanded its diameter in radial direction at a faster rate after 2 MPa. The slotted tube diameter experienced a massive expansion considering that only an extra deployment pressure of 0.5 MPa was added on top of that 2 MPa. Therefore, it is fair to say that only a small

increment of deployment pressure is needed to achieve a massive increment in slotted tube diameter. The maximum radial expansion of the slotted tube achieved under this simulation was approximately 17.11 mm, which gives a total of 57.27 mm in diameter. In short, the slotted tube has expanded up to 149% i.e. 1.5 times from its original diameter.

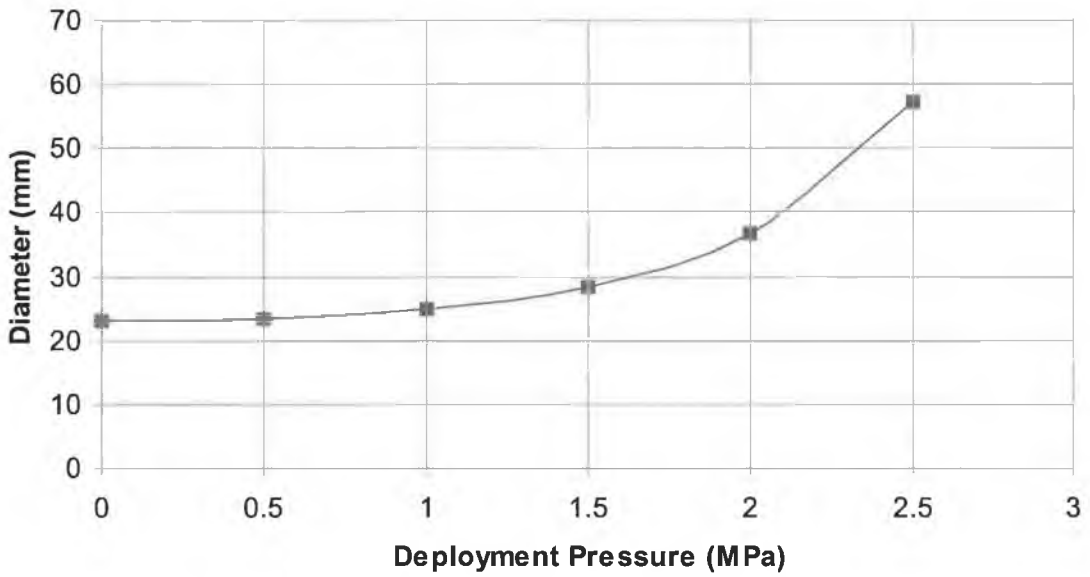

Figure 5.32: Expansion of slotted tube with deployment pressure

b) Elastic Recoil

Figure 5.33 shows the elastic recovery of the slotted tube when the pressure is released. The diameter of the slotted tube before releasing the pressure was 57.27 mm. The diameter of the slotted tube after the pressure was released was found to be 45.87 mm. The slotted tube diameter was noticed to have shrunk by 20% from the diameter obtained during the maximum deployment pressure. In spite of obtaining the higher expansion rate, it is noted that the slotted tube under this deployment pressure has shrunk 8% more in comparison with the first simulation. However, the magnitude of elastic recovery always develops at a slower rate in the beginning of the deflation process.

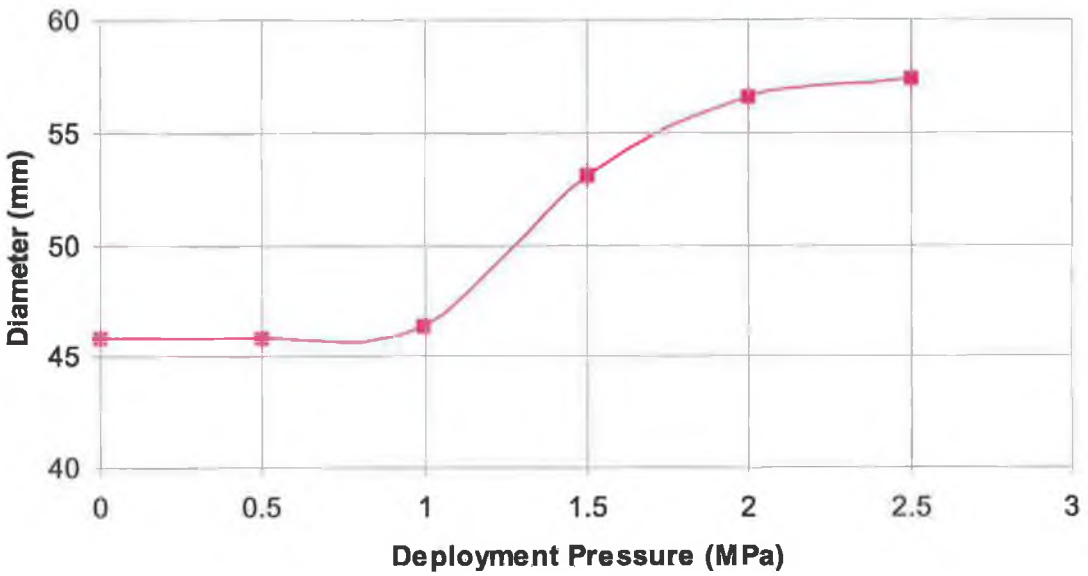

Figure 5.33: Elastic recoil of the slotted tube

c) Slotted tube foreshortening

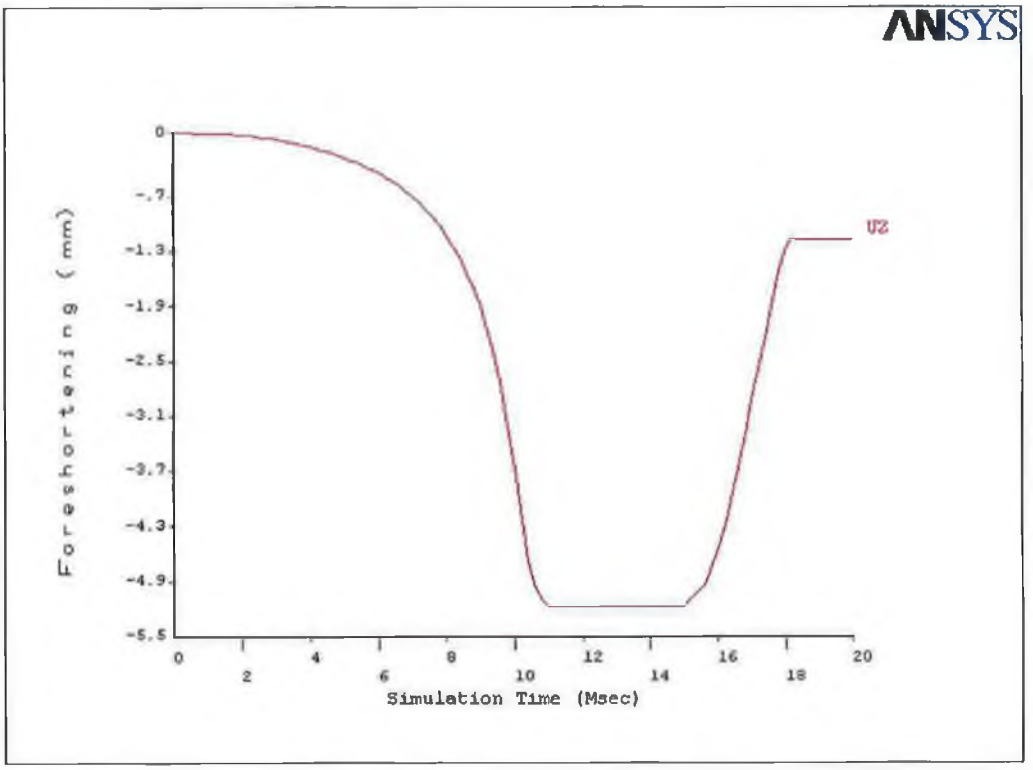

Figure 5.34: Foreshortening of the slotted tube with simulation time

Figure 5.34 illustrates the magnitude of foreshortening with simulation time. As can be seen from the graph that the foreshortening increases with time during the inflation process but decreases with time during the deflation process. As expected the foreshortening develops slowly at the onset of the dilatation process. It soon develops swiftly as the pressure increases. The maximum amount of foreshortening achieved resulting from the maximum deployment pressure was found to be 5.176 mm. However, the magnitude of foreshortening reduced to only 1.17 mm when the balloon was deflated. The percentage of foreshortening from the original length of the slotted tube after the deflation of the balloon was approximately 2.7%.

Figure 5.35 shows the ultimate geometry of the slotted tube obtained when the balloon was completely deflated. The regions of plastically deformed are more uniform even though the distinct local plastic deformation can be observed mostly along the edges of the body struts. Comparing to the lower deployment pressure it was found that the geometry of the slotted tube here was more uniformly expanded after the balloon was deflated. The end of the slotted tube tended to recover more resulting the slotted tube end leaning towards the inner direction of the tube.

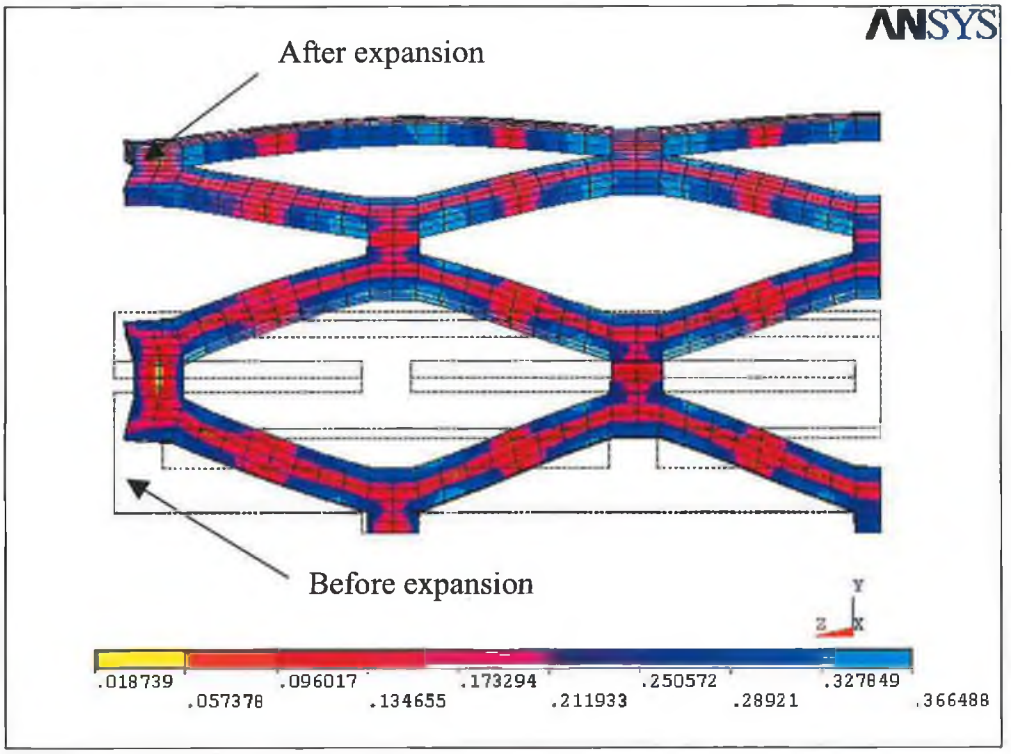

Figure 5.35: The geometry of the slotted tube before and after the expansion

5.2.3.3 Deployment pressure of 2.8 MPa

This simulation was implemented with the highest deployment pressure i.e. 2.8 MPa. It was believed from the tested simulation that this deployment pressure could expand the slotted tube to its ultimate limits just before failure from the slotted tube material. Load curve 3 from Figure 5.14 explains the load history of the pressure deployed. Figure 5.36 shows the residual stress distribution in the deformed slotted tube after deflation of the balloon by loading curve 3. Apart from the obvious geometry changes of the slotted tube compared to the previous two lower deployment pressures, the slotted tube experienced a rather uniform plastic deformation over the entire body of the slotted tube. The location of the highest stressed regions does not change despite the changes in the final deformation of the slotted tube.

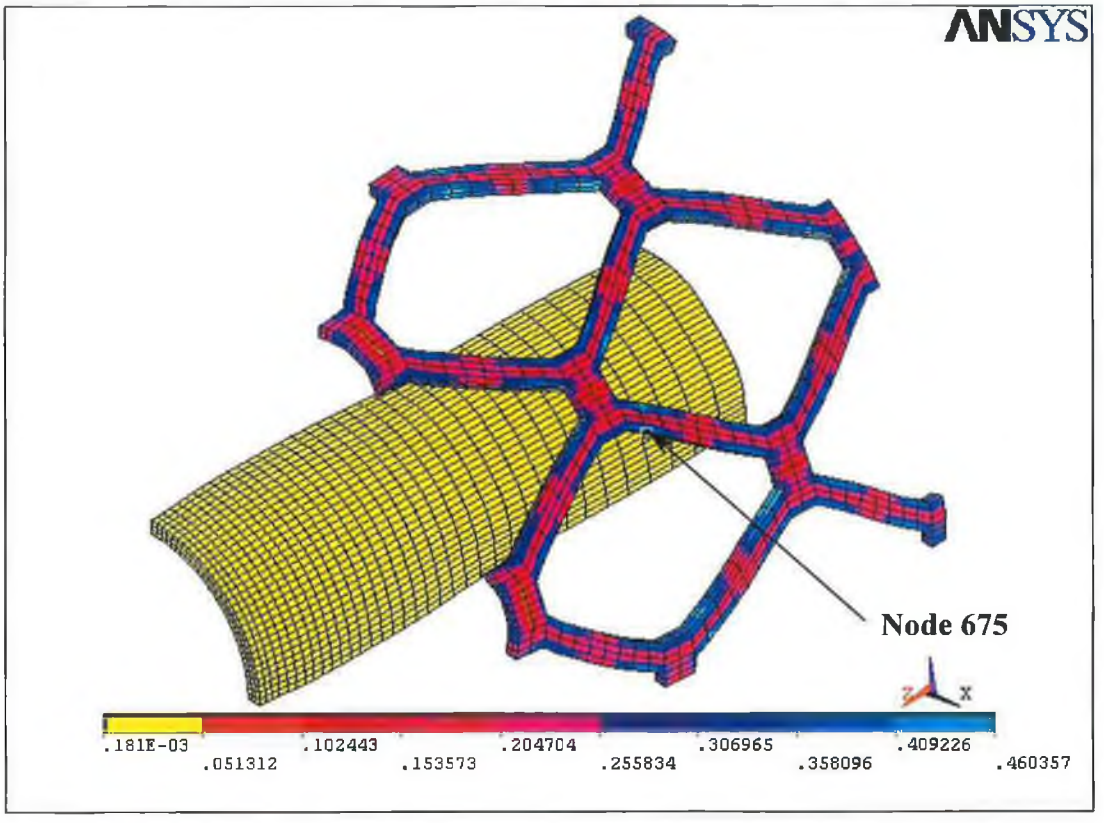

Figure 5.36: Residual stress in the deformed slotted tube by loading curve 3

Like deployment pressure of 2.5 MPa, the distribution of highest stressed region was found slightly off the centre of the slots. There was no alteration in the location of

higher stressed region except that the stress level in this region was much higher. The maximum stress developed in this region was approximately 460 MPa. The slotted tube was stressed up to 89% of the ultimate tensile strength of the material i.e. 37% more than deployment pressure of 2 MPa.

Figure 5.37 shows the development of stresses in x, y, z direction and von Mises stress at node 675 of element 811. Element 811 in this case is representative of areas where maximum stresses occurred over the total simulation time. The history of stress development due to different node location in this simulation was obviously different from the previous simulations. First, the stress in z direction increased in the compressive manner and decreased again before it reached the steady state response.

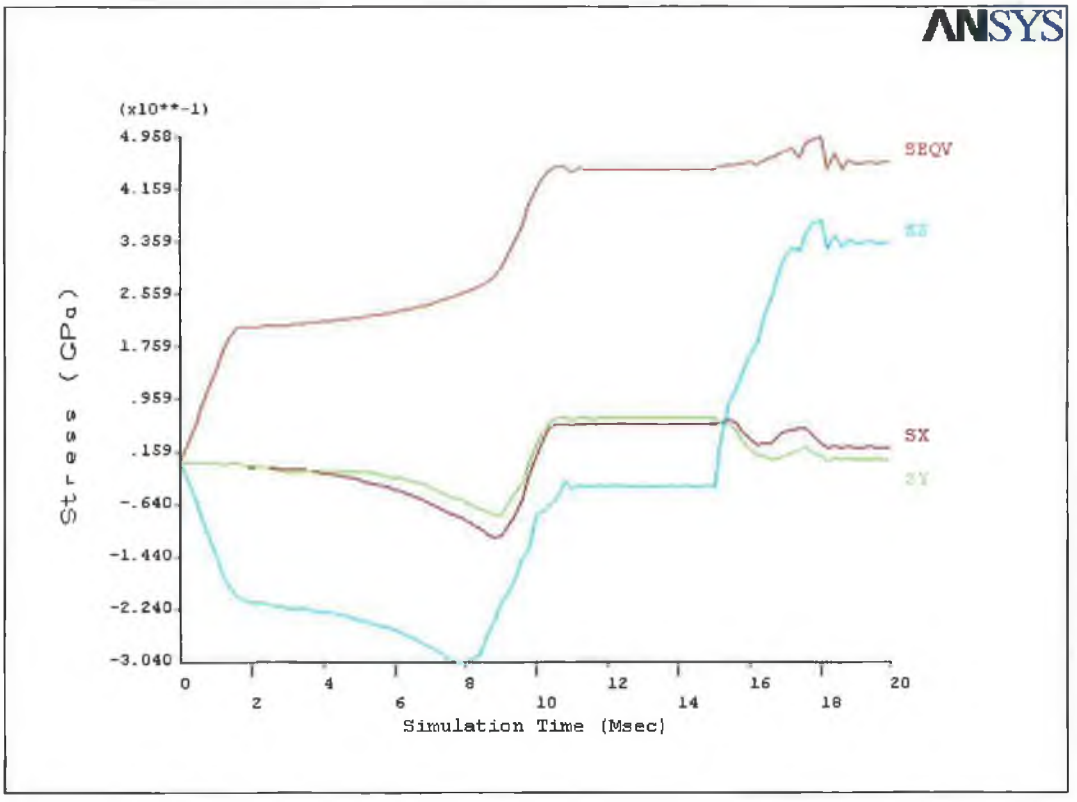

Figure 5.37: Development of stresses in node 675

This indicates that the axial compressive stress had become smaller that leading to the mode switch from compression to tension despite the increment in deployment pressure. If any component stress that undergoes mode switch, the relevant location of the structure will first go through the alteration i.e. compression to tension. This is

obvious when the stress in x and y direction switched from compression to tensile stress before the pressure was released. Nevertheless, the axial stress still dominates over the other two directional stresses. During the deflation process the stress in axial direction continued to switch from compressive to tensile stress. Releasing the pressure quickly will cause oscillation in the von Mises stress. One way of preventing this is to add system damping to the simulation. As can be seen from the figure, oscillation of the von Mises stress was reduced to the desired quasi-static value when system damping was added. Stresses in x and y direction decreased for a short period of time at the beginning of the deflation. As the deflation continued, the stresses continued to increase and then decrease again before it settled down in the tensile mode.

Figure 5.38 to Figure 5.39 detail the four different stages of response during the simulation of the slotted tube by load curve 3. Figure 5.38 shows the distribution of stress at maximum deployment pressure by the initial ramp loading. The simulation time was at 10 milliseconds and the stress generated at that time was approximately 423 MPa. Obviously, the stress achieved here was higher than the previous two lower deployment pressures. The stress was found to have increased by 4.5% when the steady state response was reached as shown in Figure 5.39.

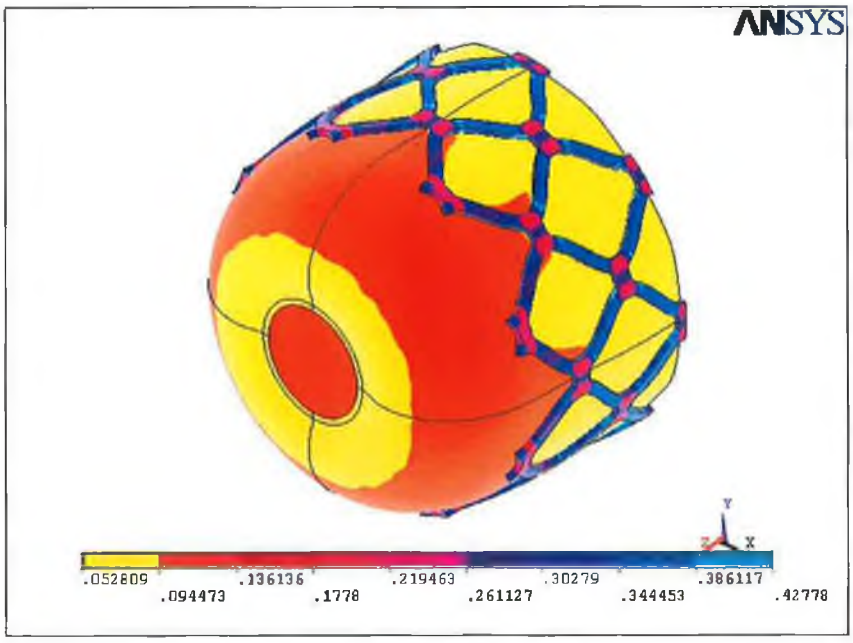

Figure 5.38: Initial ramp loading by deployment pressure of 2.8 MPa at time 10 msec

The small increment of stress engendered here was nothing but due to the dynamics effect. Basically, the material of the slotted tube was given time to fully respond itself to the load. When the material was responded to the applying deployment pressure, the von Mises stress was also settled down to a constant stress level. One obvious point to be recognised when the equilibrium state was achieved is the stress distribution in the balloon. The stress contour shown in Figure 5.39 indicates that there was no erratic stress pattern in the region near the end of the balloon. The erratic stress pattern seemed to have been improved when the equilibrium was reached.

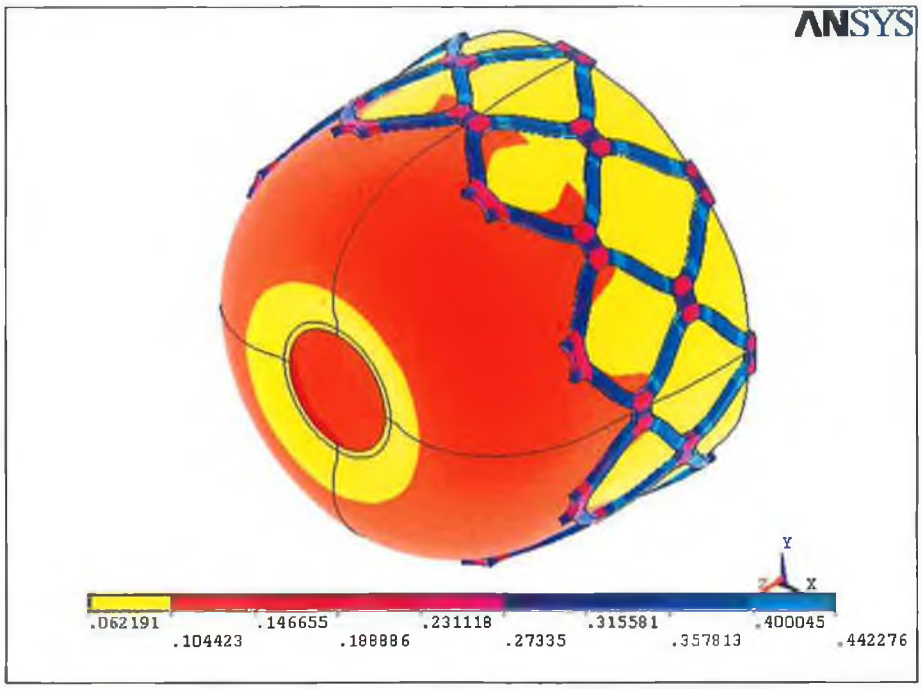

Figure 5.39: Steady state response of the slotted tube at time 15 msec

Figure 5.40 shows the von Mises stress distribution in the slotted tube when the balloon was separated from the tube. The stress at this point of time was 485 MPa. As explained before, the increment of stress at this stage was purely because of the recovery action of the slotted tube. The recovering action continued to take its time to reach the equilibrium state as the balloon was deflating. As the balloon was completely deflated from the slotted tube, the slotted tube is now reached the final deformation as shown in Figure 5.41. The maximum residual stress at this point was 460 MPa.

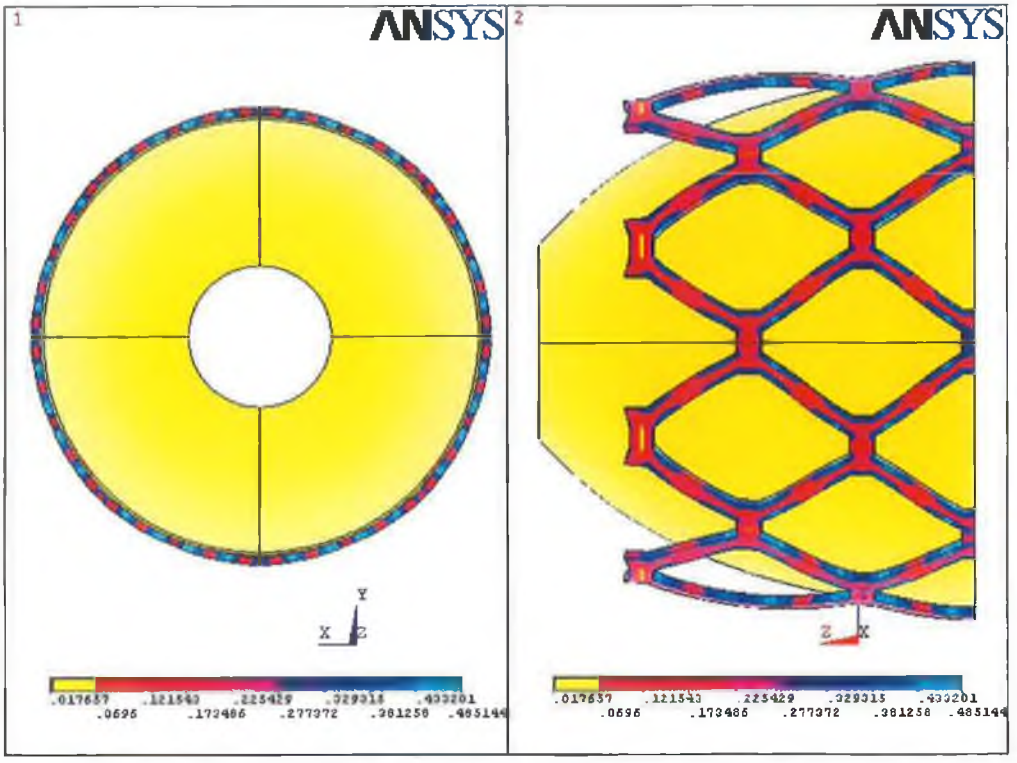

Figure 5.40: Separation of the balloon from the slotted tube at time 17.8 msec

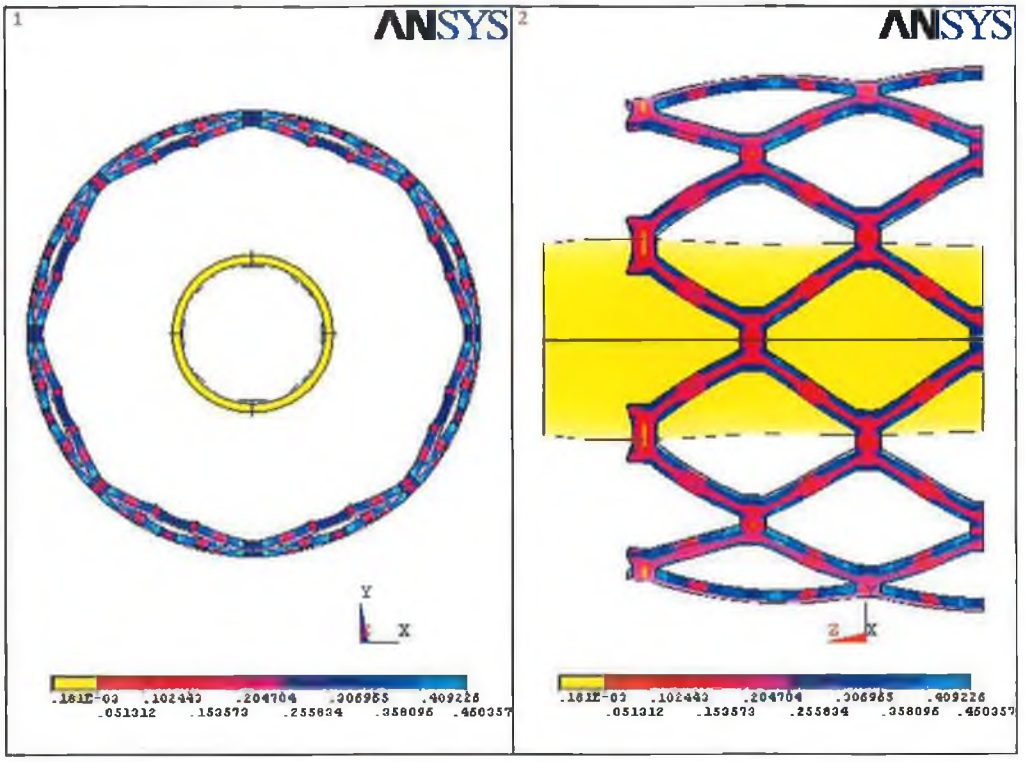

Figure 5.41: Deformation of the slotted tube at simulation time 20 msec

a) Deployment pressure vs. displacement

Figure 5.42 shows the magnitude of the slotted tube expansion in radial direction under deployment pressure of 2.8 MPa. The diameter of the slotted tube increased slowly as the pressure increased. However, it was noticed that the diameter expanded in a quicker rate when the deployment pressure of 2 MPa was reached. This shows an agreement with the magnitude of the diameter expanded as in the previous simulation i.e. 2.5 MPa. Therefore, a conclusion can be drawn in which any deployment pressure higher than 2 MPa will result in higher rate of radial expansion. Since the slotted tube expansion is a volume controlled process, it might as well to say that less pressure is required to expand the slotted tube when a certain level of expansion is reached. This information is particularly useful and important as the excessive deployment pressure even with a slight increment may result in a failure of the slotted tube.

The maximum radial expansion of the slotted tube achieved in this simulation was 25.7 mm. This gives a total of 74.4 mm in diameter at maximum pressure deployment. In this case, the slotted tube has expanded up to 224% i.e. approximately two and a quarter times from its original diameter.

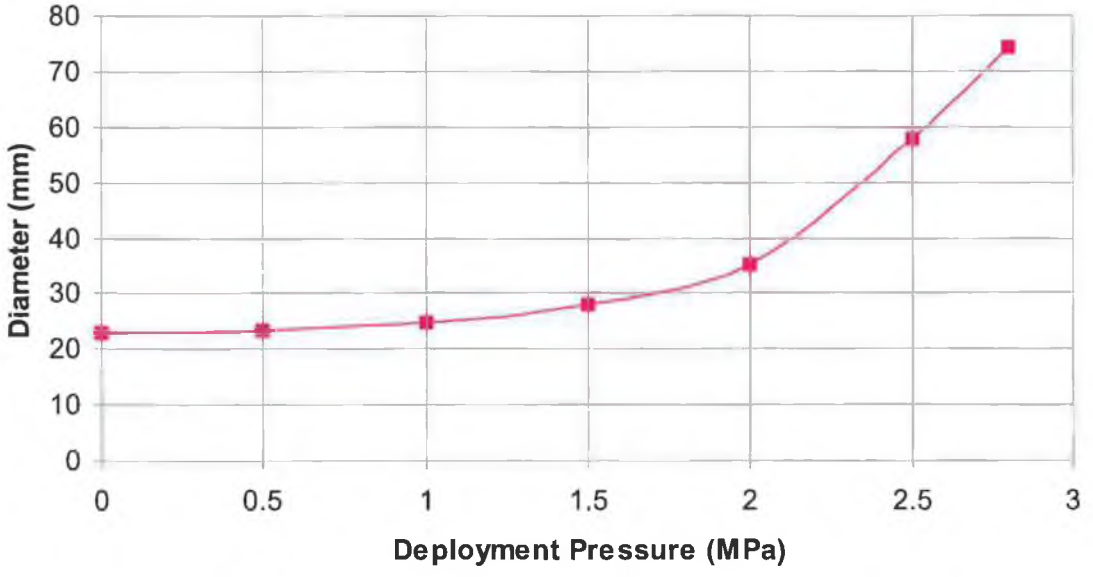

Figure 5.42: Expansion of slotted tube diameter with deployment pressure

b) Elastic recoil

Figure 5.43 shows the elastic recovery of the slotted tube when the pressure is released. The diameter of the slotted tube before releasing the pressure was 74.4 mm. The diameter of the slotted tube after releasing the pressure was found to be 63.17 mm. The slotted tube diameter was therefore to have shrunk 15% from the diameter obtained during the maximum deployment pressure. This is interesting because it was initially thought that the slotted tube could have shrunk more since higher pressure was deployed. However, it was soon found out that the location of the node selected did not represent the area where maximum shrinkage was occurred. The ultimate deformation caused by the different level of deployment pressures had affected the final structure of the slotted tube when the balloon was deflated. In the first simulation, the slotted tube experienced the maximum elastic recovery in the centre part of the structure. However, this is not the case as the maximum elastic recovery occurred in this simulation was found to be located at the ends of the slotted tube. As a result, the magnitude of shrinkage in the middle part of the slotted tube was less than the shrinkage at the end of the slotted tube.

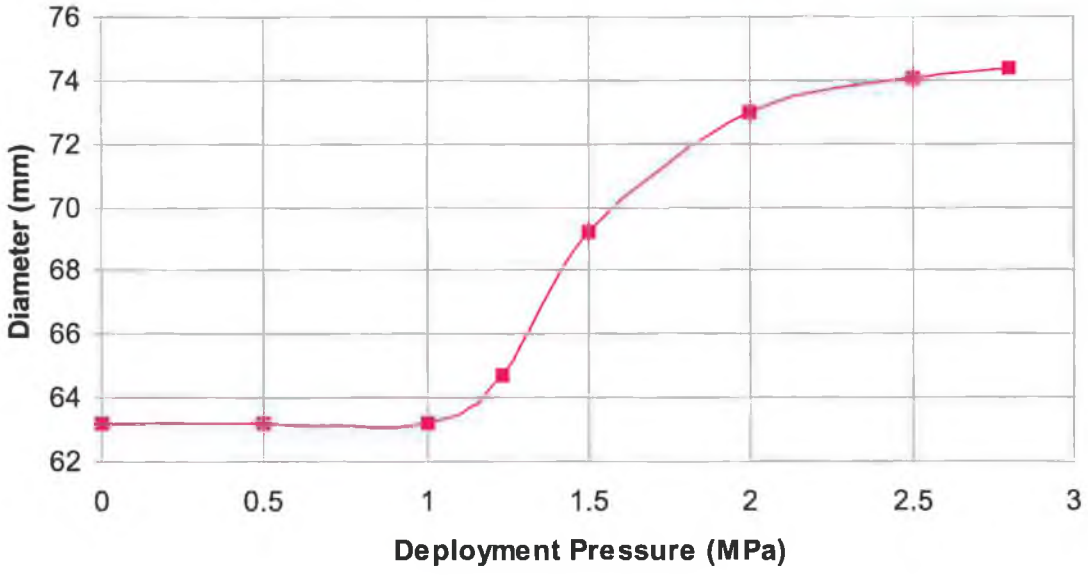

Figure 5.43: Elastic recoil of the slotted tube

c) Slotted tube foreshortening

Figure 5.44 illustrates the magnitude of foreshortening with simulation time by load curve 3. As previous two simulations, the foreshortening in this simulation increases with time during the inflation process and decreases with time during the deflation process. The total amount of foreshortening was found to be 8.29 mm at maximum pressure deployment i.e. 2.8 MPa. The amount of foreshortening reduced to 1.97 mm when the balloon was completely deflated. The reduction of the foreshortening was because of the increased and mode switch in the z stress component. The percentage of foreshortening from the original length of the slotted tube after the deflation of the balloon was approximately 4.5%.

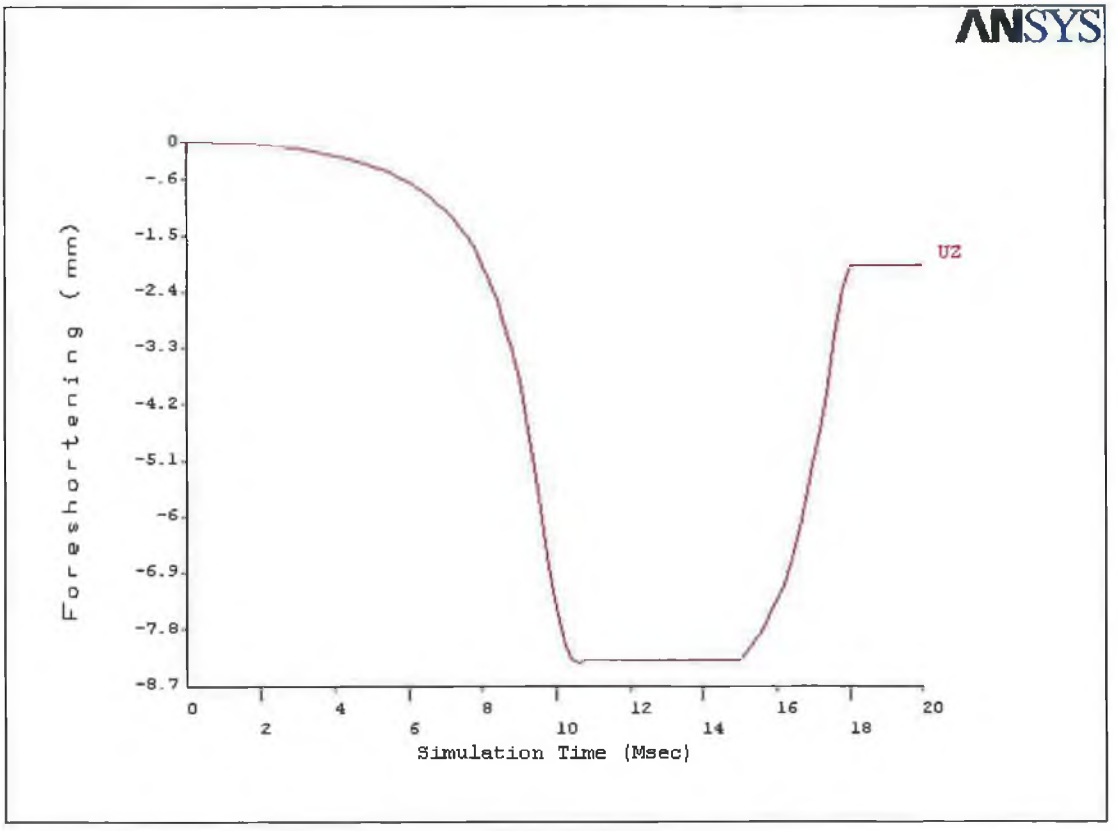

Figure 5.44: Foreshortening of the slotted tube with simulation time

Figure 5.45 shows the geometry of the slotted tube before and after the expansion when the balloon was deflated. It is noticed that the ultimate deformation of the slotted tube was not as uniform as in second simulation despite the higher expansion

in radial direction was obtained. The structure of the slotted tube was found to have bended more especially approaching the end of the slotted tube. The slotted tube was bending towards the inner direction of the tube. Highest residual stress area could still be clearly seen that is located at the corner of the slots. The lowest residual stress area was also spotted to have located near the middle of the bridging struts at the end of the slotted tube.

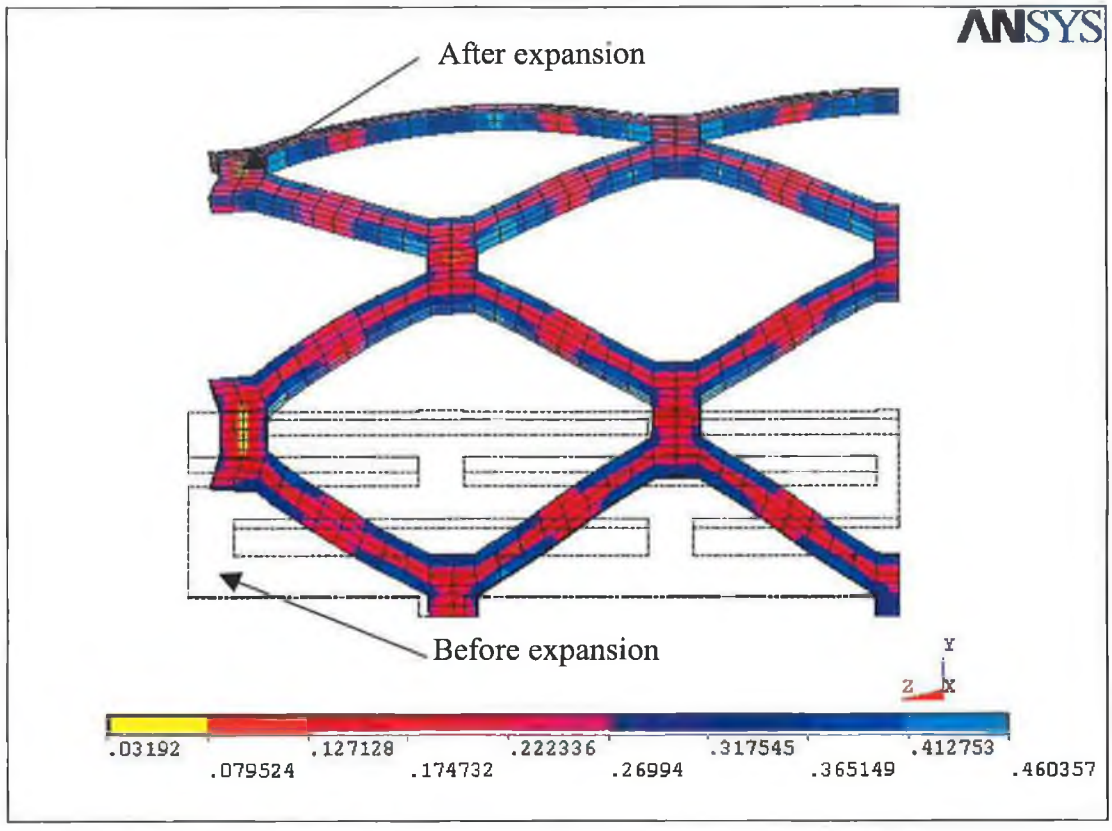

Figure 5.45: The geometry of the slotted tube before and after the expansion

5.3 Analysis of Balloon Length on Slotted Tube Expansion

The combination of inflation pressure and balloon size is believed to have affect on the vessel-wall damage and may represent a factor influencing restenosis following balloon angioplasty [105]. It is understood from the previous simulations that the deployment pressure could affect the uniformity of the ultimate structure of the slotted tube. Therefore, this section is concerned with investigating the influence of the balloon length on the slotted tube expansion.

5.3.1 Modelling

The model utilised in this section was identical to that of section 4.3 except different balloon lengths were modelled. The length of the balloon was modified in such a way that magnitude of the deformation of the slotted tube could be clearly observed and the different range of the deformation could be covered. The same geometry of the slotted tube was utilised in this simulation (i.e. 25.4 mm outer diameter and 23 mm inner diameter with 86.8 mm in length). The slotted tube was meshed with eight node explicit solid brick elements and material properties of Stainless Steel 304 were used. A bi-linear elasto-plastic material model was assumed for the slotted tube material.

The thickness of the balloon remained the same as previous section i.e. 1.2 mm with 23 mm for the outer diameter of the balloon. A hyperelastic material model was chosen to represent the balloon. A two parameter Mooney-Rivlin model with constants C(10) = 0.103176E-02 and C(01) = 0.369266E-02 was used for all three simulations. The material properties of the balloon remained unchanged (i.e. polyurethane rubber).

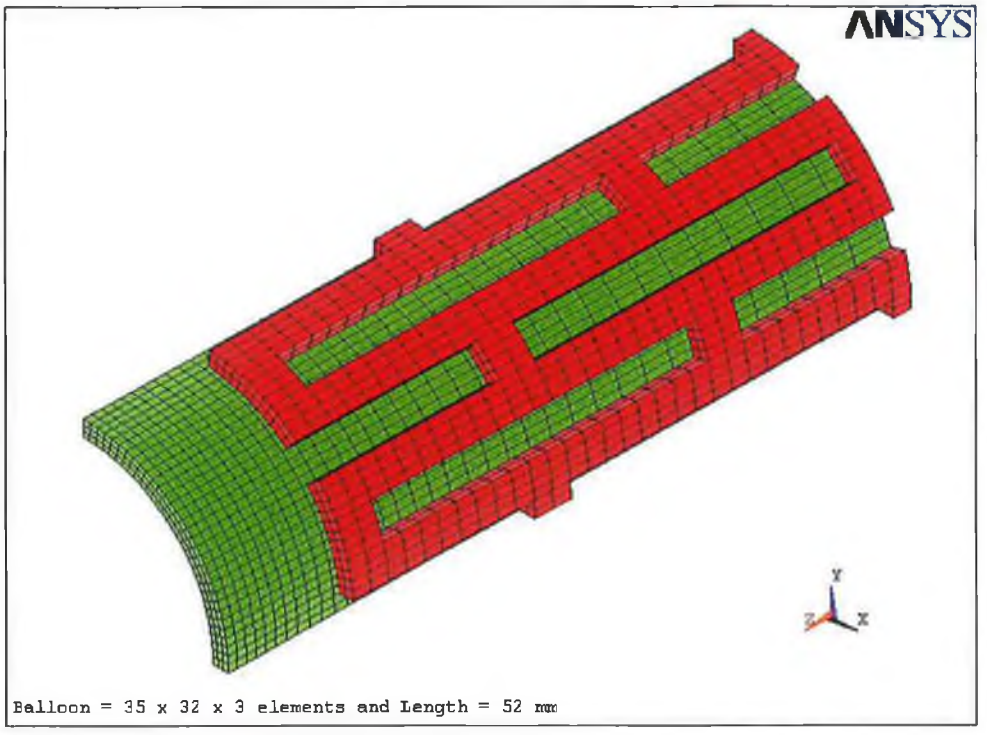

Figure 5.46: One eight of the finite element model with balloon length equal to 52 mm

Figure 5.46 shows the finite element model of one eighth of the slotted tube and the balloon. The length of the balloon used here was 104 mm, which was 17.2 mm longer than the slotted tube. The balloon consists of 3360 elements. It was discretised by 35 elements along its length and 32 elements in circumference with 3 elements across the thickness. A total of 4464 elements describe the entire model in this simulation.

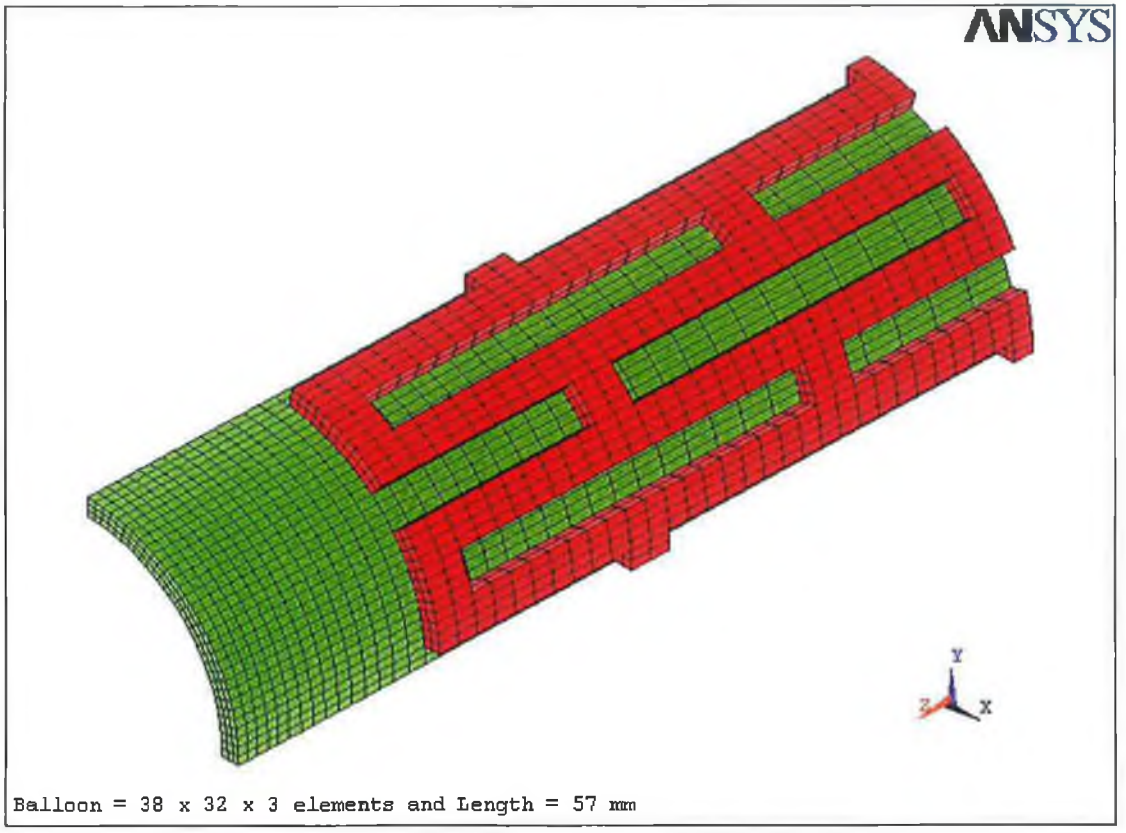

Figure 5.47: One eight of the finite element model with balloon length equal to 57 mm

Figure 5.47 shows the finite element model of one eighth of the slotted tube and the balloon for second simulation. The length of the balloon utilised here was 114 mm i.e. 27.2 mm longer than the slotted tube. The length of the balloon used in this simulation was 10 mm longer than the first model. The balloon consists of 3648 elements. It was discretised by 38 elements along its length and 32 elements in circumference with 3 elements across the thickness. A total of 4752 elements describe the entire model.

Figure 5.48 shows the finite element model of one eight of the slotted tube and the balloon for the third simulation. The balloon modelled here was the longest amongst those three simulations. The length of the balloon used was 124 mm i.e. 10 mm longer than the second simulation. The length of the balloon exposed from the end of the slotted tube was therefore equal to 18.6 mm. The balloon consists of 3840 elements. The balloon was discretised by 40 elements along its length and 32 elements in circumference with 3 elements across the thickness.

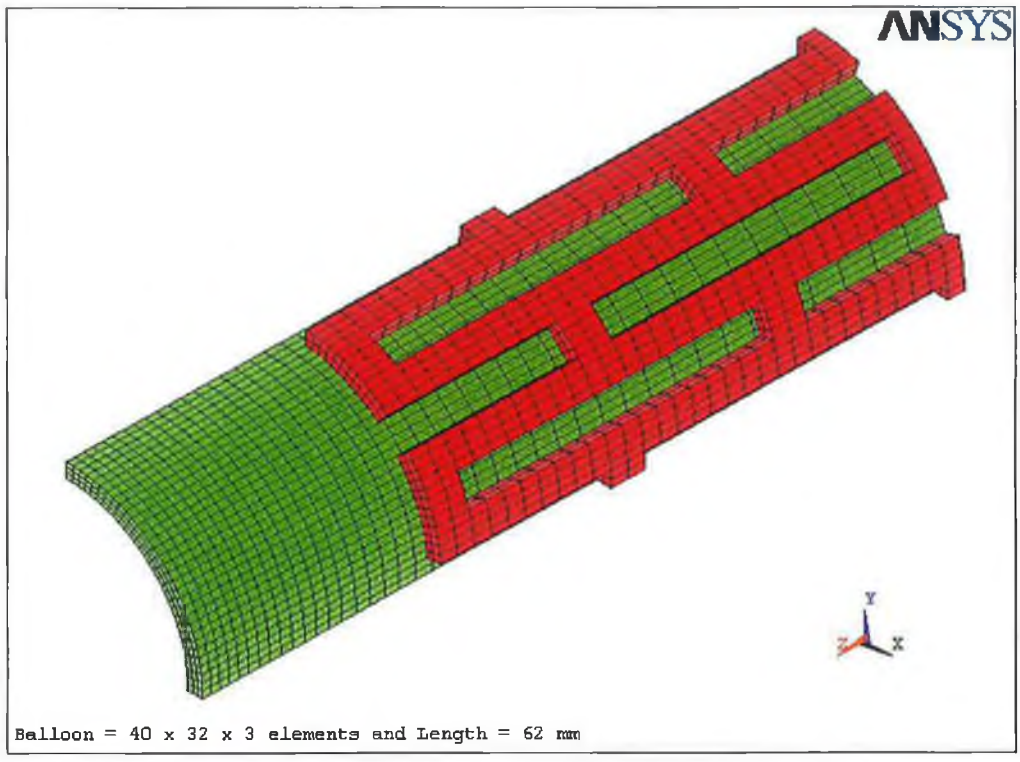

Figure 5.48: One eight of the finite element model with balloon length equal to 62 mm

5.3.2 Boundary Condition, Loading and Solution

The same boundary condition was applied to the slotted tube and the balloon as in previous section. Symmetric boundary conditions were imposed on the appropriate nodes at the symmetry edges. Three different levels of deployment pressure were used in these simulations. A different level of deployment pressures was applied on each the different models of different length of the balloon. The level of deployment pressure was applied in such a way that the slotted tube could reach a certain level of expansion.

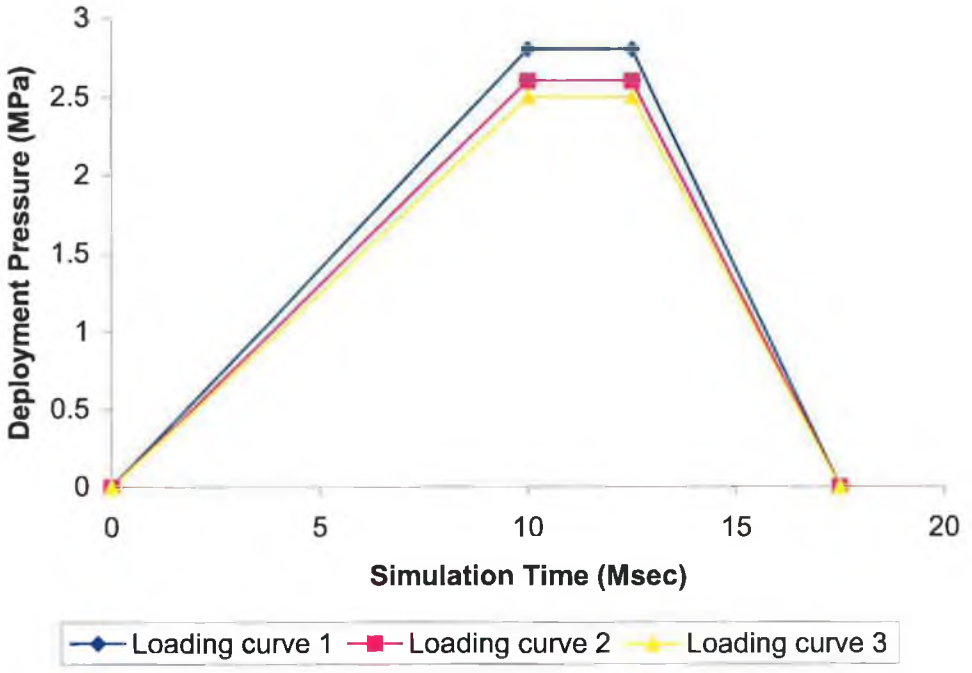

Figure 5.49: Loading curves

The first simulation of the expansion process was carried out on a balloon length equal to 52 mm with a pressure load increasing from 0 to 2.8 MPa. Loading curve 1 in Figure 5.49 describes the load history of the simulation process. The total simulation time was set to be 17.5 milliseconds. The load increased from 0 to 10 milliseconds and then held constant for 2.5 milliseconds and finally reduced to zero at 17.5 milliseconds.

The second simulation of the expansion process was carried out on a balloon length equal to 57 mm with a pressure load increasing from 0 to 2.6 MPa. Loading curve 2 in Figure 5.49 describes the load history of this simulation process. As in first simulation the load here was held constant for 2.5 milliseconds when the maximum pressure was reached. The load was gradually decreased to zero during the simulation time 12.5 to 17.5 milliseconds.

The third simulation of the expansion process was carried out on a balloon length equal to 62 mm with a pressure load increasing from 0 to 2.5 MPa. Again, the load history of this simulation process is described by loading curve 3 in Figure 5.49.

5.3.3 Result and Discussion

5.3.3.1 Stress analysis

Figure 5.50 shows the development of von Mises stress for each of the slotted tube with different length of balloon models. The graph was plotted from a node that represented the location of the maximum stresses that occurred over the total simulation time. The graph also shows that the von Mises stress in the node developed steadily over the simulation period. It can be seen from the graph that the slotted tube experienced plastic deformation at the earliest stage under the longest balloon (i.e. 62mm). The simulation time at this stage was approximately 1.4 milliseconds. This is unlike the 52 mm and 57 mm length balloon, which the slotted tube only begun to experience plastic deformation during the simulation time of 2 and 2.275 milliseconds respectively. Nevertheless, the stress in the slotted tube for 52 mm and 62 mm length balloons was very much on the same level when the steady state response was reached. The von Mises stress for the 52 mm and 62 mm length balloon at this point of time was approximately 441 MPa and 440 MPa respectively.

However, this was not the case for the 57 mm length balloon in which the stress settled slightly lower than the other two simulations. The stress in the slotted tube for this balloon length at this point of time was approximately 427 MPa. The magnitude of stresses in the slotted tube for 52 mm and 57 mm length balloons developed pretty much at the same rate during the deflation process except that the slotted tube resolved on a higher stress level for the 52 mm long balloon when the zero pressure was reached. As can be noticed from the graph as well that there is a sudden dropping of von Mises stresses which then increasing again during the deflation process. The sudden dropping of the von Mises stresses at the beginning of the deflation process was because the pressure dropped. The von Mises stresses increased again as the pressure continued to drop. This was due to the elastic recovery and the mode switch in the axial stress component either from tension to compression or from compression to tension depending on the location of the node. As can be seen from the graph, the stresses were damped down to minimum in order to avoid a dynamic effect after the separation of the balloon from the slotted tube.

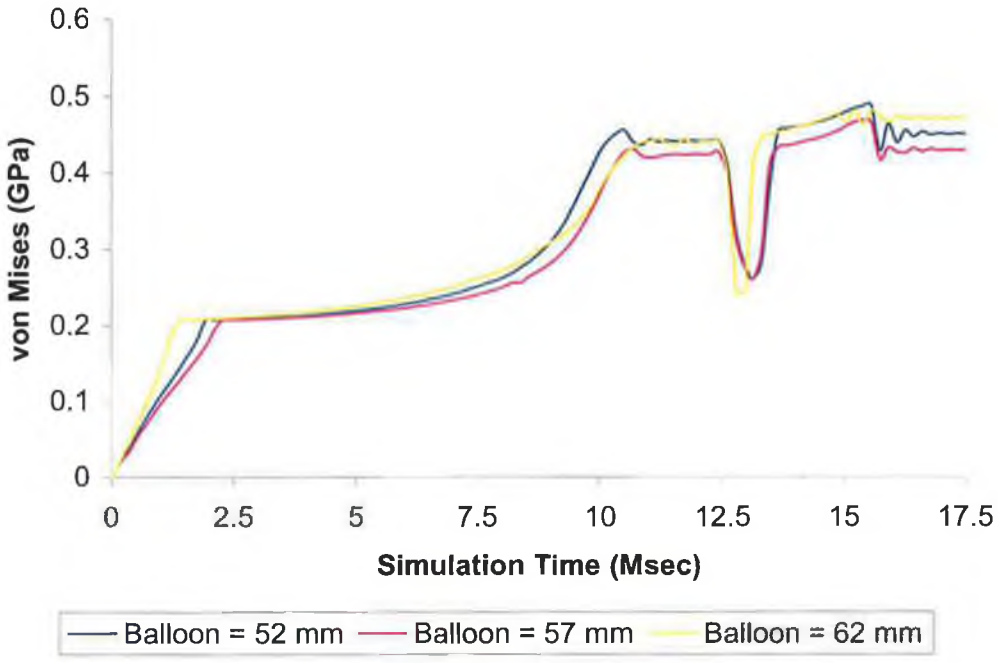

Figure 5.50: Development of stress at maximum stressed node

Figure 5.51 to Figure 5.53 show the residual stress in the slotted tube for 52 mm, 57 mm and 62 mm long balloon respectively when the deploying pressure was released to zero. The maximum residual stress remaining in the slotted tube at that point of time was approximately 461 MPa for 52 mm, 452 MPa for 57 mm and 477 MPa for 62 mm respectively. The residual stress generated from the 52 mm length balloon was not as high as the 62 mm length balloon despite this being where the highest pressure was deployed. The maximum residual stress in the slotted tube for 57 mm length balloon was the lowest compared to the other two balloon lengths. However, the regions of highest stress were found to be located in similar places regardless of the balloon length being used (they were located at the four corners of the slot). Some locations of high stress were also noticed on the other side of the slot corner i.e. between the centres of the slots.

The reason of the higher residual stress level in the slotted tube for 62 mm length balloon was thought to be because of over-expansion during the dilatation process. The end of the balloon expanded more, which forced the end of the slotted tube structure to stretch more as well. Owing to the material properties of the balloon,

which is softer compared to the material properties of the slotted tube, longer balloon length means that lower deployment pressure was needed to induce an expansion.

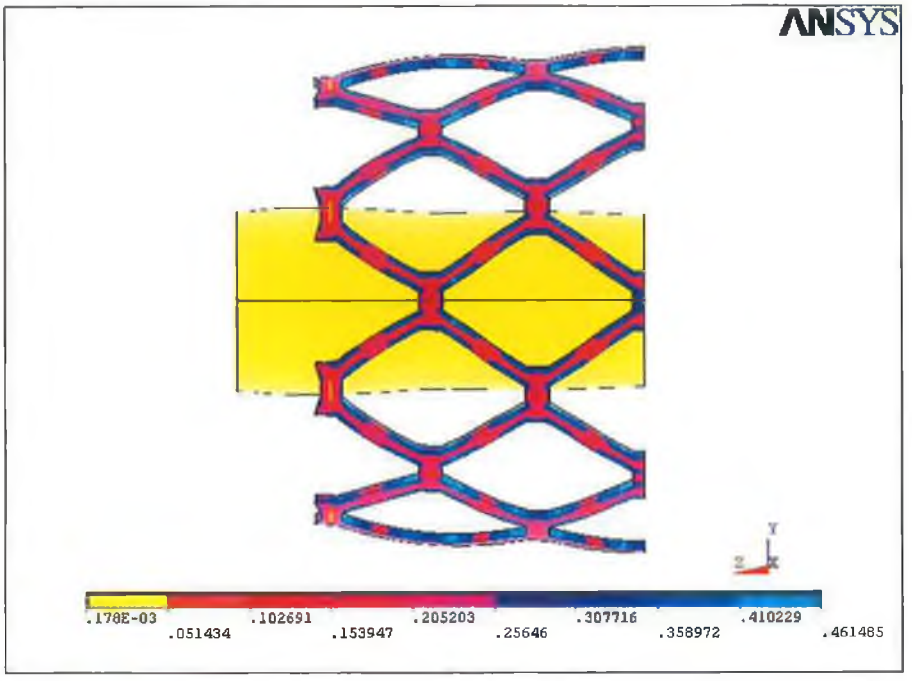

Figure 5.51: Deformation of the slotted tube after deflation by 52 mm balloon

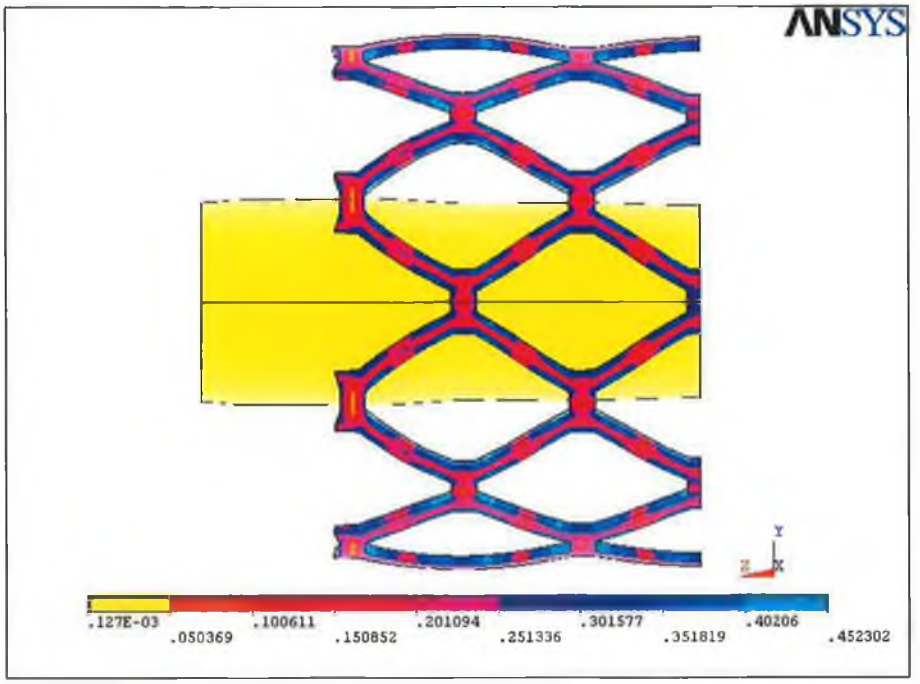

Figure 5.52: Deformation of the slotted tube after deflation by 57 mm balloon

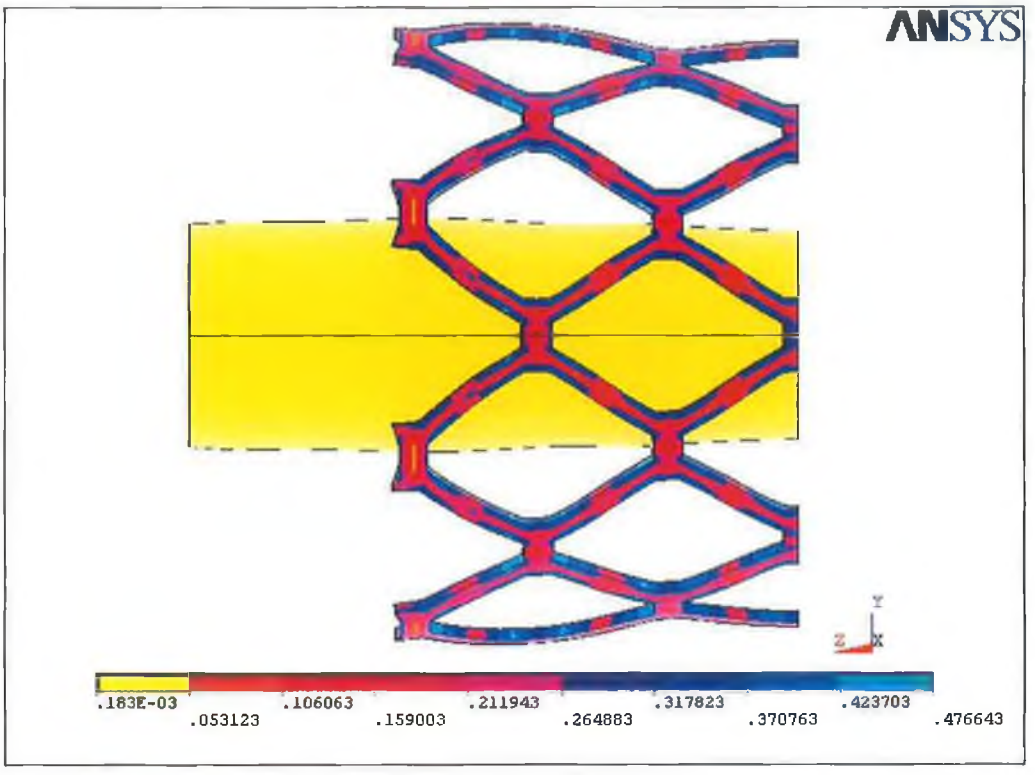

Figure 5.53: Deformation of the slotted tube after deflation by 62 mm balloon

5.3.3.2 Deployment pressure vs. displacement

Figure 5.54 shows the magnitude of the slotted tube expansion in radial direction at maximum deployment pressure for the 52 mm, 57 mm and 62 mm balloon length respectively. The radial displacement measured was based on the central part of the slotted tube. Therefore, the displacement calculated was evaluated according to the diameter changes in vertical central axis of the slotted tube. It can be seen from graph that the displacement developed smoothly as expected at the beginning of the dilatation process and begun to pick up at a faster rate when the deployment pressure of 2 MPa was reached. The trends of the graph for the 57 mm and 62 mm length balloon follow closely to each other. This indicates that it is not affected much by length of the balloon utilised. This fact is only true if the measurement is taken from the central part of the slotted tube. The magnitude of the displacement would have been different if the measurement is taken from the end of the slotted tube. This is due to the excessive bulging at the end of the slotted tube in the 62 mm length balloon which resulted in the higher radial expansion. The maximum central diameter of the slotted tube achieved at maximum deployment pressure for the 57

mm and 62 mm length balloon was approximately 70.8 mm and 70.0 mm respectively.

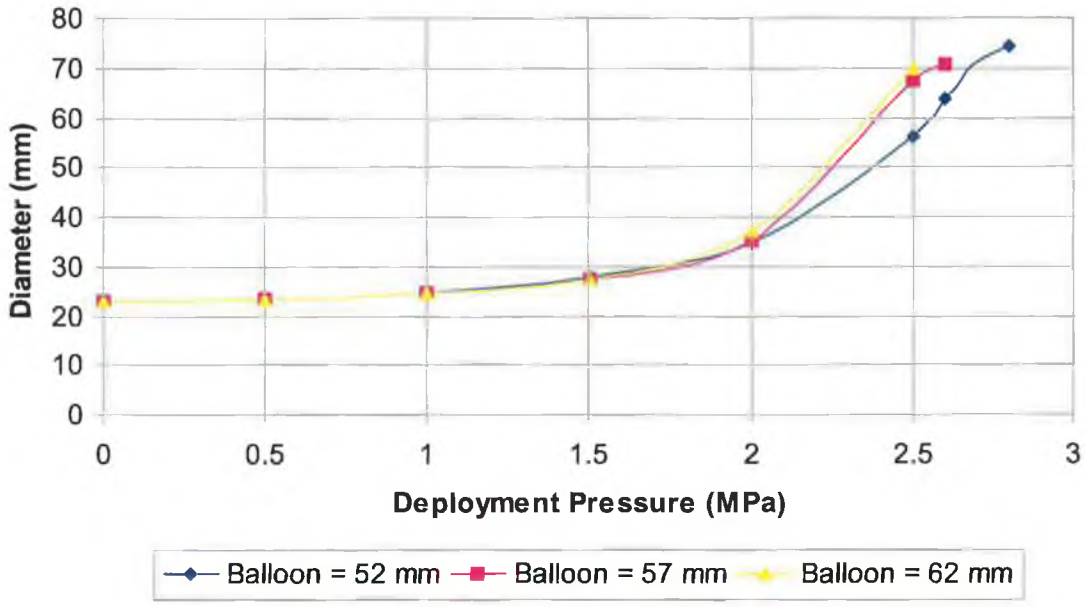

Figure 5.54: Expansion of slotted tube diameter with deployment pressure

The maximum central diameter of the slotted tube achieved at maximum deployment pressure for the 52 mm length balloon was 74.4 mm. This is the highest expansion amongst the three different lengths of the balloon. A measurement was taken on the radial expansion at the end of the slotted tube since it bended towards the inner direction that could result in lower displacement. It was found that the diameter at the end of the slotted tube was still higher than the central diameter obtained from the 57 mm and 62 mm length balloon. The diameter measured from the end of the slotted tube at maximum exerted pressure for the 52 mm balloon length was approximately 72.2 mm.

5.3.3.3 Elastic recoil

The elastic recovery is referred to the reduction in size of the slotted tube as explained in the previous section. The elastic recoil is a result of the elastic and plastic deformation of the material. The elastic unload occurred simultaneously with the deflation of the balloon since the expansion mechanism was based on the elastic-plastic behaviour of the stainless steel. The structure of the slotted tube that had not

experienced plastic deformation will go through the reversible process in which case it will play a part as the dragging force to force the structure back to its initial state.

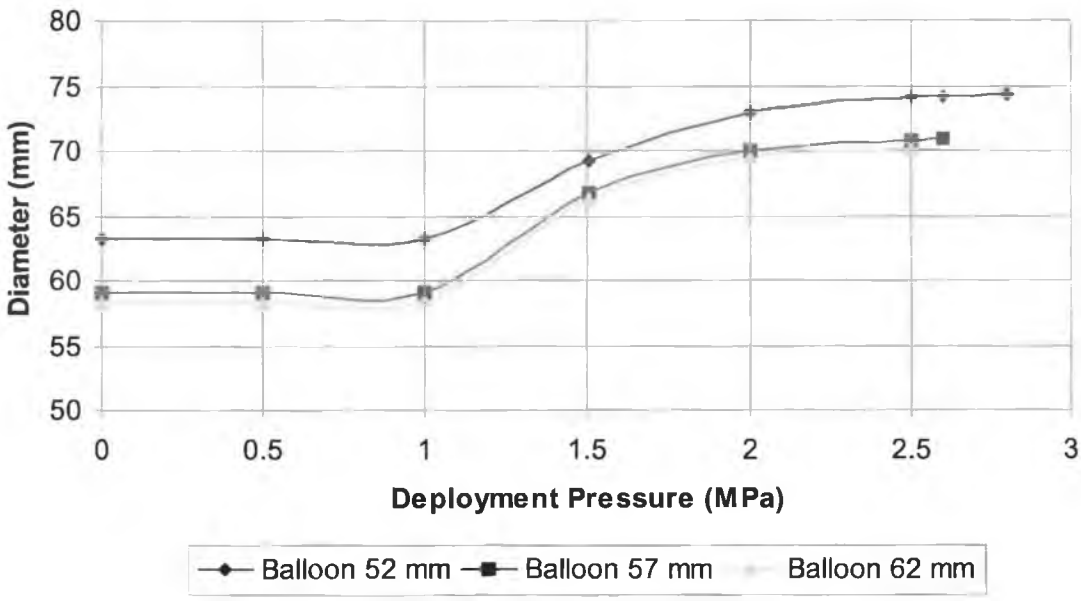

Figure 5.55: Elastic recoil of the slotted tube

Figure 5.55 shows the reduction in the slotted tubes diameter following the deflation of the balloons. It can be noticed from the graph that the elastic recovery of the slotted tube for the 57 mm and 62 mm length balloon fits closely to each other despite the fact that there was a 5 mm difference in the length of the balloon. The graph also shows that there was a big gap between the 52 mm balloon length and the other two lengths of the balloon despite the fact that there was also a 5 mm difference between these. The central diameter of the slotted tubes after the pressure was released was found to be 63.2 mm, 59.1 mm and 58.3 mm for balloon lengths 52 mm, 57mm and 62 mm respectively. For 52 mm balloon, the slotted tube diameter was noticed to have shrunk 15% from the diameter obtained during the maximum pressure. The slotted tubes for 57 mm and 62 mm were also shrunk by 16.5% and 16.8% respectively. From this results, it is fair to say that if 57 mm balloon is the standard length then 5 mm increment of the balloon length makes not much difference compared to 5 mm decrement of the length of the balloon.

5.3.3.4 Foreshortening

Figure 5.56 illustrates the magnitude of foreshortening in the slotted tubes with simulation time by three different balloon lengths. The negative values indicate the length that the slotted tube shortened. It is obvious that the slotted tube experienced the maximum foreshortening by 62 mm long balloon. The total amount of foreshortening in this case was found to be 10.3 mm at maximum pressure load. The amount of foreshortening reduced to 2.8 mm when the balloon was completely deflated. It was also noticed from the graph that the way foreshortening developed in the slotted tube was very similar to each other irrespective of the different lengths used.

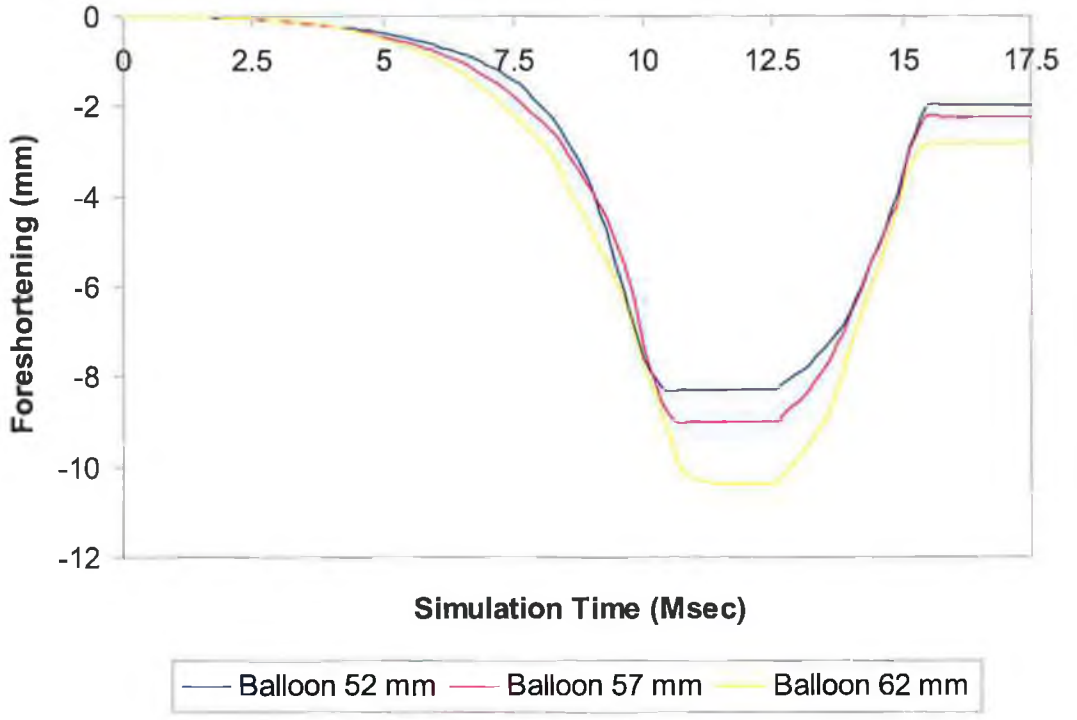

Figure 5.56: Foreshortening of the slotted tube with simulation time

The foreshortening developed slowly at the beginning of the dilatation process and then picked up gradually as the expansion continued. The foreshortening reached the maximum value and remained constant during the steady state response. The foreshortening for the case of the 52 mm and 57 mm length balloon were found to be 8.3 mm and 9.0 respectively at steady state response. The foreshortening decreased as the pressure decreased. However, the reduction in length of the slotted tube for the

57 mm balloon length was more than the 52 mm balloon length when the balloon was completely deflated. These were 2.23 mm and 1.98 mm respectively. The percentage of foreshortening from the original length of the slotted tube after the deflation of the balloons was 4.5%, 5.1% and 6.5%. So, the amount of foreshortening for the 62 mm length balloon was approximately twice as high as the foreshortening for the 57 mm length balloon compared to the 52 mm length balloon despite the fact that there was five millimetres length difference between them.

5.3.3.5 Uniformity of the slotted tube

Figure 5.57 to Figure 5.59 detailed the ultimate deformation of the slotted tubes for 52 mm, 57mm and 62 mm balloon when the balloons were deflated. The figures also show the slotted tubes geometry before and after the expansion. The effect of the balloon length on the expansion characteristics of the slotted tube is very obvious whereby the deformation of the slotted tube behaves in the very different way especially in the vicinity of the slotted tube end.

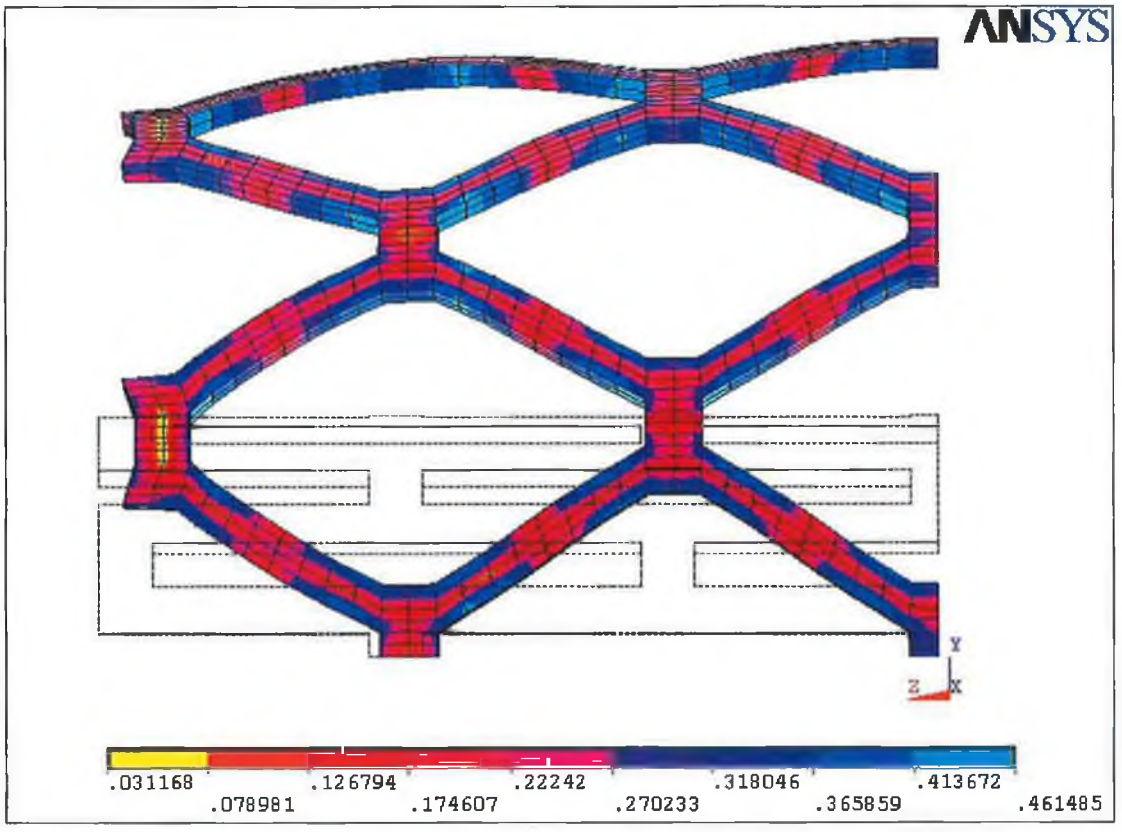

Figure 5.57: Slotted tube geometry before and after the expansion for 52 mm balloon

As can be seen from Figure 5.57 the slotted tube does not look very flat. The end of the slotted tube tended to bend towards the inner direction. The diameter at the end of this slotted tube was found to be 58.1 mm, which was 5.1 mm less than its central diameter. In spite of the fact that the diagram in Figure 5.57 does not look very uniform, the percentage difference between the central diameter and the end diameter of the slotted tube is only 8.1%.

The diagram in Figure 5.58 shows the most uniform expansion of the slotted tube. The slotted tube here was expanded using the balloon of 57 mm in length. The diameter at the end of the tube was measured and it was found to be nearly equal to the diameter obtained from the centre of the slotted tube. The diameter at the end of the slotted tube was 59.7 mm. Comparing to the diameter obtained at the central part of the slotted tube (i.e. 59.1 mm), the difference between them was only 0.6 mm. Therefore, the slotted tube under the 57 mm length balloon results in only 1% difference between the central diameter and the end diameter.

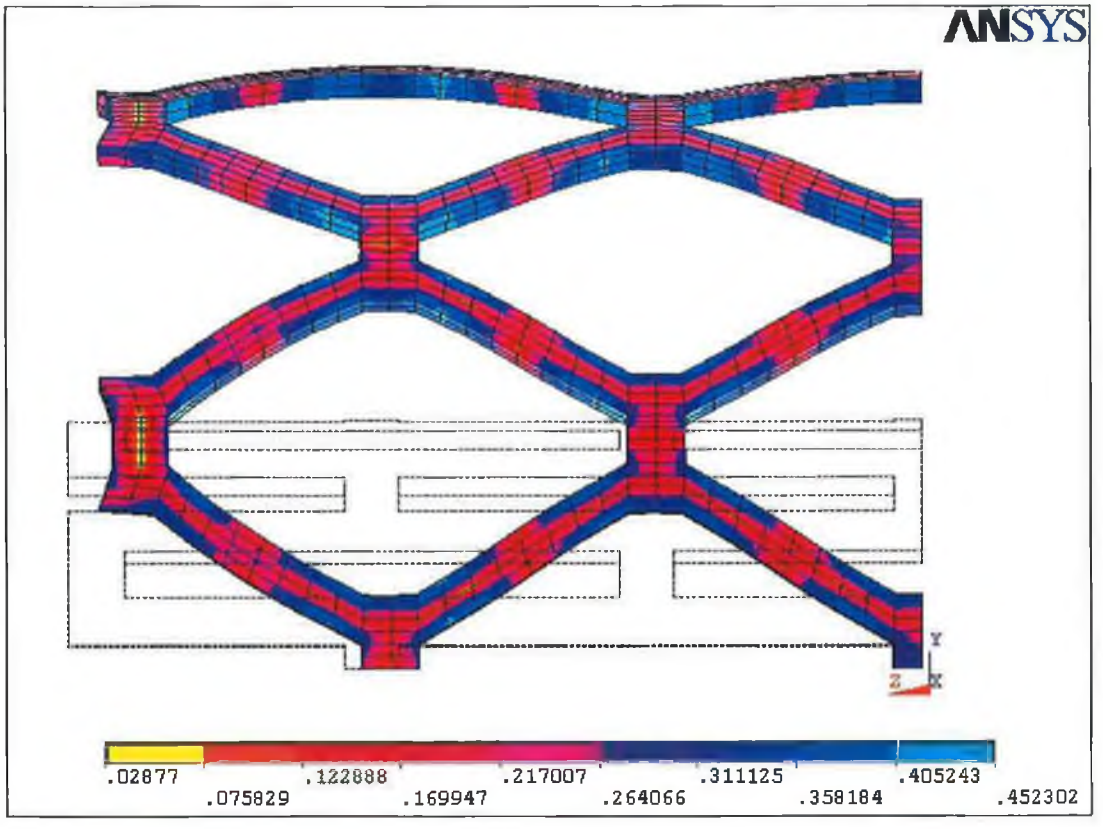

Figure 5.58: Slotted tube geometry before and after the expansion for 57 mm balloon

The diagram in Figure 5.59 shown the slotted tube for the 62 mm length balloon did not produce a flat tube either. This simulation showed that the balloon used was too long and caused excessive bending at the end of the slotted tube. The diameter at the end of the slotted tube for the 62 mm length balloon was 64.2 mm and it was 5.9 mm higher than the central diameter. The percentage difference between them was approximately 10.1%. This shows that the slotted tube under the 62 mm length balloon was the least uniform.

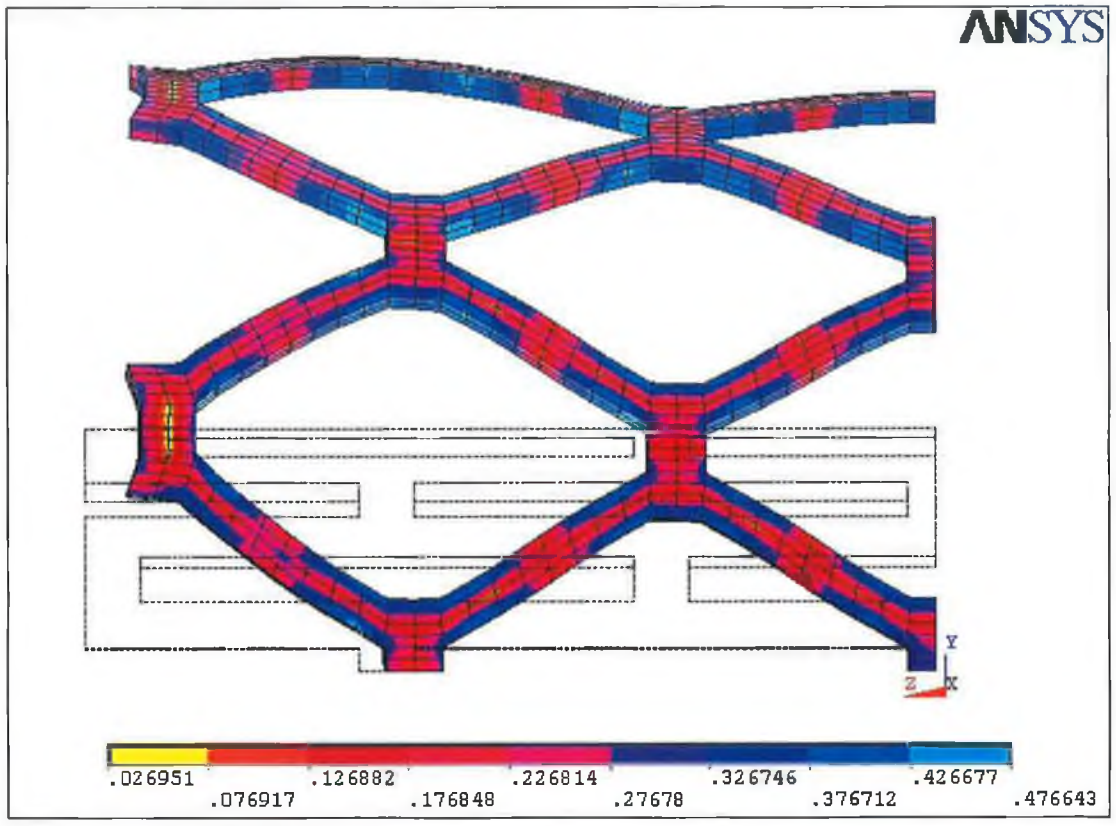

Figure 5.59: Slotted tube geometry before and after the expansion for 62 mm balloon

5.4 Analysis of Friction on Slotted Tube Expansion

Friction is another important factor that needs to be studied. It is thought that the friction could somewhat effect the foreshortening of the slotted tube expansion. However, detail studies need to be done in order to differentiate the differences. This section will detail the effect of static friction between the slotted tube and the balloon on the expansion process. The effect of varying the friction between the balloon and

the slotted was investigated by carrying out three simulations. The friction factors used for these three simulations were 0, 0.15 and 0.3 respectively. The exact value of friction is very difficult to calculate and determine. Therefore, a wide range of friction factors was chosen here to ensure that all the possibilities were included.

5.4.1 Modelling and Loading

The model used in these simulations was taken from the previous section i.e. a stainless steel slotted tube of 25.4 mm outer diameter and 23 mm inner diameter with 86.8 mm in length. The length of the balloon used was 57 mm. The fact that this model was chosen was because of the ultimate structure or the geometry of the slotted tube obtained in previous simulation was rather uniform. Each simulation used the same loading pattern. The loading pattern that used are as illustrated in loading curve 2 in Figure 5.49. The loading curve increases from 0 to 2.6 MPa within 10 milliseconds and it is held constant for 5 milliseconds before it decreases back to zero pressure load again.

5.4.2 Result and Discussion

5.4.2.1 Stress analysis

Figure 5.60 shows the development of von Mises for each of the slotted tube with different friction factors. The node was picked from the friction free model based on the location where the maximum stress occurred in the slotted tube. Although the location of the maximum stressed node for simulations with friction might not be identical to that of frictionless simulation, the same node was plotted for the simulations with friction factors 0.15 and 0.3 to make a fair comparison amongst them.

It can be seen from the graph that the development of the von Mises stresses developed steadily and identically as the pressure increased. The slotted tube with no friction included seemed to be departed at the higher level of stress compared from the plots for friction factors of 0.15 and 0.3, as it developed towards the steady state response. It was noticed that the stress generated did not vary very much despite the fact that the friction factor used in third simulation was twice as high as the second

simulation. This indicates that stresses are not significantly affected during slotted tube expansion.

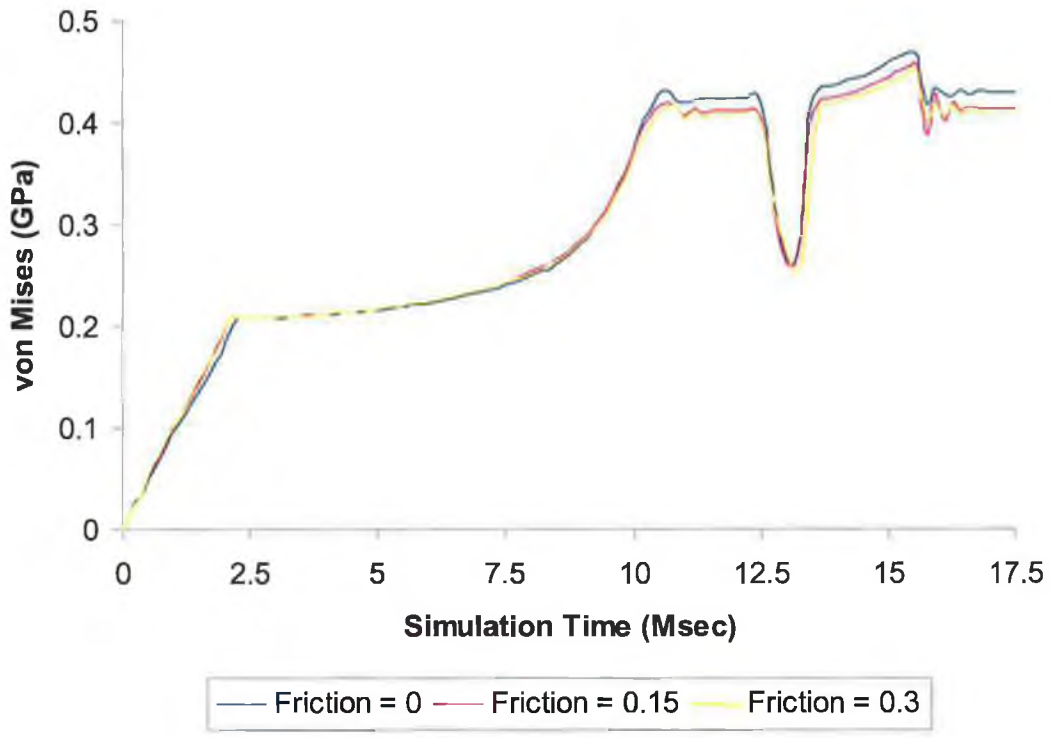

Figure 5.60: Development of stress at maximum stressed node

As the deflation process began, the von Mises stress for friction free model tended to converge and developed simultaneously with the other two higher friction factors. It is known from the knowledge gained in previous simulations that the sudden drop and rise of the von Mises stress was because of the pressure drop followed by the elastic recovery due to the mode switch in axial stress component. As soon as the stress in axial stress component increased at a slower rate the differences in von Mises stress for the friction free model become more prominent again compared to the simulations with friction included.

At the end of the simulation in which the balloon was completely deflated the residual stresses in that particular node for the three simulations were found to be 429.1 MPa, 413.7 MPa and 411.4 MPa respectively. It did not vary very much amongst the simulations with friction, only to the order of 1%. Somehow, it seemed

that friction does affect the stress but not as much as in the friction free case. This concludes that friction has a little affect on the stress generated and the affect is even smaller with increasing friction when the same location is considered.

Figure 5.61 to Figure 5.63 show the maximum residual stress in the slotted tube for friction factors of 0, 0.15 and 0.3 respectively when the balloon was deflated. The level of friction between the balloon and the slotted tube influenced the stress level of the slotted tube. The maximum stress in each case varied between 416.9 MPa and 452.3 MPa with the level decreasing with increasing friction. It was noticed that the highest stressed areas became more perceptible with increasing friction despite the fact that the level of stress generated decreasing with friction. However, the location of the highest stressed regions did not change but remained in the corners and the middle of the slots junctions.

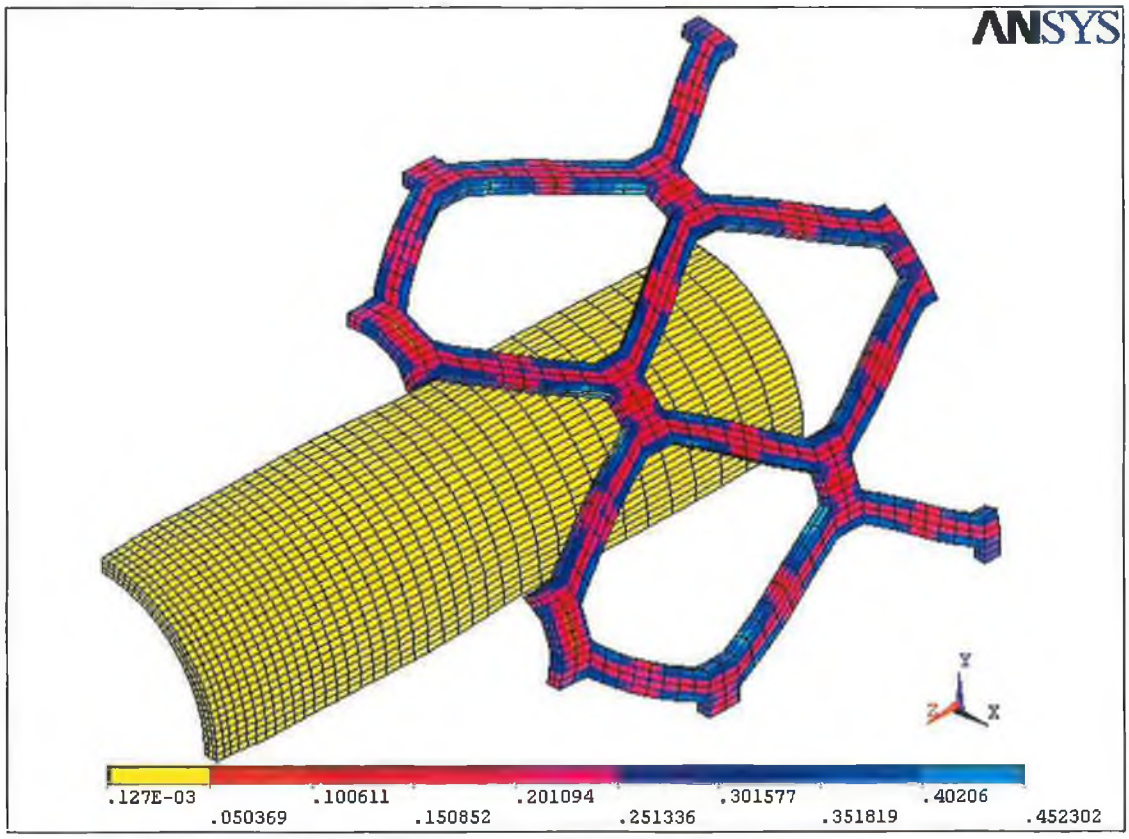

Figure 5.61: Residual stress in the slotted tube for friction factor of 0

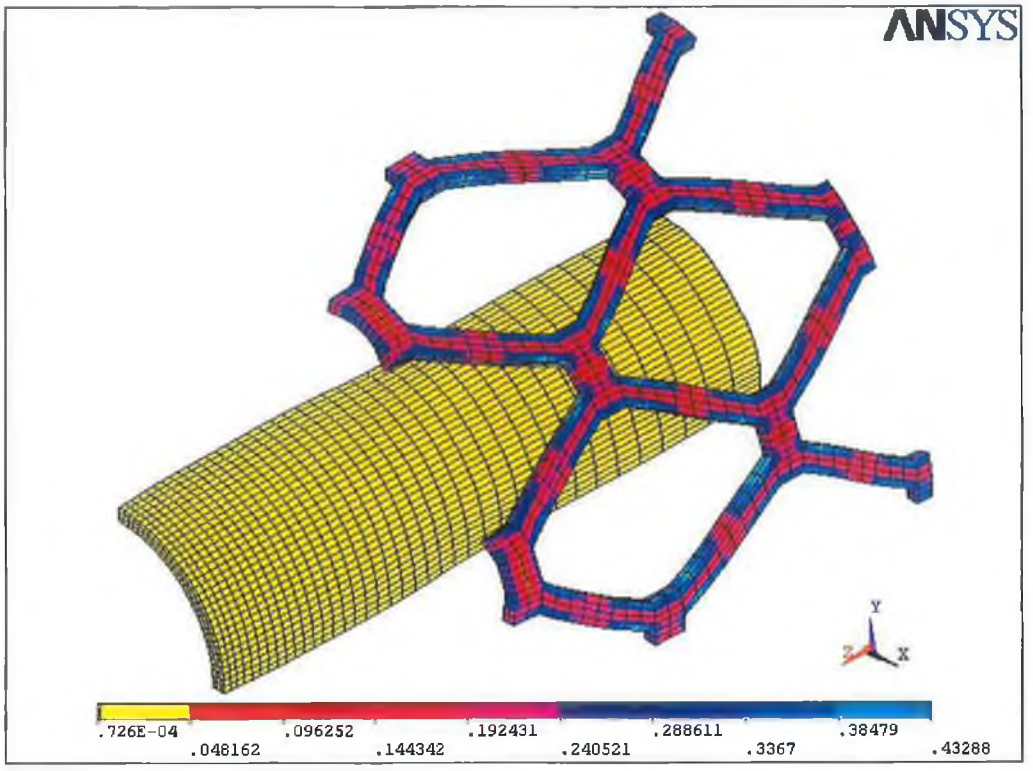

Figure 5.62: Residual stress in the slotted tube for friction factor of 0.15

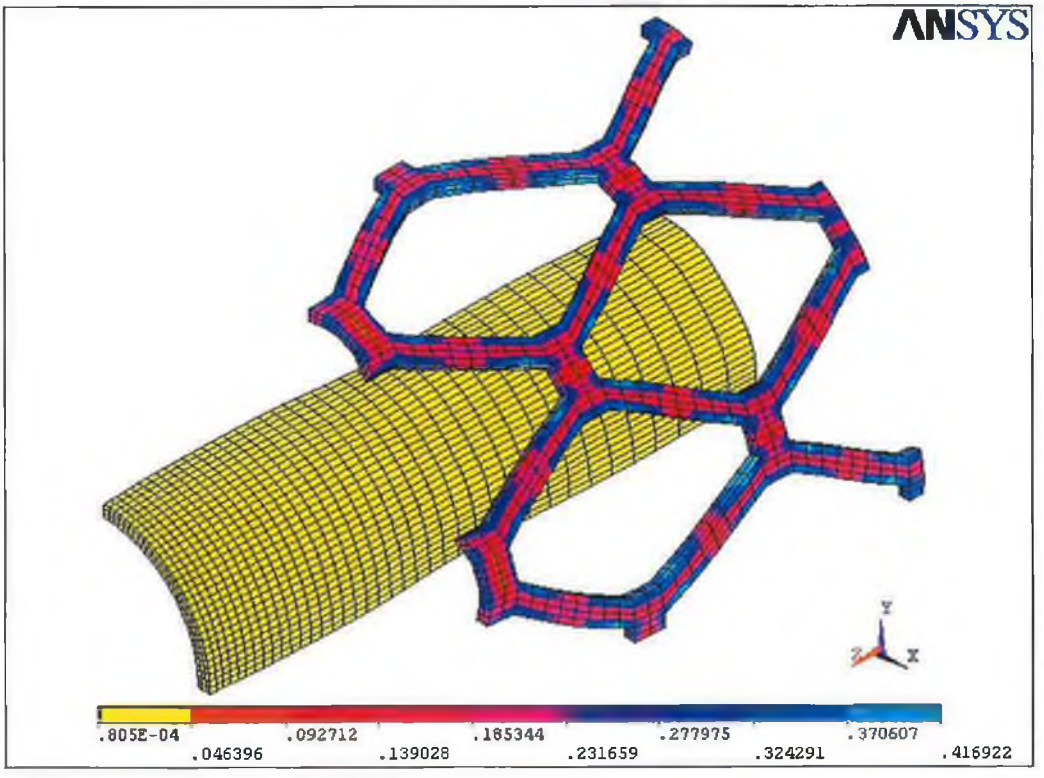

Figure 5.63: Residual stress in the slotted tube for friction factor of 0.3

5.4.2.2 Deployment pressure vs. displacement

Figure 5.64 shows the magnitude of the slotted tube expansion in the radial direction at maximum deployment pressure for friction factors of 0, 0.15 and 3 respectively. The graph shows the slotted tube diameter expanded consistently irrespective of the friction factors. The level of expansion could hardly be detected until the end of maximum deployment pressure. The maximum diameter in the central part of the slotted tube did not vary a lot. It varied between 67 mm and 70.7 mm with the level decreasing with increasing friction. With the same level of deployment pressure the diameter achieved for the higher friction factors was not as high as the friction free. The stress and the radial expansion can be related in which the lower stress in the slotted tube for the case of friction included is due to the lower level of expansion.

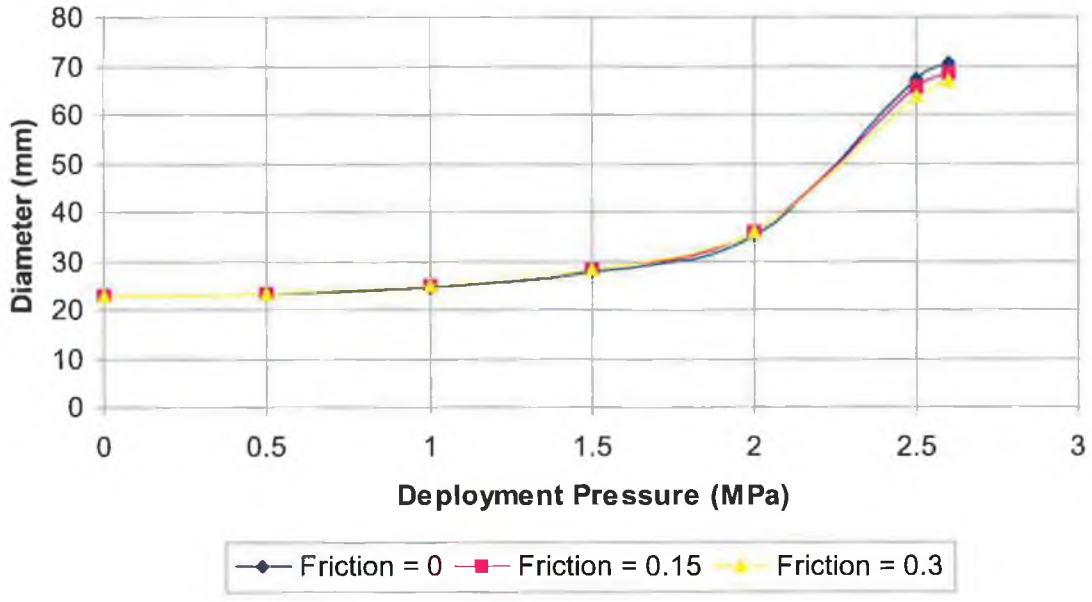

Figure 5.64: Expansion of slotted tube diameter with deployment pressure

5.4.2.3 Elastic recoil

Figure 5.65 shows the reduction of the slotted tubes diameter following the deflation of the balloons. The differences in slotted tube diameter were slowly changed during the inflation process (Figure 5.64) but it decreased in parallel throughout the course of deflation process as shown in Figure 5.65. The central diameter of the tube for the friction free simulation shrunk to 59.1 mm when the pressure was released to 0 MPa. The central diameter of the slotted tube was found to be equal to 57.4 mm and 56.0

mm when the friction factor of 0.15 and 0.3 were added. The ratio of the diameter differences was almost equal to the ratio of the friction simulated. Again, the elastic recoil decreased with increasing friction. However, the total discrepancy between the three cases was not significant: approximately 5.2 % difference.

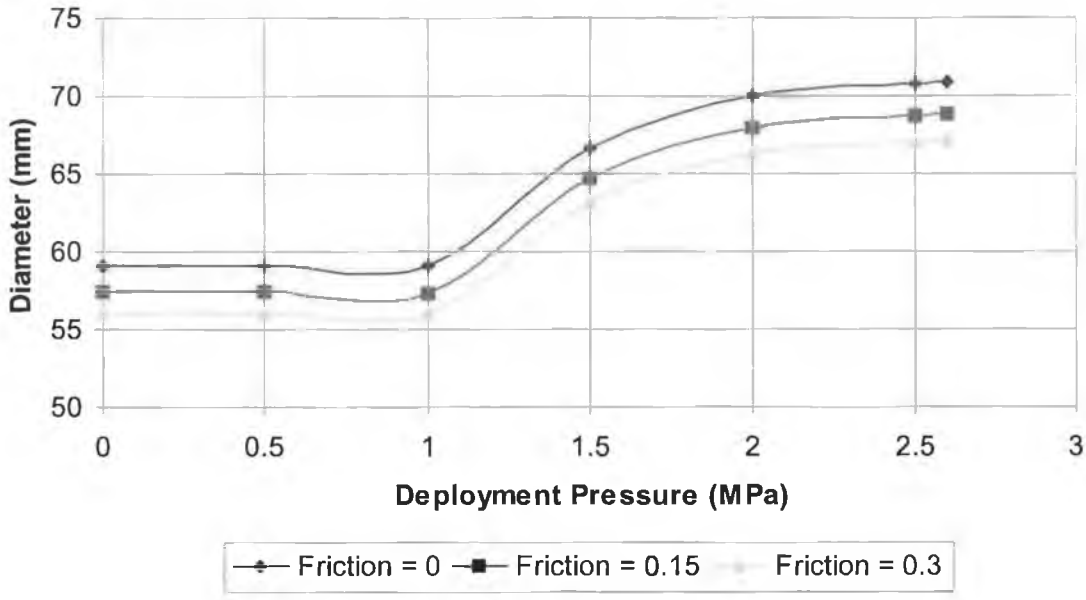

Figure 5.65: Elastic recoil of the slotted tube

5.4.2.4 Foreshortening

Figure 5.66 illustrates the magnitude of foreshortening in the slotted tubes with simulation time, by the friction factors of 0, 0.15 and 0.3 respectively. The length of the slotted tube was shortened more in the case of friction free. It had shortened by 2.23 mm when the balloon was deflated. The slotted tube seemed to be experiencing less foreshortening with the friction factor up to 0.15. The effect of the friction factors within the range of 0 to 0.15 seemed to have more influence on the foreshortening of the slotted tube. The subsequent foreshortening decreased with decreasing rate when friction factors between 0.15 and 0.3 were utilised. The total length of the slotted tube shortening was found to be 1.57 mm and 1.24 mm respectively for the case of friction factors equal to 0.15 and 0.3. The slotted tube for the friction free case had shortened 1.6 % more than for the case where a friction factor of 0.15 was used. Apart from that, the slotted tube for friction factor of 0.3 shortened by 0.8 % more compared to the friction factor of 0.15. Therefore, the result of friction for the first 0.15 value of friction factor is almost twice as effective as the

subsequent 0.15 value of friction factor. An ideal stent should not have foreshortenings more than 5 % [69] as the accurate placing and deployment of the stent would not be compromised. Although the percentage differences in foreshortening of the slotted tube with and without friction is very low, it is very important to consider the friction when it comes to the design of a real stent as the increment of friction could reduce the foreshortening of the stent.

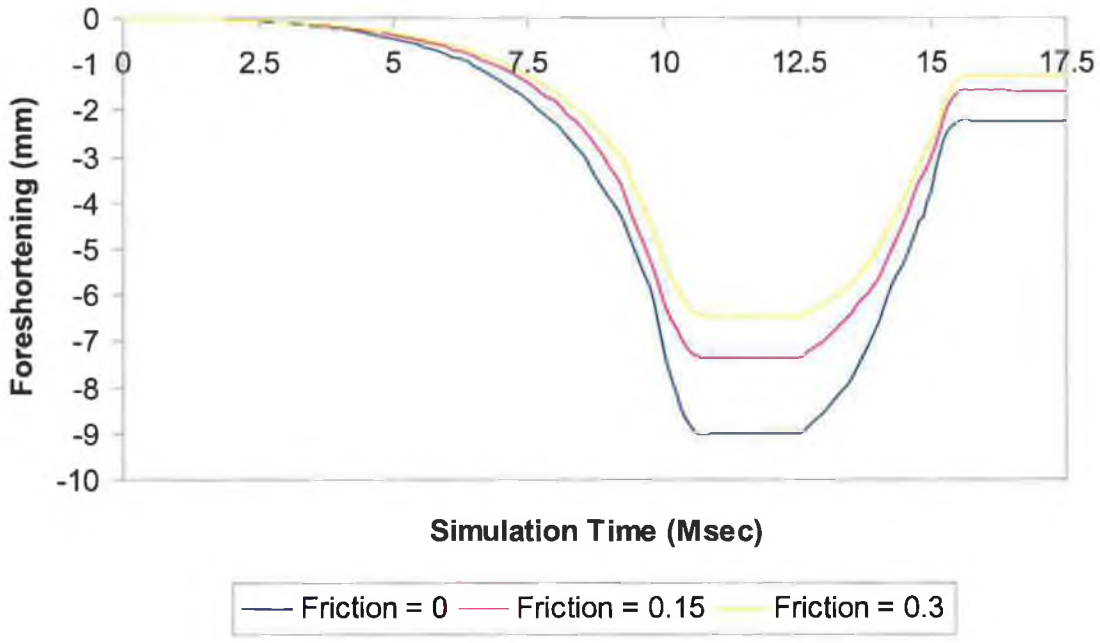

Figure 5.66: Foreshortening of the slotted tube with simulation time

5.5 Analysis of Scaling the Slotted Tube Size

Understanding the size-related development of geometry in slotted tube stent should give a rough idea about the outcome of one's specimen without experimental testing. It is widely known that to conduct an experimental test on a stent is expensive. It is not only the price of the stent itself but also the cost of setting up the experimental devices. If the geometry of a real stent could be scaled up to ten or twenty times its actual size and have it validated by carrying out experimental test, the overall cost of the experiment could be largely reduced. On the other hand, if a slotted tube could be scaled down to the size of a stent and have it analysed by computer software, the cost would be relatively reduced as well. This section will elucidate how this method was implemented and the outcome of such implementations on slotted tube expansion.

5.5.1 Modelling and Loading

Two simulations were carried out and compared with the result that has already been obtained from the original slotted tube size. The original tube size here refers to the model used in previous section (i.e. a stainless steel slotted tube of 25.4 mm outer diameter and 23 mm inner diameter with 86.8 mm in length). The length of the balloon used was 57 mm. The ANSYS pre-processor has an option that allows the nodes to move in the cylinder. The nodes can be moved from a certain original radius of "XX" to a new radius of "XX + delta". For this situation, the scale factor would be "XX + delta/XX".

The first simulation was run by scaling the slotted tube to half of its size i.e. 5 times smaller than the original slotted tube size. For instance, the length of the slotted tube used here has become 21.7 mm. The individual slot and strut widths were equal to 1.245 mm in circumferential direction. The length of the bridging strut connecting the two adjacent cells was 1.4 mm and the length of the slot has become 12.6 mm long. The model used in second simulation was scaled down to 10 times smaller than its original size. The size of the slotted tube in second simulation was as small as a real tubular stent, as the main objective in this section was to carry out these simulations to identify the feasibility of this method due to these changes. In this model, the individual slot and strut widths were equal to 0.249 mm in the circumferential direction. The bridging strut and the length of the slot were equal to 0.28 mm and 2.52 mm respectively. The detail dimensions of the three models simulated are described in Table 5.3 below.

Category	**Original tube size**	**5 times smaller**	**10 times smaller**
Number of Cells	40	40	40
Cell Size	62.748 mm^2	15.687 mm^2	0.627 mm^2
Cell Areas	2509.92 mm^2	627.48 mm^2	25.1 mm^2
Metal Surface Area	4416.41 mm^2	1104.10 mm^2	44.16 mm^2
Stent Surface Area	6926.33 mm^2	1731.58 mm^2	69.26 mm^2
Outer Diameter	25.4 mm	12.7 mm	2.54 mm
Inner Diameter	23 mm	11.5 mm	2.3 mm
Length of Stent	86.8 mm	43.4 mm	8.68 mm

Table 5.3: Dimensions of the scaled slotted tube size

After running a few simulation tests it was found that same level of deployment pressure was needed to expand the slotted tube regardless of the diameter of the tube. Therefore, the same loading pattern was used for each simulation. The loading pattern that used is illustrated in loading curve 2 in Figure 5.49. The loading curve increases from 0 to 2.6 MPa within 10 milliseconds and it is held constant for 5 milliseconds before it decreases back to zero pressure load again.

5.5.2 Result and Discussion

5.5.2.1 Stress analysis

Figure 5.67 to Figure 5.69 shows the residual stresses in each slotted tube when the balloon was deflated. It was evident that the stresses did not vary too much when the size of the slotted tube was reduced as would be expected. This was due to the fact that the same level of pressure was deployed and the geometry of the slotted tube was identical too. The location of the maximum residual stress was found to be located in the same region irrespective of the size of the slotted tube. These regions were located at the four corners and the middle of the slots. From these results, it is evident that the stress distribution over the slotted tube stent remains invariant so long as the geometry of the slotted tube increases or decreases proportionally. The residual stresses on the largest to the smallest slotted tube stent when the balloon was deflated were found to be 452.3 MPa, 453.7 MPa and 468.9 MPa respectively. It was calculated that the differences between them were less than 3.6%, which indicates a reliable result. The slight variation of the stress on the slotted tube was thought to be due to the variation in the characteristic length of the smallest element which might affect the calculation of the stress, strain and so on. The length of the elements was shortened when the size of the slotted tube was reduced.

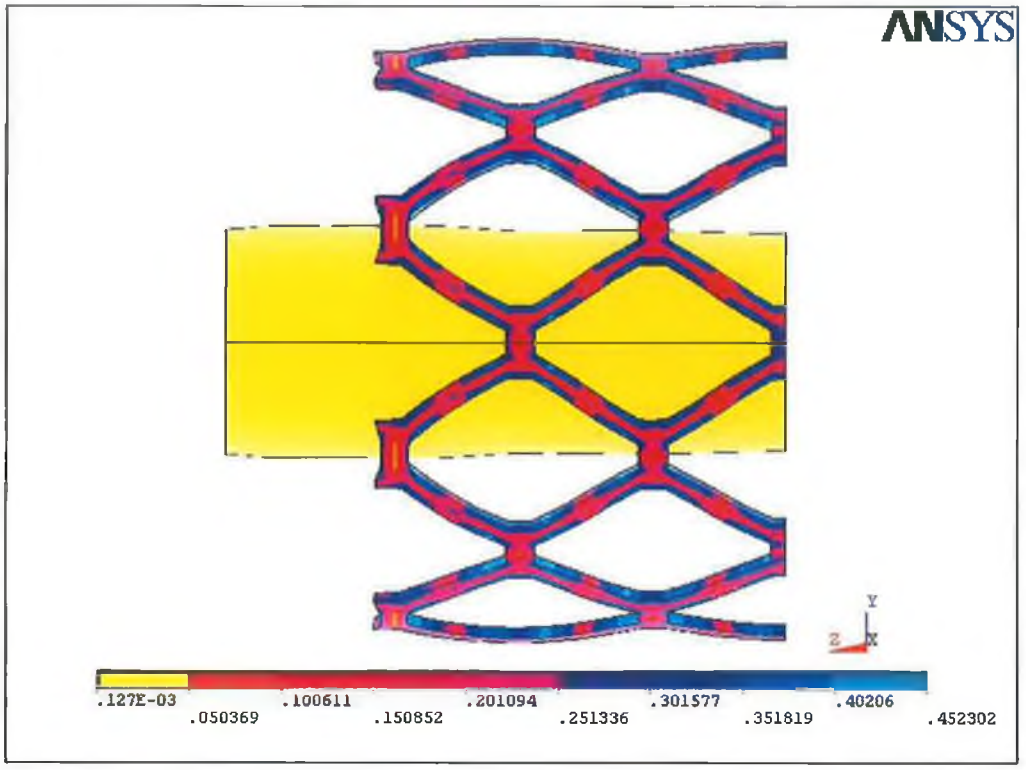

Figure 5.67: Deformation of the slotted tube after expansion by scaling factor of 1

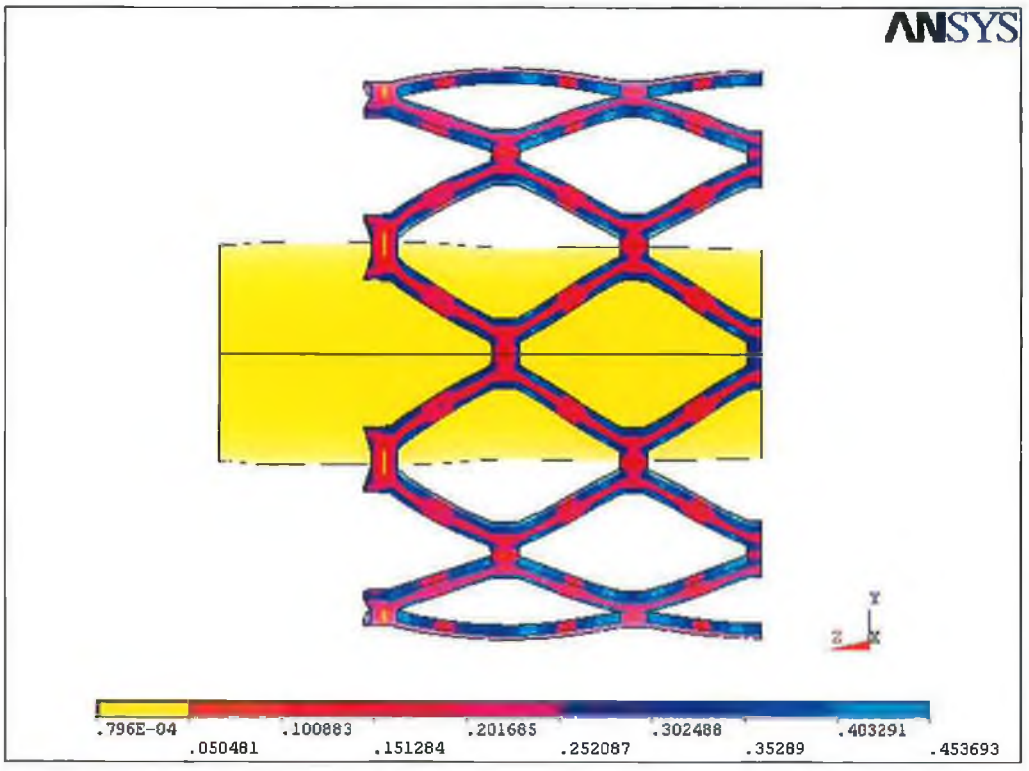

Figure 5.68: Deformation of the slotted tube after expansion by scaling factor of 0.5

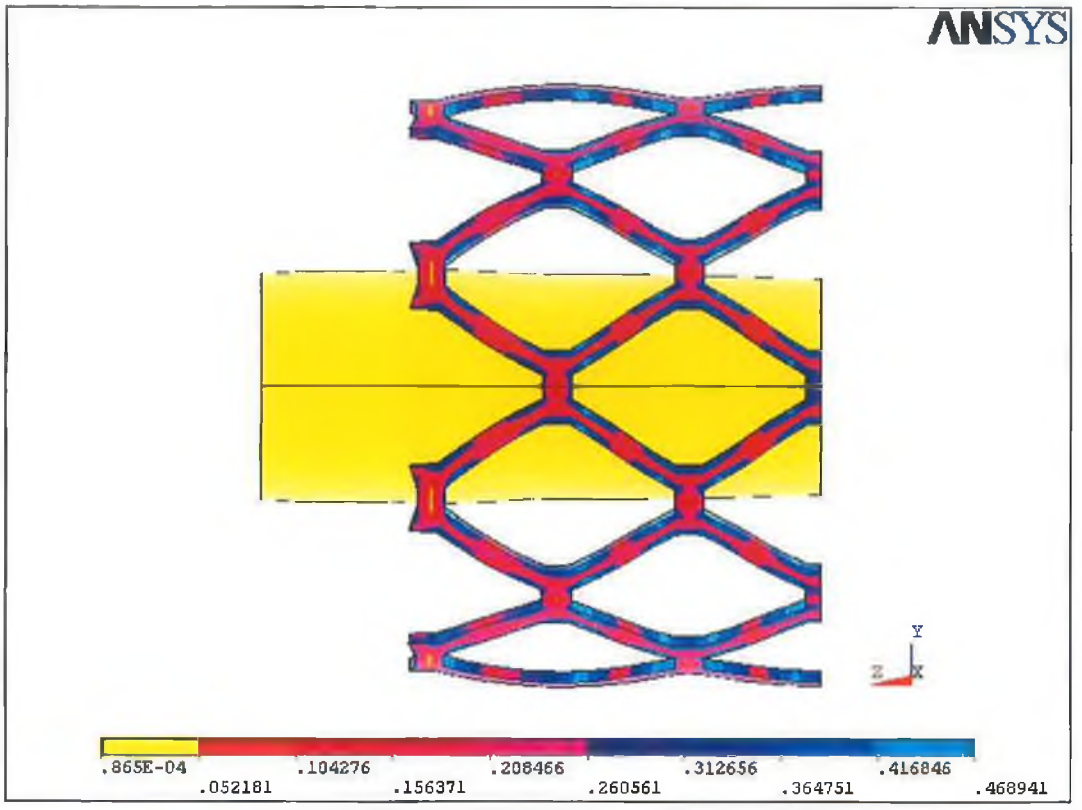

Figure 5.69: Deformation of the slotted tube after expansion by scaling factor of 0.1

Performing large deformation simulations on models with symmetric geometry and obtaining symmetric results can be most difficult. Everything must be identical from the very start and the calculated loads, strains, stresses of similar nodes or elements must be almost identical throughout the thousands of time steps taken to complete the simulation. Numerical round-offs will start to accumulate and small differences can become large differences if the deformations are large and an extensive number of time steps are made.

5.5.2.2 Deployment pressure vs. displacement

Figure 5.70 shows the magnitude of the slotted tube expansion in radial direction at maximum deployment pressure for scaling factors of 1, 0.5 and 0.1 respectively. The diameter of the slotted tube for the scaled slotted tubes developed consistently as for the original tube size (scale factor = 1). The only difference between them was the magnitude of the expansion as a result of scaling the slotted tube size. Table 5.4 illustrates the diameter of each slotted tube achieved at every increment pressure level of 0.5 MPa throughout the dilatation process.

Pressure Load (MPa)	Diameter (mm)		
	Scaling Factor = 1	Scaling Factor = 0.5	Scaling Factor = 0.1
0	23	11.5	2.3
0.5	23.2605	11.6241	2.3242
1	24.5705	12.2392	2.4464
1.5	27.5698	13.684	2.7308
2	35.0888	17.466	3.506
2.5	67.37	33.756	6.83
2.6	70.764	34.966	7.052

Table 5.4: Diameter achieved for three different scaling factors

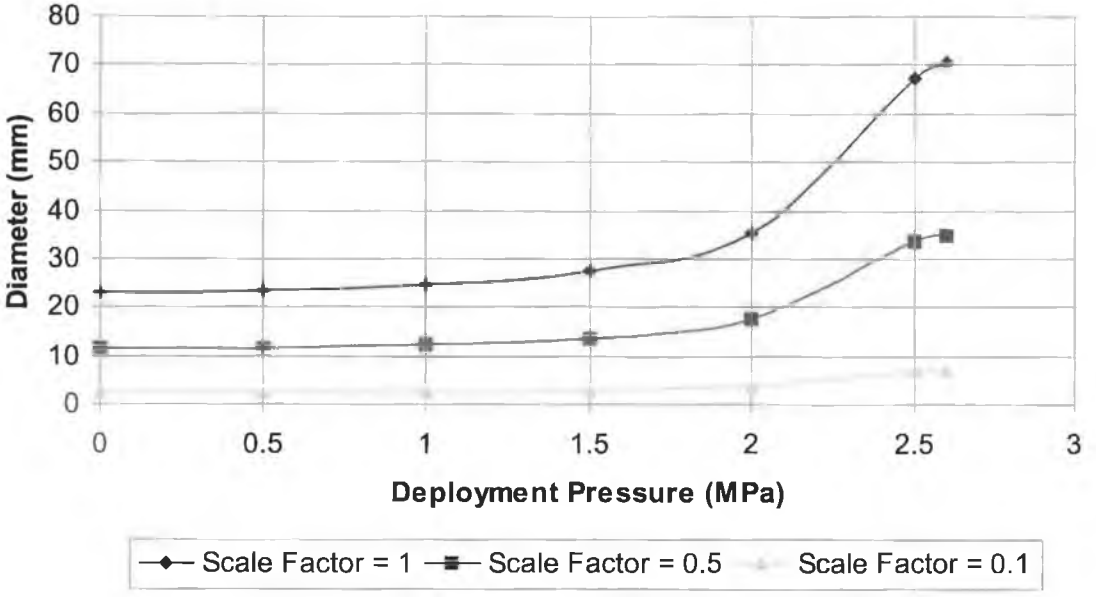

Figure 5.70: Expansion of slotted tube diameter with deployment pressure

The figures shown in Table 5.4 indicate that the slotted tube diameter increases by different rates at different level of pressures. However, the expansion level of the slotted tube occurred almost at the same ratio. It was known that the slotted tube of scaling factor 0.5 was half the size of the original slotted tube size (scaling factor 1) whereas, the slotted tube for scaling factor of 0.1 was ten times smaller than the original slotted tube size. It was noticed that the diameters obtained for each slotted tube of different scaling factors at each pressure level were based on the ratio of the

size of the slotted tube. For example, at pressure level of 1 MPa the diameter achieved from scaling factor 0.5 was half of the diameter achieved from the scaling factor 1. Also, the diameter achieved from the scaling factor 0.1 was ten percent of the scaling factor 1 which shown an agreement with the ratio of the slotted tubes in term of size. At maximum deployment pressure, the diameters achieved for the scaling factor 1, 0.5 and 0.1 were 70.76 mm, 34.97mm and 7.05 mm respectively.

5.5.2.3 Elastic recoil

Figure 5.71 shows the reduction of the slotted tubes diameter following the deflation of the balloons. The slotted tube diameters were gradually decreased during the deflation process until the pressure level of 1 MPa was reached. Table 5.5 shows the diameter of each slotted tube achieved at every decrement pressure level of 0.5 MPa throughout the deflation process.

Pressure Load (MPa	Diameter (mm)		
	Scaling Factor = 1	Scaling Factor = 0.5	Scaling Factor = 0.1
0	59.098	29.302	5.9
0.5	59.098	29.302	5.9
1	59.058	29.288	5.9032
1.5	66.694	32.678	6.566
2	69.954	34.46	6.944
2.5	70.702	34.924	7.044
2.6	70.764	34.966	7.052

Table 5.5: Elastic recoil of the slotted tubes

The figures presented in Table 5.5 indicate that the diameter achieved for the three different scaling factors at each level of pressure during the deflation process is closely followed the ratio of the size of the slotted tubes. The central diameter of the slotted tubes for the scaling factor 1, 0.5 and 0.1 was found to have shrunk to 59.1 mm, 29.3 mm and 5.9 mm respectively when the pressure was released to zero mega Pascal. As would have noticed that the ultimate diameter for the scaling factor 1 after elastic recovery was almost half of the size bigger than scaling factor of 0.5 and ten

times bigger than the scaling factor of 0.1. The ratio of the diameter differences was almost equal to the ratio of the size of the slotted tube. The total discrepancy between the three cases was insignificant and it was less than 0.01%.

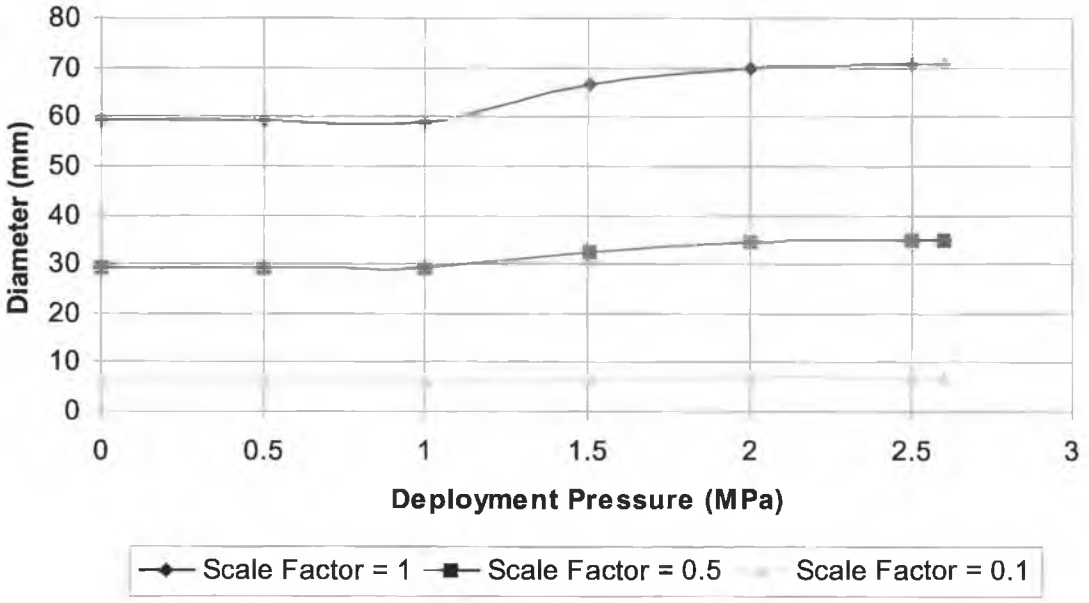

Figure 5.71: Elastic recoil of the slotted tube

5.5.2.4 Foreshortening

Figure 5.72 illustrates the magnitude of foreshortening in the slotted tubes with simulation time by the scaling factors of 1, 0.5 and 0.1 respectively. The foreshortening length of the slotted tubes shortened was found to be 2.231 mm, 1.115 mm and 0.235 mm respectively for the case of scaling factors equal to 1, 0.5 and 0.1. The statistic again shown that the foreshortening also had a close relationship with the scaling factor. The amount of foreshortening of a slotted tube could be said to reduce as much as twice for the same geometry but half size of the slotted tube.

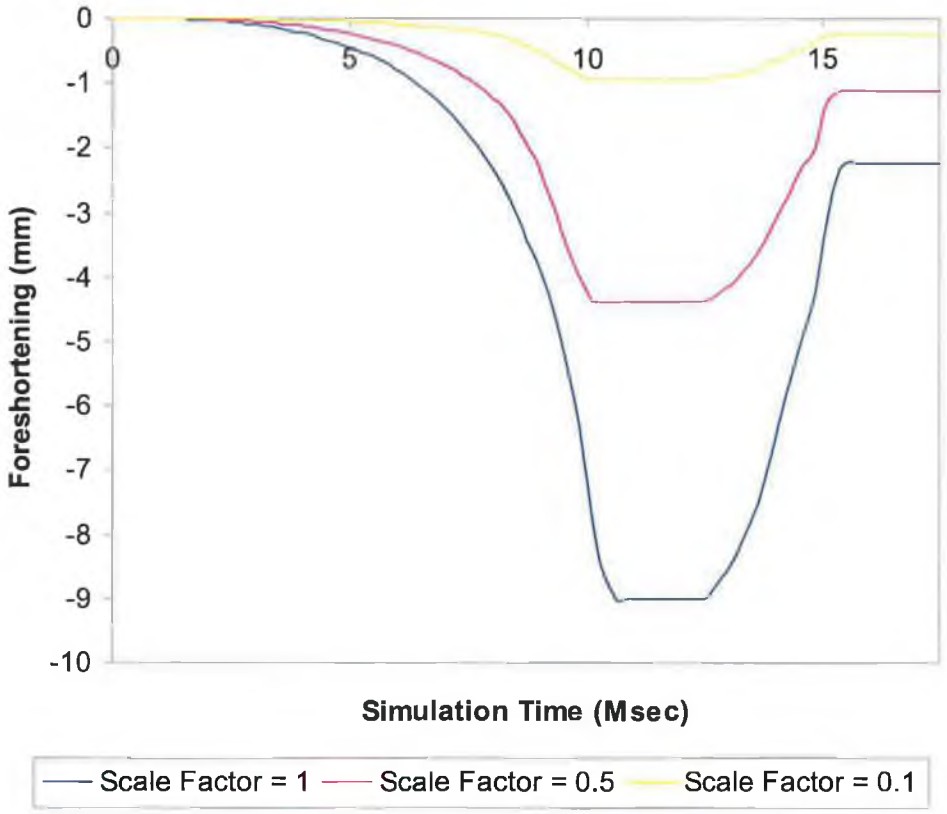

Figure 5.72: Foreshortening of the slotted tube with simulation time

5.6 Analysis of Stent Production Defects

Production defects in a stent during the manufacturing process is difficult to detect. The stent is so small and hard to produce that it will need a high capacity laser beam to cut the slots without even considering the accuracy. At this size, physical prototypes are usually hit or miss due to the accuracy of the laser. The accuracy is often very hard to maintain and even though such accuracy is maintained, there are always some tolerances allowed during the manufacturing processes. The analysis of slotted tube stent production defect is detailed in this section. The effect of the slotted tube stent imperfection on stress analysis, radial expansion, deformation characteristic etc. was examined and reported.

5.6.1 Modelling and Loading

The geometry of the slotted tube stent used in this investigation was extracted from previous section except that few modifications were made on the original geometry to model the imperfection. The geometry of the slotted tube was modified in such a way that the dimensions of the strut were no longer identical. Two elements were removed from each strut to reflect the changes of the defects in the slotted tube as shown in Figure 5.73. The size of a single defect area is 0.744 mm^2 (1.4 mm in length and 0.62 mm in width). The length of the balloon used in this investigation was 57 mm and the thickness of the balloon was 1.2 mm. The outer and inner diameter of the balloon was 23 mm and 20.6 mm respectively. The material properties of polyurethane rubber were used again to represent the balloon. A two parameter Mooney-Rivlin material model was used in this simulation with C(10) = 0.103176E-02 and C(01) = 0.369266E-02.

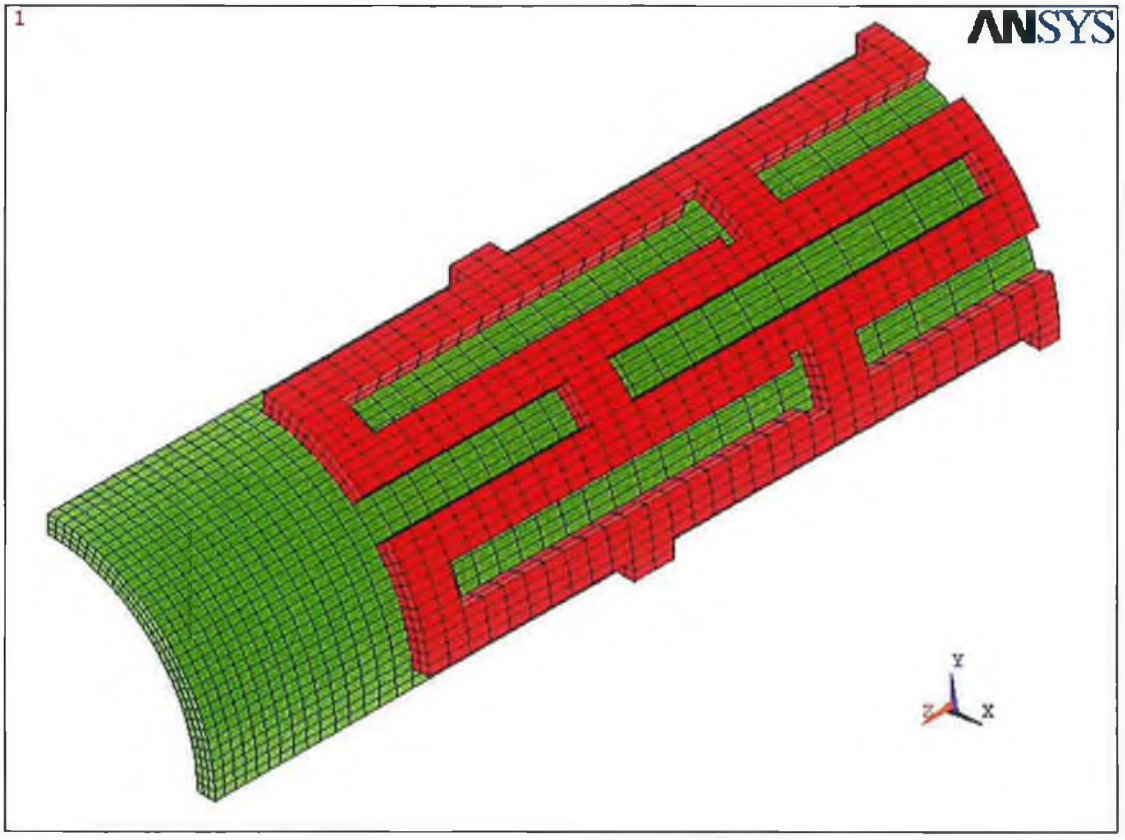

Figure 5.73: Finite element model of the slotted tube imperfection

The loading curve in Figure 5.74 describes the load history of the simulation process. The total simulation time was set to be 17.5 milliseconds. In this simulation, the pressure load increases from 0 to 2.6 MPa at simulation time of 10 milliseconds and remains constant for 2.5 milliseconds and finally reduces to 0 at a simulation time of 17.5 milliseconds.

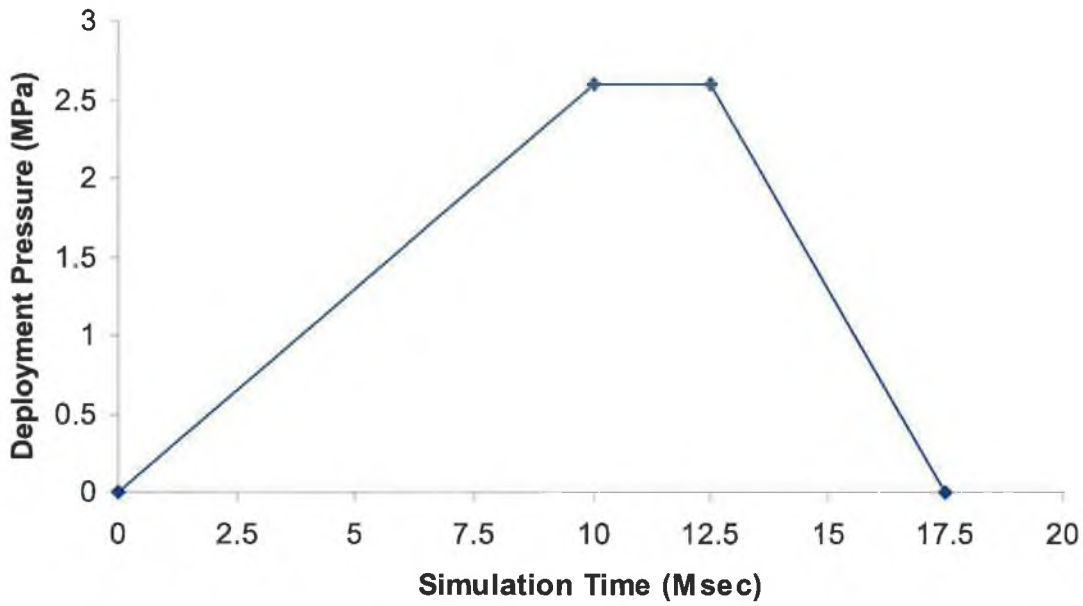

Figure 5.74: Loading curve

5.6.2 Result and Discussion

5.6.2.1 Stress analysis

Figure 5.75 shows the residual stress distributed in the slotted tube stent when the balloon was deflated. The maximum residual stress at that time was approximately 479 MPa. Given that the same amount of pressure was deployed, the residual stress in the case of geometry imperfection (479 MPa) is higher comparing to the perfect slotted tube geometry (452 MPa) as shown in Figure 5.52. The overall stress in the imperfect geometry slotted tube was well distributed despite the existence of the flaw.

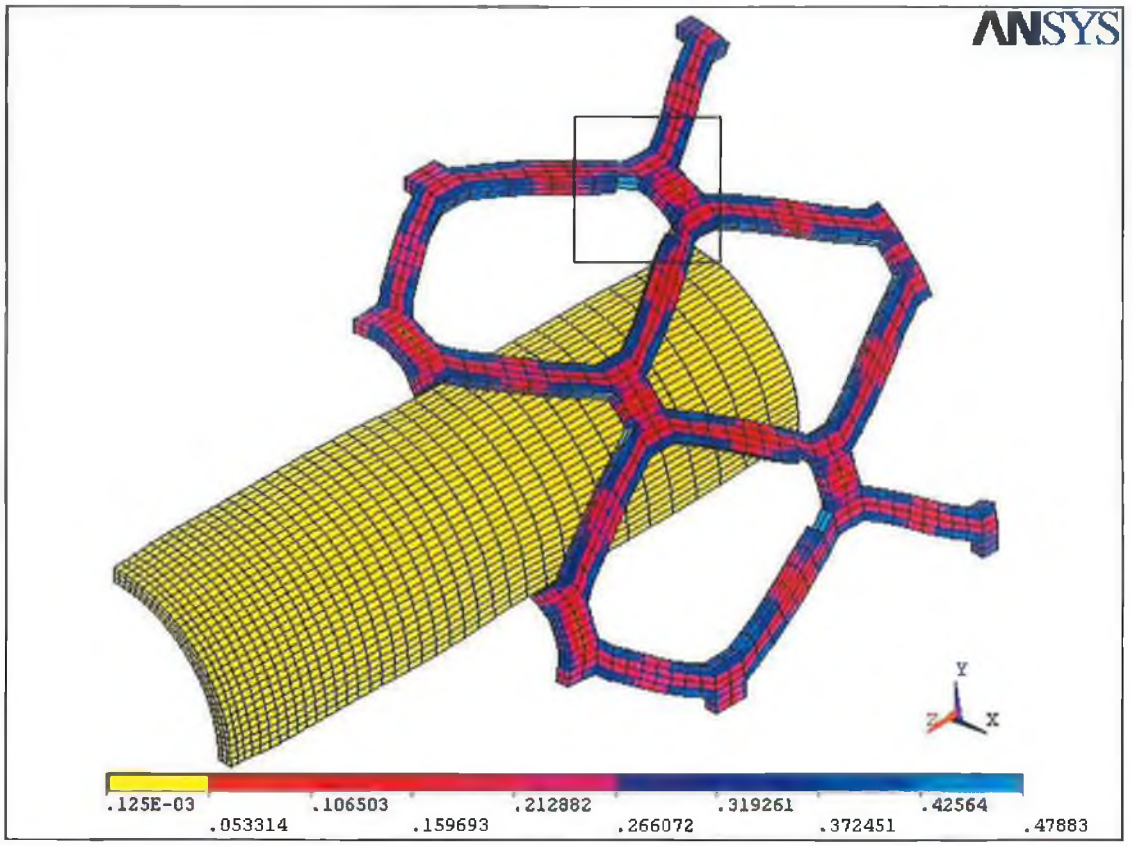

Figure 5.75: Residual stress in the slotted tube after deflation

The material for the flawless geometry slotted tube was stretched up to about 87.4% of the ultimate tensile strength of the properties. On the other hand, the material for the flawed slotted tube experienced 92.6% plastic deformation of the ultimate tensile strength. However, the higher von Mises stress generated in the imperfection slotted tube was due to the localised deformation. The weakest part of the structure appeared to be located at the defected area and leads to the earlier failure of the slotted tube. The weakness of the structure at the defected area prevented the slotted tube from keeping the stresses low at the same level of expansion as the flawless slotted tube. The percentage of residual stress difference between the perfect and imperfect geometry was approximately 6%.

Figure 5.76 shows the close up view of one of the defected areas and the maximum stress induced by the flaws as highlighted in Figure 5.75. As can be clearly seen that the stress concentrates on the defected area. The maximum stress occupies the whole surface of the two layers of elements. It was found that the maximum von Mises

stress also existed on the opposite side of the defected areas. This is obviously due to the imperfect structure that causes the other side of the strut to experience the maximum stress as well.

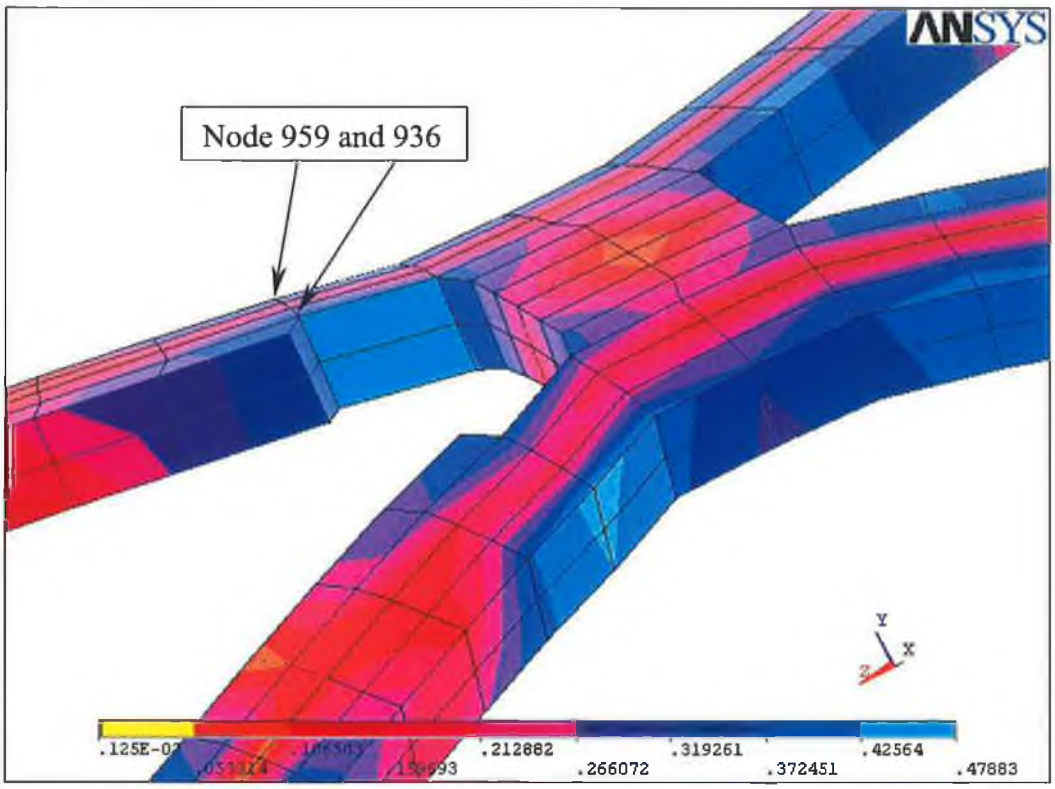

Figure 5.76: Close up view of the defected area

Figure 5.77 shows the development of von Mises stress at nodes 959 and 936. These two nodes represent the maximum von Mises stress developed in the slotted tube. Node 936 is located at top surface of the junction of the defected area as can be seen in Figure 5.76. Node 959 is located at exactly the other end of the defected area. It seems that the higher stress developed at the opposite side of the defected area. It was noticed that the stress history at the middle area of the slot (e.g. node 959) tends to develop gradually without dropping during the deflation of the process. On the other hand, the nodes that are located near the corner of the slot (e.g. node 936) tend to have "V" shape kind of stress history at the beginning of the deflation process.

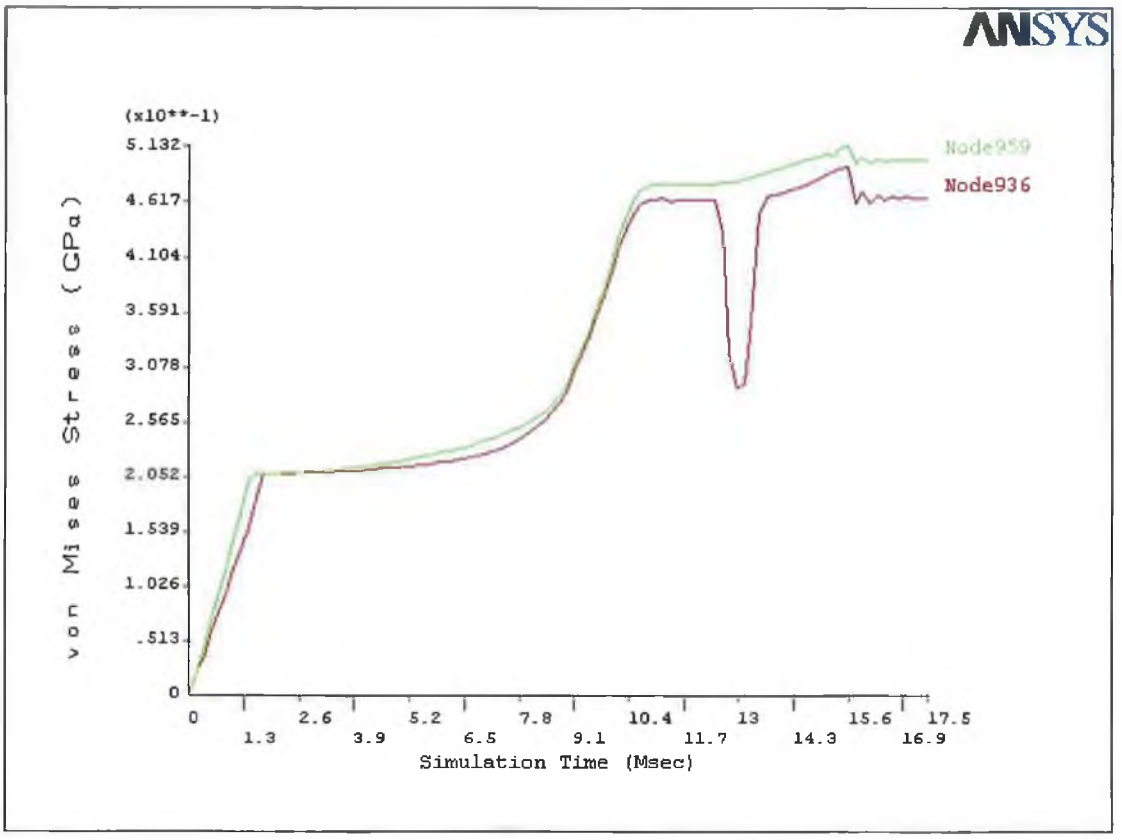

Figure 5.77: Development of stress at node 959 and 936

Two graphs were plotted in order to investigate the behaviour of the stresses developed in those two nodes. Figure 5.78 show the development of von Mises stress together with three principal and directional stresses in node 959. It can be seen from the figure that there were two phases involved. The first phase is the inflation of the balloon and the second is the deflation of the balloon.

During the first phase (inflation), the principal stresses tend to follow closely to the directional stresses. The maximum principal stress (S3) developed identically to the directional stress Z (SZ), which indicates that longitudinal stress dominated the initial phase of the process. The principal stress 1 (S1) took over from principal stress 3 and became prominent at the end of the inflation process. At this stage, the stress in x direction seems very likely to dominate principal stress 1, which might indicate that hoop stress is playing the major role now. One point should be noted is that the maximum principal stress can change direction at any time during the loading, especially when dynamic effects come into play such as that when the balloon is

deflated. The direction of the principal stresses cannot be determined unless a simple model and loading is used. Principal stress 2 follows closely to the directional stress y all the way to the end of the process. This indeed gives a very good indication that the principal stress 2 referred to the radial stress since the location of the node is almost parallel to the y-axis.

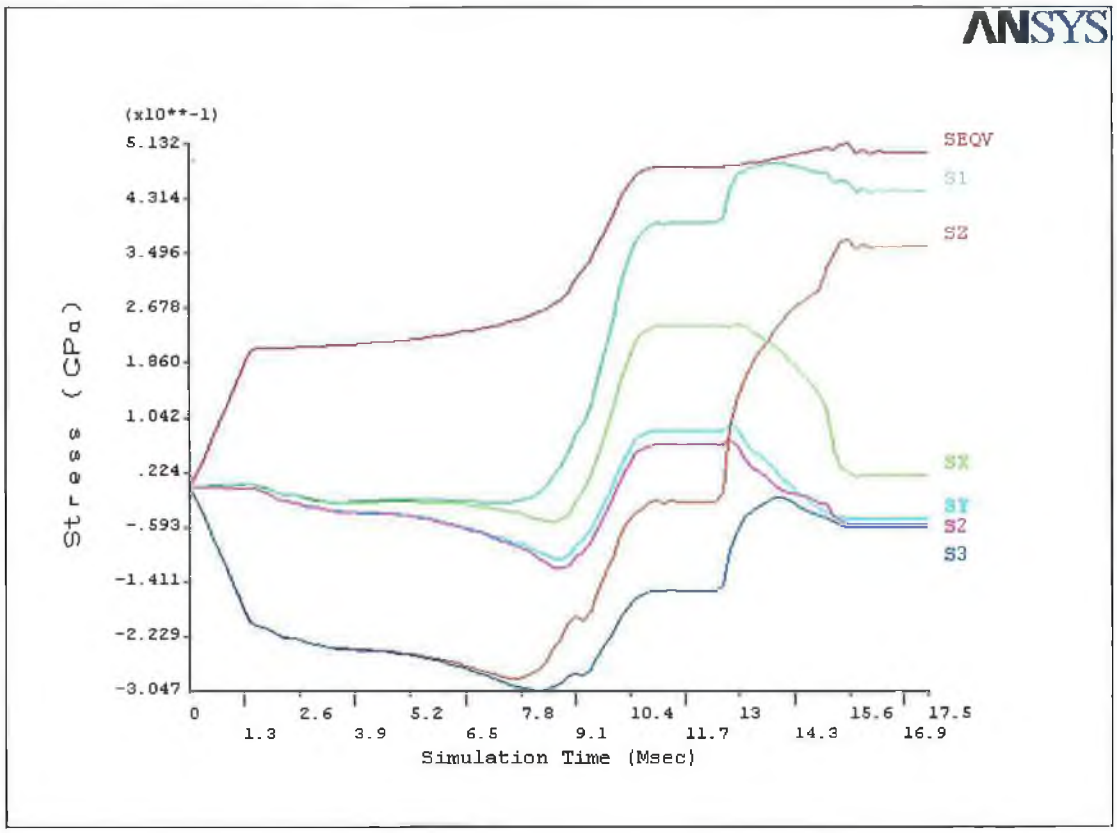

Figure 5.78: Development of von Mises, principal and directional stress at node 959

It is well known that von Mises stress consists of three principal stresses. Principal stress 1 and 2 were in the tensile manner and the principal stress 3 was in the compressive manner at the onset of the deflation process as can be seen in Figure 5.78. The reason von Mises stress increased gradually during the deflation process is due to the compressive stress in principal stress 3. Principal stress 1 provided the increment in von Mises stress due to the decrement of principal stress 2 (tensile manner) and 3 (compressive manner).

Figure 5.79 shows the development of von Mises stress, three principal and directional stresses in node 936. Directional stress Z tends to follow closely to the principal stress 1 at the initial stage. It soon looses its possession and begins to follow the principal stress 3 at approximate time of 3.9 milliseconds.

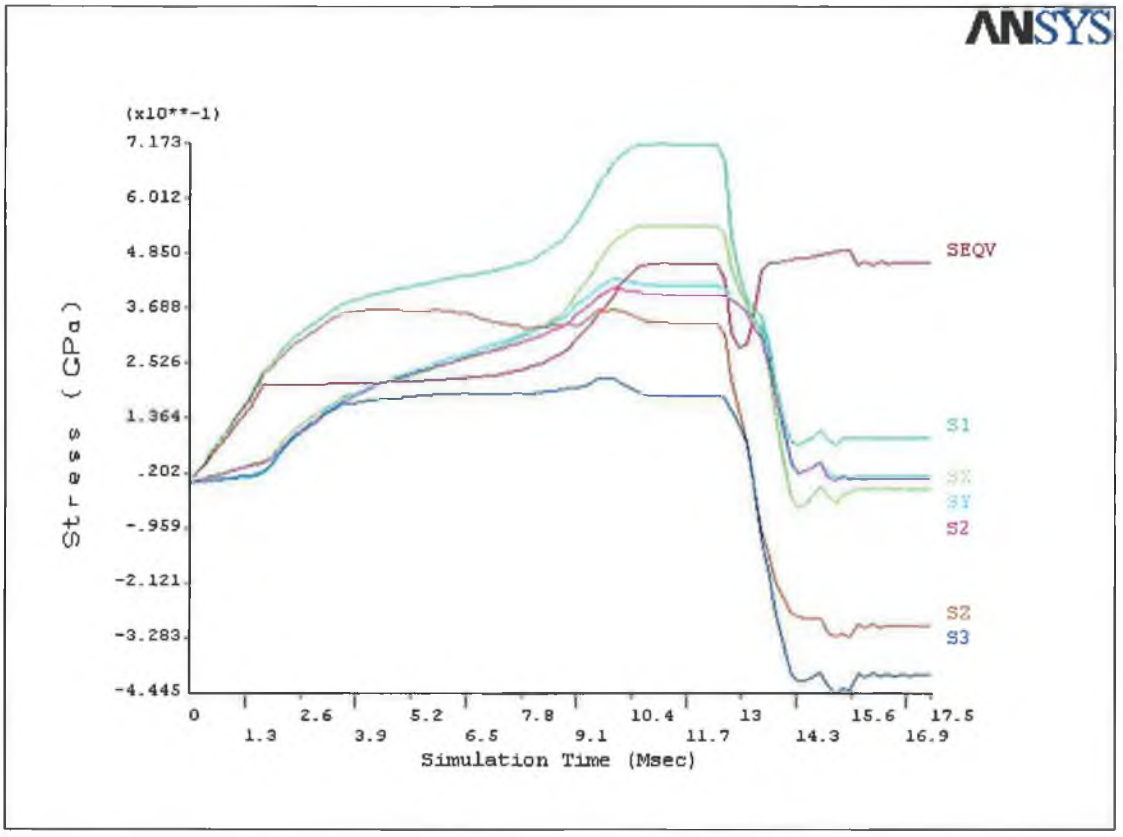

Figure 5.79: Development of von Mises, principal and directional stress at node 936

Unlike node 959, most of the stresses in node 936 were in the tensile manner throughout the process. The von Mises stress dropped because of the dropping in all three principal stresses in tensile manner. The von Mises stress begins to pick up as soon as it reaches the lowest point of stress during the deflation process. The increment of the von Mises stress here is due to the course of changing direction from tensile to compressive stress in principal stress 3 that seems very likely to be in z direction. The defected area was pulled in the tensile manner at the beginning of the dilatation process. The defected area was stretched in a compressive manner as soon as the pressure load was released. This is unlike the situation at node 959 in

which tensile force seemed to dominate the deformation characteristic in that area during the deflation process.

5.6.2.2 Deployment pressure vs. displacement

Figure 5.80 shows the magnitude of the central slotted tube diameter at maximum deployment pressure during the dilatation process. The original and the imperfection slotted tube seemed to develop identically towards the end of the dilatation process. However, the defected slotted tube experienced higher level of expansion at the same level of deployment pressure when the pressure level of 1.5 MPa was achieved.

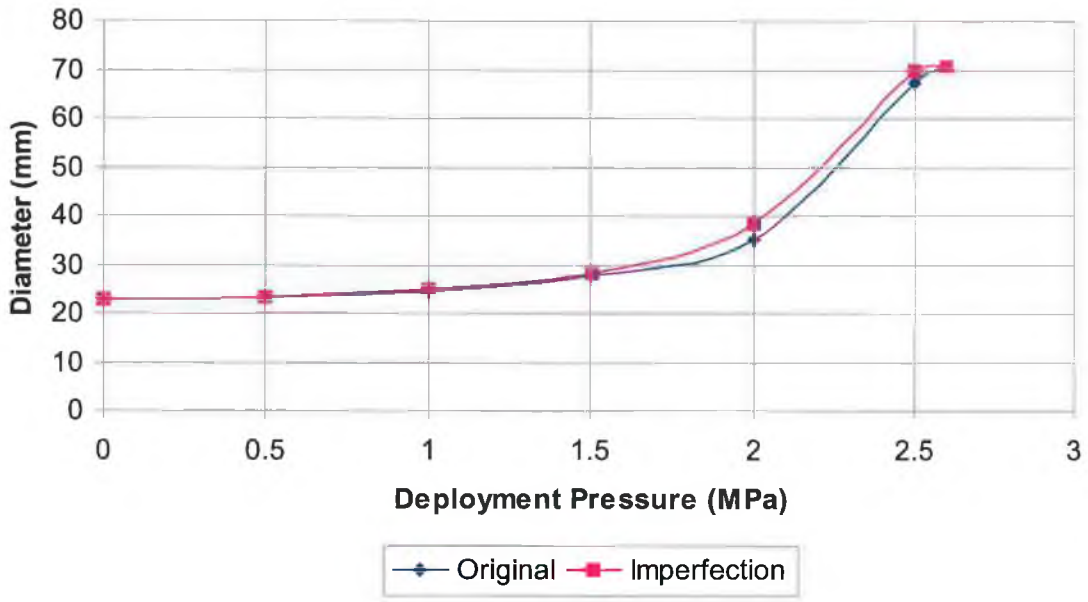

Figure 5.80: Expansion of slotted tube diameter with deployment pressure

Apparently, this is due to the imperfect structure of the slotted tube. The weakness of the structure allows the body struts of the slotted tube to open up quicker than the flawless geometry. As a result, the imperfect slotted tube experienced the higher level of expansion. The original and the imperfect slotted tube might experience a different level of expansions but the magnitude of discrepancy was insignificant. The maximum diameter of the original and the imperfect slotted tube achieved were 70.76 mm and 70.77 mm respectively.

5.6.2.3 Elastic recoil

Figure 5.81 shows the reduction of the original and imperfection slotted tube central diameter during the deflation process. The graph shows that the elastic recovering of the imperfect slotted tube is identical to that of original slotted tube despite the existence of the flaws. The central diameter of the flawless and defected geometry was found to be 59.1 mm and 59.13 mm respectively. Both of them experienced 16.5% shrinkage from the maximum diameter obtained during the maximum deployment pressure.

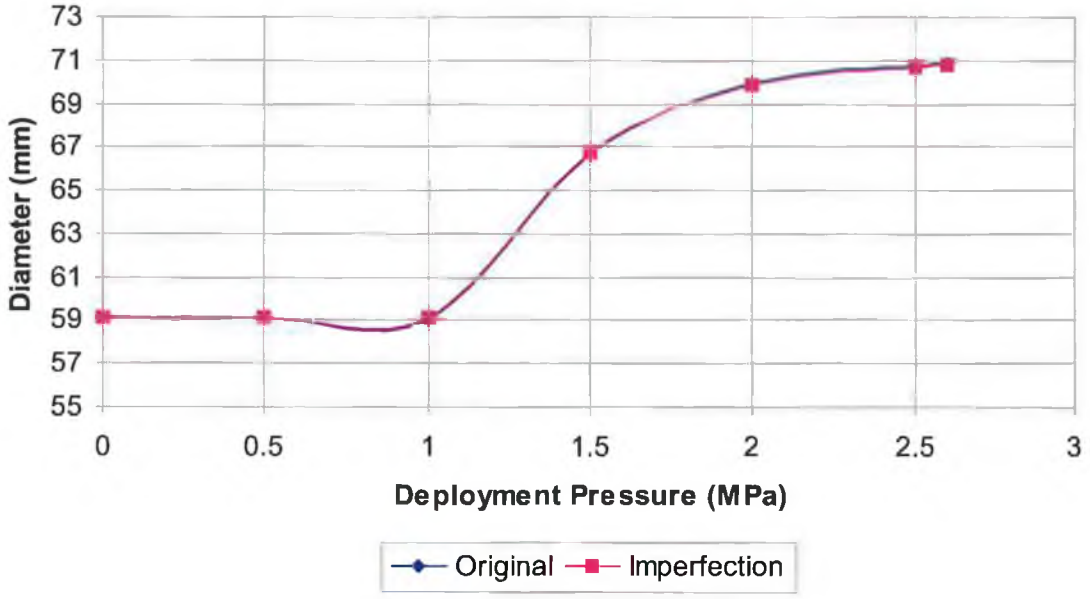

Figure 5.81: Elastic recoil of the flaw and flawless slotted tubes

5.6.2.4 Foreshortening

Figure 5.82 shows the development of foreshortening with simulation time for the original and imperfect slotted tube respectively. The graph shows there is insignificant discrepancy of foreshortening between original and imperfect slotted tubes during and after the simulation process. The length of the slotted tubes shortened was found to be 2.23 mm and 2.39 mm after the deflation process.

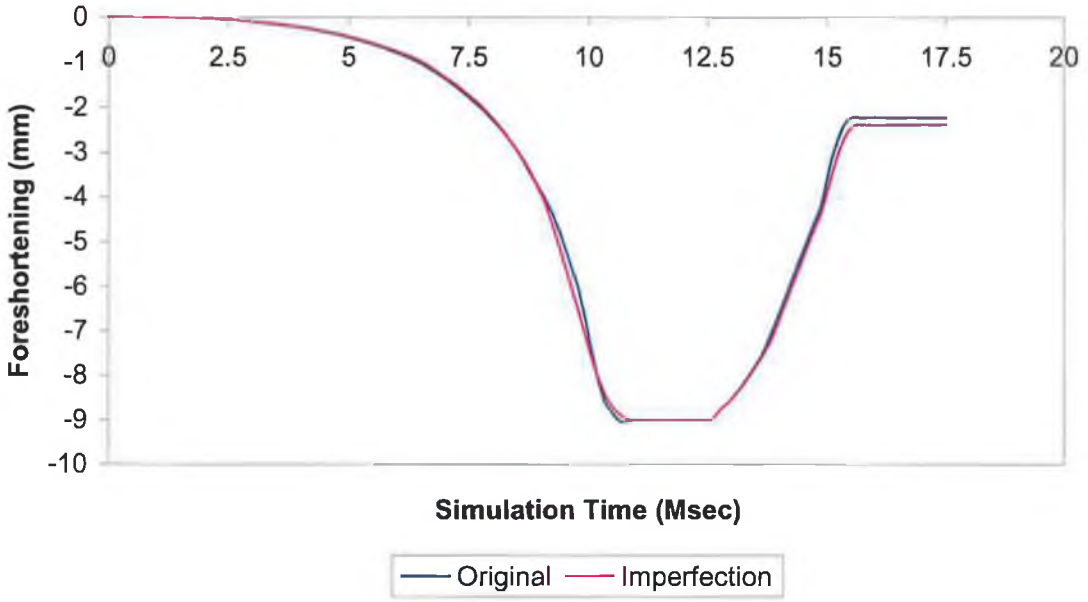

Figure 5.82: Foreshortening of the original and imperfection slotted tubes

5.7 Analysis of Balloon Thickness on Slotted Tube Expansion

Balloon thickness is one of the major factors that will affect the outcome of the expansion characteristic of stent following stent deployment. The optimal balloon thickness for the purpose of stent dilatation has not been defined. However, a larger balloon very often been called as an oversized balloon was evidenced as a cause to restenosis [105]. The section will detail the effect of the balloon thickness on the expansion characteristic, stress distribution, degree of expansion and foreshortening of the stent.

5.7.1 Modelling and Loading

Three simulations were carried out to examine the effect of the balloon thickness on the expansion characteristic of the slotted tube stent. The slotted tube model utilised in this section was identical to the last few section i.e. 25.4 mm outer diameter and 23 mm inner diameter with 86.8 mm in length. However, the thickness of the balloons was altered. The balloons were modified to three different thickness based on the ratio of 0.5:1:1.5. Assuming that the nominal balloon thickness is equal to the thickness of the slotted tube stent i.e. 1.2 mm, then the smaller size of the balloon is

equivalent to half size of the nominal balloon, which is only 0.6 mm. Similarly, the bigger size balloon was modelled to be 1.8 mm in thickness. In spite of the changes made for the balloon thickness, the length of balloon was kept constant for all the three simulations i.e. 114 mm long.

Figure 5.83 to Figure 5.85 show the finite element models of one-eighth of the slotted tube with different balloon thickness respectively. The balloons were discretised by 35 elements along its length and 32 elements in circumference with 3 elements across the thickness for the smaller size and nominal balloon thickness. As for the bigger size balloon thickness, it was discretised by 35 elements along its length and 32 elements in circumference with 4 elements across the thickness.

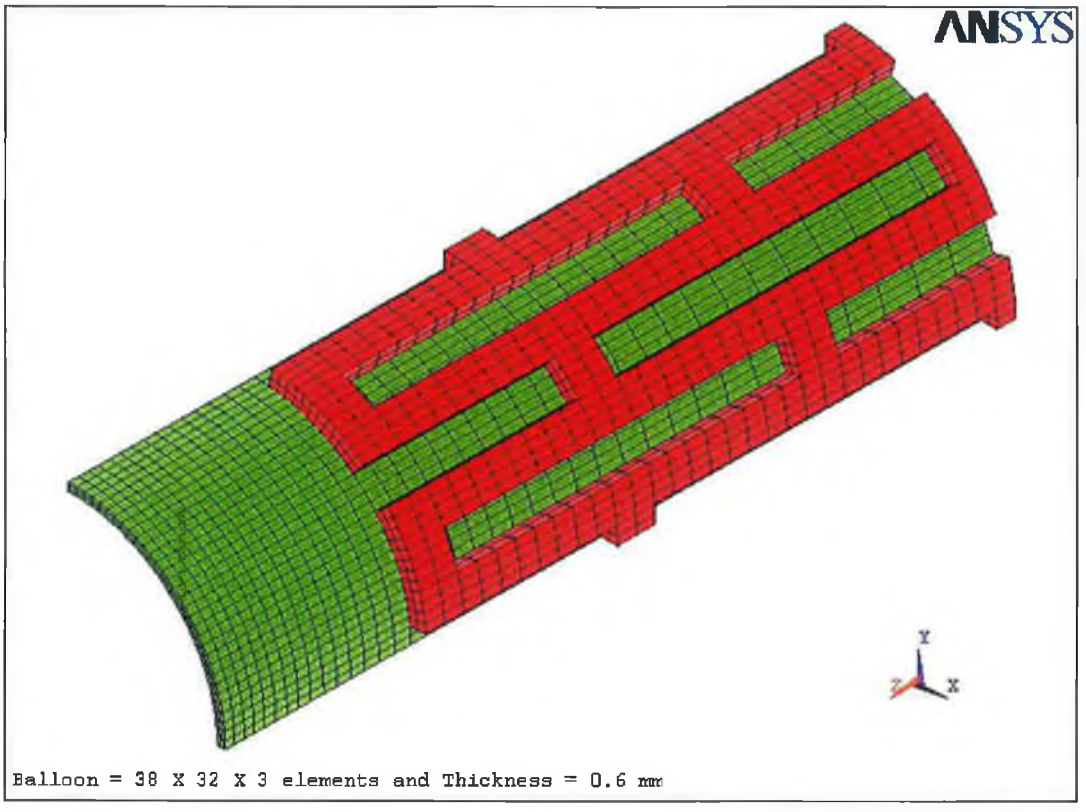

Figure 5.83: One eight of the finite element model with balloon thickness = 0.6 mm

A two parameter Mooney-Rivlin constants with C(10) = 0.205715E-02 and C(01) = 0.743122E-02 were used for all three simulations. The material properties for the balloon here were assumed twice as tough as the balloon material properties been used in previous simulations.

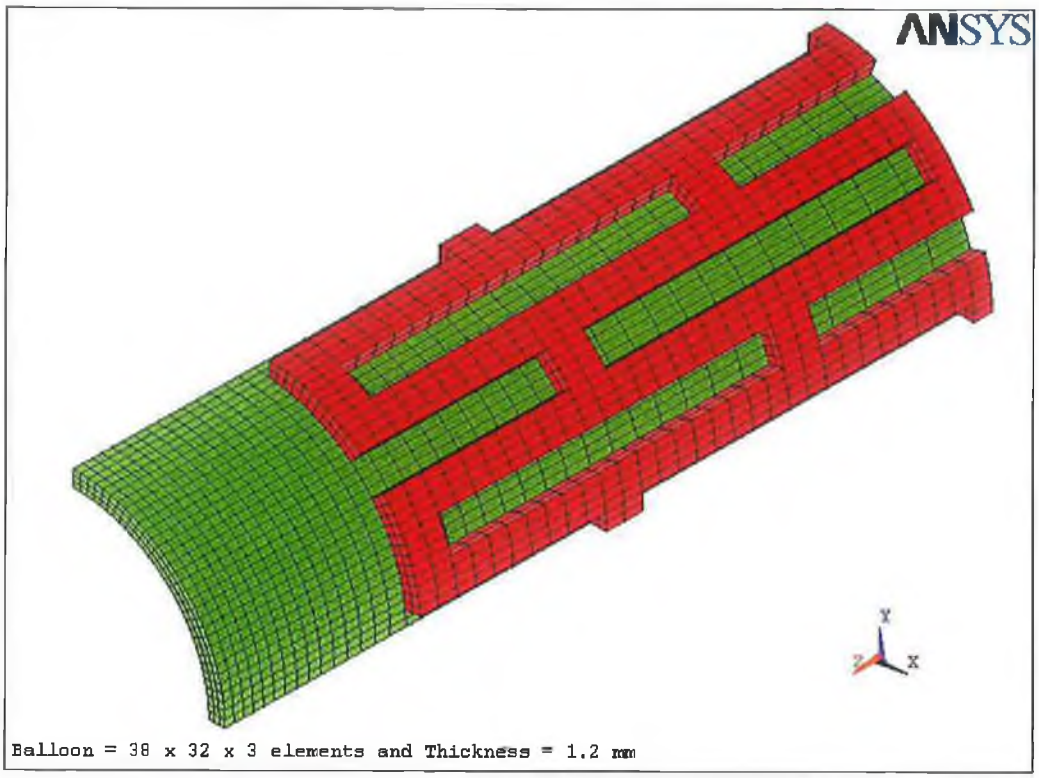

Figure 5.84: One eight of the finite element model with balloon thickness = 1.2 mm

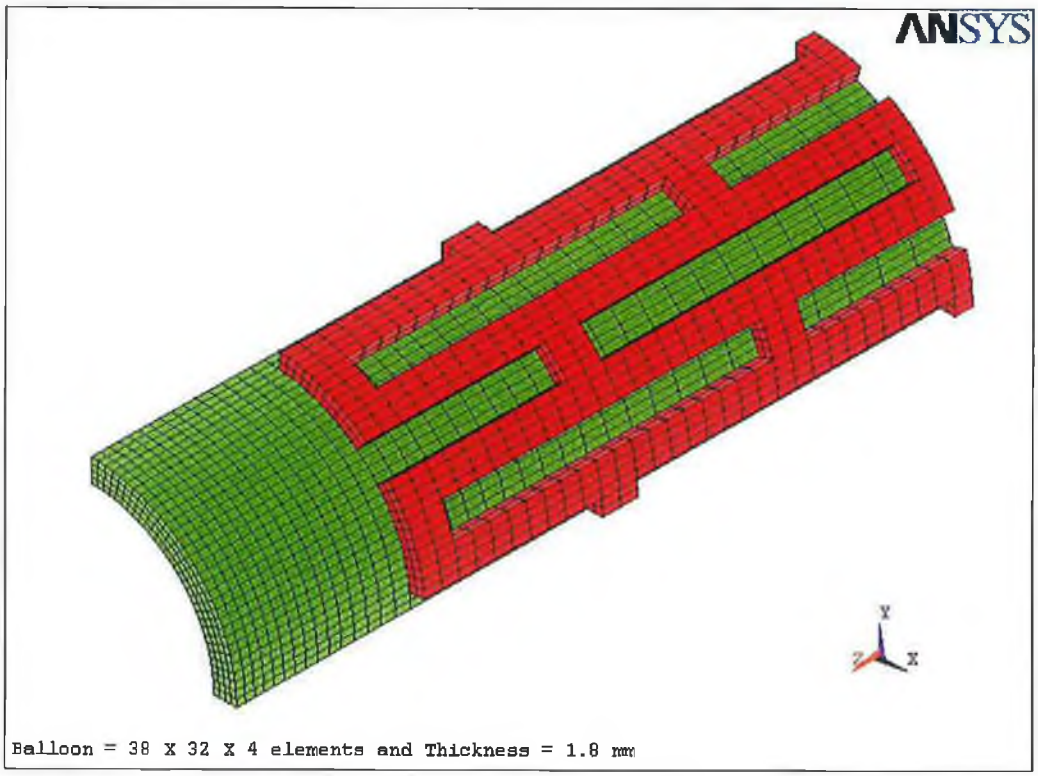

Figure 5.85: One eight of the finite element model with balloon thickness = 1.8 mm

The original material properties were utilised initially but it was found that the material was too soft and unable to properly expand the slotted tube when running the simulation with the thinner size balloon. It caused an excessive bulging near the end of the slotted tube, which ultimately resulted in failure of the balloon material. Therefore, the stress strain curve of the polyurethane material was modified in such a way that the material will have a higher elastic modulus. These changes enable the simulations to run successfully and a fair comparison could be made.

Different levels of deployment pressure were applied according to the different thickness of balloons used. Higher pressure was needed in order to expand the slotted tube by thicker balloon. Figure 5.86 shows the load history of the simulation process for the three different balloons thickness.

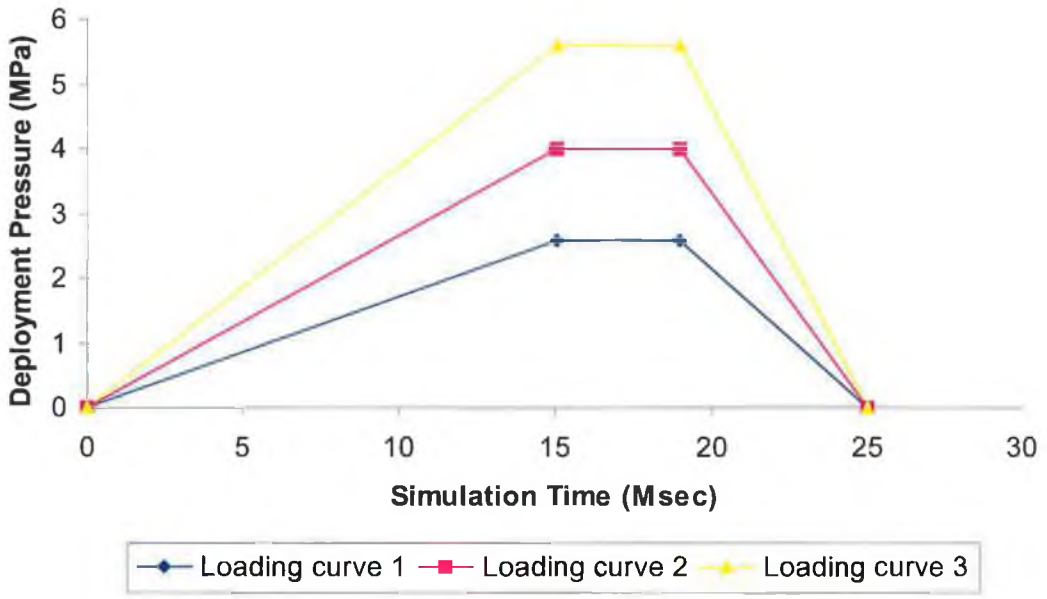

Figure 5.86: Loading curves

Load curve 1 in Figure 5.86 describes the load history applied on the balloon thickness of 0.6 mm for the simulation process. The load increased from 0 to 15 milliseconds and then held constant for 4 milliseconds and finally reduced to zero at time 25 milliseconds. The second simulation of the expansion process was carried out on a balloon thickness of 1.2 mm. The load curve 2 describes the load history used for the simulation. The load applied here was much higher than the first simulation. The maximum deployment pressure applied was 4 MPa. The third simulation of the

expansion process was carried out on a balloon thickness of 1.8 mm. This was the thickest balloon being used and it required the highest deployment pressure amongst the three simulations. The maximum deployment pressure applied was 5.6 MPa. As in the first simulation, the load was held constant for 4 milliseconds and then reduced to zero pressure at the time of 25 milliseconds.

5.7.2 Result and Discussion

5.7.2.1 Stress analysis and uniformity

Figure 5.87 shows the residual stress distributed in the slotted tube for a balloon thickness of 0.6 mm when the deploying pressure was released to zero. The maximum residual stress in the slotted tube at that point of time was approximately 472 MPa. Given that the geometry of the slotted tube and the length of the balloon were identical for the three simulations, the stresses generated over the entire slotted tube were purely depending on the level of the deployment pressure and also the thickness of the balloon. The expansion characteristics of the slotted tube were therefore influenced by the variation of the balloon thickness that was in contact with the slotted tube stent.

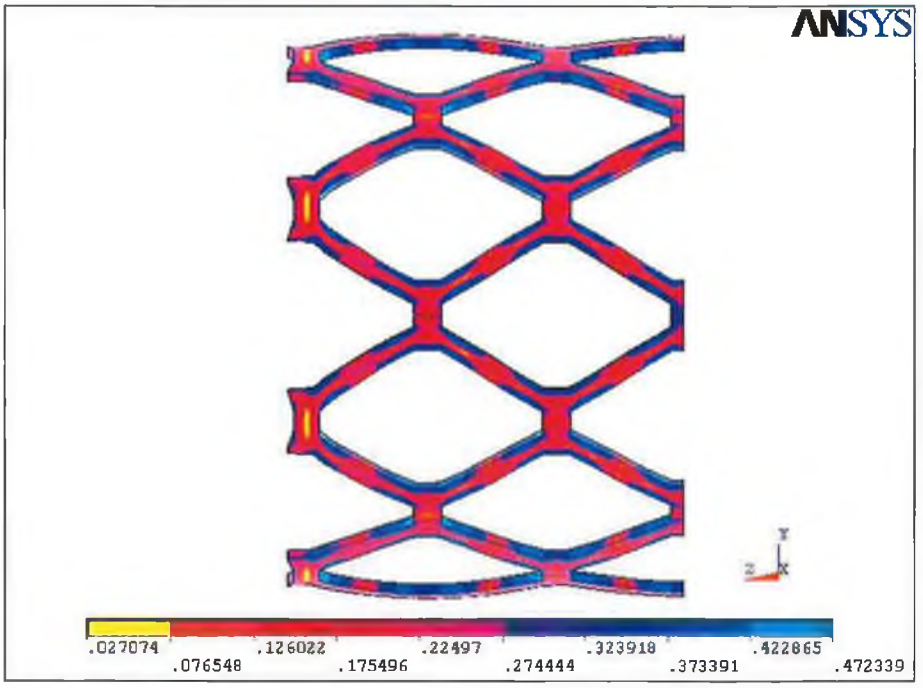

Figure 5.87: Residual stress in the deformed tube by 0.6 mm balloon thickness

In the case of 0.6 mm thickness, the force required to initiate the expansion was lower. This was due to the fact that only a little force needed to distend the balloon simultaneously. Most of the force was used to expand the slotted tube. There was very little pressure lost from the initial level of the deployment pressure when it came to the interference point between the outer surface of the balloon and the inner surface of the slotted tube.

Figure 5.88 shows the deformation of the balloon at maximum deployment pressure. The smaller thickness of the balloon caused the distal and proximal of the balloon to open up first and easily. As a result, the balloon transformed into a more uniform shape and moulded itself around the slotted tube stent as it inflated. Nevertheless, it was found that the distal and proximal of the balloon always maintained a higher level of displacement (apple shape) until a point at which the slotted tube was finally fully opened up. At this point, the slotted tube was almost level with the balloon. When the balloon was deflated, the slotted tube retained its deformed shape and it was the most uniform amongst the three balloons thickness modelled as can be seen from the figures.

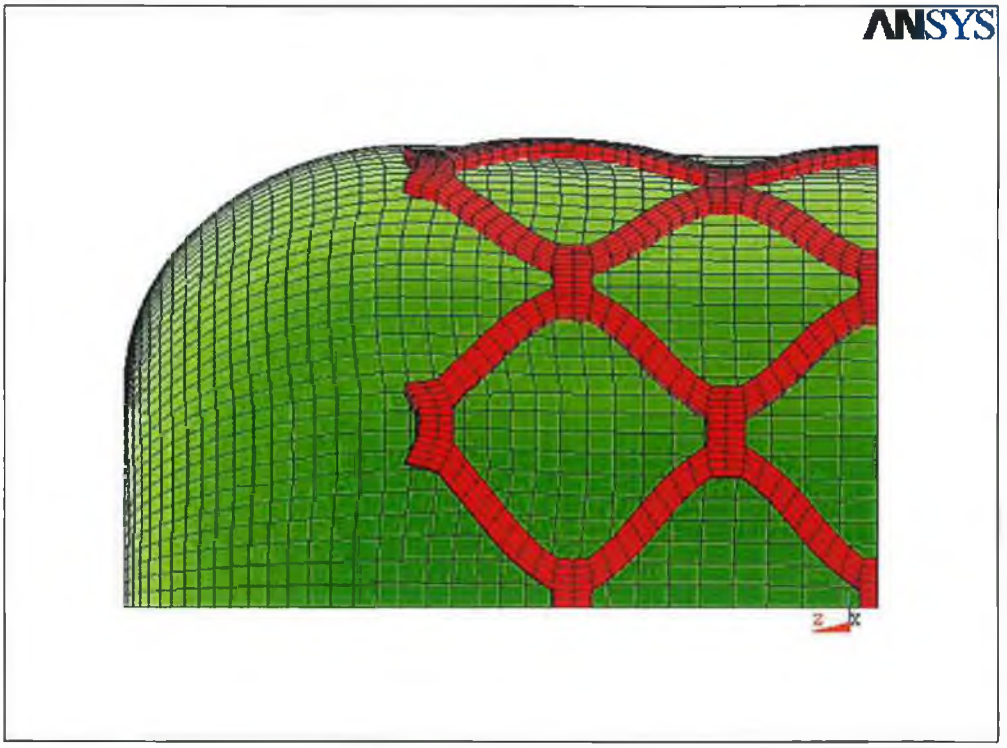

Figure 5.88: Deformation of 0.6 mm balloon at maximum deployment pressure

Figure 5.89 shows the residual stress distributed in the slotted tube for the balloon thickness of 1.2 mm when the deployment pressure was released to zero. The maximum stress in the slotted tube was 473 MPa at the four corners of the slots. The deformation characteristic by 1.2 mm balloon thickness was somewhat different. At the beginning of the expansion process, the distal and proximal of the balloon did not bulge as much as in the case of thinner balloon. It required a lot more pressure to perform the job. It was discovered that all the slotted tube expansions begun from the ends and slowly transferred force to the centre, which finally caused the centre part of the slotted tube to open up. At one point, the slotted tube seemed to expand in a uniform manner as shown in Figure 5.90. This point was the point that almost levelled with the balloon as described earlier for the thinner balloon. The pressure load at this point in time was 3.4 MPa. The distal and proximal of the balloon gradually expanded in a smaller magnitude compared to the centre part of the balloon after passing this point. The middle section of the balloon became weaker due to the constraints at the distal and proximal of the balloon. As a result, the slotted tube experienced a higher deformation at the central part and formed an ellipse like shape together with the balloon. Figure 5.91 shows the ultimate deformation of the balloon and slotted tube at maximum deployment pressure.

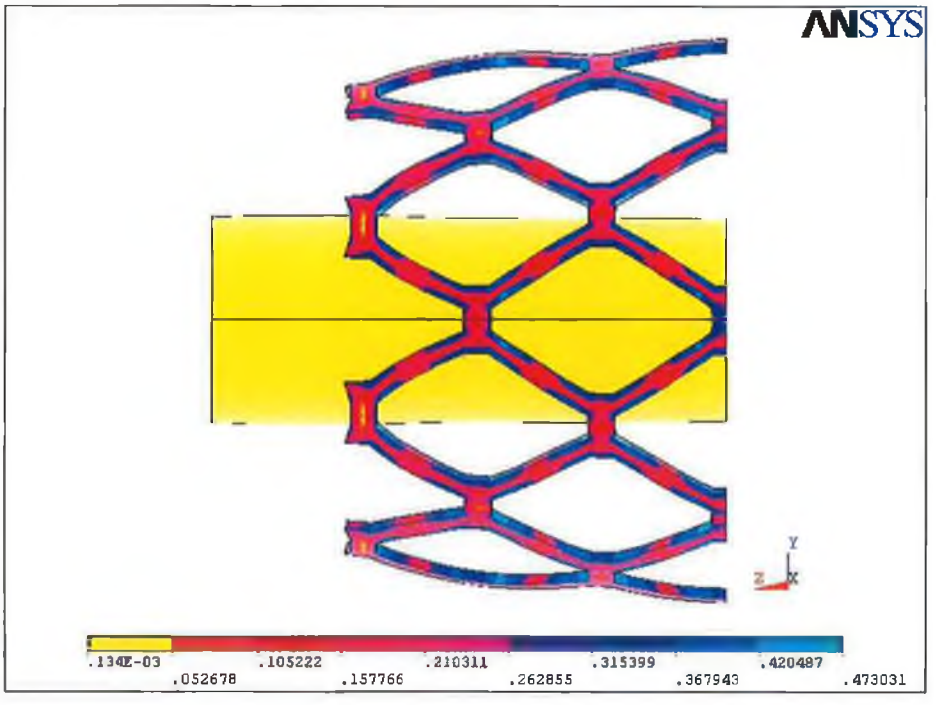

Figure 5.89: Residual stress in the deformed tube by 1.2 mm balloon thickness

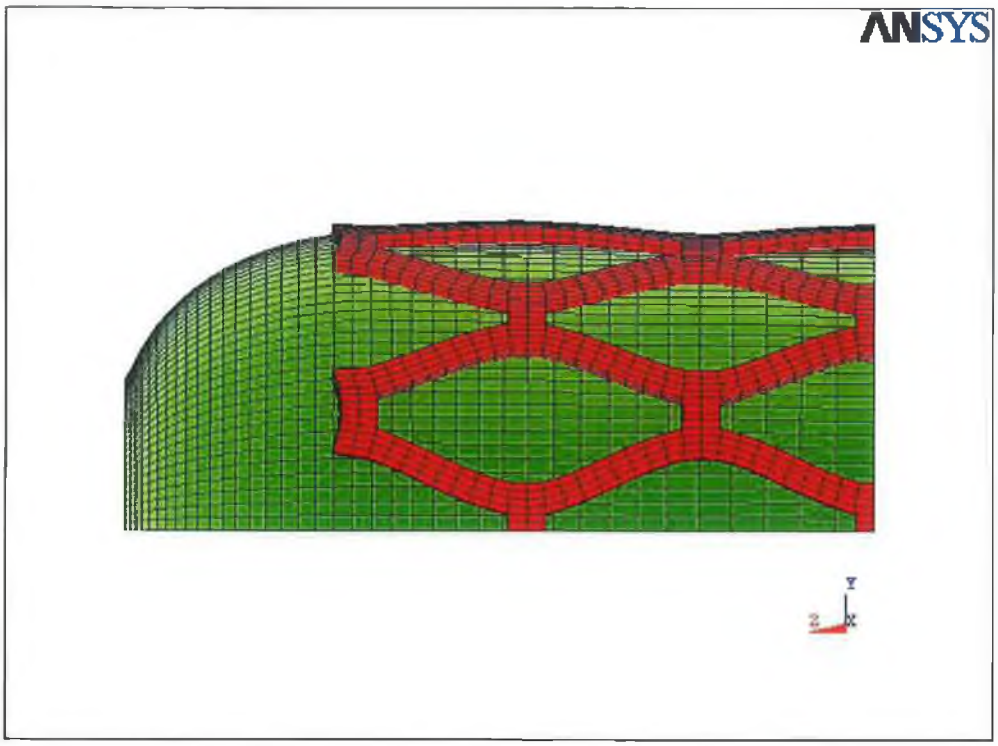

Figure 5.90: Deformation of the balloon and slotted tube at time 12.75 msec

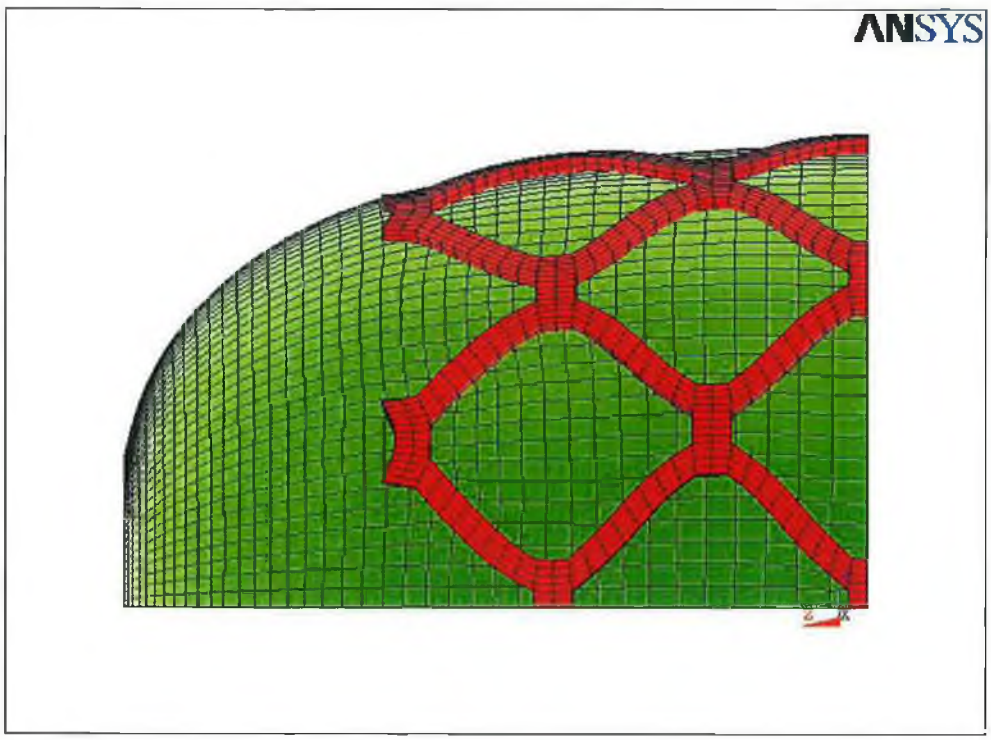

Figure 5.91: Deformation of 1.2 mm balloon at maximum deployment pressure

Figure 5.92 shows the residual stress distributed in the slotted tube for the balloon thickness of 1.8 mm when the deployment pressure was released to zero. The maximum residual stress at that time was 475 MPa. Given that all three balloons thickness increased by the same value i.e. 0.6 mm, it was fair to compare the stress in the slotted tube at different level but same amount of pressure increment as well. For instance, the stress level at pressure level of 5.4 MPa (thickness 1.8 mm) was compared to the stress level at pressure of 4 MPa (thickness 1.2 mm) and 2.6 MPa (thickness 0.6 mm). So, there was 0.6 mm thickness increment in each balloon together with 1.4 MPa increment in pressure. The purpose was to check in the slotted tube to see if there were any significant change in stresses between them. It was found that the stresses in the slotted tube for the three cases were 472 MPa (thickness 0.6 mm), 473 MPa (thickness 1.2 mm) and 460 MPa (thickness 1.8 mm) respectively. These figures suggested that the increment of thickness by the same ratio as well as the deployment pressure did not have a major effect on the maximum stress generated.

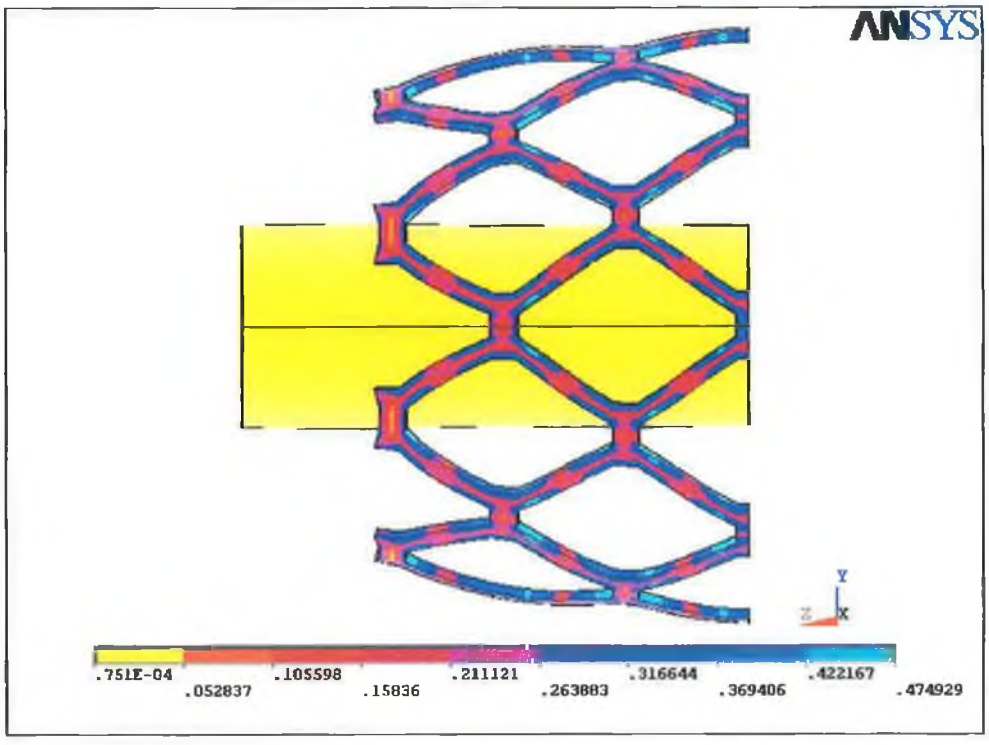

Figure 5.92: Residual stress in the deformed tube by 1.8 mm balloon thickness

However, the same approach was taken to measure the uniformity of the slotted tube in those three cases. The radial displacement in the centre of the slotted tube was taken to make comparison with the radial displacement in the end of the slotted tube. It was found that the discrepancies between the two radial displacements from the thinnest to the thickest balloon were +1.56 mm, -3.08 mm, and -4.65 mm respectively. A higher discrepancy indicates the slotted tube is less uniform, assuming that zero millimetre represents the perfect uniformity. Therefore, the thinnest balloon caused an excessive expansion at the ends of the slotted tube. The thickest balloon caused the least uniform expansion of the slotted tube.

Figure 5.93 shows the deformation of the slotted tube and the balloon at the point that they both were at the same level. At that point, the expansion process was as if returning to the initial expanding conditions except that the slotted tube already opened up and the force in the balloon is no longer uniform. More force was needed to bulge the distal and proximal of the balloon and less pressure was needed for further expansion mainly because the bond structure of the struts was weakened. Owing to these reasons, the central part of the slotted tube begun to bulge excessively. This can be seen from Figure 5.94 that shows the deformation of the slotted tube and the balloon at maximum deployment pressure.

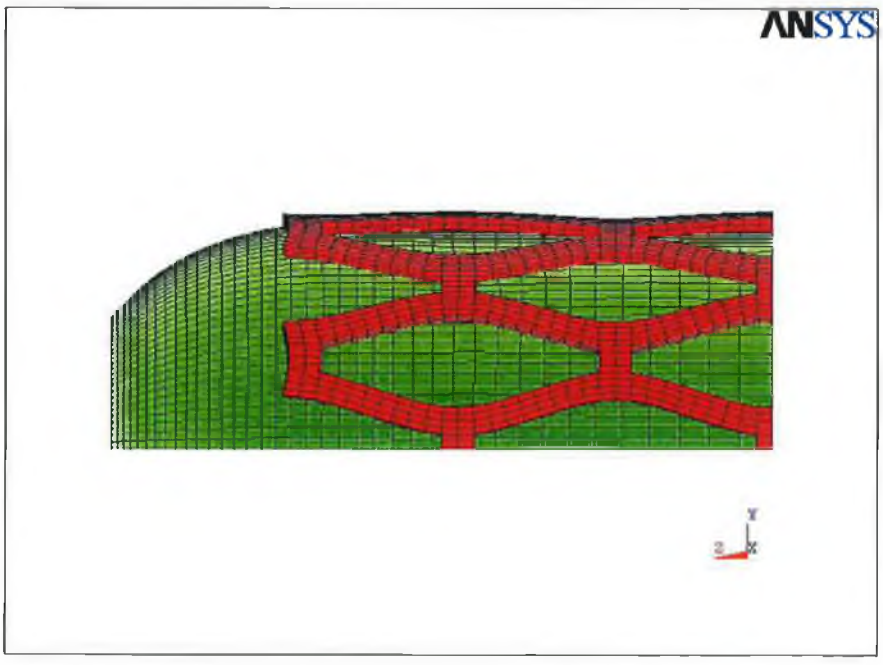

Figure 5.93: Deformation of the balloon and slotted tube at time 11.5 msec

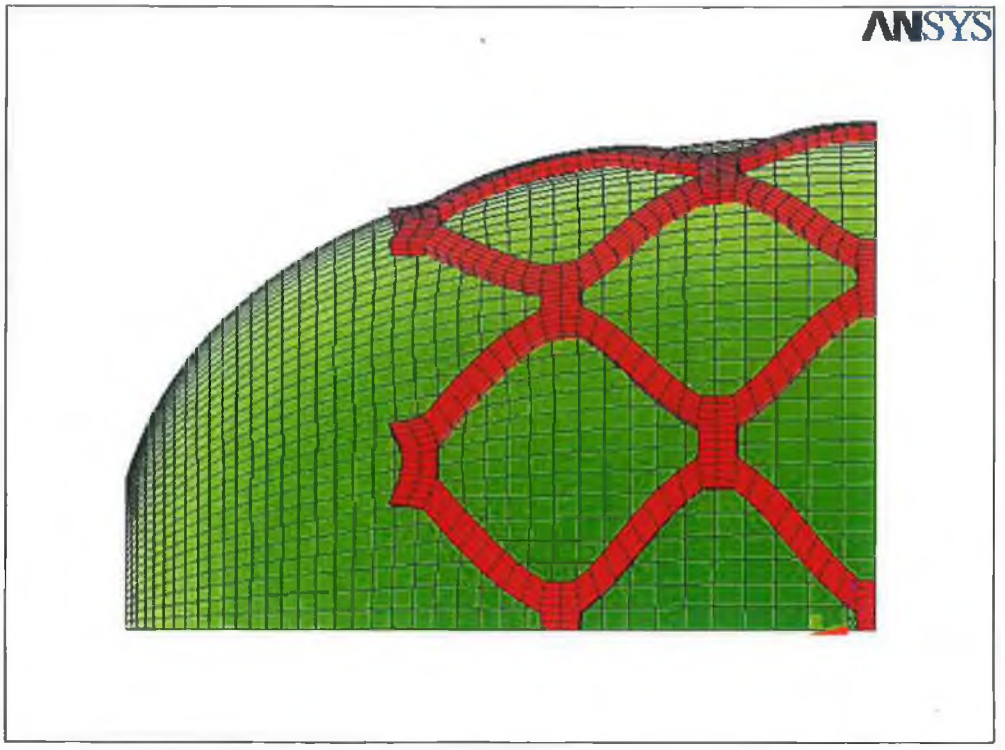

Figure 5.94: Deformation of 1.8 mm balloon at maximum deployment pressure

5.7.2.2 Deployment pressure vs. displacement

Figure 5.95 shows a graph that plotted for the development of the slotted tube central diameter at different level of pressure deployment. The graph shows the relationship between the diameters obtained at same level of pressure for the different thickness of balloons was irrelevant. For instance, at pressure level of 2 MPa the differences in diameter obtained from 0.6 mm and 1.2 mm balloon thickness were much higher compared to the differences in diameter obtained from 1.2 mm and 1.8 mm balloon thickness despite the fact that they both were increased by the same value of thickness i.e. 0.6 mm. Nevertheless, the pressure increases with increasing balloon thickness. At the same level of displacement the deployment pressure needed for 1.8 mm was almost twice as much as for 0.6 mm balloon thickness, whereas the pressure needed for 1.2 mm was one and a quarter of the 0.6 mm balloon thickness. This indicates that increase the pressure proportionally to the thickness of the balloon would result in the same level of displacement. The ratio of the three balloon thicknesses was 0.6 : 1.2 : 1.8 which equals to the ratio of 1 : 2 : 3. It was found that the ratio of the pressure load to achieve the same level of radial displacement was 1 :

1.5 : 2. This indicates that the magnitude of increment in the pressure load was lower than the magnitude of increment in the balloon thickness.

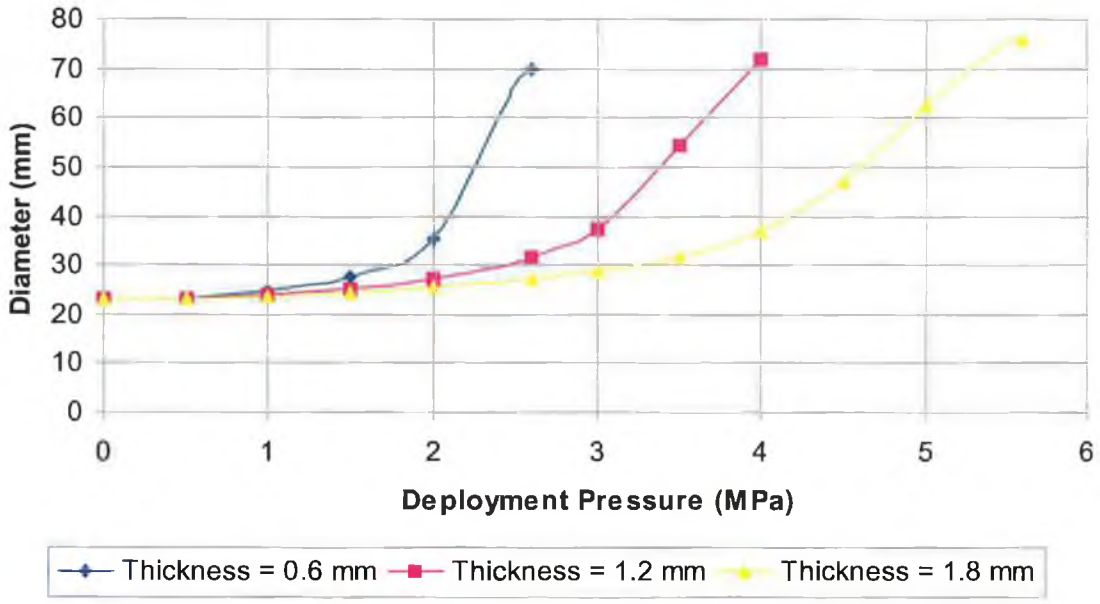

Figure 5.95: Expansion of slotted tube diameter with deployment pressure

5.7.2.3 Elastic recoil

Figure 5.96 shows the reduction of the slotted tubes diameter following the deflation of the balloons. At pressure level of 1 MPa, the slotted tube diameter decreased from 69.7 mm to 58.1 mm for the balloon thickness of 0.6 mm. The total decrement of diameter was therefore 11.6 mm, which was about 16.6% from the maximum diameter expansion. As for the balloon thickness of 1.2 mm, the slotted tube experienced the elastic recoil until the pressure of 2 MPa was reached. The central slotted tube diameter decreased from 71.8 mm to 61 mm at this pressure level. Therefore, the discrepancy between them was 10.8 mm and the percentage of decrement from the maximum diameter expansion was about 15%. The elastic recoil for the balloon thickness of 1.8 mm stopped at the highest pressure i.e. approximately 3.5 MPa. The central diameter of the slotted tube dropped from 75.9 mm to 65.6 mm. The total diameter dropped was 10.3 mm and the percentage of decrement from maximum expansion was 13.6%. This figures showed that the balloon thickness might have a little effect on the elastic recoil of the slotted tube. However, there was no strong statistic to show that they were strongly related. This

was due to the fact that the structure of the slotted tube and the ultimate shape of deformation had changed. In which case, the uniform expansion was no longer accounted for.

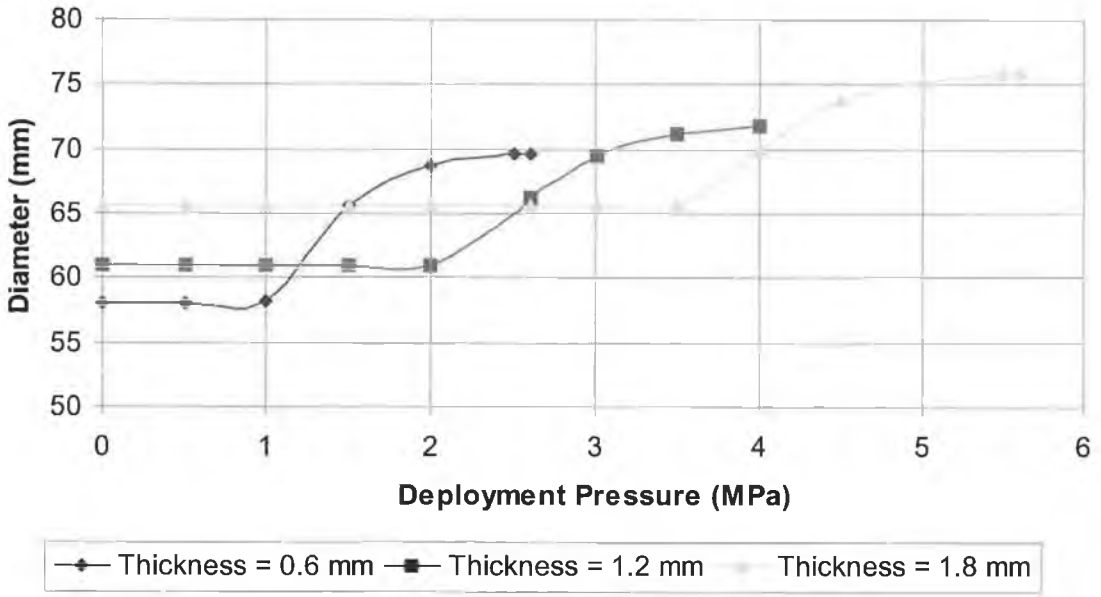

Figure 5.96: Elastic recoil of the slotted tube

5.7.2.4 Foreshortening

Figure 5.97 shows the foreshortening of the length of the slotted tube throughout the dilatation process. As expected the foreshortening of the slotted tube developed gradually. Three deployment pressure levels were selected in order to identify the effect of the balloon thickness on the foreshortening of the slotted tube. One deployment pressure from each case was chosen to make comparison between them. The foreshortening achieved for the balloon thickness of 0.6 mm at pressure level of 2.6 MPa was 8.11 mm. As for the balloon thickness of 1.2 mm, the foreshortening measured was 6.94 mm at the pressure level of 3.9 MPa. Similarly, by the same increment of pressure and balloon thickness in the third simulation the foreshortening achieved was 6.38 mm. The magnitude of foreshortening seemed to be decreasing with increasing balloon thickness. This was due to elasticity of the balloon at the distal and proximal. As explained before, thicker balloon prevented itself from expanding uniformly. As a result, the integration between the slotted tube and the balloon forced the former one to follow the way of expansion of the balloon. In other

word, the slotted tube here moulded itself around the balloon rather than letting the balloon mould around the slotted tube.

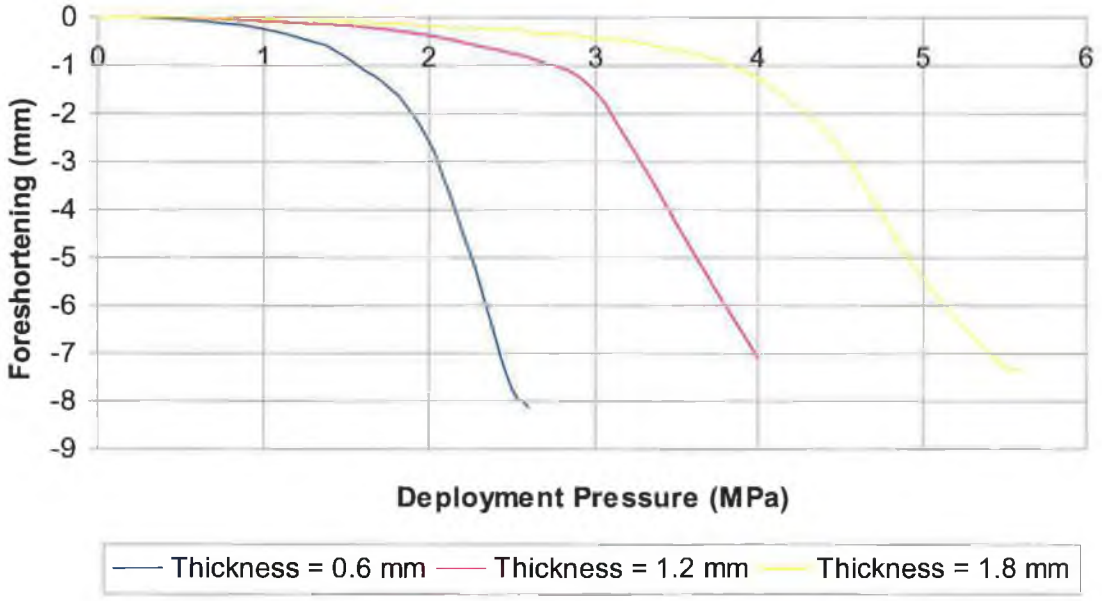

Figure 5.97: Foreshortening of the slotted tube with pressure

5.8 Analysis of Slotted Tube Stent Geometry

At deployment, stent struts provide a frame over which the vascular is stretched. One aspect of damage that induced by stent is strut-imposed vascular injury. This injury is often regards as neointimal hyperplasia (abnormal increase in number of cells). It is believed that the stent design may affect the neointimal growth. Understanding the expansion characteristics of different stent geometry may allow novel strategies for device design and use.

5.8.1 Modelling and Loading

Apart from the design 1 that identical to previous sections, four different designs of slotted tube stent were modelled in this section. The simulations were carried out to expand five stainless steel slotted tube stent of 25.4 mm outer diameter and 23 mm inner diameter. The length of the slotted tube stent was varied with four of them having an equal length i.e. 86.8 mm. The final one was modelled to be 95.2 mm. Each of the stent was modelled to have different design. Design 1 contains an equal

width amongst the slots and the struts. Design 2 possesses wider slots in which the slots were modelled to be 20 % wider than design 1. On the contrary, design 3 was modelled to have wider struts and the slots were calculated to be 20 % narrower than design 1. The width of the struts and the slots in design 4 remains as in design 1 except that the length of the slots was increased by 10 %. Design 5 was modelled to have more struts and slots. The number of the struts and slots were increased by 50 % compared to the other designs. The dimensions of the five different designs are shown in Figure 5.98 to Figure 5.102.

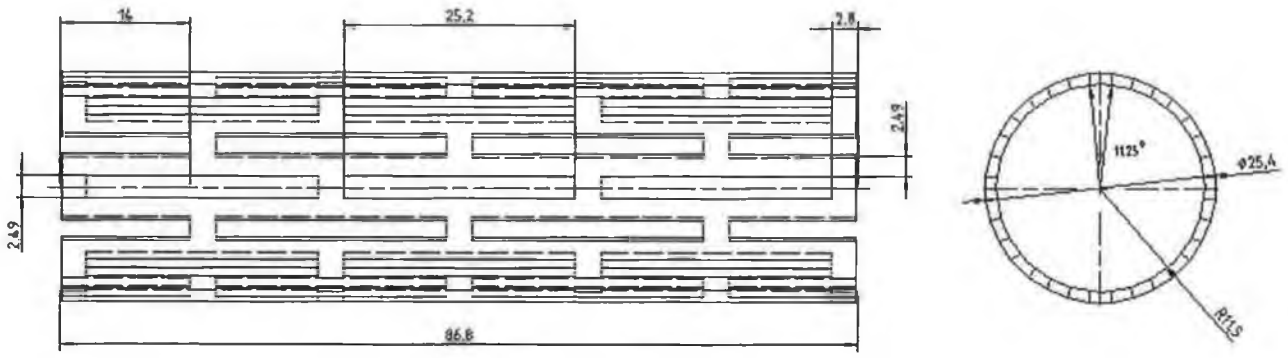

Figure 5.98: Geometry of the slotted tube for design 1

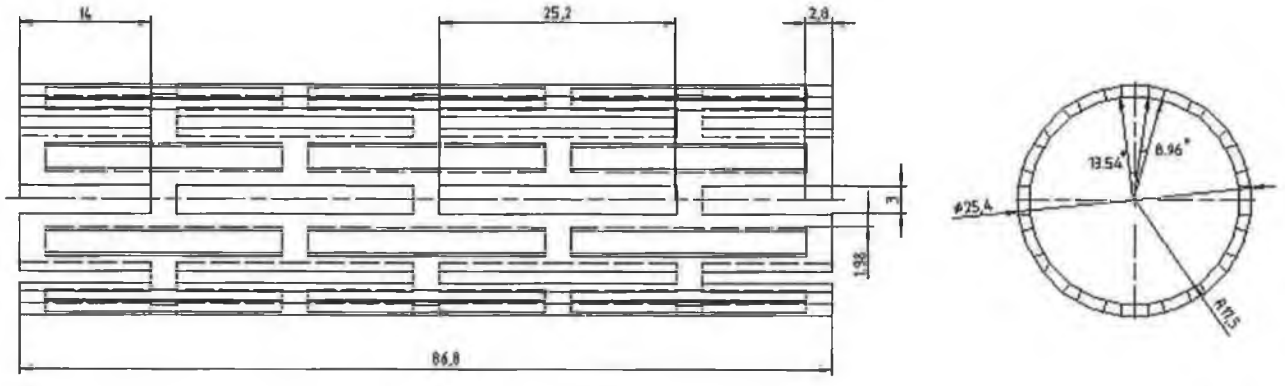

Figure 5.99: Geometry of the slotted tube for design 2

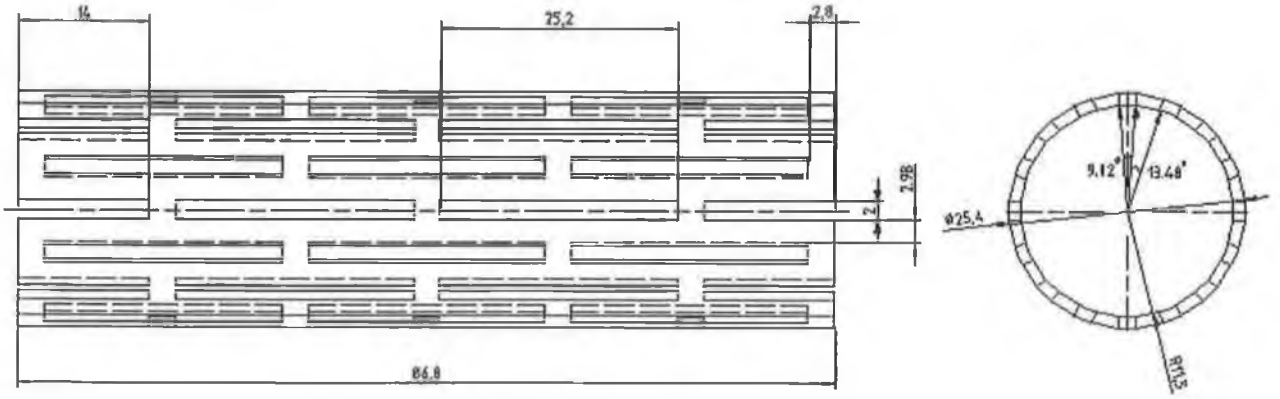

Figure 5.100: Geometry of the slotted tube for design 3

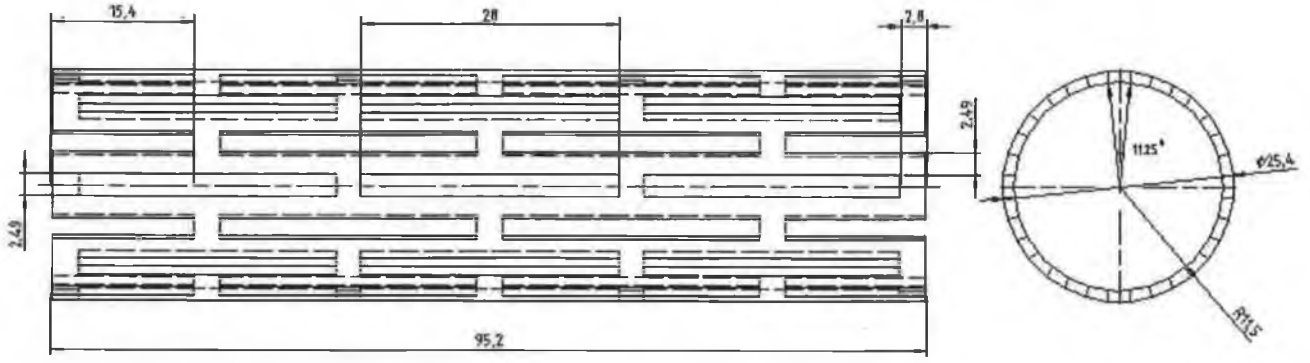

Figure 5.101: Geometry of the slotted tube for design 4

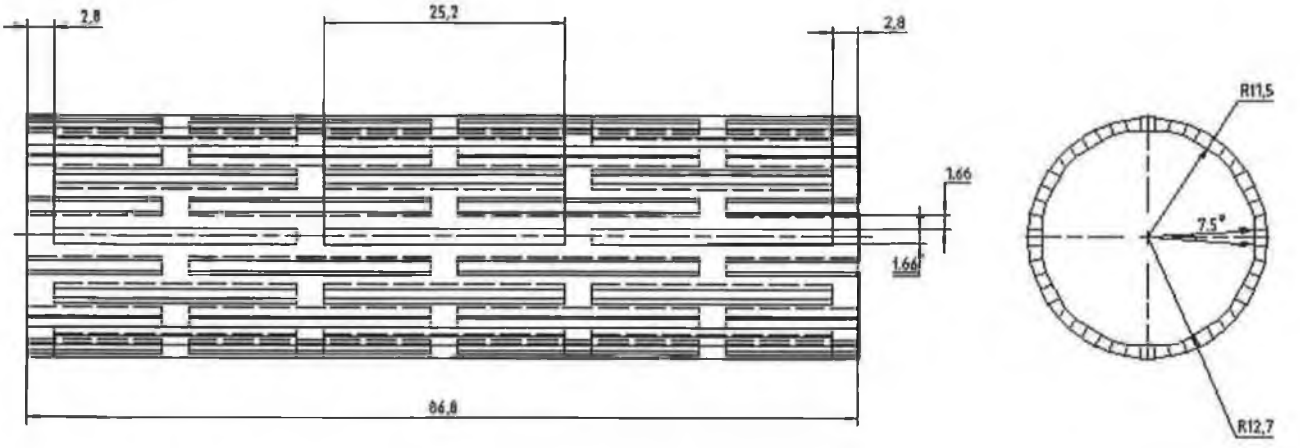

Figure 5.102: Geometry of the slotted tube for design 5

Table 5.6 shows the summary of the dimensions for the five slotted tube stents. Design 2 contains the least metal surface area. It is followed by design 4, 5, and 3. It is noticed that design 1 contains the same metal surface area as in design 5 despite the fact that the number of slots for the later design is 50 % more than the former one. All of the designs cover the same stent surface area by 6926.33 mm^2 except design 4.

Category	**Design 1**	**Design 2**	**Design 3**	**Design 4**	**Design 5**
Width of Slot	2.49 mm	3 mm	2 mm	2.49 mm	1.66 mm
Width of Strut	2.49 mm	1.98 mm	2 mm	2.49 mm	1.66 mm
Length of Slot	25.2 mm	25.2 mm	25.2 mm	28 mm	25.2 mm
Length of Bridging Strut	2.8 mm	2.8 mm	2.8 mm	2.8 mm	2.8 mm
Number of Slots	40	40	40	40	60
Slot Size	62.748 mm^2	75.6 mm^2	50.4 mm^2	69.72 mm^2	41.832 mm^2
Slot Areas	2509.92 mm^2	3024 mm^2	2016 mm^2	2788.8 mm^2	2509.92 mm^2
Metal Surface Area	4416.41 mm^2	3902.23 mm^2	4910.33 mm^2	4090.03 mm^2	4416.41 mm^2
Stent Surface Area	6926.33 mm^2	6926.33 mm^2	6926.33 mm^2	6878.83 mm^2	6926.33 mm^2
Outer Diameter of Stent	25.4 mm	25.4 mm	25.4 mm	25.4 mm	25.4 mm
Inner Diameter of Stent	23 mm	23 mm	23 mm	23 mm	23 mm
Length of Stent	86.8 mm	86.8 mm	86.8 mm	95.2 mm	86.8 mm

Table 5.6: Summary of dimensions for the five different designs

Finite Element Model										
Model	Design 1		Design 2		Design 3		Design 4		Design 5	
	N.E.	N.N.	N.E.	N.N.	N.E.	N.N.	N.E.	N.N	N.E.	N.N.
Balloon	3648	5148	4320	6072	3648	5148	4800	6732	4800	6732
Stent	1104	2133	856	1749	1048	2001	1200	2313	3312	6180
Total	4752	7281	5176	7821	4696	7149	6000	9045	8112	12912

Table 5.7: Number of elements used

Figure 5.103 to Figure 5.107 show the finite element models of one-eight of the slotted tubes for the five designs after meshing. Each design contains different density of meshes. The length of the balloons is also varied with each stent. This is to

ensure the uniformity of the stent after the expansion. The details of the finite element models are described in Table 5.7, where N.E. is the number of elements and N.N is the number of nodes consisted in the model.

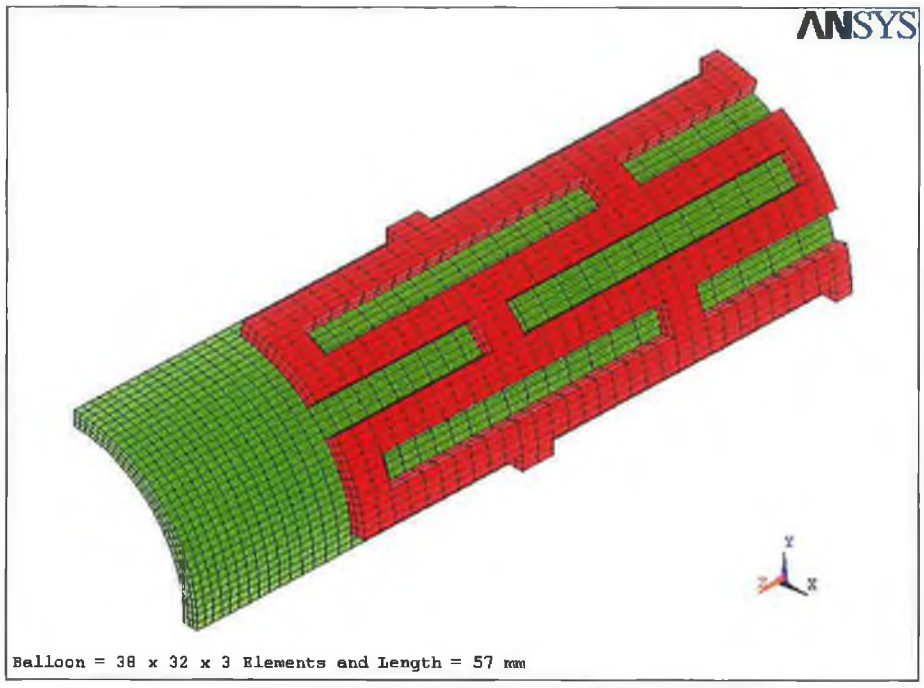

Figure 5.103: Finite element model of the design

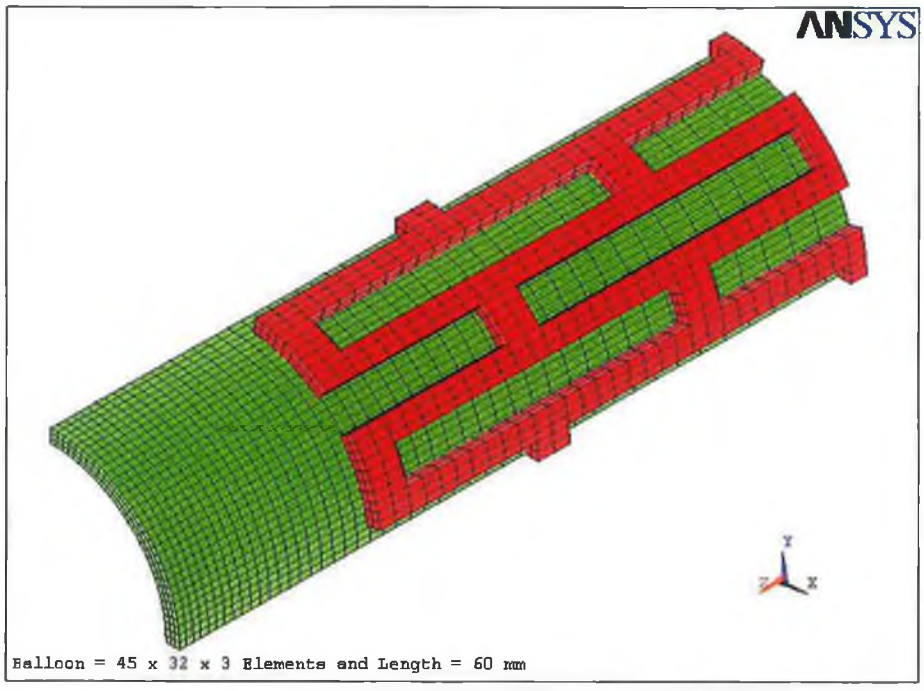

Figure 5.104: Finite element model of the design 2

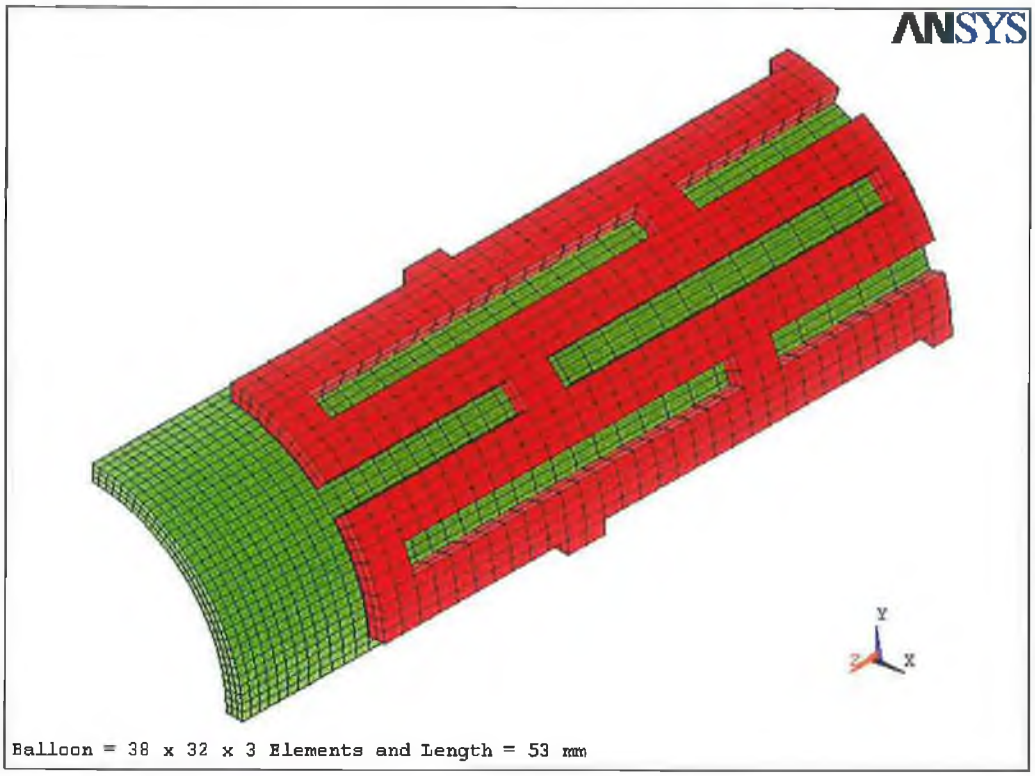

Figure 5.105: Finite element model of the design 3

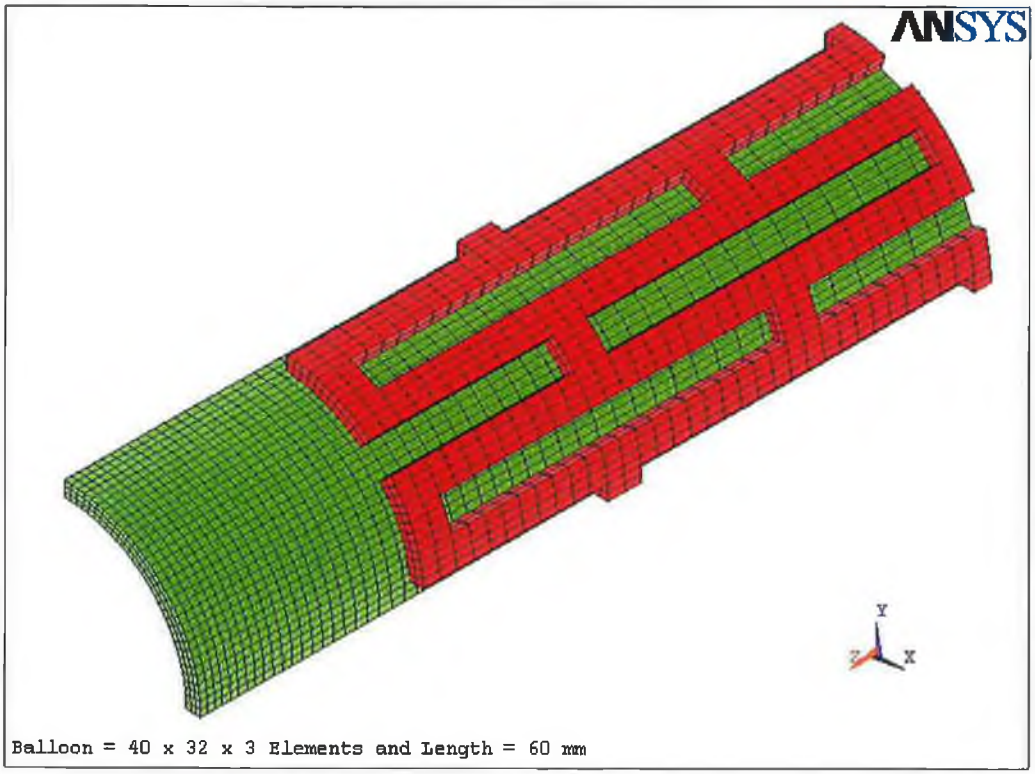

Figure 5.106: Finite element model of the design 4

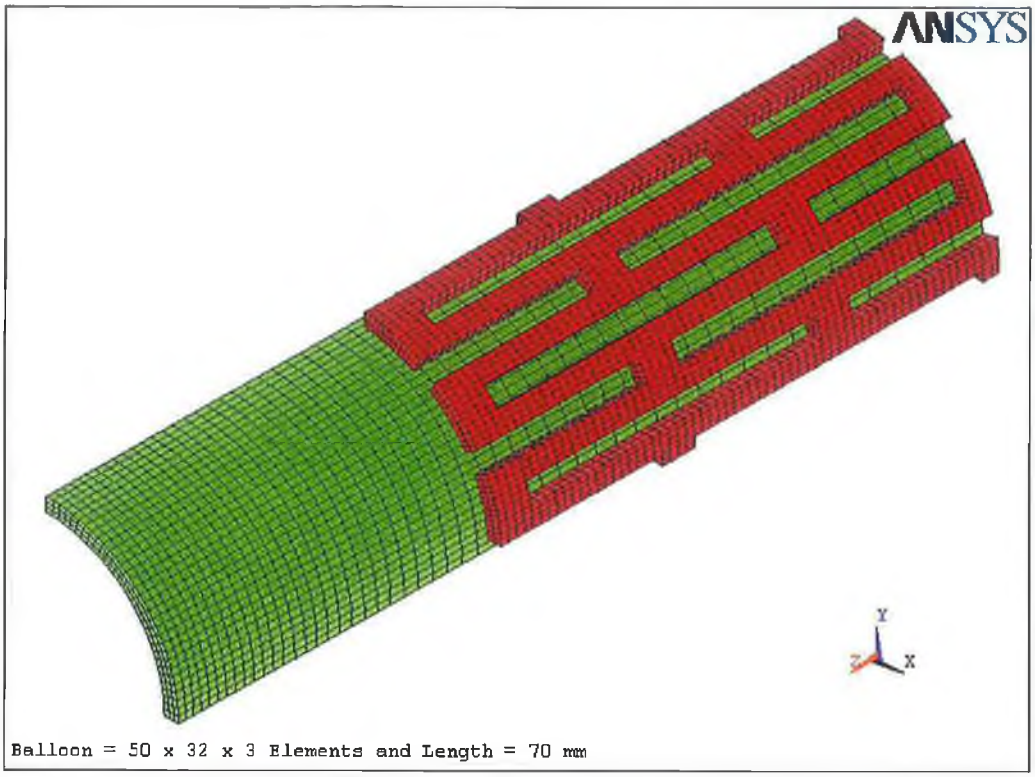

Figure 5.107: Finite element model of the design 5

The material properties of Stainless Steel 304 was utilised to represent all the slotted tube stents. Polyurethane with equal toughness was used to represent the balloons. The pressure applied on the inner surface of the balloons was varied with each design except design 2 and 4. The variation of the deployment pressure is to ensure all of the slotted tube stents expand to a certain limit for comparison in an impartial manner. For instance, all stents must expand at least up to approximately 87 % of its failure strength i.e. 450 MPa.

The load histories of the five simulations process are shown in Figure 5.108. As can be seen from the figure as well that the simulation time is varied for different designs. The simulation time here is not a real time as the quasi-static solution was intended. Due to the different density of mesh, pressure load etc. the simulation time needed is also varied. This is to allow the solution to converge to the equilibrium status. In this case, the dynamics effect is reduced to the minimum value if it is not completely eliminated. Design 3 requires the highest pressure load i.e. 3 MPa to induce the expansion since the struts of the stent are much stronger than the rest of the stents. Design 5 needs the least pressure load i.e. 1.85 MPa as it has the smallest

strut width. The maximum pressure loads applied for design 1, 2, and 4 are 2.6 MPa, 2.35 MPa, and 2.35 MPa respectively. Again, design 2 and 4 have the similar load history throughout the entire simulation process.

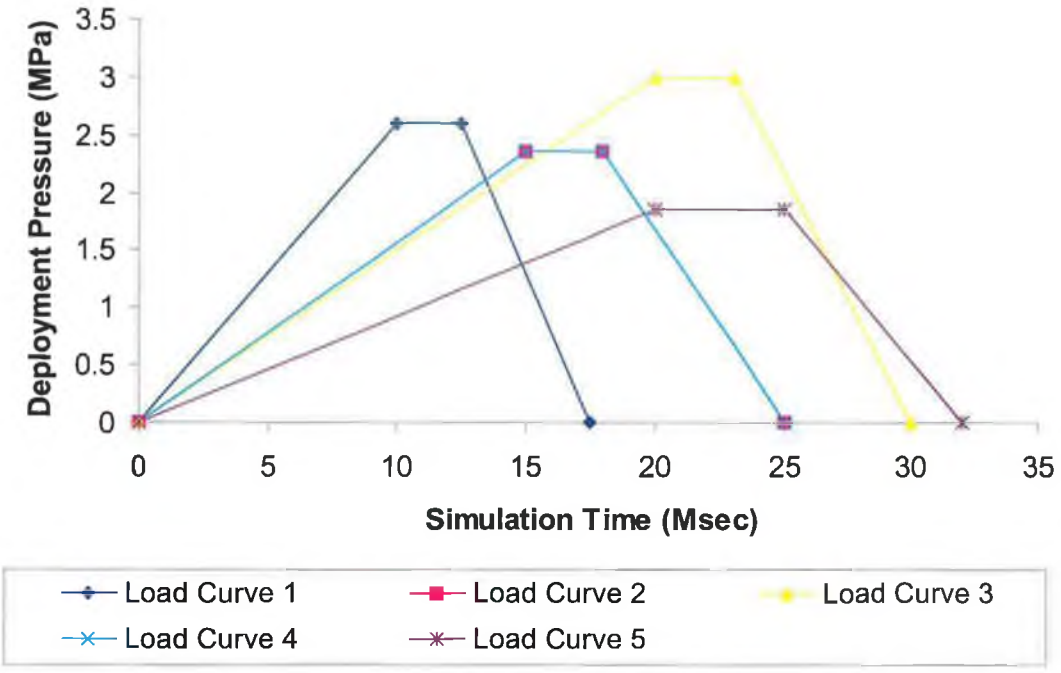

Figure 5.108: Loading curves

5.8.2 Result and Discussion

5.8.2.1 Stress analysis

Figure 5.109 to Figure 5.113 shows the distribution of residual stress in the slotted tube stents for each design after the deflation process. It can be seen from the figures that the highly stressed area are localised in the corners of the slots irrespectively of the design structure of the struts. Major stress was also found localised in the middle of the slots except for design 5. It appears that the increment on the number of the struts produces some effects on the strength of that region. The expansion characteristic of the designs is unvaried. During the inflation process the proximal and distal ends of the expanding balloon, which is unconstrained by the shorter stent inflated first and causing the overlying stent to open nonuniformly into a dumbbell shape. The centre of the slotted tube stent opened with increasing pressure and causing a contraction along its longitudinal axis.

It can be seen from Figure 5.109 that the minor stressed regions are located at the end, middle of the struts and the bridging struts of the slotted tube stent. However, the minimum stressed area is located at the end of the stent as can be easily seen from the figure. Design 1 is modelled to have an equivalent width for the stent struts and the slots. The minor stress seems to occupy one-third of the struts and it looks as if a chain with beads. The beads that constituted of lower stress cover the entire width of the struts. The maximum residual stress that remained in the slotted tube stent after deflation was approximately 452 MPa.

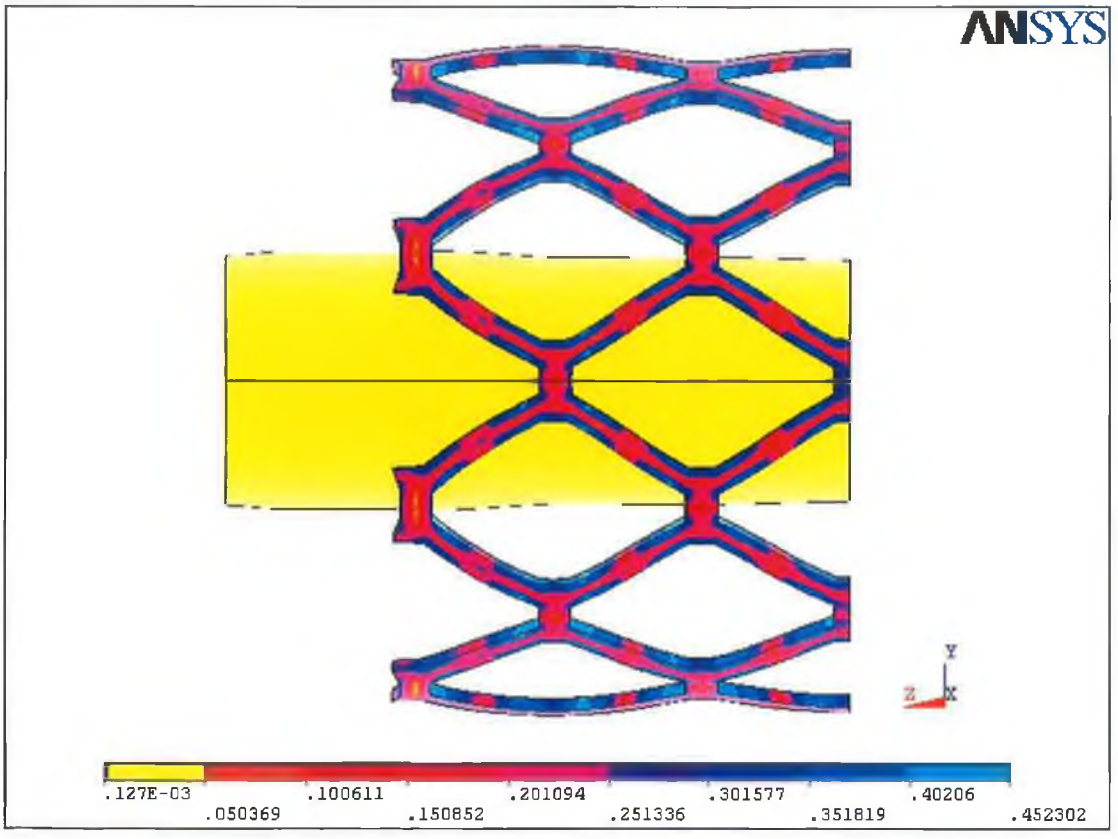

Figure 5.109: Residual stress in the deformed tube for design 1

As described before, design 2 was modelled to have wider slots and narrower struts. The minor stress regions are located at the same areas as in design 1. However, the lowest stressed region that located at the end of the stent is even more prominent. It can be clearly visualised in Figure 5.110. The minor stresses areas have become wider and less concentrated. The beads are larger than design 1 and tend to scatter unevenly. The distribution of residual stress in this figure shows that this design is

easier to expand compared to the design 1 as it has the weaker struts structure. The maximum residual stress that remained in the slotted tube stent for design 2 after deflation was approximately 453 MPa. The residual stress here is almost levelled with the design 1 but the deployment pressure for the design 2 is lesser than the design 1 which is only 2.35 MPa.

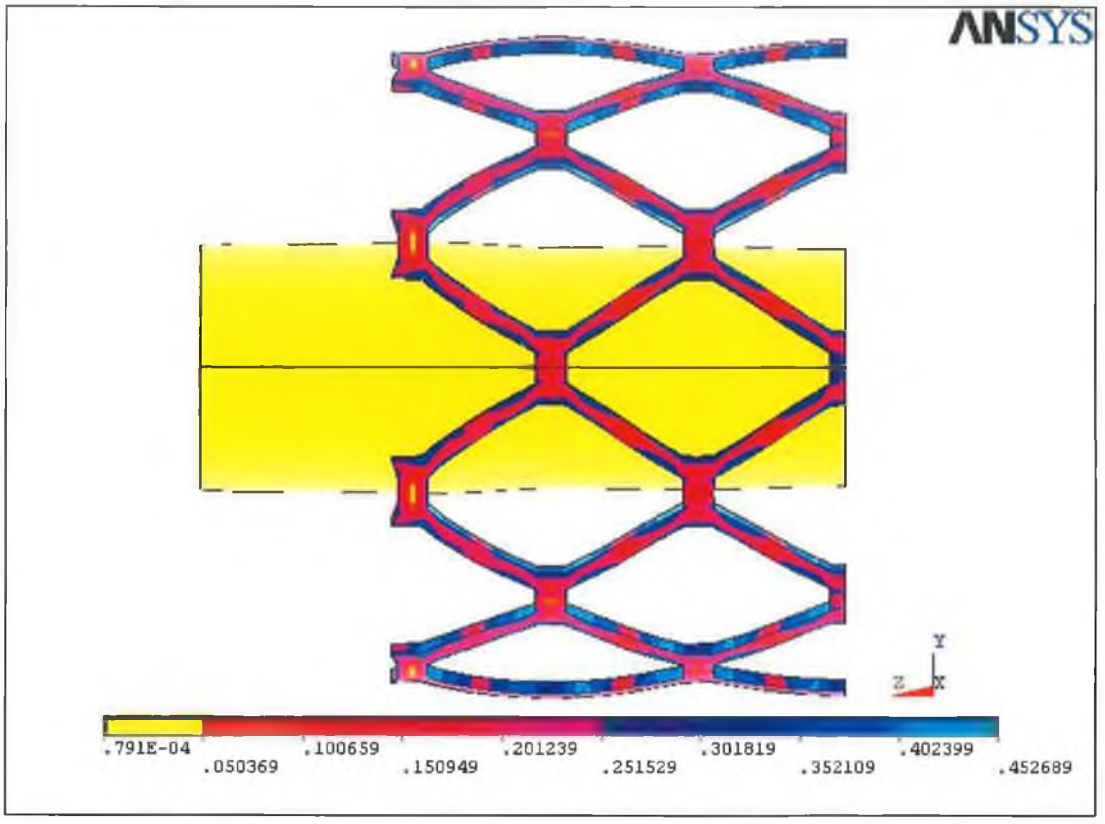

Figure 5.110: Residual stress in the deformed tube for design 2

The distribution of residual stress in Figure 5.111 shows that this design is much stronger than the previous two designs. More regions of the body struts experienced the higher stress level. It is noticed that the chain is broken in the body struts near the end of the slotted tube stent. The beads that represent the lower stress region could hardly visualise in the bridging struts and the higher stress level occupies this region. As a result, higher pressure load needs to be applied to induce the expansion. The minimum stress area that located at the end of the stent did not change despite the changes in the struts width of the design. The maximum residual stress that remained in the slotted tube stent for design 3 after deflation was approximately 477 MPa.

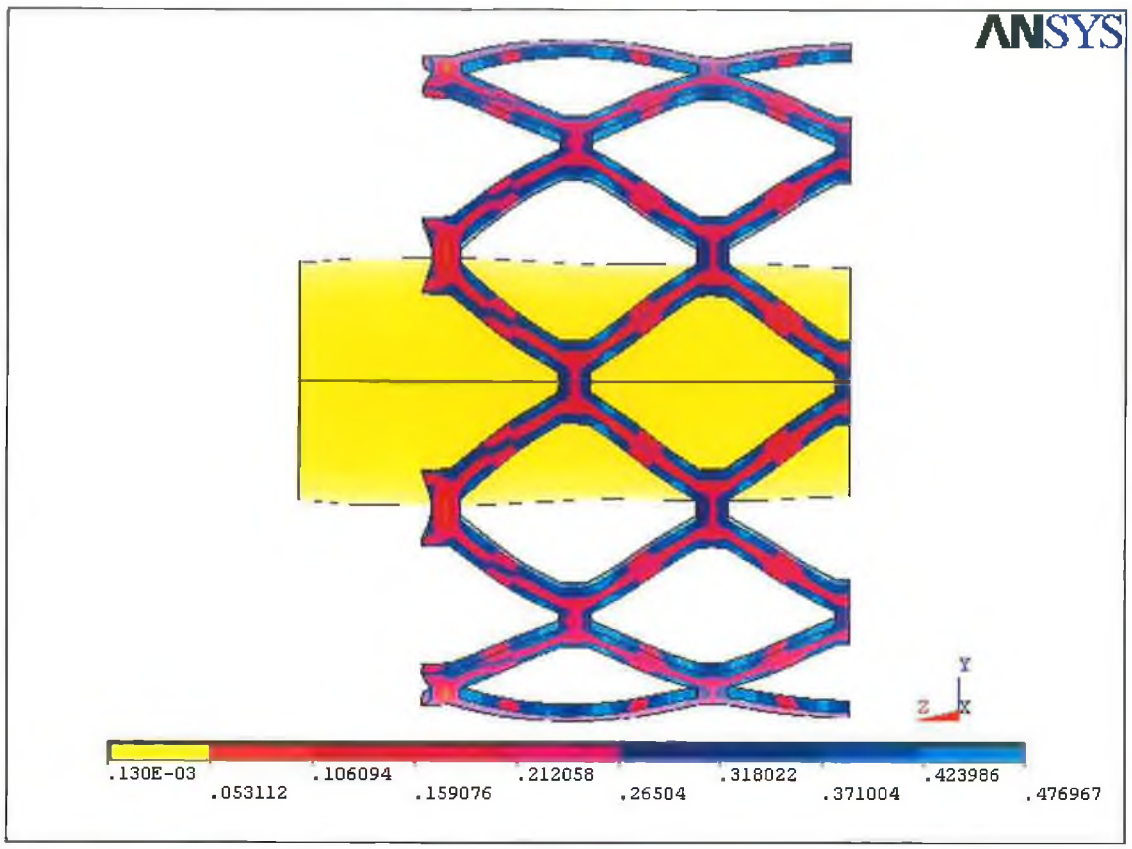

Figure 5.111: Residual stress in the deformed tube for design 3

The width of the strut in design 4 is identical to that of design 1. The only difference between them is the length of the strut. It was designed to have longer struts by 10 % than the design 1. The distribution of the residual stress in Figure 5.112 resembles the distribution of stress in design 1. The shape of the chain and the beads can be clearly seen. The maximum and minimum residual stresses are located in the same areas as in design 1. This indicates that the increment on the length of the struts do not have a major effect on the stress distribution in the slotted tube stent.

The same pressure load was applied in design 1 and 4. The maximum residual stress after the deflation process for design 4 is only experienced a slight variation of stress in comparison with the maximum residual stress in design 1. The stress at that point in time was approximately 465 MPa.

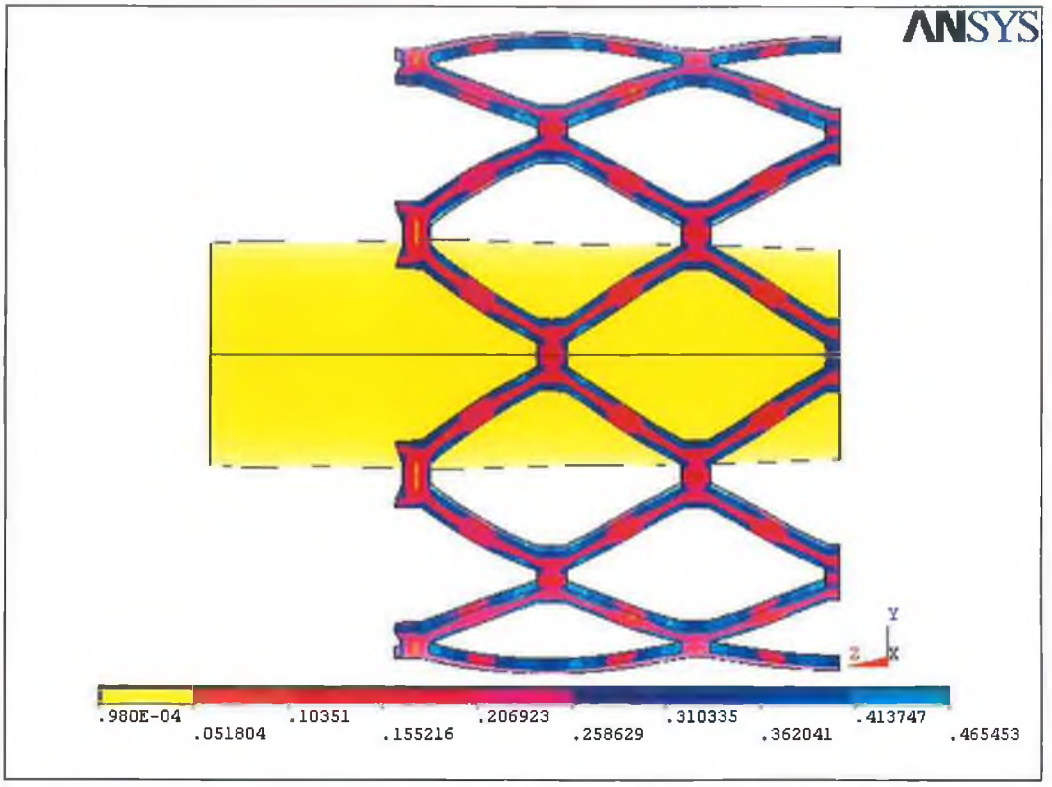

Figure 5.112: Residual stress in the deformed tube for design 4

Increasing the number of slots in design 5 make less material available for expansion of the slotted tube stent due to the smaller struts. Figure 5.113 shows the distribution of the residual stress in the deformed tube for design 5. It seems that the minimum stress shifted its location from the end of the stent to the middle of the body struts. This is unlike the previous four designs where the minimum stress was found to be located at the end of the stent. The beads covered wider area and the bridging struts seemed to be fully occupied by the lower stress level. This makes the slotted tube weak and extremely easy to expand. The pressure deployed was only 1.85 MPa and the residual stress achieved after deflation was approximately 469 MPa. The higher stressed regions were more concentrated in design 5 and the body struts experienced lower stress at most of the time. It is also evident that the structure of the slotted tube seemed to have smoother curvature around the slots. This indicates that the body struts experienced more bending in this case. More number of struts produces smoother curvature of the struts structure and therefore increases the circularity of the slotted tube stent.

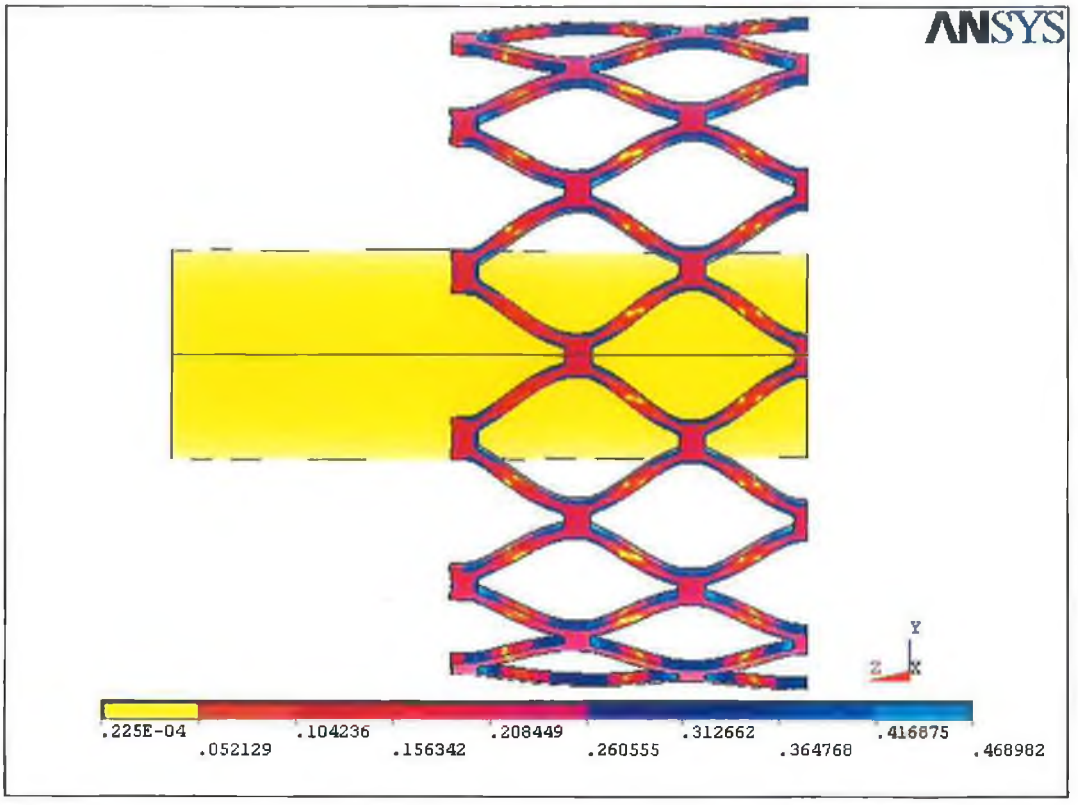

Figure 5.113: Residual stress in the deformed tube for design 5

5.8.2.2 Deployment pressure vs. displacement

Figure 5.114 shows the development of the five slotted tube central diameters at different levels of pressure loads. Design 5 that is more numerous in term of struts and slots, experiences the highest magnitude of expansion. This is followed by the design 4, 2, and 1. Design 3 experiences the least expansion in the radial direction at the same level of pressure load. The expansion rate for design 2 and 4 indicate that twenty percent wider slots from the original width almost gave the same result as of ten percent increment on the length of the slots.

It is possible to make comparison for each design on the level of expansion achieved based on the same level of pressure load. For instance, the diameter achieved for design 1 to 5 read as 31.68 mm, 37.46 mm, 27.65 mm, 40.65 mm and 90.07 mm at pressure load of 1.85 MPa. These data suggest that number of struts produces beneficial effect on the expansion in radial direction of the slotted tube stent.

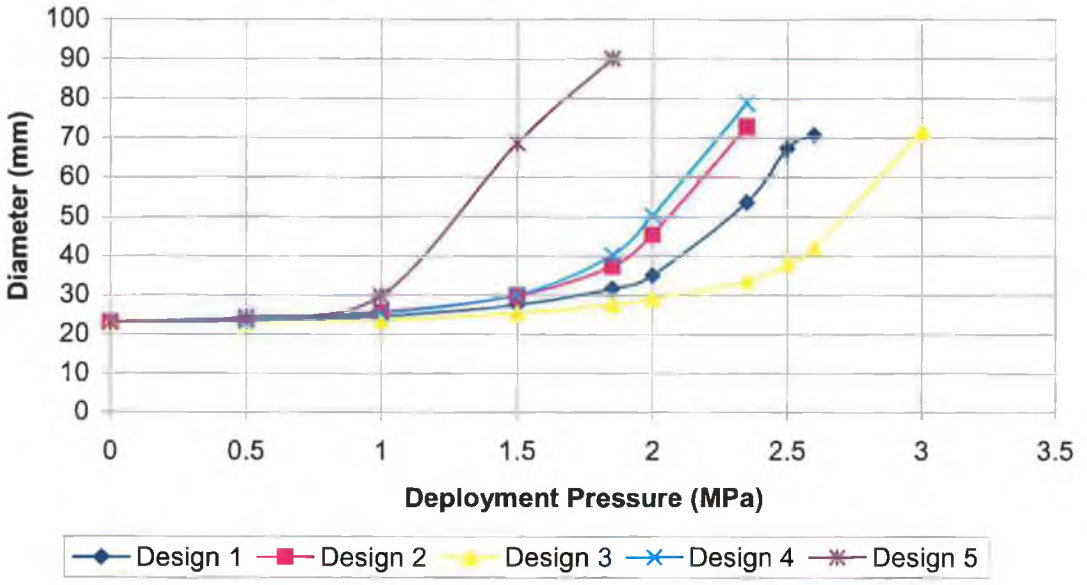

Figure 5.114: Expansion of slotted tube diameter with deployment pressure

Increasing the strut length might have a slight advantage over the reduction in strut width to achieve the higher level of expansion. Increasing the strut width by the same percentage but higher pressure load on the other hand is not as effective as reducing the strut width with lower pressure load. The maximum diameters achieved at maximum deployment pressure for design 1 to 5 were 70.8 mm, 72.96 mm, 71.88 mm, 78.86 mm and 90.06 mm.

5.8.2.3 Elastic recoil

Figure 5.115 shows the reduction of the central diameters for each design during the deflation process. The curves show that the stent diameters decrease with the decreasing pressure load. However, the stent diameters stop decreasing eventually at the pressure level around 1 MPa. This is due to the separation of the balloon from the stent and the fact that the tube had undergone the plastic deformation. The radial strength of the slotted tube kept the tube in deformed shape and prevented it from recoil.

The curve of design 3 shows the ability of the wider struts stent from experiencing excessive elastic recoil. The stent reduced its central diameter from 71.88 mm to 63.08 mm when the deflation process was ended. The stent may have detrimental

effects due to its difficulty to expand during the inflation process and the flexibility of the stent is limited. However, it also produces beneficial effects after deployment as the stent would be able to withstand the compressive force of a vascular wall from collapsing.

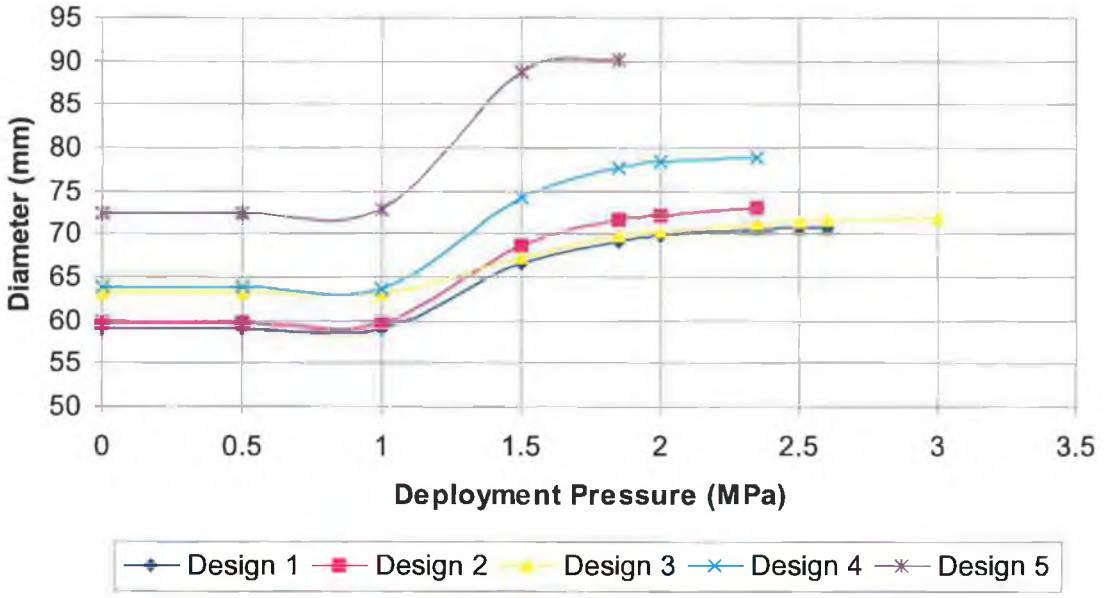

Figure 5.115: Elastic recoil of the slotted tube stents

Table 5.8 shows the details of the slotted tubes diameter after elastic recoil. Design 5 experienced the maximum shrinkage i.e. 19.70 %. This was followed by design 4, 2, 1, and finally design 3. The statistic shows that the percentage of shrinkage for design 5 is nearly equal to design 4 despite the fact that the former design achieved much higher expansion in radial direction.

Design	Diameter at maximum pressure (mm)	Diameter after elastic recoil (mm)	Discrepancy (mm)	Percentage of shrinkage (%)
Design 1	70.858	59.098	11.76	16.60
Design 2	72.962	59.756	13.206	18.10
Design 3	71.878	63.088	8.79	12.23
Design 4	78.852	63.738	15.114	19.17
Design 5	90.066	72.326	17.74	19.70

Table 5.8: Percentage shrinkage of the slotted tubes

5.8.2.4 Foreshortening

Figure 5.116 illustrates the magnitude of foreshortening with deployment pressure during the deflation process by design 1, 2, 3, 4, and 5 respectively. It can be seen from the graph that the foreshortening decreases with pressure load during the onset of the deflation process. The foreshortening reduced to a constant value when the pressure of 1 MPa was reached.

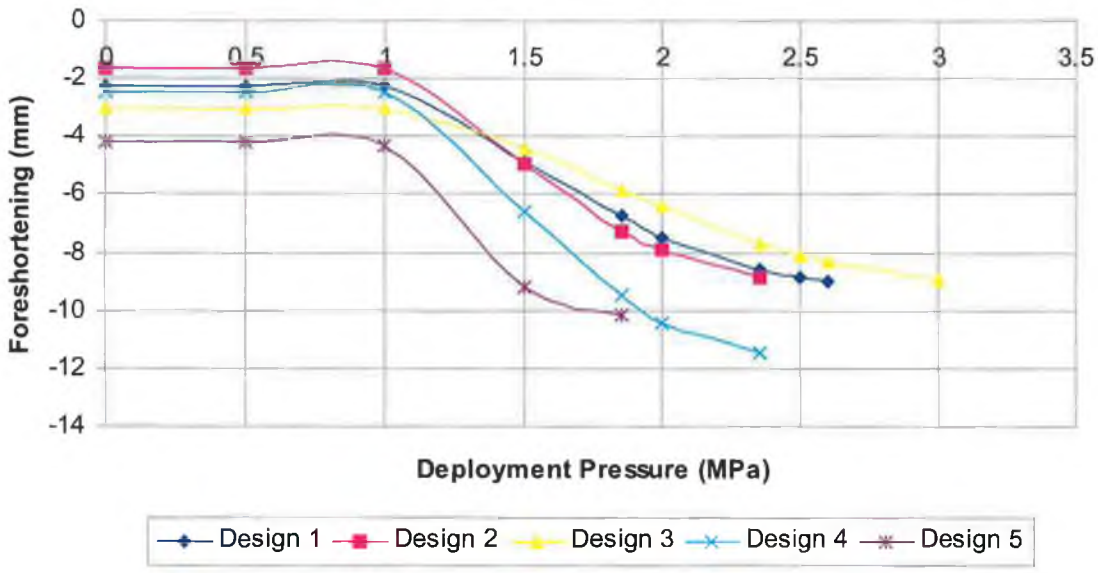

Figure 5.116: Foreshortening of the slotted tubes with deployment pressure

The foreshortening of the slotted tube stents remained in the constant value throughout the rest of the deflation process after 1 MPa despite there were small variations toward the 0.5 MPa. The foreshortening corresponds with the stent diameter. Any increase in length of the stent is accompanied by a corresponding decrease in stent diameter. Therefore, any alteration in the stent diameter reflects the changes in the length of the stent.

Table 5.9 shows the details of the foreshortening for each design after the deflation process. The negative sign represents the shortening of the stent from its original length. It is noticed that design 2 experienced the least foreshortening i.e. 3.74 % from its original length. It is followed by design 1, 4, 3 and 5. The design 5 that seemed to be second significant in experiencing the shrinkage in diameter had a

highest percentage of foreshortening compared to the other designs. This was probably due to the features of the design that enhanced the foreshortening. Design 4 had the highest value of foreshortening at maximum pressure load but it reduced to a considerably low value when the pressure was released to zero. The recovering of the foreshortening before and after the deflation process was the highest amongst those five designs. Design 3 experienced the second highest percentage of foreshortening despite it had the lowest percentage of shrinkage. The statistics show that the width of the struts has a direct impact on the foreshortening of the stent. Foreshortening increases when struts width increases and vice versa. The statistics also show that the length of the struts does not have too much impact on the foreshortening. Increasing the number of slots will increase the foreshortening as well.

Design	Foreshortening at maximum pressure (mm)	Foreshortening after elastic recoil (mm)	Discrepancy (mm)	Percentage of foreshortening (%)
Design 1	- 8.992	- 2.231	- 6.761	5.14
Design 2	- 8.876	- 1.625	- 7.251	3.74
Design 3	- 8.890	- 3.018	- 5.872	6.95
Design 4	- 11.494	- 2.457	- 9.037	5.16
Design 5	- 10.187	- 4.165	- 6.022	9.60

Table 5.9: Percentage foreshortening from the original length of the slotted tubes

5.9 Simulation of Balloon, Stent, Plaque and Artery

The main objective of this section is to investigate the expansion characteristic of slotted tube stent with the present of plaque and artery. The effect of the reformation of the occlusion by plaque and artery on slotted tube stent after the deployment was investigated. The correlations between stent-plaque contact area and deployment pressure was also analysed. The stresses in the plaque and artery due to the interference of slotted stent were reported.

5.9.1 Modelling and Loading

The ANSYS Finite Element Package was used to develop the geometry of the plaque and artery. A three-dimension finite element model of a stenosed artery was created and a simulation of a stent implantation procedure was performed. The arterial wall and the plaque were modelled in such a way that the plaque surface was not in contact with the slotted tube stent at the beginning of the dilatation process. The geometry of the plaque was modelled to become thicker at the centre of the plaque volume. The inner diameters of the plaque were modelled to be 47 mm at proximal (situated nearest to point of origin) and 35.4 mm at distal (situated farthest from point of origin). The plaque was assumed to be flat for a length of 46 mm from proximal. The thickness of the plaque was assumed to be identical throughout the distance from proximal i.e. 0.8mm. On the contrary, the thickness of the plaque at the distal was 5.8 mm.

The total length of the plaque and arterial wall were identical. They were 65 mm in length. The inner surface of the artery was attached to the outer surface of the plaque. The inner and outer surface of the arterial wall was taken as 23.5 mm and 25.1 mm respectively from the central axis. The thickness of the arterial wall was therefore 1.6 mm distal and proximal to the stenosis and extrapolated across the stenosis. The arterial wall was assumed to be uniformly thick. The geometry of the slotted tube stent and the balloon was taken from section 5.3 with the balloon length equal to 57 mm and thickness 1.2 mm. The distance between the plaque surface at proximal and slotted tube surface was 5 mm.

Figure 5.117 shows the entire assembly of the finite element model for the balloon catheter, slotted tube stent, plaque and arterial wall. The balloon consists of 3648 elements. It was discretised by 38 elements along its length and 32 elements in circumference with 3 elements cross the thickness. The slotted tube stent consists of 1104 elements. The slotted tube was discretised by 31 elements along its modelled length and 32 elements in circumference with 2 elements across the thickness. The plaque consists of 1095 elements and the artery consists of 1050 elements. Both of them were discretised along its length by 20 elements for 46 mm from distal and 15

elements for 19 mm to proximal. The finer mesh was used at the proximal to accurately capture the stresses generated. The plaque was discretised only 1 element across the thickness at distal but 7 elements at the proximal. There were 15 elements division in the circumference direction for both the plaque and the arterial wall. The thickness of the arterial wall was discretised by 2 elements. A total of 6897 elements describe the entire model.

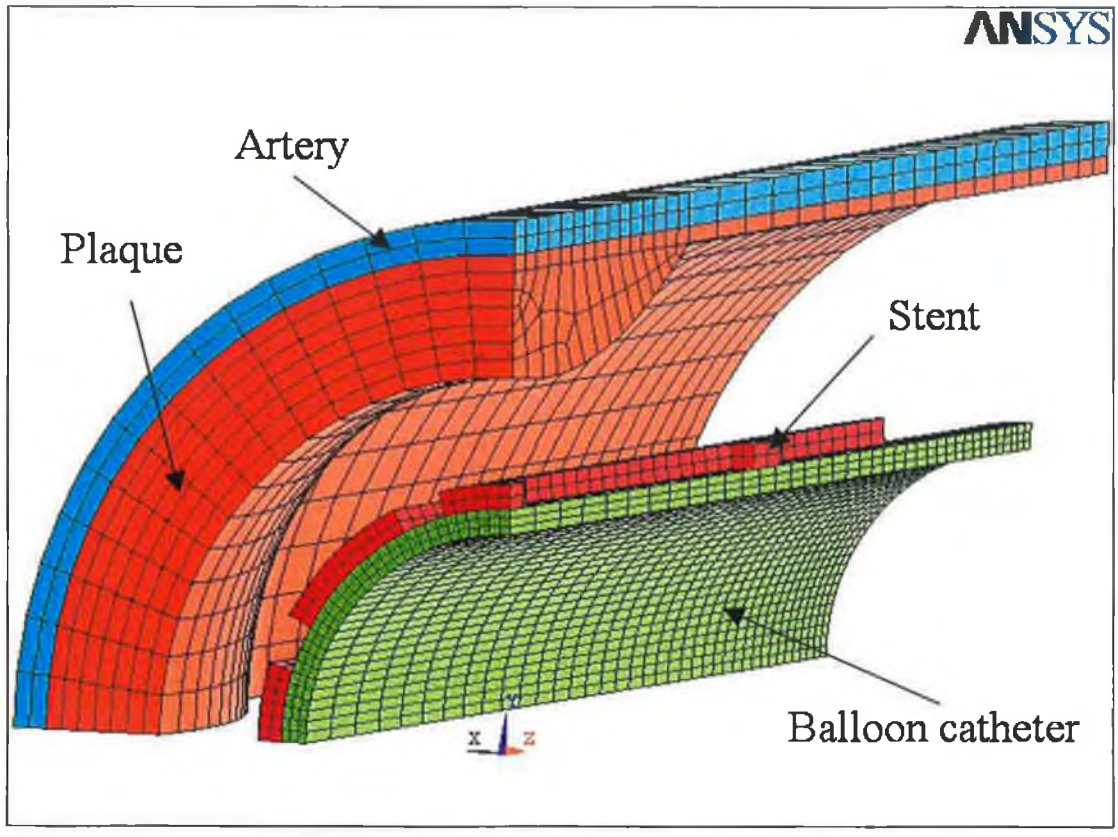

Figure 5.117: Finite element model of the entire assembly

Displacement limitations were placed upon some nodes. The nodes at the edges of symmetry were restrained in the appropriate directions. Nodes that parallel to x axis were not allowed to move in y direction, whereas nodes that parallel to y axis were not allowed to move in x direction. All the nodes at the proximal were constrained in z direction so that only the radial expansion was allowed. At the other end, all the nodes at the distal except slotted tube stent were tethered in all directions. Theses restrictions were needed in order to avoid translation or rotation of the model but freely allowed the expansion in radial direction.

The material models used for the plaque and arterial wall were defined as linear isotropic and nearly incompressible. The material properties of the plaque and artery were based on the information available in the literature [105]. Table 5.10 gives the material property values used.

Finite Element Model				
Parameter	**Balloon**	**Stent**	**Plaque**	**Artery**
Material	Polyurethane	Stainless Steel 304	Calcified plaque	Carotid arteries
Element Type	8-node explicit solid	8-node explicit solid	8-node explicit solid	8-node explicit solid
Material Model	Hyperelastic	Bi-linear Isotropic	Linear Isotropic	Linear Isotropic
Elastic Modulus	C(10) = 0.103176E-02 C(01) = 0.369266E-02	193 GPa	0.00219 GPa	0.00175 GPa
Poisson's Ratio	0.495	0.27	0.499	0.499
Density	1.07e-06 kg/mm^3	7.86e-06 kg/mm^3	--	--
Tangent Modulus	--	0.692 GPa	--	--

Table 5.10: Material properties used

An automatic single surface contact algorithm was introduced for the contact interfaces. Single surface contact is established when a surface of one body contacts itself or the surface of another body. This contact option allows all external surfaces within a model to come into contact. The definitions of contact and target surface are not necessarily. The outer surface of the balloon was allowed to contact with the inner surface of the plaque and the slotted tube stent. The outer surface of the slotted tube was allowed to contact with the inner surface of the plaque as well. There was no contact established between the outer surface of the plaque and the inner surface of the arterial wall as it was part of the atherosclerotic arteries.

Figure 5.118 shows the load history of the simulation process. The pressure load was applied on the inner surface of the balloon. The balloon expands and causes the slotted tube stent to expand as well. As a result, the slotted tube stent will press the plaque against the arterial wall. The pressure load increases gradually from 0 to 2.65 MPa for 25 milliseconds. The load is held constant for 7 milliseconds and then decreased from 2.65 MPa to 0 MPa. The simulation time at the end of the process is 42 milliseconds.

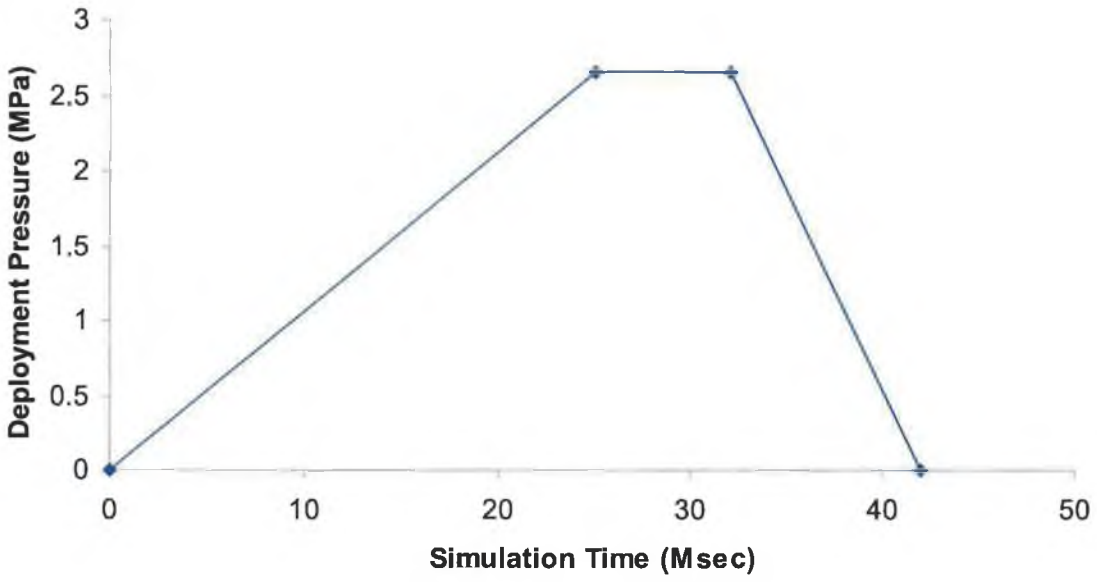

Figure 5.118: Loading curve

5.9.2 Result and Discussion

5.9.2.1 Stress analysis within stent, plaque and arterial wall

Figure 5.119 shows the residual stress distributed within the slotted tube stent when the balloon is deflated. The maximum stress location does not change despite the present of plaque and arterial wall. The major von Mises stresses are localised in the corners of the slots and the minor von Mises stresses are localised in the middle of the body struts. As before, the minimum stresses were found to be located at the bridging struts near the end of the slotted tube stent. A small region of peak stresses were visualised near the middle of the slots junctions as well.

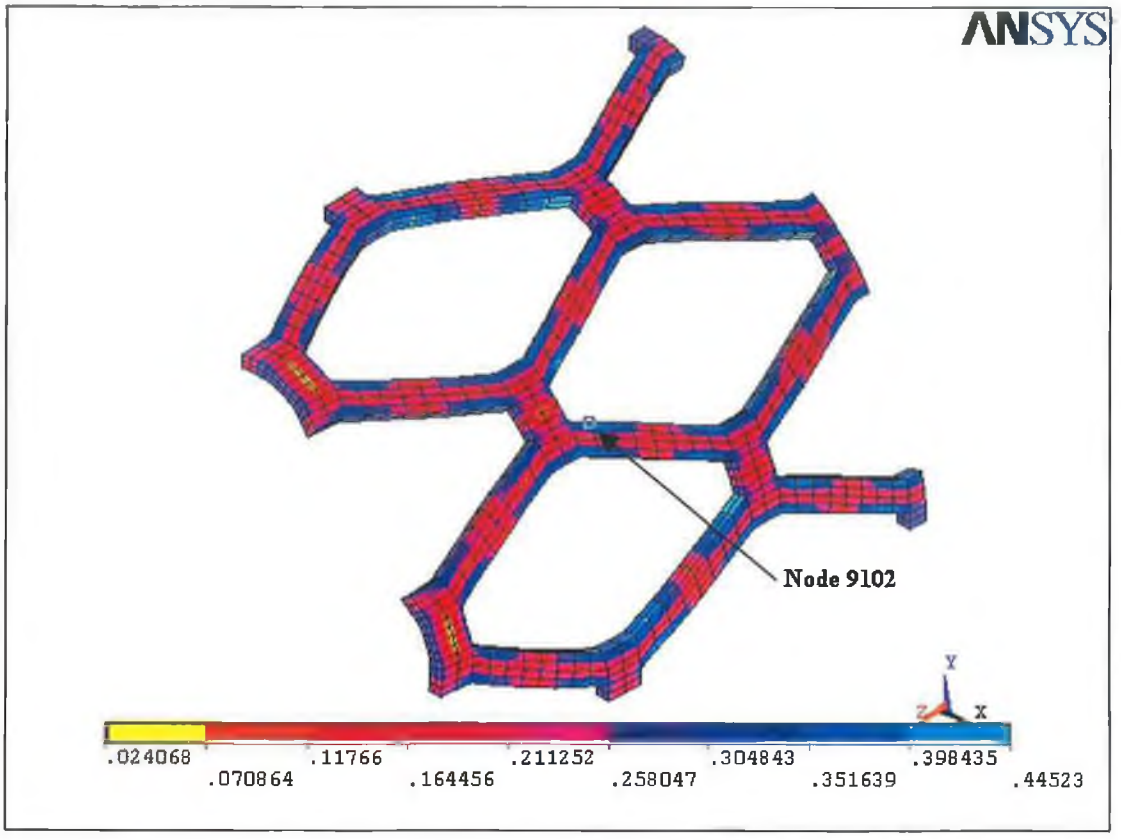

Figure 5.119: Residual stress in the slotted tube after deflation

Figure 5.120 shows the development of von Mises stress and the three directional stresses at node 9102. Node 9102 that attached to the element 6382 is the representative of the maximum stresses occurred over total simulation time. All the directional stresses are in tensile mode during the dilatation process. The stress in z direction could be regarded as the axial stress. As can be seen from the figure that the axial stress dominates the initial expansion of the process. As soon as the material reaches it yield point, the stresses in x and y direction begin to pick up comprehensively. The three directional stresses soon meet up at a point when approaching the maximum pressure load before it settles at its own level of stress during the equilibrium state.

A small erratic von Mises stress is visualised during the deflation process. This might be due to the recovering action induced by the plaque and the arterial wall. The arterial wall is elastic by nature. In spite of the elastic recovery by the slotted tube itself, the arterial wall provides the radial force that enhances the recovery action due

to its elastic nature. The von Mises stress dropped at the onset of the deflation process. The von Mises stress increased again as soon as the axial stress switched from tensile mode to compression mode. The von Mises stress dropped for the second time when the balloon was separated from the slotted tube.

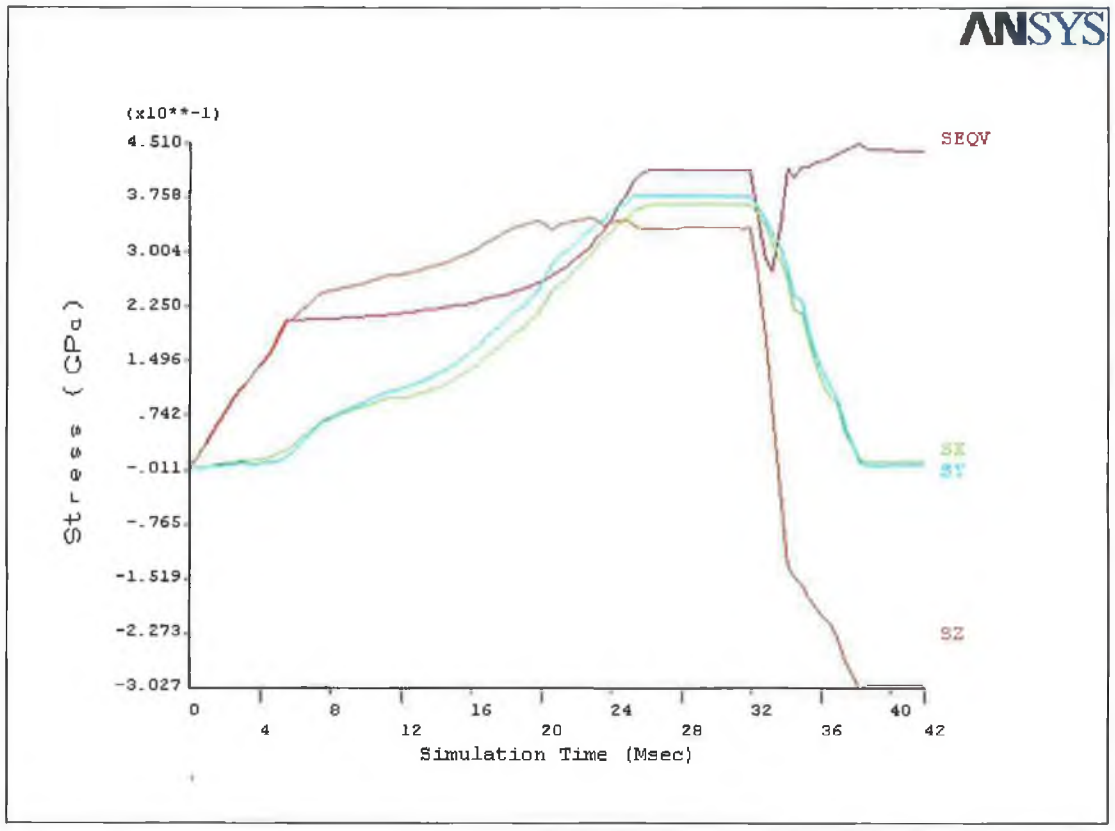

Figure 5.120: Development of stresses in node 9102

Figure 5.121 shows the von Mises stress distribution within the slotted tube stent at maximum deployment pressure. The resulting stress distribution gives an indication of the physical changes that occurred under the ramp loading. The most prominent increments in curvature after the placement of the slotted tube stent were visualised near the stent edges, although a slight non-significant straightening of the vessel was noted in the distal. These prominent edge effects were due to the much higher stiffness of the slotted tube with respect to the plaque and the arterial wall. The peak von Mises stress is still visualised at the four corners of the slots. The body struts experienced a greater stress level due to the expansion of the balloon and the compression of the plaque and the arterial wall.

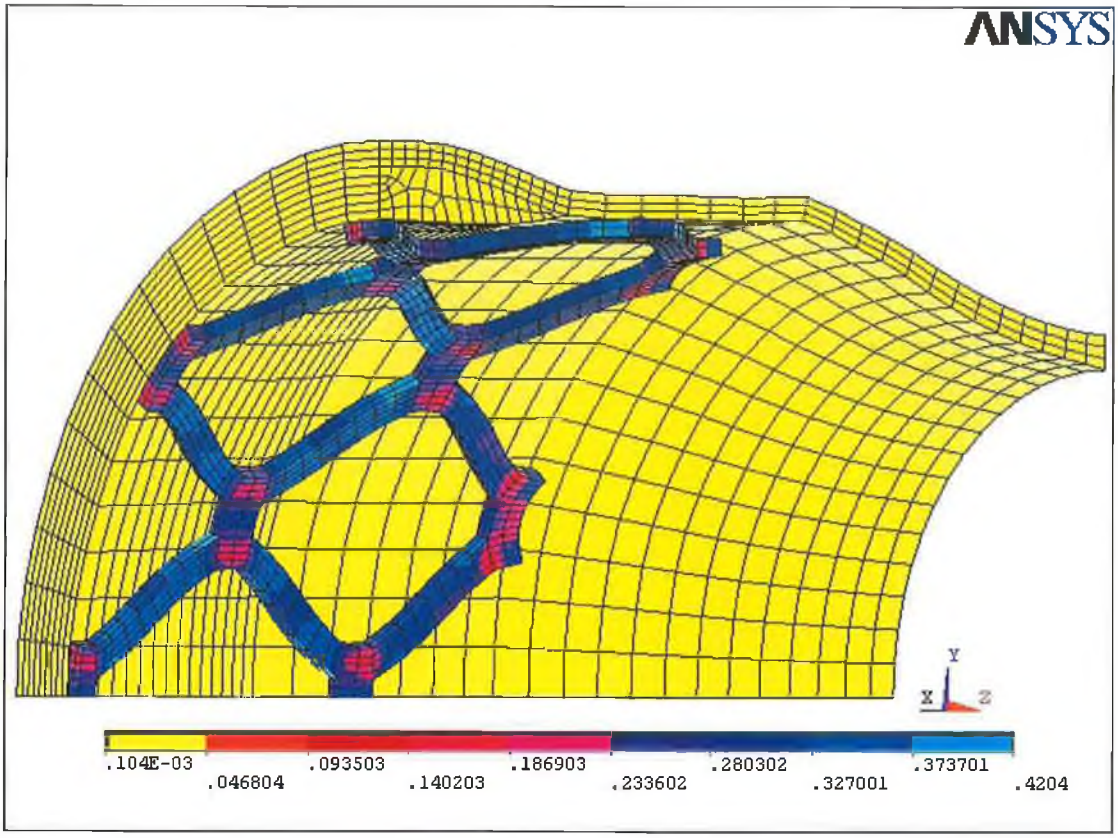

Figure 5.121: Slotted tube stent in place at maximum load

Figure 5.122 shows the residual stress distribution within the slotted tube stent when the balloon is deflated. The slotted tube stent prevents the plaque and the arterial wall from recoil. The increment of the curvature at the stent edges was not as serious as in the dilatation process especially at maximum load. This is due to the elastic recoil of the slotted stent itself and the recovery action from the plaque and the arterial wall. The maximum stress levels remained localised at the four corners of the slots. The maximum stress was also visualised at the middle section of the slots. A near constant stress distribution throughout the body struts was spotted at maximum load as shown in Figure 5.121. However, the stresses within the slotted tube stent seem to be divided into sections when the balloon was completely deflated. The distribution of higher and lower stress could be clearly seen. The lower stress was found to be located at the middle of the body and the bridging struts.

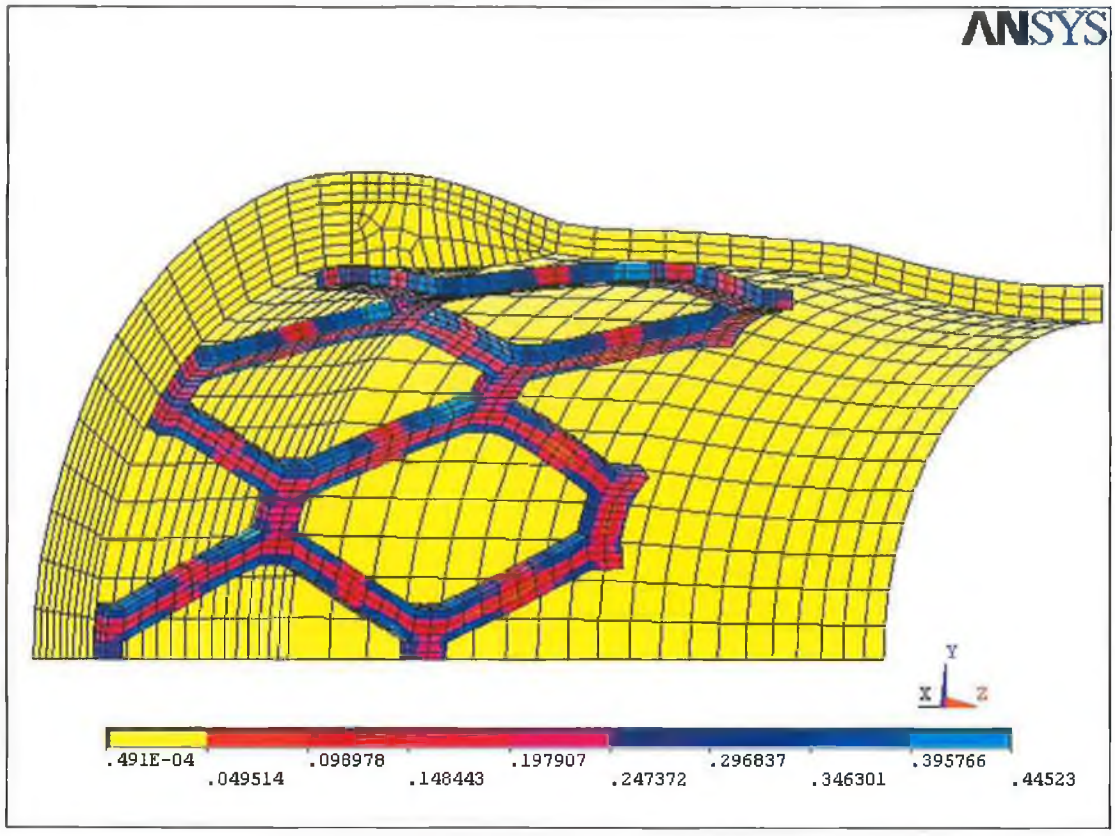

Figure 5.122: Slotted tube stent in place when the balloon is deflated

Figure 5.123 shows the von Mises stress distribution in the stented cylindrical vessel. The maximum von Mises stress are observed near the symmetry edge of the plaque. This indicates that there is a risk of plaque rupture as a result of the greater stress. The regions exhibiting the greatest stress in the models were also the locations at which most plaque ruptures have been reported to occur [106]. The von Mises stress gradually increased along the distance from proximal to distal. The high stresses at the plaque-artery interface arise from the different material properties of the arterial wall and the plaque. The surface irregularities produce stress concentrations. The stress concentration at the symmetry edge of the calcified plaque was due to the difference in stiffness between the plaque surface and the slotted tube stent. Apart from that, the prominent curvature of the calcified plaque geometry at the symmetry edge also contributes to the stress concentration.

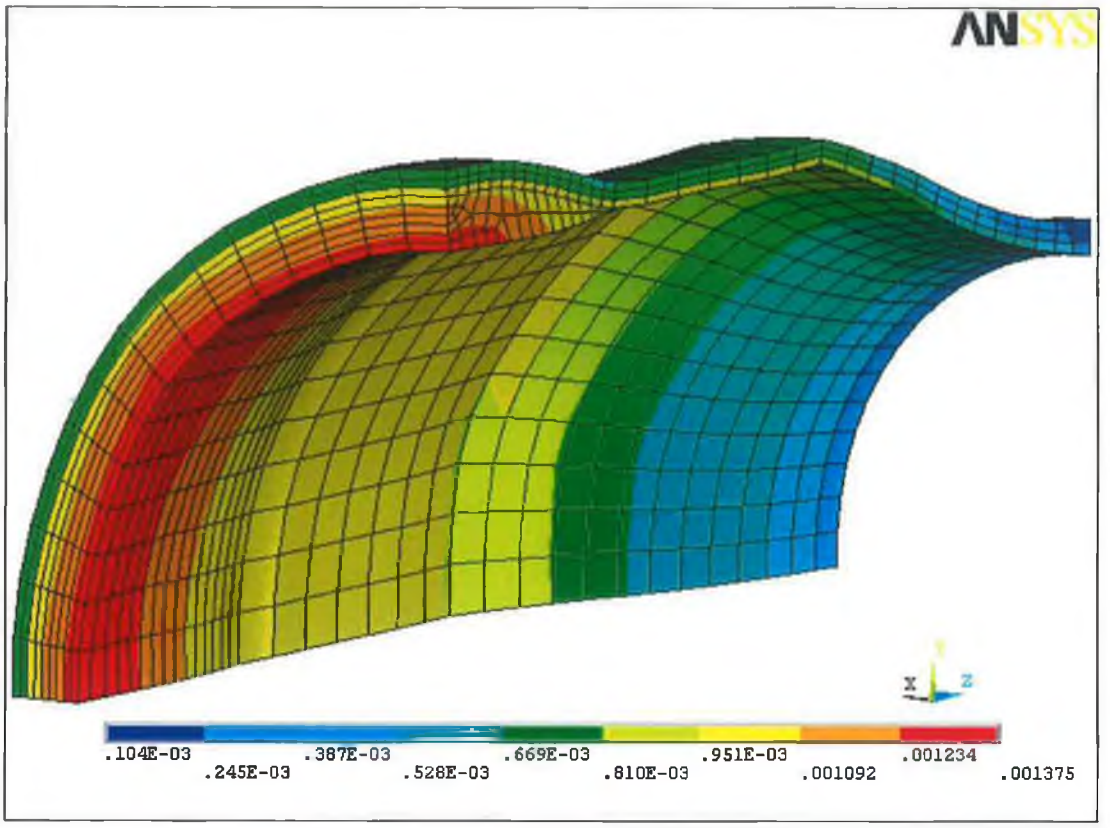

Figure 5.123: The stress distribution of the plaque and artery

Figure 5.124 shows the distribution of von Mises stress from inner surface of the plaque to the outer surface of the arterial wall at the symmetry edge. Two locations were picked to investigate the development of the von Mises stress experienced across the thickness of the plaque and the arterial wall at the symmetry edge. The node on the inner surface of the plaque at distal where the contact occurred with the stent strut was one of these locations. The other one was located at the area where there was no contact between the stent strut and the inner plaque surface. This location was at middle of the stent slot. The graph shows that the area where the plaque has a contact with stent struts, experiences a higher level of stress. However, the von Mises stress across the plaque and the arterial wall develops identically and simultaneously. The stress drops when the distance from the inner surface of the plaque increases. The stress continues to drop at the boundary (5.8 mm), where the plaque and arterial wall are bonded together in the model.

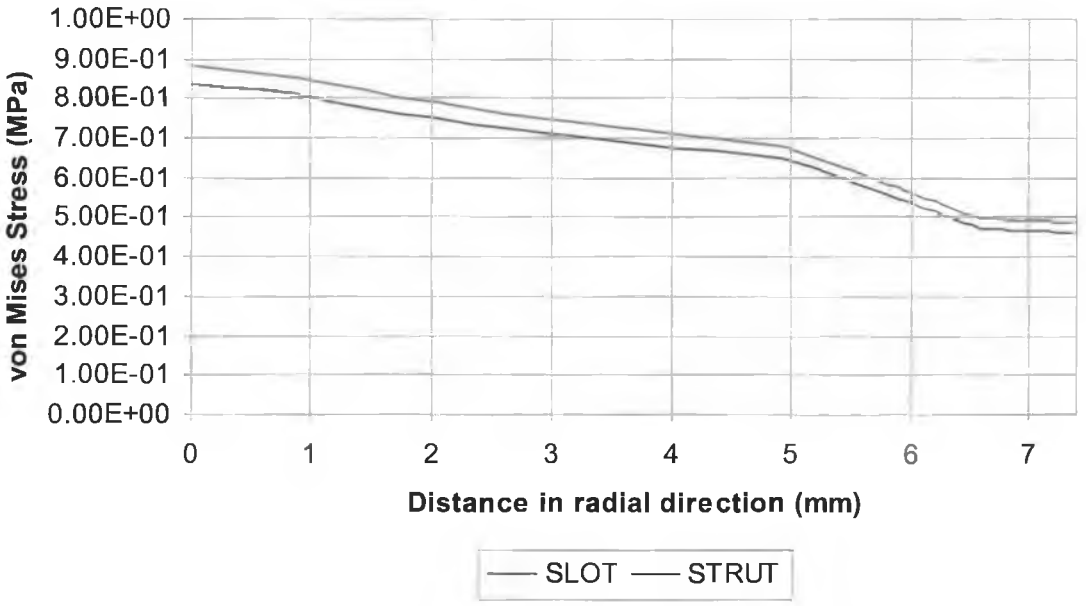

Figure 5.124: The von Mises stress across the thickness of the plaque and artery

The total distance from inner surface of the plaque to the outer surface of the arterial wall is 7.4 mm. The von Mises stress at the contacted area (strut) at the inner surface of the plaque is 0.883 MPa. In the other hand, the von Mises stress at the non-contacted area (slot) is 0.838 MPa. The presence of the stent struts increased the level of the stress by 5.4 % in the plaque and the arterial wall. The variation of the stress in the plaque and the arterial wall became smaller as the distance from the inner surface of the plaque increased. At the outer surface of the arterial wall, the percentage of different between them is only 5.1 %.

5.9.2.2 Expansion characteristic

Likewise, the slotted tube stent begins an expansion at its both ends. The stent struts then slowly open up as the pressure load continues to supply. It was at time 18 milliseconds that the slotted tube stent began to come into contact with the inner surface of the plaque. The pressure level at that time was 1.8 MPa. The geometry of the calcified plaque was created in such a way that it was thicker at the central section. It is due to this reason that the central section of the slotted tube stent was first making the contact with the plaque in this particular case. The edges of the slotted tube stent came into contact with the plaque at approximate time of 19.1 milliseconds. The slotted tube pressed the calcified plaque against the arterial wall as

the pressure load increased. The plaque was squeezing in between the arterial wall and the stent. Apart from the crack that will initiate within the plaque, the calcified plaque was so stiff that resulted in the expansion of the arterial wall as well.

Figure 5.125 shows the expansion of the slotted tube diameters with and without the presence of plaque and artery. The slotted tube stent needs a higher pressure load to achieve the same level of expansion with the presence of plaque and artery. The maximum deployment pressure for the cases with and without the plaque and artery were 2.6 MPa and 2.65 MPa respectively. The diameter achieved with the presence of plaque and artery was lower despite the pressure load applied was higher. At the pressure level of 2.6 MPa, the diameter achieved for both cases were 70.76 mm and 63.28 mm respectively. The plaque was thinning by 17.3 % from its original thickness (symmetry edge) in this model at the end of the process. The diameter obtained was 63.64 mm at maximum pressure load for the slotted tube without the presence of plaque and artery.

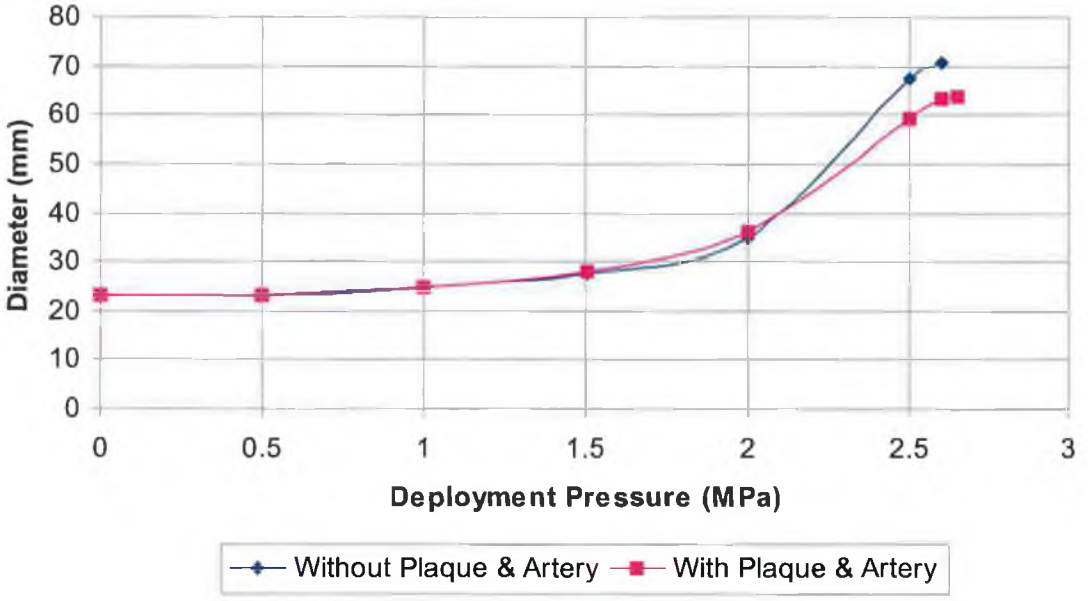

Figure 5.125: Expansion of slotted tube diameters with deployment pressure

Figure 5.126 shows the elastic recoil of the slotted tubes for the cases of with and without the presence of plaque and artery. The elastic nature of the arterial wall enhances the magnitude of the elastic recovery of the slotted tube stent. The diameter of the slotted tubes reduced to 59.1 mm and 50.58 mm respectively at the end of the

deflation process. The original inner diameter of the plaque that was 35.4 mm at the symmetry edge widened to 51.78 mm at the end of the deflation process. The slotted tube stent was shrunk by 20.5 % from the maximum diameter achieved during the maximum pressure load. Comparing to the stent without the presence of plaque and artery, which was 16.5 % shrinkage, the former figure strongly suggests that extra precaution needs to be taken as the alteration in the ultimate diameter obtained might present problems after the stent deployment. These problems often refer to as stent restenosis (re-narrowing). The stiffness of the slotted tube stent after deployment is required to act as a permanent scaffold to prevent the vessel from the tissue prolapsed. The flexibility of stent before deployment and the stiffness in radial direction of stent after deployment once again prove to be a major consideration during the stent designs.

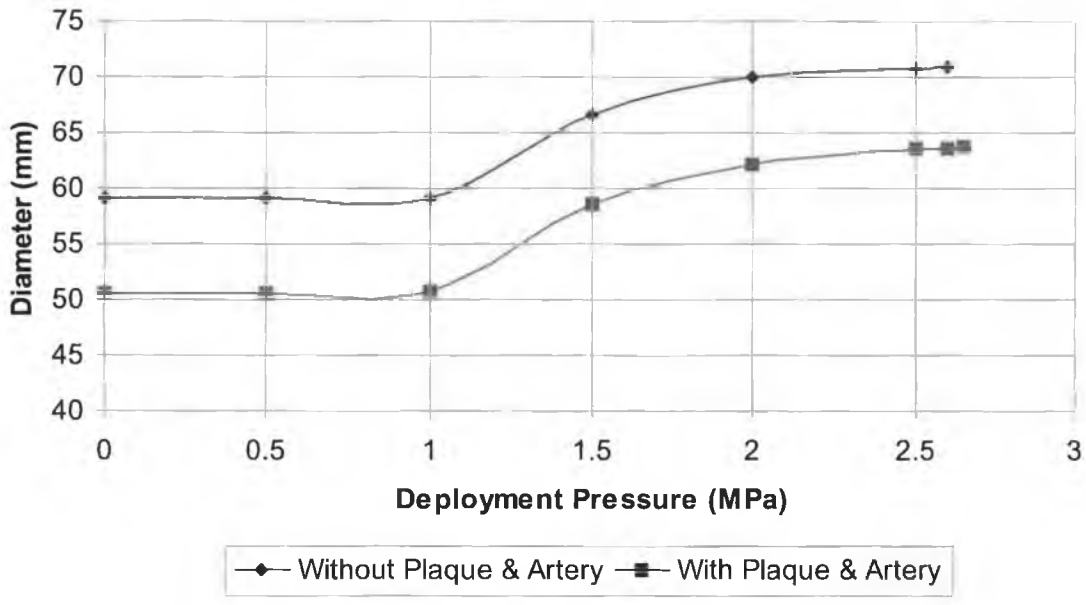

Figure 5.126: Elastic recoil of the slotted tubes

Figure 5.127 illustrates the magnitude of foreshortening in the slotted tube with the presence of plaque and artery with simulation time. The magnitude of foreshortening in the slotted tube stent relates to the magnitude of the expansion in radial direction. The foreshortening is directly proportional to the diameter expanded. The result shows in the case of slotted tube stent the increment in the radial expansion will result in the increment of the foreshortening. The amount of foreshortening was 0.6418 mm at the end of the deflation process.

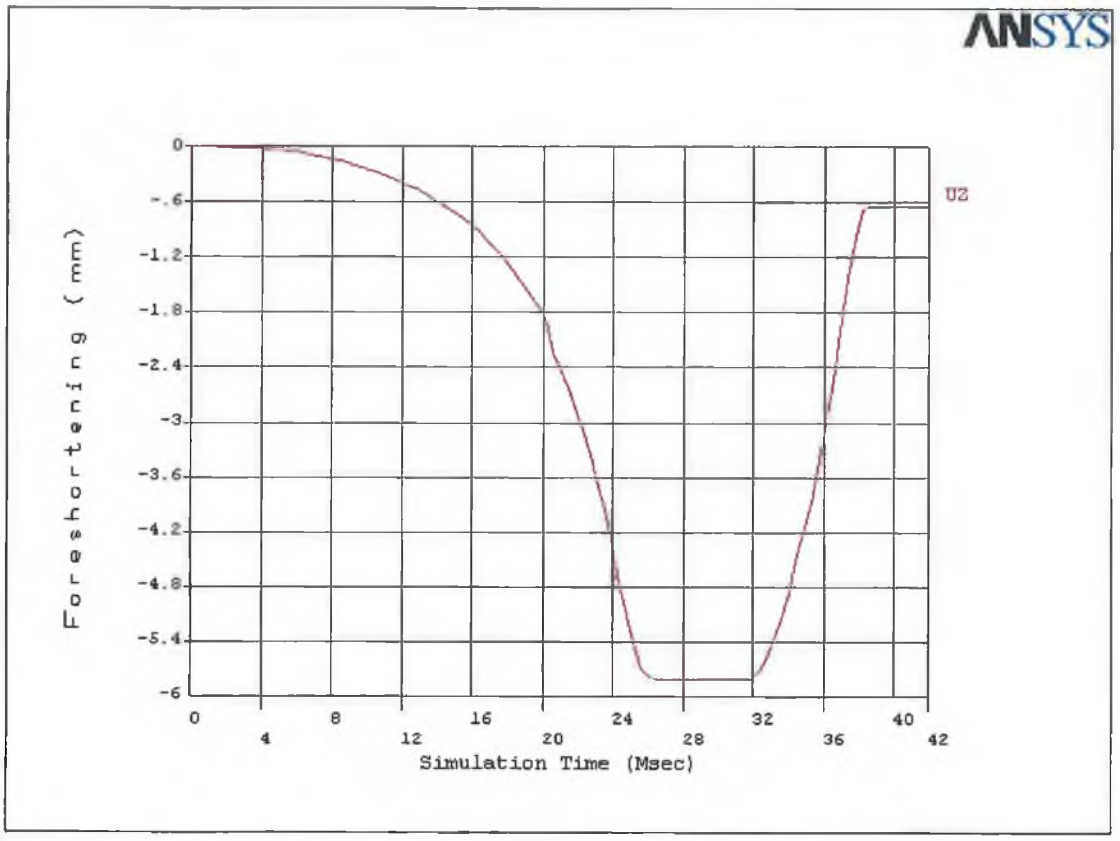

Figure 5.127: Foreshortening of the slotted tube with simulation time

Chapter 6

EXPERIMENTAL WORK

6.1 Introduction

This chapter outlines the process undertaken in order to carry out the experiment on slotted tube stents, in order to aid in the validation of finite element results.

6.2 Experimental Equipment

The test rig consists of two shelves secured on a movable platform. Figure 6.1 shows the upper shelf section with the specimen in place. Figure 6.2 shows the entire platform of the test rig.

- The **Lower shelf** contains
    - A unit of manual (hand) pump 4.5 cc per stroke, containing two cylinders, enclosed in a protective casing
    - One cylinder acted as an oil reservoir feeding the second cylinder
    - The second cylinder provides stability in pressure
    - A leaver that attaches to the hydraulics pump

- The **Upper shelf** contains
  - A Polycarbon safety cover
  - Quick release clamps on Polycarbon cover
  - A pressure gauge (0 – 60 Bar)
  - A pressure release valve (shut off valve)
  - A test bed mounting frame which supports inflow and outflow nozzles
  - A spillage tray to collect any spillage during or after the experimental test

- **Other supplementary materials**
  - Piping connecting the pumping unit to the inflow and outflow nozzles and the spillage tray
  - Two tapered collars (washer) to prevent the ends of balloon from deviation during the expansion process
  - Two jubilee clips for securing the balloon tube to the inflow and outflow nozzles
  - Ratchet for tightening up the jubilee clips

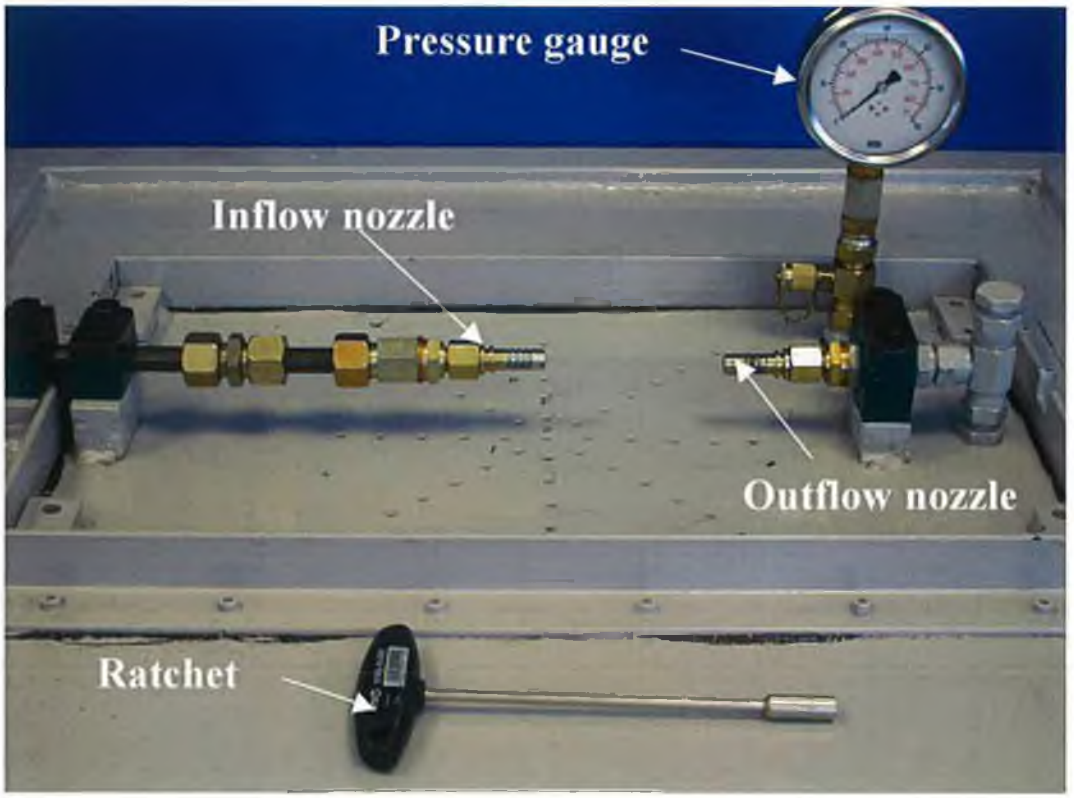

Figure 6.1: Upper shelf section with specimens in place

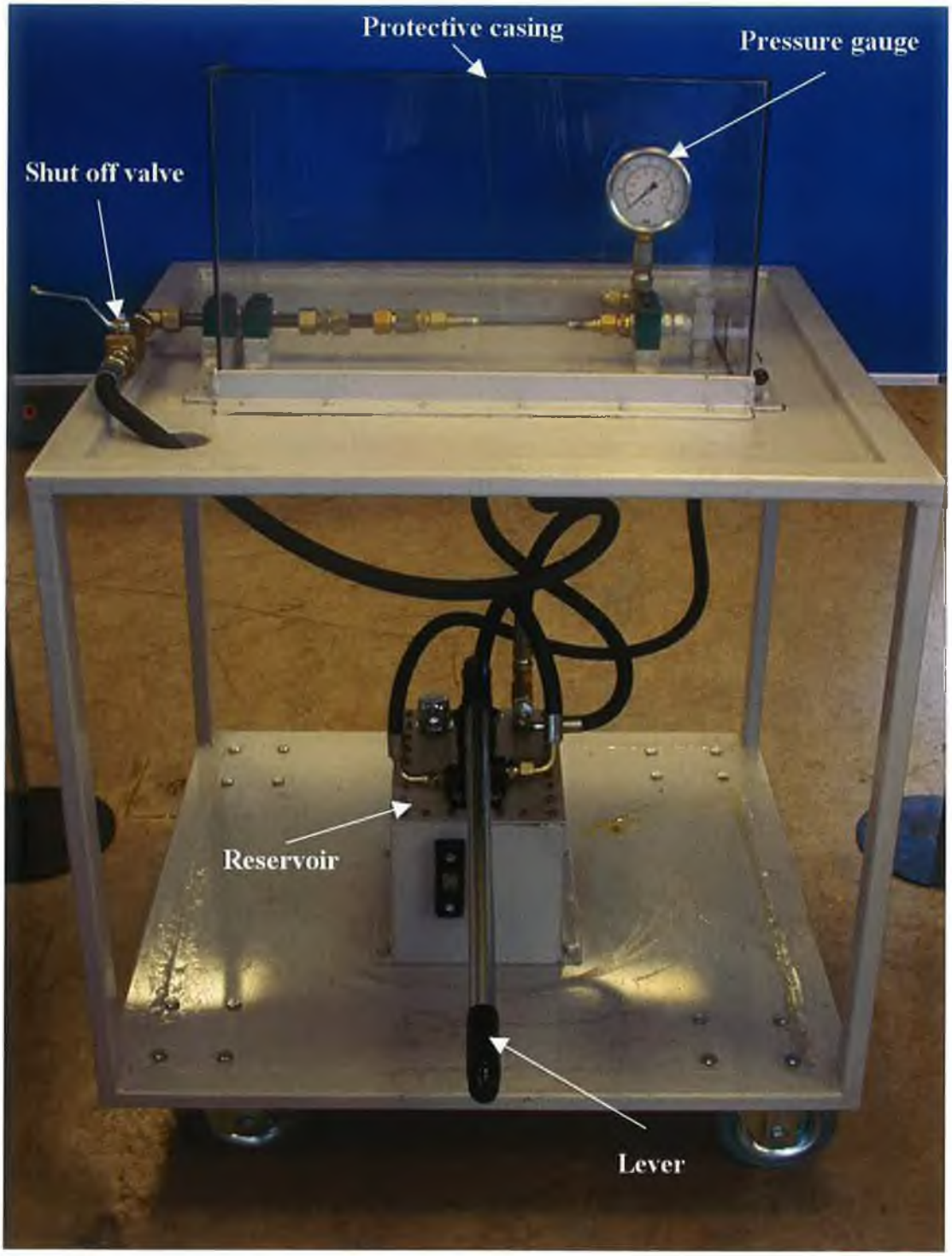

Figure 6.2: Entire assembly of the apparatus

6.3 Material Used

The slotted tube stents are made of Stainless steel 304. They were manufacturing by 3D laser cutting. The inner and outer diameters of the stent read as 23 mm and 25.4 mm with 86.8 mm in length. The details dimension of the stents is described in section 5.8. Figure 6.3 to Figure 6.7 illustrate the different geometry of stents.

- The **specimens** consist of
    - Expansion medium i.e. balloon tube (Polyethylene and PVC)
    - Slotted tube stents with different geometries as described in section 4.9

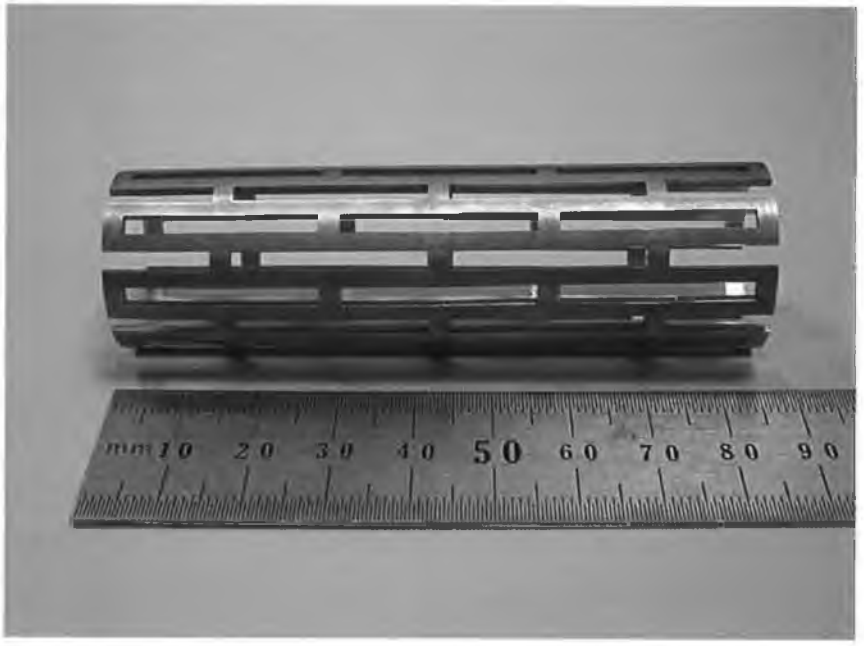

Figure 6.3: Design 1 (width of slot = width of strut)

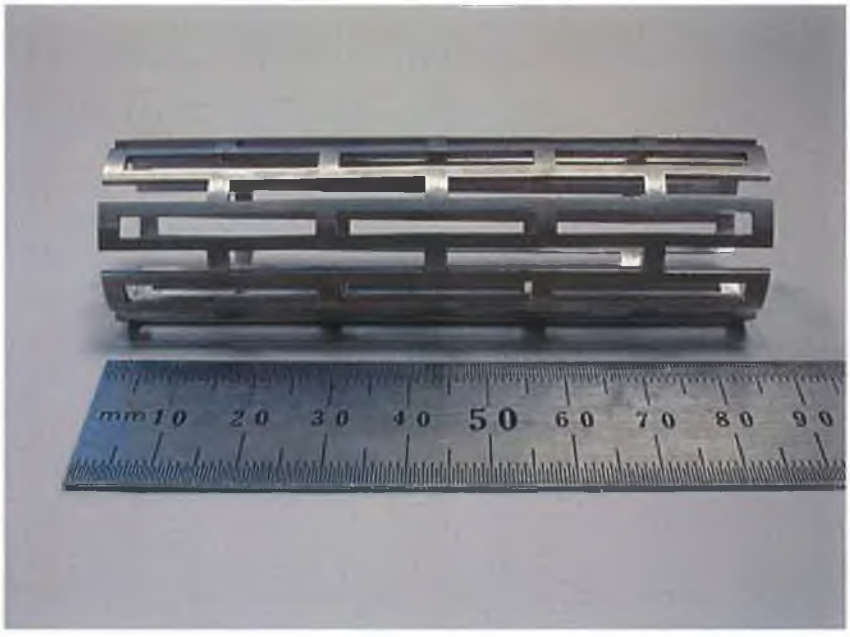

Figure 6.4: Design 2 (20 % increase in width of the slot)

Figure 6.5: Design 3 (20 % decrease in width of the slot)

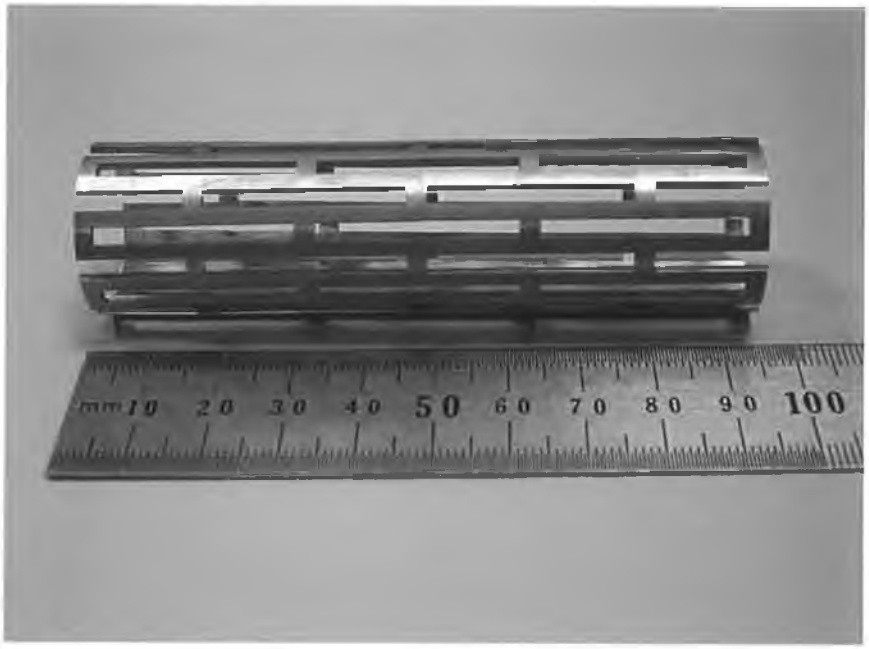

Figure 6.6: Design 4 (10 % increase in length of the slot)

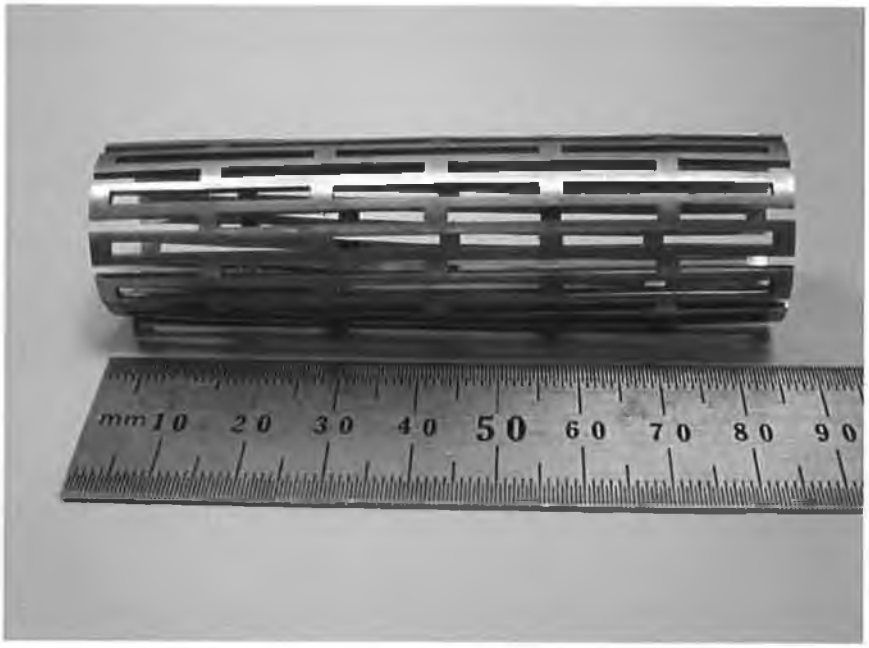

Figure 6.7: Design 5 (50 % increase in the number of slot)

6.4 Experimental Procedures

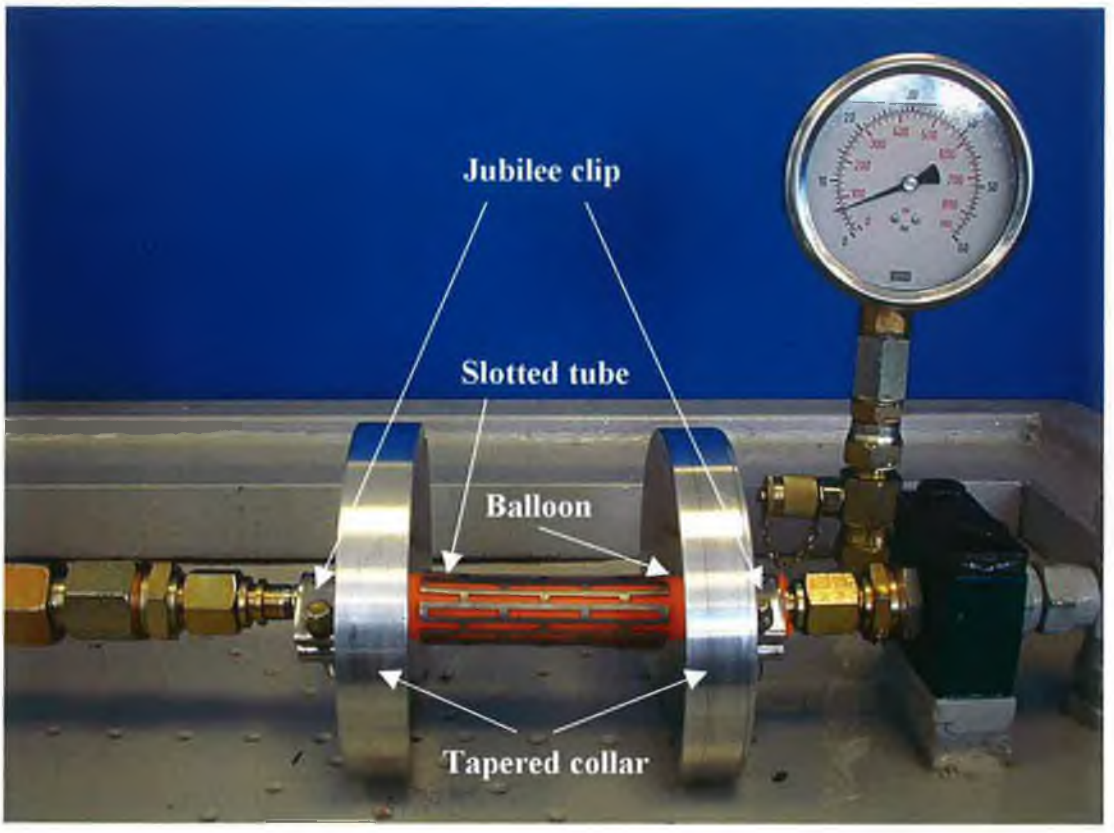

Figure 6.8: Slotted tube in place

Figure 6.8 shows the slotted tube is in the position for expansion process. The steps involved in carrying out the experiment are as follows:

1. Attach a balloon tube to the outflow nozzle and add a jubilee clip for securing the balloon tube to the nozzle.
2. Add a collar follow by a stent then another collar in that order.
3. Attach a second jubilee clip to the inflow nozzle.
4. Attach the unconnected end of the balloon tube to the inflow nozzle and secure under the jubilee clip.
5. Secure all clips tightly with the ratchet.
6. Take initial reading of the stent at its centre and each end.
7. Cover the test bed mounting frame with the protective casing.

8. Attach the leaver to the pump.
9. Apply gradual pressure by pumping slowly with the leaver.
10. Measure the ends and central diameter of the stent at every 5 bars increment of pressure load.
11. Monitor the reading on the pressure gauge until certain level of pressure is reached depending on the geometry of the stents.
12. Release the pressure by opening the shut off valve so that the oil returns to the reservoir.
13. Repeat from step one for the next specimen.

6.5 Result and Discussion

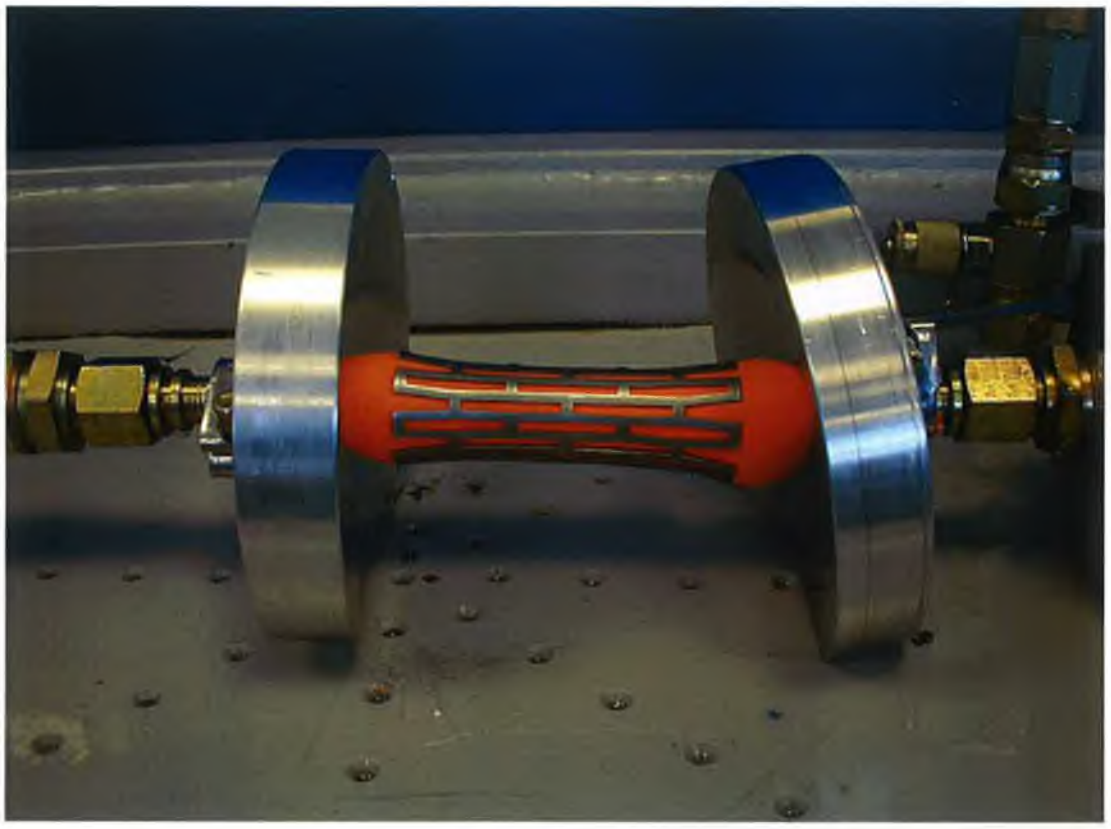

Figure 6.9: The expansion of the slotted tube by polyethylene rubber

Figure 6.9 shows the expansion of the slotted tube at pressure load of approximately 1 MPa. The central and the end diameter of the slotted tube at that point of time were 25.78 mm and 30.90 mm respectively. Further expansion was not allowed as the

balloon burst at the right hand side before it reached the targeted pressure load. The excessive bulging at right hand side of the balloon contributed to the rupture of the balloon. The tapered collars dislocated from its position during the expansion process. The cause of dislocation was due to the expanding balloon forcing the tapered collar bending towards one end. The dislocations of the tapered collars exaggerated the non-uniformity of the expanding balloon as the pressure load increased.

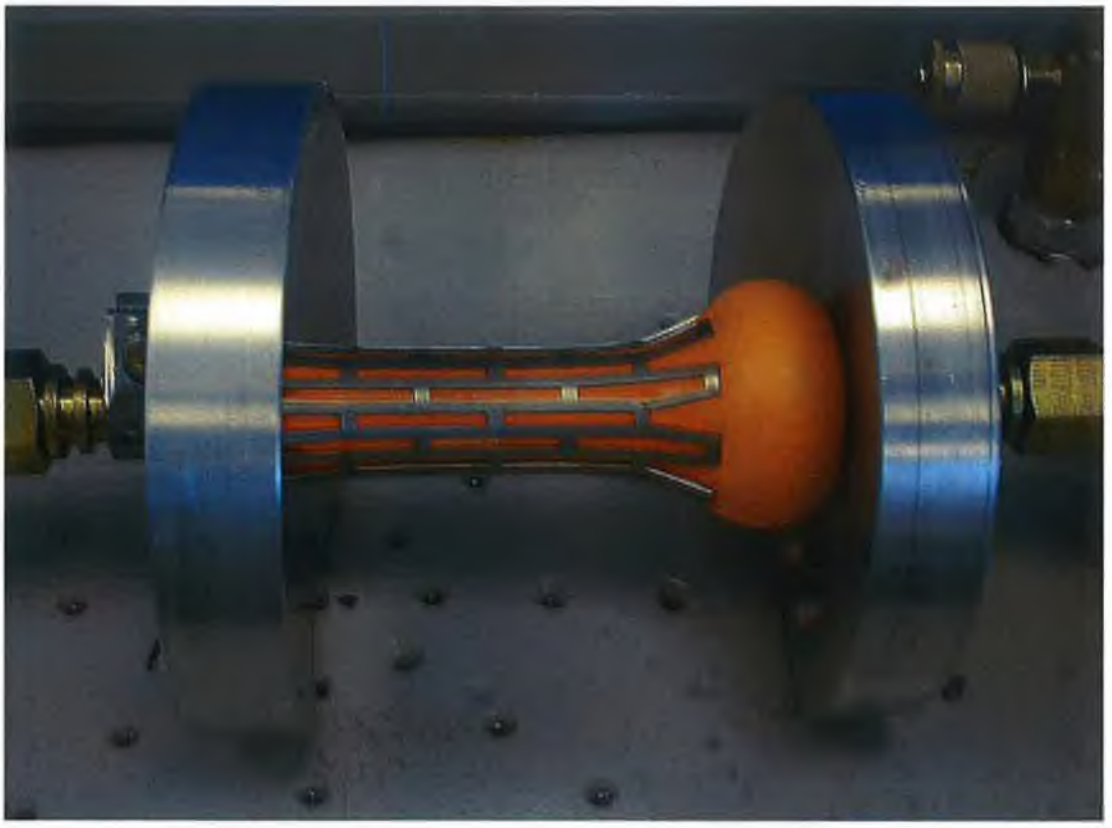

Figure 6.10: The expanding balloon near the point of rupture

Figure 6.10 shows the expansion of the slotted tube with the balloon in the vicinity of rupture point. As can be seen from the figure that the balloon formed into a dumbbell kind of shape on the right hand side. It only managed to deform at one end of the slotted tube. The balloon seemed to be too soft as an expansion medium for the slotted tube expansion.

After several more tests, it was felt that an experiment is needed to carry out on the balloon alone was necessary in order to understand the expansion behaviour of the balloon itself. The balloon was easily expanded but in a non-uniform way as expected. One end of the balloon slacked and burst as the pressure increased. A few more experiments were then carried out on new specimens with lower strength. The outcomes of the tests were found to be the same. Most of the specimens were found to only expand to a certain degree and at one end of the slotted tube as shown in Figure 6.11. The non-uniformity of expansion of the balloon is responsible for the failure for the further expansion of the slotted tube.

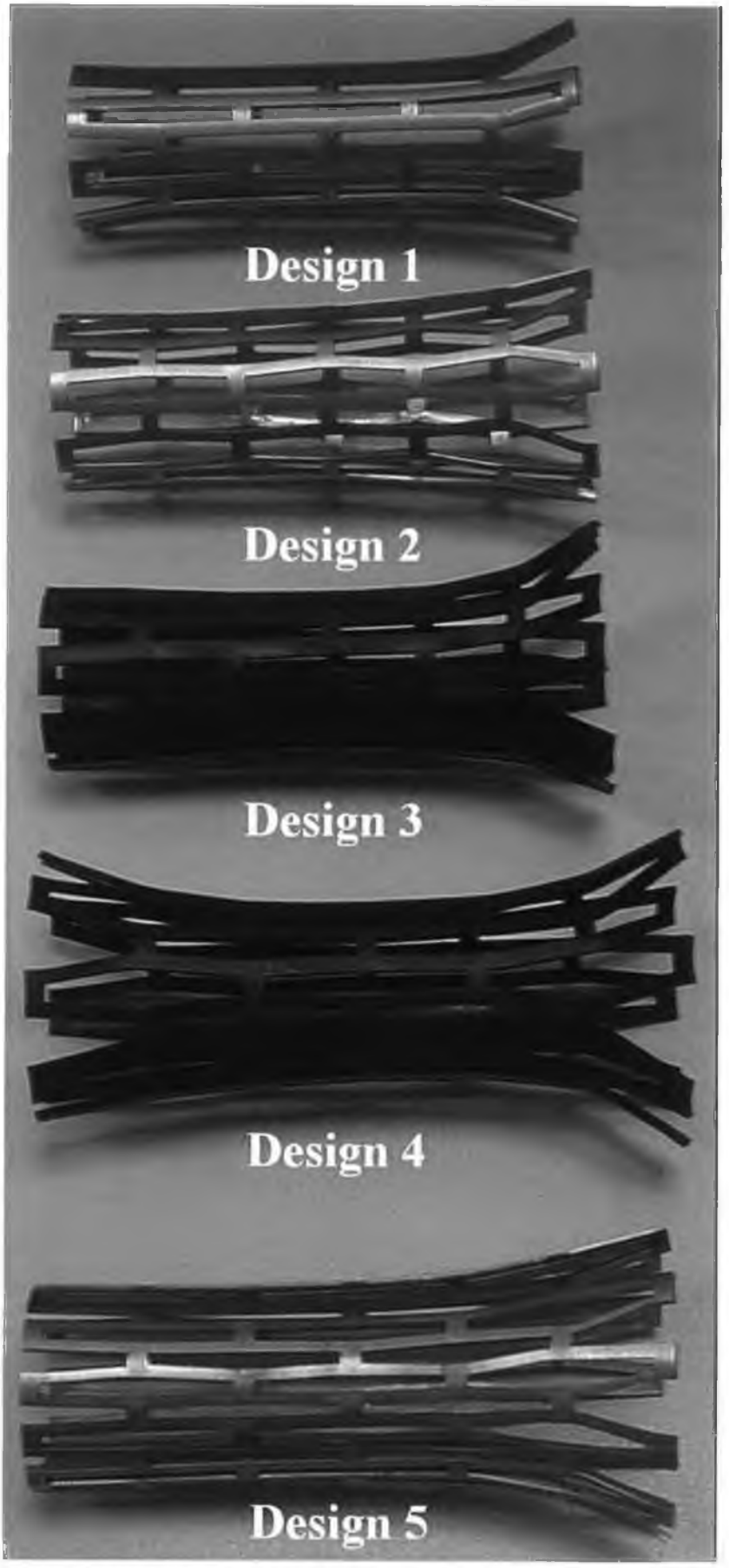

Figure 6.11: Slotted tubes after the expansion process by polyethylene balloon

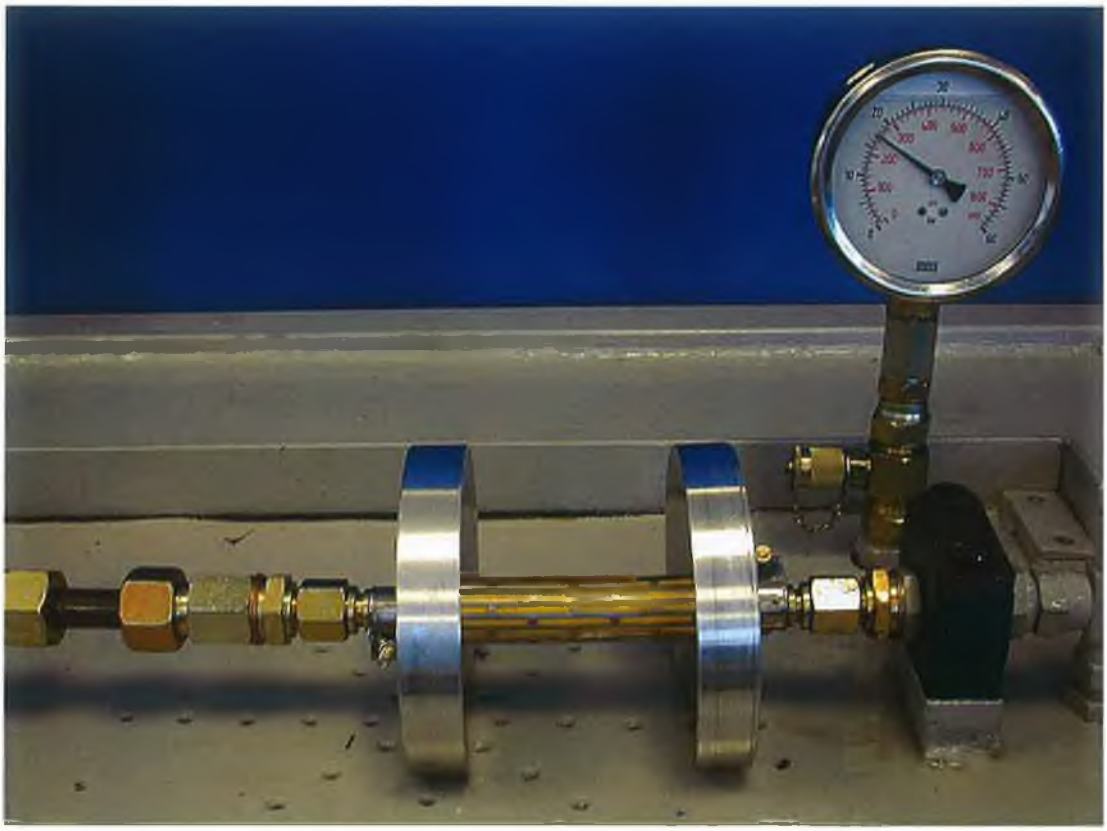

Figure 6.12: The expansion of the slotted tube by PVC

Figure 6.12 shows the expansion of the slotted tube at pressure load of approximately 2 MPa. The central and end diameter of the slotted tube at that point in time was 28.9 mm and 28.38 mm. As noticed, this type of balloon enables the slotted tube to expand more uniformly and the expansion was not only occurred at one end of the slotted tube (Figure 6.13). However, it was also noticed that the pressure dropped during the expansion of the slotted tube. The pressure dropped was due to the expansion of the slotted tube. The expansion of the slotted tube resulted in the decrease in pressure as it is controlled by the volume of the fluid in the pipes. The expansion in radial direction increases when the pressure increases. Nevertheless, as the supply of pressure stopped and reached the targeted 2 MPa, the expansion continued slowly. This was due to the tensile force exerted by the fluid and also some structures of the slotted tube had experienced some deformation that made further expansion easier. So, the volume increased as the deformation continued without the supply of the fluid. As a result, the pressure dropped from the initial 20 MPa to 1.7 MPa.

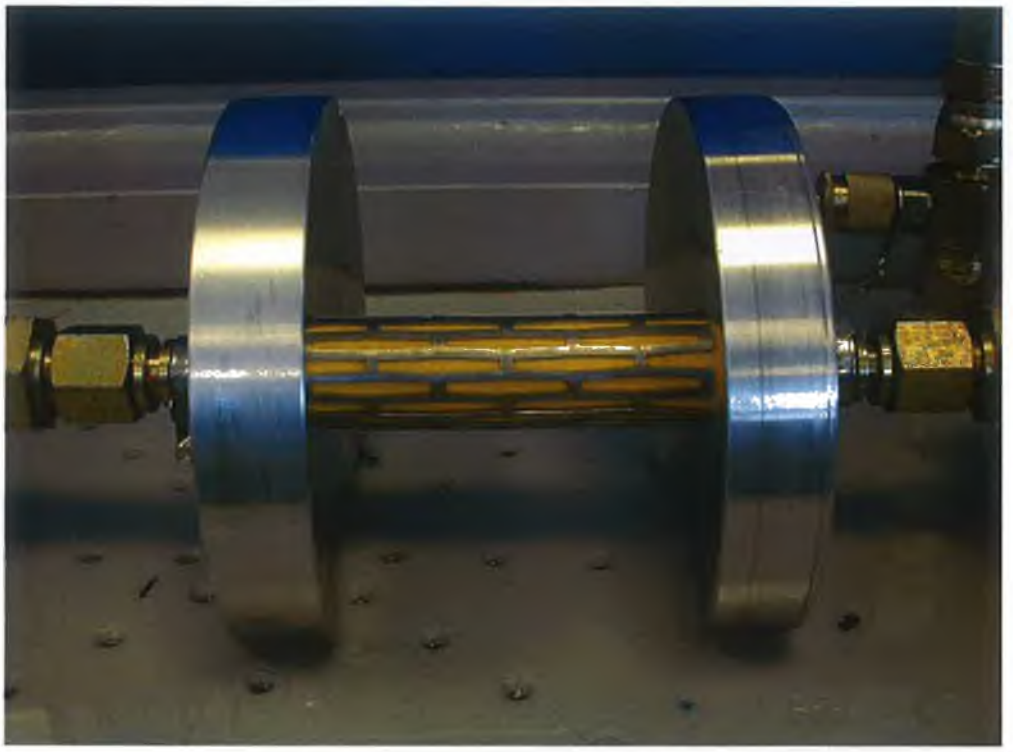

Figure 6.13: Closer view of the slotted tube during the expansion process

Figure 6.14 shows the expansion of the slotted tube as the pressure increased to 2.5 MPa. It was noticed that the expansion on the right hand side of the slotted tube became less prominent compared to the central part. The central and the end diameter of the slotted tube at this point of time were 30.46 mm and 29.62 mm respectively. Likewise, the pressure dropped during the expansion process even though it was increased to the targeted 2.5 MPa. The pressure settled at 1.6 MPa at the end of the expansion process. As the pressure increased, some areas of the balloon expanded unsteadily and a little bubble began to emerge which could be seen on the surface near the end of the balloon. This indicates that the balloon would burst at anytime if further pressure is exerted and indeed the balloon burst before the next 0.5 MPa increment of pressure was reached. The central and end diameter of the slotted tube when the balloon burst were 32.68 MPa and 34.74 mm. Figure 6.15 shows the slotted tube before and after the expansion.

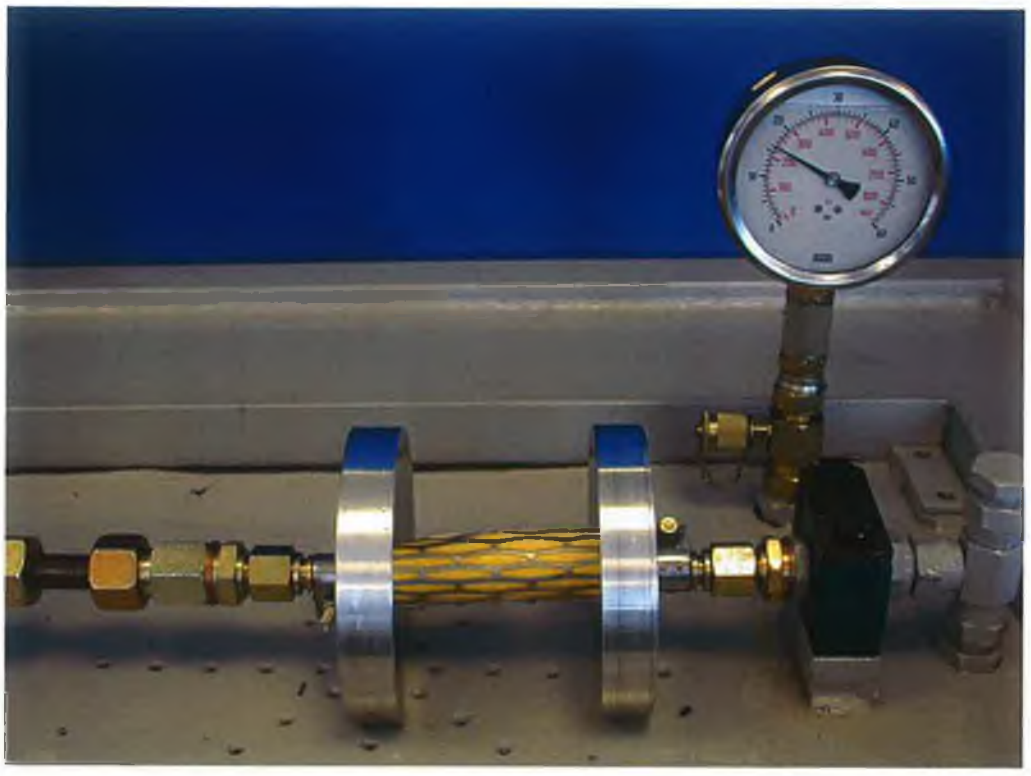

Figure 6.14: The expansion of slotted tube at 2.5 MPa

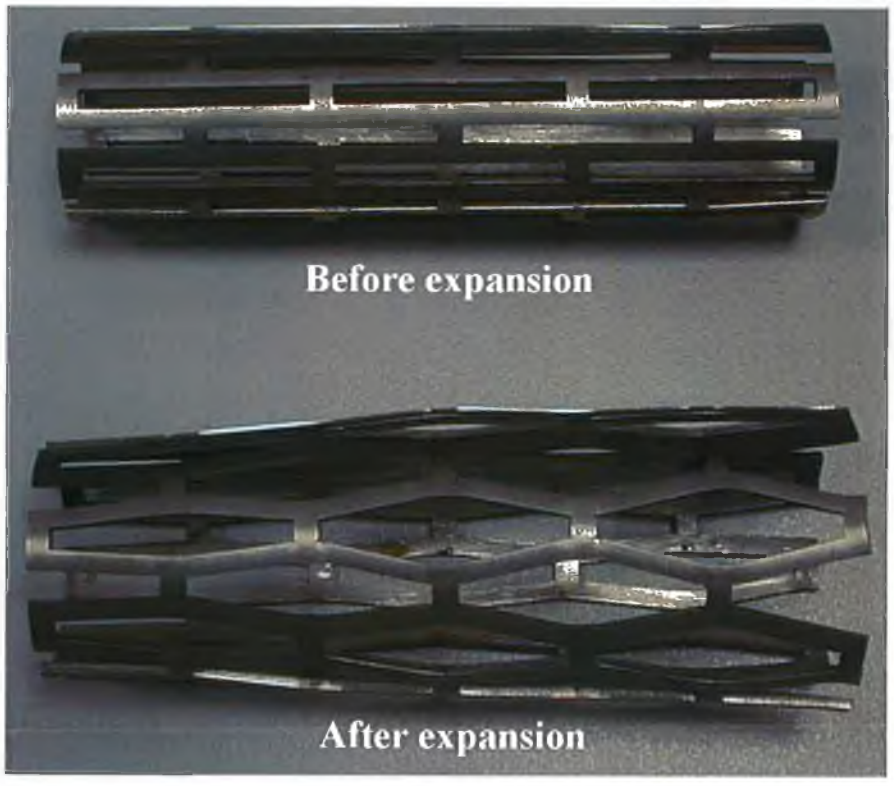

Figure 6.15: The expansion of the slotted tube after the rupture of the balloon

Figure 6.16 shows the results of the expanded slotted tubes by PVC balloon material. It seems that the ultimate deformation of the slotted tubes are subject to the balloon material. The results obtained using the PVC as the expansion medium seems to be able to manage the slotted tube expansion to a certain degree and the outcomes are more encouraging. However, it seems to have failed to expand uniformly as the case with polyethylene balloon material. The slotted tube also tends to open up only at one end of the tube. This may be due to the material itself being too stiff and the inconsistency of the slots width during the machining process.

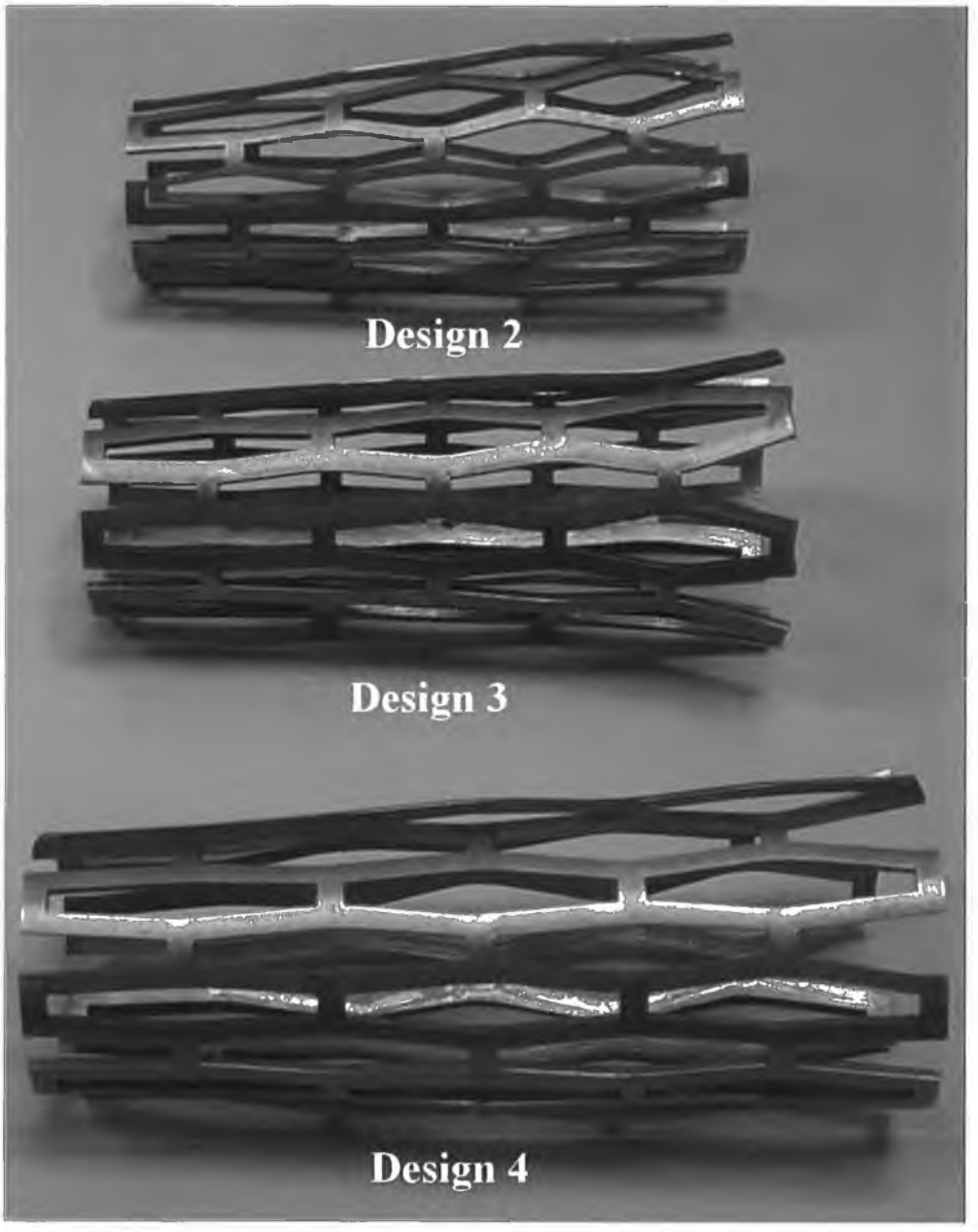

Figure 6.16: Slotted tubes after the expansion process by PVC balloon material

Chapter 7

CONCLUSIONS

7.1 Expansion of Slotted Tube Stent without Balloon

- Smaller pressure and lower pressure rate will probably generate greater potential diameter but it also can introduce buckling of the stent, which is not desirable on stent deployment.
- Higher pressure rates will result in higher stresses in the stent for similar levels of deformation.
- Pressure load produces different states of stress in stent. The state of stress in stent is varied with the application of different load rate. The ultimate geometry obtained is dependent on the load rate applied.
- Higher rate of pressure generates higher stress but lower radial displacement.
- Higher pressure rate improves the geometry of the stent.
- The contraction of the stent is high in proportion to the expanded diameter when lower pressure rate comes into account.
- The understanding of the expansion characteristics serves as a fundamental knowledge towards later investigations.

7.2 Expansion of Slotted Tube Stent with Balloon

- A better understanding of the dilatation behaviour of stent is gained. To conduct an experiment in vivo is extremely expensive. With the help of finite element analysis, it is possible to look into the details of a particular design or technology.
- A great understanding of the software is essential to correctly approach the problem and simulate the particular problem as closely as possible.
- It is possible to establish a relationship for the initially unknown pressure with a dynamic analysis program like LS-DYNA.
- A detailed analysis of the stent leads to a good understanding of the flaws and consequently failure or success of the design. This analysis also provides the information for further investigation.

7.3 Analysis of Deployment Pressure on Slotted Tube Stent Expansion

- The diameter of slotted tube stent increases significantly when a certain level of pressure is reached depending on the design structure of the stent.
- Different nodes in different locations of the geometry produce different stress history.
- Four stages of response during the inflation and deflation process are initial ramp loading, steady state response, release of pressure, and separation of balloon.
- Higher deployment pressure produces greater expansion in the radial direction but it is achieved at the expense of foreshortening of the stent.
- Higher deployment pressure might increase the expansion in the radial direction but it does not necessarily increase the uniformity of the slotted tube stent.

7.4 Analysis of Balloon Length on Slotted Tube Stent Expansion

- Moderate balloon length is a necessity in order to produce a uniform slotted tube stent after expansion.
- Longer balloon length requires lower pressure load to achieve a similar level of expansion in the radial direction during the dilatation process.
- The length of balloon has an impact on the elastic recoil of a slotted tube stent. Longer balloon length will generally encourage elastic recovery and hence reduce the diameter of the tube.
- Excessive length of balloon results in over-expansion of slotted tube stent.
- Longer length of balloon also contributes to greater foreshortening.

7.5 Analysis of Friction on Slotted Tube Stent Expansion

- Increasing friction between the balloon and the slotted tube stent results in a lower level of expansion and less stress in the deformed component.
- Higher pressure is needed to achieve the same level of expansion with friction included. This is due to the fact that the stress generated in the slotted tube during the expansion is not as high as in the friction free case.
- Elastic recoil decreases with increasing friction value.
- The use of the friction value reduces the foreshortening of a stent.

7.6 Analysis of Scaling the Slotted Tube Stent Size

- Finite element simulations are able to predict reliable results for the same geometry but different sizes of slotted tube stents.
- As a result, experimental tests could be carried out to validate the results for the bigger slotted tube size (which is cheaper to manufacture) and compare with a real stent.
- Higher scaling factor results in higher stent diameter and the diameter achieved at each level of pressure closely follows the ratio of the size of the slotted tube.

7.7 Analysis of Slotted Tube Stent Production Defect

- The results from the analyses suggest that the slotted tube stent is not very sensitive to imperfections.
- Stress concentrations are found to be located at the areas where the flaws exist.
- The statistics show that the discrepancy of stresses between the flaw and flawless slotted tube is insignificant despite the stress concentration in the imperfect slotted tube.
- The imperfect slotted tube stent experiences higher levels of expansion for the same level of deployment pressure but the magnitude of discrepancy is insignificant. This indicates that the response of the body struts to the ultimate deformation of the tube geometry, as a whole, is not strongly connected.

7.8 Analysis of Balloon Thickness on Slotted Tube Stent Expansion

- The analyses show that balloon thickness affects the uniformity of slotted tube stent enormously if the same elasticity and length of the balloon is assumed.
- Balloon thickness has little effect on the distribution of stress in the slotted tube despite the fact that higher pressure is applied and a thicker balloon is utilised.
- Increasing the pressure proportional to the thickness of balloon results in nearly the same level of radial displacement. However, the magnitude of increment in pressure load is lower than the magnitude of increment in balloon thickness.
- The magnitude of elastic recoil and foreshortening decreases with increasing balloon thickness.
- A thicker and stiffer balloon material allows the slotted tube to mould itself around the balloon rather than letting the balloon mould around the slotted tube.

7.9 Analysis of Slotted Tube Stent Geometry

- Altering the stent strut configuration and number has practical effects on the clinical use of vascular stents, as the magnitude of expansion will change.
- If a stent consists of same number of struts and slots, increasing the length of the slots may be better than increasing the width of the slots as a higher expansion rate would be achieved.
- Increasing the length of struts does not have a major effect on the stress distribution in slotted tube stent.
- Increasing the number of slots make more material available for expansion of slotted tube stent and effectively increases the expansion rate.
- Increasing the strut number and regularity of strut distribution provides a more circular shape of stent and therefore more circular vascular lumen after deployment of stent. This may have a significant impact on biological effects after implantation.
- The analyses attest to the importance of stent geometry as a whole and may serve as guidelines for future stent design and the choice between stents of differing designs.
- Increasing the length of struts might have a major impact on elastic recoil but it has a minor impact on the foreshortening.
- Foreshortening increases with increased strut width.

7.10 Simulation of Balloon, Stent, Plaque and Artery

- The simulation successfully demonstrated the function and the application of slotted tube stent in which the artery is successfully opened and the stent remained in the artery as a scaffold.
- The results of the present study demonstrate that stents are able to withstand the remodelling of artery and plaque that otherwise may have contributed to restenosis.
- Finite element analyses demonstrated that maximum surface contact stress grew higher at a point where the plaque surface and struts surface come into contact, reflecting greater degrees of plaque extrusion between struts.

- Although the geometry of the plaque and artery are not an ideal realistic model of a human stenosed artery, it demonstrates the possible regions of higher stresses that would be induced within the vessel. This data, therefore, provides new insights regarding the utility of stents in the treatment of atherosclerotic lesions.

7.11 Experimental Work

- It was learnt that the slotted tube stent begins its expansion at both ends of the tube. Despite this, the data was inconclusive in showing uniform expansion due to the failure to maximise its expansion ability.
- If the expansion medium is too soft the slotted tube expansion tends to develop more at the ends of the stent.
- It gives a good indication that the models developed could be expanded to a proper shape if the right expansion medium is used.
- Although the slotted tube stents failed to expand properly the feel of "how" and "where" the expansion occurs is gained which will help in future studies.

7.12 Thesis Contribution

Stent implantation is a non-surgical method that is becoming increasingly important and widely used to treat coronary artery disease as it holds several advantages over other methods. The understanding of the mechanism in terms of the mechanical point-of-view to date has been very limited and important aspects such as stent expansion characteristic, stress and strain conditions in the deformed shape, strut-related injuries, and effects of altering various parameters under various conditions have been largely unknown. As a result failures in the stent deployment process have been common and mostly discussed only in the medical and biological aspect. This has indeed raised a major concern in cardiology and stent technology. The simulations of this work will contribute significant knowledge in this area for future comparative studies of mechanical performance of stents. This includes the design of new stents and also mechanical performance in clinical practice. In eliminating

failures, the aid of the detailed simulation analyses may help the application of stent technology to step into a new era. In particular, the simulations in this work have provided:

- A methodology in which expansion characteristics, deployment pressure, radial expansion, elastic recoil, foreshortening etc. can be predicted and estimated.
- A wide range of different geometry models and variable designs in which the detrimental and beneficial effects on slotted tube stent expansion were identified.
- The state of stress, magnitude of expansion, elastic recoil and foreshortening in the deformed slotted tube stent during the dilatation and deflation process.
- An insight regarding the utility of stents in the treatment of atherosclerotic arteries.
- An insight regarding the sensitivity of the slotted tube stent.
- The possibility of scaling the stent to a preference size and still maintaining the accuracy of result.
- The stent models can be used with modelling methodology as a probe to investigate the issues concerning the mechanical action of the artery walls on the stent in future.
- The understanding of the mechanism of interaction between balloon catheter, stent, plaque and arterial wall. This may help to limit the failure of stent implantation and shed lights on the issue of stent restenosis that has not been solved.

7.13 Recommendations for Further Work

- Vascular injury during stent placement provokes thrombosis and restenosis. Two major mechanisms of damage are stent strut-related injury and balloon-artery interactions. Broad variations in stent design and techniques of deployment attest to a lack of data for precisely studying stent-related artery injuries.

- The human artery consists of several layers such as intimal layers, medial layers and adventitial layer. The intima is the innermost layer and the adventitia is the outermost layer. The media is somewhere in between the two layers. Each layer of the arterial wall consists of different mechanical properties. Therefore, further investigation should be carried out with the three layers of arterial wall included.
- Different type of plaque caps contains different material properties. Three different types of plaque caps that range from softest to toughest are cellular plaque cap, fibrous plaque cap and calcified plaque cap. The same approach can be used to simulate different plaque caps.
- Stainless steel was used as the tube material in all simulations in this work. It is possible to rerun the models used to examine the results of using different tube materials.
- CFD analysis can be undertaken to study the arterial response to pulsating flow that may have influence on the movement of the stent away from its intended location after it has been inflated.

REFERENCES

[1] D. M. Cosgrove, The cardiac report, Discoveries In Cardiovascular Disease And Treatment Interventional Cardiology, 1999.

[2] D. R. Holmes III and R. A. Robb, Processing, Segmentation, and Visualization of Pre- and Post Stent Coronary Arteries Using Intra-Vascular Ultrasound, Conference on Image Display, 1998, Vol. 3335, 72-82.

[3] MedicineNet.com, Coronary artery bypass graft (CABG) surgery, http://www.medicinenet.com:80/script/main/Art.asp?li=MNI&ArticleKey=308.

[4] S. B. King III, N. J. Lembo, W. S. Weintraub, et al. A randomized trial comparing coronary angioplasty with coronary bypass surgery, The New England Journal of Medicine, 1994, Vol. 331, 1044-1050.

[5] MedicineNet.com, Percutaneous Transluminal Coronary Angioplasty (PTCA), http://www.medicinenet.com:80/script/main/Art.asp?li=MNI&ArticleKey=271.

[6] A. P. George, Stenting, Cardiology Advisory Board of Heart Center Online.

[7] D. R. Holmers, R. E. Vliestra, H. C. Smith, et al., Restenosis after percutaneous transluminal coronary angioplasty (PTCA): A report from the PTCA registry of the National Heart, Lung and Blood Institute, American Journal of Cardiology, 1984, Vol. 53, 77-81.

[8] R. Erbel, M. Haude, H. W. Hopp, et al., Coronary-artery stenting compared with balloon angioplasty for restenosis after initial balloon angioplasty, N. Eng. J. Med., 1996, Vol. 339, 1672-1678.

[9] A. I. Lituchy, Atherectomy, Heart Center Online.

[10] A. Javey, Laser Angioplasty: Application of excimer lasers in angioplasty, The World of Science.

[11] G. S. Mintsz, B. N. Potkin, G. Keren, et al. Intravascular ultrasound evaluation of the effect of rotational atherectomy in obstructive atherosclerotic coronary artery disease, Circulation, 1992, Vol. 86, 1383-1393.

[12] A. I. Maclsaac, T. S. Bass, M. buchbinder, at al. High speed rotational atherectomy: Outcome in calcified and non calcified coronary artery lesions, J. Am. Coll. Cardiol., 1995, Vol. 26, 731-736.

[13] A. I. Lituchy, Laser Angioplasty, Heart Center Online.

[14] R. E. Kuntz, R. D. Safian, M. J. Levine, et al., Novel aproach to the analysis of restenosis after the use of three new coronary devices, Journal of American College of Cardiology, 1992, Vol. 19, 1493-1499.

[15] Lemaitre, et al., Inventional Cardiology, The Cowen Report, 1996.

[16] J. M. Rankin and I. M. Penn, Coronary Stenting: A global perspective, American College of Cardiology, 1998, 22-25.

[17] P. W. Serruys. P. E. Jaegere, F. Kiemeneij, et al., A comparison of balloon-expandable-stent implantation with balloon angioplasty in patients with coronary artery disease, N. Engl. J. Med, 1994, Vol. 331, 489-495.

[18] D. L. Fischman, M. B. Leon, D. S. Baim, et al., A ramdomized comparison of coronary-stent placement and balloon angioplasty in the treatment of coronary artery disease, N. Engl. J. Med, 1994, 331, 496-501.

[19] D. S. Baim, J. P. Carrozza, Stent thrombosis: Closing in on the best preventive treatment, Circulation, 1997, Vol. 95, 1098-1100.

[20] G. J. Karrillon, M. C. Morice, E. Benveniste, et al., Intracoronary stent implantation without ultrasound guidance and with replacement of conventional anticoagulation by antiplatelet therapy: 30-day clinical outcome of the French Multicenter Registry, Circulation, 1996, Vol. 94, 1519-1527.

[21] A. Schomig, F. J. Meumann, A. Kastrati, A randomized comparison of antiplatelet and anticoagulant therapy after placement of coronary artery stents, N. Engl. J. Med., 1996, Vol. 334, 1084-1089.

[22] A. Kastrati, A. Schoemig, S/ Schuelen, et al., Predictive factors of restenosis after coronary stent placement, Journal of American of College of Cardiology, 1997, Vol. 30, 1428-1436.

[23] M. Gottsauner-Wolf, D. J. Lincoff, E. J. Topol, Restenosis-- an open profile, Clinical Cardiology, 1997, Vol. 19, 347-356.

[24] J. W. Currier, D. P. Faxon, Restenosis after percutaneous transluminal coronary angioplasty: Have we been aiming at the wrong target?, Journal of American College of Cardiology, 1995, Vol. 25, 516-520.

[25] D. P. Faxon, T. A. Sanborn, V. J. Weber, et al., Restenosis following transluminal angioplasty in experimental atherosclerosis, Arteriosclerosis, 1984, Vol. 4, 189-195.

[26] L. Freitag, R. Eicker, B. Linz, et al., Theoretical and experimental basis for development of dynamic airway stent. European respiratory Journal, 1994, Vol. 7, 2038-2045.

[27] P. Wong, W. H. Leung, C. M. Wong, Migration of the Ave micro coronary stent, Catheterization and Cardiovascular Diagnosis, 1996, Vol. 38, 267-273.

[28] H. Bjarnason, D. W. Hunter, M. R. Crain, et al., Collapse of a Palmaz stent in the subclavian vein, American Journal of Roentgenology, 1993, Vol. 160, 1123-1124.

[29] A. C. Einsenhauer, T. C. Piemonte, D. E. Gossman, et al., Extraction of fully deployed coronary stents, Catheterization and Cardiovascular Diagnosis, 1996, Vol. 38, 393-401.

[30] H. Hautmann, R. M. Huber, Stent flexibility: an essential feature in the treatment of dynamic airway collapse, European Respiratory Journal, 1996, Vol. 9, 609-611.

[31] K. Rosenfield, R. Schainfeld, A. Pieczek, et al., Restenosis of endovascular stents from stent compression, Journal of American of College of Cardiology, 1997, Vol. 29, 328-338.

[32] M. L. Woodall, The need for standartization testing for safety and efficacy of permanent implant stents, Journal of Invasive Cardiology, 1996, Vol. 8, 471-477.

[33] C. Rogers, E. R. Edelman, Endovascular stent design dictates experimental restenosis and thrombosis, Circulation, 1995, Vol. 91, 2995-3001.

[34] S. Sheth, F. Litvack, V. Dev, et al., Subacute thrombosis and vascular injury resulting from slotted-tube nitinol and stainless steel stents in a rabbit carotid artery model, Circulation, 1996, Vol. 94, 1733-1740.

[35] C. T. Dotter, Transluminally placed coilspring endarterial tube grafts: Long-term patency in canine popliteal artery, Investigative Radiology, 1969, Vol. 4, 327-332.

[36] C. T. Dotter, R. W. Buschmann, M. K. McKinney, J. Rosch, Transluminal expandable nitinol coil stent grafting: Preliminary report, Radiology, 1983, Vol. 147, 259-260.

[37] A. Cragg, G. Lund, J. Rysary, et al., Nonsurgical placement of arterial endoprostheses: a new technique using nitinol wire, Radiology, 1983, Vol. 147, 261-263.

[38] D. Maass, L. Kropf, L. Egloff et al, Transluminal implantation of intravascular "double helix" spiral prostheses: Technical and biological considerations, *ESAO Proc* 9, 1982, 252-256.

[39] D. Maass, C. L. Zollikofer, F. Largiader and A. Senning, Radiological follow-up of transluminally inserted vascuular endoprostheses: An experimental study using expanding spirals, *Radiology*, Vol. 152, 1984, 659-663.

[40] D. Maass, D. Demierre, D. Deaton, et al, Transluminal implantation of self-adjusting expandable prostheses: Principles, techniques, and results, *Prog. Artif. Org.*, 1983, 979-987.

[41] C. L. Zollikofer, F. Antonucci, G. Stuckmann, P. Mattieas and E. K. Salomonowitz, History overview on the development and characteristics of stents and future outlooks, *CardioVascular and International Radialogy*, Vol. 15, 1992, 272-278.

[42] V. Sigwart, J. Puel, V. Mirkovitch, et al, Intravascular stents to prevent occlusion and restenosis after transluminal angioplasty, *N Engl J Med*, Vol. 316, 1987, 701-706.

[43] R. Moer, Y. Myreng, P. Molstad, et al., Stenting small coronary arteries using two second-generation slotted tube stents: Acute and six-month clinical and angiographic results, Catheterization and cardiovascular interventions, 2000, Vol. 50, 307-313.

[44] J. M. T. Charles, Stenting in Europe, what lessons can we learn? Development of a stent classification system based on a survey of European clinical experiences, Catheterization and Cardiovascular Diagnosis, 1998, Vol. 45, 217-232.

[45] R. B. Ziad, Elchanan Bruckheimer, C. L. Jon, et al., Implantation of balloon-expandable stents for coarctation of the aorta: Implantation data and short-term results, Catheterization and Cardiovascular Diagnosis, 1996, Vol. 39, 36-42.

[46] A. Roguin, E. Grenadier, B. Peled, et al., Acute and 30-day results of the serpentine balloon expandable stent implantation in simple and complex coronary arterial narrowings, American Journal of Cardiology, 1997, Vol. 80, 1155-1162.

[47] J. J. Goy, U. Sigwart, P. Vogt, et al., Long-term follow-up of the first 56 patients treaated with intracoronary self-expanding stents (the Lansanne experience), American Journal of Cardiology, 1991, Vol. 67, 569-572.

[48] P. W. Serruys, B. H. Strauss, K. J. Beatt, et al., Angioplasty follow-up after placement of a self-expnading coronary-artery stent, N Eng J Med, 1991, Vol. 324, 13-17.

[49] C. Charnsangavej, H. Carrasco, S. Wallace, et al, Stenosis of the vena cava: Preliminary assessment of treatment with expandable metallic stents, *Radiology*, 1986, 161, 295-298.

[50] F. Joffre, J. Puel, C. Imbert, et al, Use of a new type of self-expanding vascular stent prosthesis: Early clinical results, *Presented at the 72nd Scientific Assembly and Annual Meeting of the Radiological Society of North America*, Chicago, 1986 November 30-December 5.

[51] J. C. Palmaz, R. R. Sibbitt, S. T. R. Reuter, et al, Expandable intraluminal graft: A preliminary study, *Radiology*, Vol. 156, 1985, 73-77.

[52] J. C. Palmaz, S. A. Windeler, F. Garcia, et al, Atherosclerotic rabbit aortas: Expandable intraluminal grafting, *Radiology*, Vol. 160, 1986, 723-726.

[53] J. C. Palmaz, R. R. Sibbitt, S. R. Reuter, et al, Expandable intrahepatic portacaval shunt stents: Early experience in the dog. *AJR*, Vol. 145, 1985, 821-825.

[54] J. C. Palmaz, F. Garcia, R. R. Sibbitt, et al, Expandable intrahepatic portacaval shunt stents in dogs with chronic portal hypertension, *AJR*, Vol. 147, 1987, 1251-1254.

[55] J. C. Palmaz, R. R. Sibbitt, F. O. Tio, et al, Expandable intraluminal vascular graft: A feasibility study, *Surgery*, Vol. 99, 1986, 199-205.

[56] J. C. Palmaz, D. T. Kopp, H. Hayashi, et al, Normal and stenotic renal arteries: Experimental balloon-expandable intraluminal stenting, *Radiology*, Vol. 164, 1987, 705-708.

[57] J. C. Palmaz, Balloon-expandable intravascular stent, *AJR*, Vol. 150, 1988, 1263-1269.

[58] R. A. Schatz, J. C. Palmaz, F. O. Tio, et al, Balloon-expandable intracoronary stents in the adult dog, *Circulation*, Vol. 76, 1987, 450-457.

[59] H. C. Herrmann, M. Buchbinder, M. Cleman, et al, Emergent use of balloon-expandable stenting for failed percutaneous transluminal coronary angioplasty, *Circulation*, Vol. 86, 1992, 812-819.

[60] M. Haude, R. Erbel, H. Issa, et al, Quantitative analysis of elastic recoil after balloon angioplasty and after intracoronary implantation of balloon expandable Palmaz-schatz stents, *J Am Coll Cardiol*, Vol 21, 1993, 26-34.

[61] G. S. Roubin, A. D. Cannon, S. K. Agrawal, et al, Intracoronary stenting for acute and threatened closure complicating percutaneous transluminal coronary angioplasty, *Circulation*, Vol. 85, 1992, 916-927.

[62] P. De Jaegere, P. W. Serruys, M. Bertrand, et al, Wiktor stent implantation in patients with restenosis following balloon angioplasty of a native coronary artery, *J Am Coll cardiol*, Vol. 69, 1992, 598-602.

[63] U. Sigwart, R. H. Haber, G. J. Kowlachuk, et al, The new ACS metallic stent: Experimental and clinical experience, *Circulation*, Vol. 88, 1993, I-646 (Abstract).

[64] D. Keane and P. W. Serruys, Different stents for different coronary lesions, *Recent Advances in Cardiology*, 1995, 45-67.

[65] R. Balcon, R. Beyar, S. Chierchia, et al., Recommendations on stent manufacture, implanatation and utilization, European Heart Journal, 1997, Vol. 18, 1536-1547.

[66] S. M. Lugate, D. C. Potter, European derectives on medical devices, BMJ 1993, Vol. 307, 459-460.

[67] J. V. De Giovanni, Medical devices: new regulations, new responsibilities, Br. Heart J, 1995, Vol. 73, 401-402.

[68] Julio C. Palmaz, Intravascular stenting: from basic research to clinical application, Cardiovascular and Interventional Radiology, 1992, Vol. 15, 279-284.

[69] G. David Jang and Paulo A. Ribeiro, The ideal characteristics of a coronary stent, Rev. Port. Cardiol., 1999, Vol. 18 (Supl. I), 87-95.

[70] C. L. Zollikofer, I. Largiader, W. F. Bruhlmann, et. Al., Endovascular stenting of veins and grafts, Preliminary clinical Experience, Radiology, 1988, Vol. 167, 707-712.

[71] J. A. Barra, A. Volant, J. P. Leroy, et. al., Constrictive perivenous mesh prosthesis for preservation of vein integrity, J. Thorac. Cardiovasc. Surg., 1986, Vol. 92, 330-336.

[72] M. J. Thubrikar, J. W. Baker, S. P. Nolan, Inhabition of atherosclerosis associated with reduction of arterial intramural stress in rabbits, Arteriosclerosis, 1988, Vol. 8, 410-420.

[73] H. Bjarnason, D. W. Hunter, M. R. Crain, et al., Collapse of a Palmaz Stent in the subclavian vein, American Journal of Radiology, 1993, Vol. 160, 1123-1124.

[74] J. C. Palmaz, Intravascular stents: Tissue-stent interactions and design considerations, American Journal of Radiology, 1993, Vol. 160, 613-618.

[75] G. P. Teitelbaum, W. G. Bradley and B. D. klein, MR imaging artifacts, feromagnetism and magnetic torque of intravascular filters, stents, and coils, Radiology, 1988, Vol. 166, 657-664.

[76] C. Hehrlein, M. Zimmermann, J. Metz, et al., Influence of surface texture and charge on the biocompatibility of endovascular stents, Coronary Artery Disease, 1995, Vol. 6, 581-586.

[77] I. D. Scheerder, K. Wang, J. Sohier, et al., Metallic surface treatment using electrochemical polishing decreases thrombogenicity and neointimal hyperplasia after coronary stent implantation in a porcine model, *J Am Coll Cardiol*, Vol 31, 1998, 277A.

[78] B. D. Ratner, A. B. Johnston, T. J. Lenk, Biomaterial surfaces, Journal Biomed. Mater. Res., 1987, Vol. 21, 59-89.

[79] A. Kastrati, J. Dirschinger, P. Boekstegers, et al., Influence of stent design on 1-year outcome after coronary stent placement: A randomized comparison of five stent types in 1,147 unselected patients, Catheterization and Cardiovascular Interventions, 2000, vol. 50, 290-297.

[80] K. H. Barth, R. Virmani, J. Froelich, et al., Paired comparison of vascular wall reactions to Palmaz stents, Strecker tantalum stents, and Wallstents in canine iliac and femoral arteries, Circulation, 1996, Vol. 93, 2161-2169.

[81] S. Sheth, F. Litvack, V. Dev, et al., Subacute thrombosis and vascular injury resulting from slotted tube nitinal and stainless steel stents in a rabbit carotid artery model, Circulation, 1996, Vol. 94, 1733-1740.

[82] J. C. Squire, C. Rogers and E. R. Edelman, Stent geometry during inflation influences later restenosis, Circulation, 1996, Vol. 94, 259.

[83] A. Colombo, P. Hall, S. Nakamura, et al., Intracoronary stenting without anticoagulation accomplished with intravascular ultrasound guidance, Circulation, 1995, Vol. 91, 1676-1688.

[84] S. Nakamura, P. Hall, A. Gaglione, et al., High pressure assisted coronary stent implantation accomplished without intravascular ultrasound guidance and subsequent anticoagulation, J. Am. Coll. Cardiol. 1997, Vol. 29, 21-27.

[85] T. Akiyama, C. Di Mario, B. Reimers, et al., Does high-pressure stent expansion induce more restenosis?, J. Am. Coll. Cardiol. 1997, Vol. 29, 268.

[86] J. Dirschinger, A. kastrati, F. J. Neumann, et al., Influence of balloon pressure during stent placement in native coronary arteries on early and late angiographic and clinical outcome: A randomized evaluation of high-pressure inflation, Circulation, 1999, Vol. 100, 918-923.

[87] A. L. Golberf, A. Colombo, C. DiMario, et al., Does the use of aggressive stent dilatation lead to more late loss and restenosis?, J. Am. Coll. Cardiol. 1997, Vol. 29, 269.

[88] M. P. Savage, D. L. Fischman, J. S. Douglas, et al., The dark side of high pressure stent deployment, J. Am. Coll. Cardiol. 1997, Vol. 29, 270.

[89] S. E. Borgersen and R. L. Sakaguchi, Simulation inflation of a vascular stent using 3-Dimensinal non-linear FEA contact analysis, American Society of Mechanical Engineering, 1994, Vol. 28, 129A.

[90] E. C. Teo, Q. Yuan and J. H. Yeo, Design optimization of coronary stent using finite element analysis, ASAIO Journal, Vol. 46, 201A.

[91] C. Dumoulin and B. Cochelin, Mechanical behaviour modelling of balloon-expandable stents, Journal of Biomechanics, 2000, Vol. 33, 1461-1470.

[92] D. Y. Tseng, C. Rogers and E. R. Edelman, Effects of stent geometry, balloon compliance and deployment pressure on balloon-artery interactions during stent placement: A finite element analysis approach, Circulation, 1997, Vol. 96, 404A.

[93] C. Rogers, D. Y. Tseng, J. C. Squire, et al., Balloon-artery interactions during stent placement: A finite element analysis approach to pressure, compliance, and stent design as contributors to vascular injury, Circulation, 1999, Vol. 84, 378-383.

[94] H. Brauer, J. Stolpmann, H. Hallmann, et al., Measurement and numerical simulation of the dilatation behaviour of coronary stents, Messung und Rechnergestutzte Simulation des Verhaltens marktgangiger koronarer Stentsysteme, 1999, Vol. 30, 876-885.

[95] F. D. Whitcher, Simulation of in vivo loading conditions of Nitinol vascular stent structures, Computers and Structures, 1997, Vol. 64, 1005-1011.

[96] S. T. S. Al-Hassani, S. J. Burley and K. Kormi, A finite element simulation of angioplasty stent expansion in a partially closed artery, Abaqus Users' Conference, 1999.

[97] Etave, G. Finet, M. Boivin, et al., Mecahnical properties of coronary stents determined by using finite element analysis, Journal of Biomechanics, 2001, Vol. 34, 1065-1075.

[98] J. Bathe, Finite Element Procedures, Prentice-Hall International, 1996.

[99] Structural non-linearities (Training Manual), ANSYS Release 5.5, ANSYS, Inc., 1999.

[100] J. O. Hallquist, LS-DYNA3D Theoretical manual, Livermore Software Technology Corporation, Livermore, California, USA, 1993.

[101] ANSYS/LS-DYNA User's Guide, Release 5.4, ANSYS Inc., Houston, 1997.

[102] Explicit Dynamics with ANSYS/LS-DYNA (Training Manual), Release 5.6, ANSYS Inc., 2000.

[103] R. C. Hibbeler, Mechanics of Materials, 2d.ed, New York, Macmillan, 1994.

[104] A. J. Carter, D. Scott, L. R. Bailey, et al., Stent Design: In the "ends" it matters, J. Am. Coll. Cardiol., 1997, Vol. 29, 2259A.

[105] A. I. Veress, D. G. Vince, P. M. Anderson, et al., Vascular mechanics of the coronary artery, ASAJO, 2000, Vol. 89, II/92-II/100.

[106] A. I. Veress, J. F. Cornhill, E. E. Herderick, et al., Age-related development of atherosclerotic plaque stress: a population-based finite-element analysis, Coronary Artery Desease, 1998, Vol. 9, 13-19.

[107] I. K. De Scheerder, K. Wang, E. V. Verbeken, et al., Stent deployment pressure defines the stent/vessel wall relationship and has important implications for early and late outcome, J. Invasive Cardiol., 1998, Vol. 10 (3), 151-157.

Appendix 1:

LIST OF PUBLICATIONS

1. S. N. David Chua, B. J. MacDonald and M.S. J. Hashmi, Ouasi-static analysis of slotted tube (stent) expansion, Proceedings of 6th Biennial Conference on Engineering System Design and Analysis, Istanbul, Turkey, 2002.

2. S. N. David Chua, B. J. MacDonald and M.S. J. Hashmi, Finite element simulation of stent and balloon interaction, Proceedings of The International Conference on Advanced Materials Processing Technologies [AMPT'01], Madrid, Spain, 2001, 783-790.

3. S. N. David Chua, B. J. MacDonald and M.S. J. Hashmi, Finite element simulation of stent expansion, Journal of Materials Processing Technology, 2001, Vol. 120, 335-340.